TECHNISCHE UNIVERSITÄT WIEN
Vienna University of Technology

Dissertation

Numerical Modeling of the Blast Furnace Process
Injection of Auxiliary Reducing Agents Into the Raceway

ausgeführt zum Zwecke der Erlangung des akademischen Grades eines Doktors der technischen Wissenschaften unter der Leitung von

Univ. Prof. Dipl.-Ing. Dr. techn. Dr. h.c. Anton Friedl
Ass. Prof. Dipl.-Ing. Dr. techn. Michael Harasek

Institut für Verfahrenstechnik,
Umwelttechnik und Technische Biowissenschaften

Eingereicht an der Technischen Universität Wien
Fakultät für Maschinenwesen und Betriebswissenschaften

von

Dipl.-Ing. Christian Maier
Matr. Nr.: 9925510
Dreyhausenstraße 26/1/11, 1140 Wien

Wien, am 12. Juni 2015

„Jedes Naturgesetz, das sich dem Beobachter offenbart,
lässt auf ein höheres, noch unerkanntes schließen.“

Alexander Freiherr von Humboldt

Abstract

The purpose of the iron blast furnace is to chemically reduce and physically convert iron oxides to metallic liquid iron. Being invented centuries ago, this process was continuously improved, finally arriving at nowaday's efficient process. Even though today various routes for iron production are available, the blast furnace still states the major route for production of hot metal, worldwide the percentage of hot metal production estimates to approx. 95 %.

Besides iron bearing materials, flux and hot blast an essential feed necessary to operate a blast furnace is metallurgical coke that is fed on top of the furnace together with ores and various additives. Coke serves as a reaction partner for the reduction of iron oxides to produce metallic iron. Additionally to that it also forms a slowly descending porous supporting pillar that allows liquid hot metal and slag to trickle downwards, while gases injected via tuyères near the bottom of the furnace flow upwards to be withdrawn from the top of the shaft. The iron producing industry attempts to reduce coke rates in order to decrease the overall consumption of energy and primary raw materials. A promising strategy to lower coke consumption is to inject auxiliary carbon carriers via lances positioned in the tuyères in order to partially substitute coke. In the vicinity of the tuyère opening, the injected material is partially oxidized, delivering a share of the heat necessary to melt iron ores and for endothermic reactions. For optimal utilization a maximal conversion degree is desired in this zone.

This work aims to investigate the conditions near the tuyères at direct injection of auxiliary reducing agents. Due to the extreme conditions, experimental observation of operating blast furnaces is very difficult and therefore quite limited. The alternative chosen here is to apply the methods of computational fluid dynamics. Models have been developed to describe conversion of metallurgical coke and injected alternative reducing agents such as waste plastics, liquid hydrocarbons, pulverized coal and natural gas in the blast furnace raceway. The code is based on the solver ANSYS FLUENT®. The specific functionality necessary to describe the blast furnace process was implemented by introducing user-defined subroutines that were compiled and linked to corresponding solver interfaces. Right in front of the tuyère opening, a cavity is formed by hot blast injection at high speed. The shape of this so-called raceway is introduced based on a porous media approach avoiding the high computational effort of a more detailed formulation of multiphase flow. A new method was implemented that introduces an additional computational grid where conservation equations are solved for metallurgical coke. Consequently, this approach accounts not only for the gas flow in the blast furnace, but also aims at the examination of the movement and thermochemical conversion of the bed of solid coke particles. Reaction mechanisms were implemented to calculate the high temperature conversion of injected materials, homogeneous gas-phase reactions as well as coke utilization by heterogeneous reactions. By introducing proper addressing routines between the grid zones, the solver can also be run in parallel. This allows for the solution of flow problems in complex geometries in acceptable calculation times.

The successfully validated simulation model was applied to blast furnace A, operated by **voest**alpine Stahl GmbH in Austria. This unit is equipped to utilize a wide range of alternative reducing agents including heavy fuel oil, crude tar, natural gas, processed

waste plastics and pulverized coal. The introduction of waste plastics offers the promising opportunity to chemically recycle the material and also to utilize the energy contained in the hydrocarbons.

According to the modeling results, the liquid hydrocarbon spray is readily evaporated and consumed right within tuyère and raceway core in the time frame of several milliseconds. Processed waste plastics are injected in size classes in the range of several millimeters, whereby a different thermal behavior is provoked: The internal temperature profile of plastics is strongly inhomogeneous, thermolysis is restricted to zones near the particle surface. Consequently, plastic particles pass the raceway cavity, therefore thermal utilization takes place in regions with low oxygen partial pressures and gasification is favored. The residence time of plastic particles prior to full gasification was found to be in the order of several seconds. Devolatilization of injected coal particles is finished before the raceway boundary is reached. Due to the high stoichiometric oxygen demand for combustion of volatiles, endothermic gasification reactions are of high importance as oxygen partial pressures are low in the surroundings of the remaining char particles. According to the modeling results, approx. 80 % of the injected coal feed is converted in the raceway cavity.

The developed modeling tool offers the opportunity to study the conditions in the vicinity of blast furnace tuyères at varying operating conditions and geometric setups, delivering detailed insight to processes during feed utilization without the need for costly experimental observation. The results contribute to a better understanding of the processes, supporting the efforts to further decrease emissions and consumption of primary resources.

Kurzfassung

Hochöfen werden betrieben, um flüssiges Roheisen durch chemische Reduktion und physikalische Umwandlung von Eisenerzen zu gewinnen. Bereits vor Jahrhunderten wurde dieses Prinzip der Eisenproduktion gefunden – seither wurde die Technologie stetig verbessert und zum heutigen effizienten Hochofenprozess weiterentwickelt. Heutzutage stehen alternative Prozessrouten zur Verfügung, weltweit läuft mit ca. 95 % des Roheisenvolumens der überwiegende Großteil der Roheisenproduktion aber noch immer über den Hochofen ab.

Zusammen mit eisenhältigen Erzen, Schrottfraktionen und Schlackebildnern wird mit metallurgischem Koks ein weiterer wesentlicher Einsatzstoff dem Hochofen zugeführt. Dieser dient als Reaktionspartner zur Reduktion der oxidischen Eisenverbindungen und hat auch die wichtige Aufgabe, im Hochofen eine poröse Schüttung auszubilden. In den Hohlräumen fließen geschmolzenes Eisenoxid, Roheisen und Schlacke langsam nach unten zur Herdzone, während mit dem Heißwind eingebrachte Gase aufwärts strömen und oben als Gichtgas abgezogen werden. Die Eisenindustrie ist bestrebt, den spezifischen Koksbedarf zu senken, um den Verbrauch an primären Rohstoffen und Energieträgern zu reduzieren. Eine effiziente Methode stellt den Eintrag alternativer Kohlenstoffträger durch Eindüsung über Lanzen in den Blasformen dar, um so einen Teil des Kokses zu ersetzen. Diese Einsatzstoffe werden im Bereich vor den Blasformöffnungen teilweise oxidiert und decken so einen Teil des Wärmebedarfs für endotherme Reaktionen und Schmelzprozesse. Damit eine optimale Verwertung stattfindet ist eine möglichst vollständige Umsetzung in diesem Bereich erforderlich.

Ziel der vorliegenden Arbeit ist die Untersuchung der Bedingungen im Bereich der Blasformen bei Eindüsung alternativer Reduktionsmittel. Experimentelle Studien sind aufgrund der extremen Bedingungen in Hochöfen nur eingeschränkt möglich. Die hier gewählte Alternative beruht auf der mathematischen Modellierung mit den Methoden der numerischen Strömungssimulation. Dazu wurden Modelle zur Beschreibung des Hochofenprozesses im Bereich der Heißwindeindüsung entwickelt. Besonderes Augenmerk lag auf der Abbildung der thermochemischen Umsetzung von metallurgischem Koks und einer Reihe alternativer Reduktionsmittel wie Kunststoffabfallfraktionen, Schweröl, Kohlestaub und Erdgas. Das Simulationsprogramm wurde aufbauend auf den finite Volumen-Solver ANSYS FLUENT® entwickelt. Die spezifische Funktionalität zur Modellierung des Hochofenprozesses wurde durch Erweiterung des Gleichungslösers um benutzerdefinierte Programmroutinen eingeführt, welche kompiliert und an den entsprechenden Schnittstellen in den Lösungsalgorithmus eingebunden wurden. Durch das Einblasen des Heißwindes mit hohen Geschwindigkeiten wird im Hochofen unmittelbar vor den Blasformen jeweils ein Hohlraum gebildet. Im Modell wird die Form dieser sogenannten Raceway über Porositätsmodelle abgebildet, wodurch der wesentlich höhere Rechenaufwand detaillierterer Mehrphasenmodelle vermieden werden kann. Eine neue Methode zur Beschreibung der Mehrphasenströmung wurde implementiert: In dieser wird ein weiteres Rechengitter eingeführt, auf welchem die Bilanzgleichungen für metallurgischen Koks gelöst werden. Es wird also nicht nur die Gasphase im Hochofen betrachtet, sondern auch die Strömung und thermochemische Umwandlung der Kokspartikel berechnet. Reaktionsmechanismen wurden eingeführt, die die Umsetzung der eingedüsten alternativen

Reduktionsmittel, homogene Gasphasenreaktionen und heterogene Reaktionen der Koksphase beschreiben. Eine spezielle Adressierungsroutine zwischen den beiden Gitterzonen ermöglicht es, den Solver zu parallelisieren. Dadurch ist es möglich, auch die Strömung in komplexen Geometrien in vertretbaren Rechenzeiten zu berechnen.

Das validierte Simulationsmodell wurde auf den Hochofen *A* angewendet, betrieben von **voest**alpine Stahl GmbH in Österreich. Dieser Hochofen kann mit einer breiten Palette alternativer Reduktionsmittel wie Schweröl, Teere, Erdgas, Kunststoffabfallfraktionen und Kohlestaub beaufschlagt werden. Die Verwertung von Kunststoffabfällen ermöglicht es, diese Kohlenwasserstoffe chemisch wiederzuverwerten und gleichzeitig auch deren Energieinhalt zu nutzen.

Den Simulationsrechnungen zufolge werden eingedüste flüssige Kohlenwasserstoffe durch Ausbildung eines feinen Sprühnebels vollständig im Bereich der Blasform und innerhalb der Racewayzone in Verweilzeiten im Bereich von Millisekunden verdampft. Kunststoffpartikel werden auf Größenverteilungen von einigen Millimetern aufbereitet, wodurch beim Einblasen in den Hochofen ein stark inhomogenes Temperaturprofil innerhalb der Partikel induziert wird. Die Erwärmung bleibt auf einen engen Bereich nahe der Partikeloberfläche beschränkt, Thermolyse findet nur hier statt. Aufgrund deren Größe durchqueren die Kunststoffpartikel die Raceway mit dem eingeblasenen Heißwind, die Zersetzung findet daher vermehrt in Bereichen statt wo Sauerstoffpartialdrücke niedrig sind und daher bevorzugt Vergasungsreaktionen ablaufen. Bis zur vollständigen Umsetzung liegen die für die Kunststoffpartikel berechneten Verweilzeiten im Bereich einiger Sekunden. Beim Eintrag gemahlener Kohle werden die flüchtigen Bestandteile der Kohle vollständig freigesetzt, bevor die Partikel die Racewaygrenze erreicht haben. Die Flüchtigen weisen bei deren Umsetzung einen hohen stöchiometrischen Sauerstoffbedarf auf. Die Sauerstoffpartialdrücke in der Umgebung der nach der Pyrolyse verbleibenden Koksrückstände sind daher niedrig und Vergasungsreaktionen durch CO_2 und H_2O spielen eine wichtige Rolle bei der Umsetzung. Den Berechnungen zufolge werden bei den untersuchten Eindüsraten ca. 80 % der eingeblasenen Kohle innerhalb der Raceway umgesetzt.

Das entwickelte Hochofenmodell ermöglicht es, die Bedingungen in der näheren Umgebung der Blasformöffnungen bei verschiedenen Betriebsbedingungen zu berechnen und diese zu vergleichen, ohne dass aufwändige experimentelle Untersuchungen angestellt werden müssen. Es kann so ein detaillierter Einblick gegeben werden, der zu einem besseren Prozessverständnis führt und so zu einer weiteren Reduktion von Emissionen und Primärenergieverbrauch beitragen kann.

Contents

List of Figures

List of Tables

Publications

The following journal articles, conference papers and presentations have arisen from aspects of the work performed in the preparation of this thesis.

Journal publications

- Maier, C., Jordan, C., Harasek, M., Feilmayr, C., and Thaler, C.: Implementation and Validation of a Three-Dimensional Multiphase-CFD-Model for Blast Furnace Processes. *Chemical Engineering Transactions*, Vol. 29, 2012, pp. 925–930. doi: 10.3303/CET1229155.

- Maier, C., Jordan, C., Knepper, M., Babich, A., Senk, D., Feilmayr, C., Thaler, C. and Harasek, M.: Numerical and Experimental Study of Alternative Reductant Injection into the Raceway of the Blast Furnace. *Berg- und Hüttenmännische Monatshefte*, Vol. 158, No. 11, 2013, pp. 453–454. doi: 10.1007/s00501-013-0191-3.

- Maier, C., Jordan, C., Harasek, M., Feilmayr, C., and Thaler, C.: Investigation of Alternative Reducing Agent Injection into the Raceway of Blast Furnaces using CFD. *Chemical Engineering Transactions*, Vol. 35, 2013, pp. 1345–1350. doi: 10.3303/CET1335224.

- Jordan, C., Maier, C., Harsfalvi, Z., Kiss, B., and Harasek, M.: Optical and numerical analysis of droplet breakup. *Chemical Engineering Transactions*, Vol. 39, 2014, pp. 1735–1740. doi: 10.3303/CET1439290.

Conference presentations

- Maier, C., Jordan, C., Harasek, M., Feilmayr, C. and Thaler, C.: Development and Validation of a CFD-Model for Heterogeneous Transfer Phenomena in Blast Furnace Processes. *5^{th} International Conference from Scientific Computing to Computational Engineering IC-SCCE*, Athens, Greece, July 4-7, 2012, pp. 162–169. ISBN: 978-960-98941-9-7.

- Maier, C., Jordan, C., Harasek, M., Feilmayr, C. and Thaler, C.: Implementation and Validation of a Three-Dimensional Multiphase-CFD-Model for Blast Furnace Processes. *15^{th} Conference on Process Integration, Modelling and Optimisation for Energy Saving and Pollution Reduction*, Prague, Czech Republic, August 25-29, 2012. ISBN: 978-88-95608-20-4.

- Maier, C., Jordan, C., Feilmayr, C., Thaler, C. and Harasek, M.: CFD-Simulation of the Blast Furnace Process: Injection of Heavy Oil and Plastic Particles into the Raceway. *AISTech, The Iron and Steel Technology Conference and Exposition, Pittsburgh*, PA, USA, May 6-9, 2013, pp. 595–607. ISBN: 978-1-935117-32-2.

- Maier, C., Jordan, C., Harasek, M., Feilmayr, C. and Thaler, C.: Investigation of Alternative Reducing Agent Injection into the Raceway of Blast Furnaces using CFD. *16th Conference on Process Integration, Modelling and Optimisation for Energy Saving and Pollution Reduction*, Rhodes, Greece, September 29 - October 2, 2013. ISBN 978-88-95608-26-6.

- Maier, C., Jordan, C., Harasek, M., Feilmayr, C. and Thaler, C.: CFD-Modellierung der Eindüsung fester und flüssiger Einsatzstoffe in den Hochofen bei verschiedenen Prozessbedingungen. *VDI Jahrestreffen der Fachgruppen Computational Fluid Dynamics, Mischvorgänge und Rheologie*, Würzburg, Deutschland, Februar 24-25, 2014.

- Maier, C., Jordan, C., Feilmayr, C., Thaler, C. and Harasek, M.: CFD-Modeling Study of the Blast Furnace Raceway with Direct Injection of Auxiliary Reducing Agents. *AISTech, The Iron and Steel Technology Conference and Exposition*, Indianapolis, Ind., USA, May 5-8, 2014, pp. 583–592. ISBN: 978-1-935117-41-4.

- Maier, C., Jordan, C., Feilmayr, C., Thaler, C. and Harasek, M.: Multi-Scale Modeling of Hydrocarbon Injection into the Blast Furnace Raceway. *10th International Conference on CFD in Oil & Gas, Metallurgical and Process Industries*, Trondheim, Norway, June 17-19, 2014, pp. 2C1-091. ISBN: 978-82-14-05741-6

- Maier, C., Jordan, C., Feilmayr, C., Thaler, C. and Harasek, M.: Numerical Analysis of Injection of Liquid Hydrocarbons, Processed Waste Plastics and Pulverized Coal into Blast Furnace Raceways. *AISTech, The Iron and Steel Technology Conference and Exposition*, Cleveland, Ohio, USA, May 4-7, 2015, pp. 1569–1580. ISBN: 978-1-935117-46-9.

1 Introduction

The development of the human civilization was strongly influenced by iron and steel, being broadly used e.g. in agriculture, construction, households, medicine and of course machine building. Thus, besides coal and cotton, steel is one of the principal materials upon which the industrial revolution was based [1]. Still steel is one of the most important materials used in construction work, industry and daily life products. After the oil crisis (1974 to 1976, caused by an oil embargo by OPEC-states in 1973), the annual production of crude steel more or less stagnated until the 1990s. Since then, the steel production has increased considerably [1, 2, 3]. Up to now, the world-wide steel demands are still growing (see fig. 1.1). The main reason for increase in production rates in the last decade is the rapid economic development in China (see the charts in fig. 1.2).

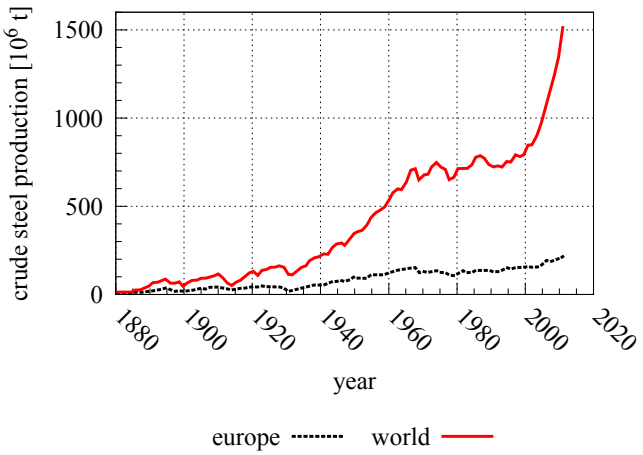

Figure 1.1: Annual crude steel production (data source: [1]).

Worldwide, in total $1513 \cdot 10^6$ tons of crude steel were produced in the year 2011, of which $570 \cdot 10^6$ tons originated from recycling of scrap. Therefore, almost 40 % of the annual steel demand is covered by reuse of valuable ferrous scrap, allowing for the overall reduction of CO_2 emissions by 58 %, as compared to steel production from primary resources alone [4, 5]. To cover the needs, the gap of steel demands has to be closed by steel production from primary resources.

In the earth crust, following oxygen, silica and alumina, iron is the fourth most abundant element with a share of approx $4.7\,\%_{w/w}$. Therefore, after alumina, iron is the secondly most existing metal in our environment. Most of the iron is bound in oxides and is available as iron ore. Only a minor number of the known iron-containing minerals are feasible for economically efficient production of hot metal [3]. Most important for the production of raw iron from ores are hematite (Fe_2O_3) and magnetite (Fe_3O_4). These oxides are found in the crust in different kinds of ores with an average iron content of $60 - 65\,\%$ [6].

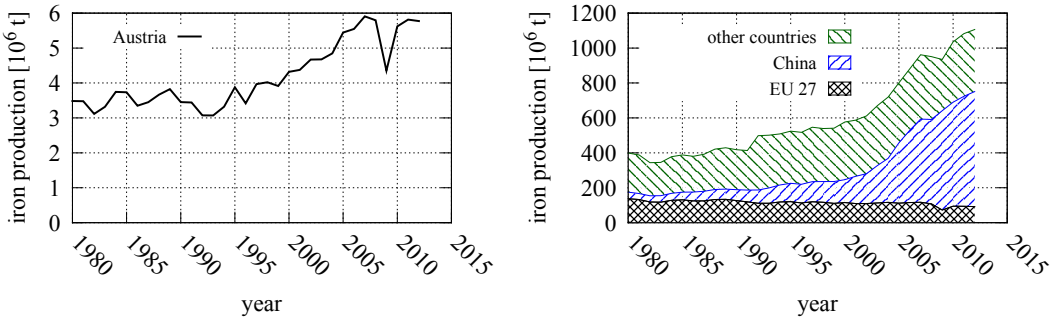

Figure 1.2: Iron produced in blast furnaces in selected regions in the world, left: Austria, right: worldwide (data source: [6]).

The principle of iron production is based on the reduction of iron oxides contained in the ores using carbon as a reducing agent. 98 % of the mined ore is finally processed to steel, whereas undesired elements such as phosphorus, sulfur, oxygen and hydrogen are removed to concentrations below 0.1 % and also the carbon content is reduced to values below 2.06 % [6, 7]. Furthermore, alloy elements such as e.g. chromium, nickel and manganese are added to produce steel qualities with various properties according to the needs.

Raw materials that are necessary for the hot metal production are iron bearing materials (ores and/or scrap) and fuels to supply heat needed for reactions and melting processes, mainly originating from fossil sources such as coal, oil and natural gas. Auxiliary agents are necessary to achieve stable process characteristics. These are primarily slag formers (flux, e.g. limestone $CaCO_3$, dolomite $CaMg(CO_3)_2$, olivine $(Mg, Mn, Fe)_2[SiO_4]$, calcium fluoride CaF_2, silica SiO_2).

Currently, most of the world-wide commercial raw iron production is done applying either the blast furnace process, direct reduction of iron ore or smelting-reduction processes.

Blast furnace processes still state the major route for ironmaking from iron ore with a percentage of hot metal production of approx. 95 % [1, 8, 9, 10]. This is also based on the fact that the technology was invented more than 500 years ago and has continuously evolved, resulting in an energy and resource efficient technology to produce raw iron. The process is very stable, a wide range of metallic feedstock can be processed in the blast furnace, also allowing for the reuse of various recycled charges including scrap and by-products of iron and steel processing plants. However, iron-bearing material (lump iron ore, sinter and pellets) has to be charged in well-defined form concerning e.g. particle sizes to ensure proper melting characteristics. This arises the need for the installation of sinter or pelletizing plants that produce larger particle fractions from iron bearing materials with very low particle sizes.

Moreover, the main reducing agent used in blast furnaces is coke. The operation of coke plants arises some challenges related to environmental as well as economic issues, but the introduction of alternative reducing agents to substitute coke allows to significantly reduce coke consumptions rates (see also fig. 1.8) [1, 11].

Alternative production routes for hot metal have been developed to overcome aforementioned shortcomings of the blast furnace, namely the direct reduction (DR) and smelting reduction (SR) processes. These relatively new technologies have in common to entirely replace coke as the main reducing agent by other carbon carriers.

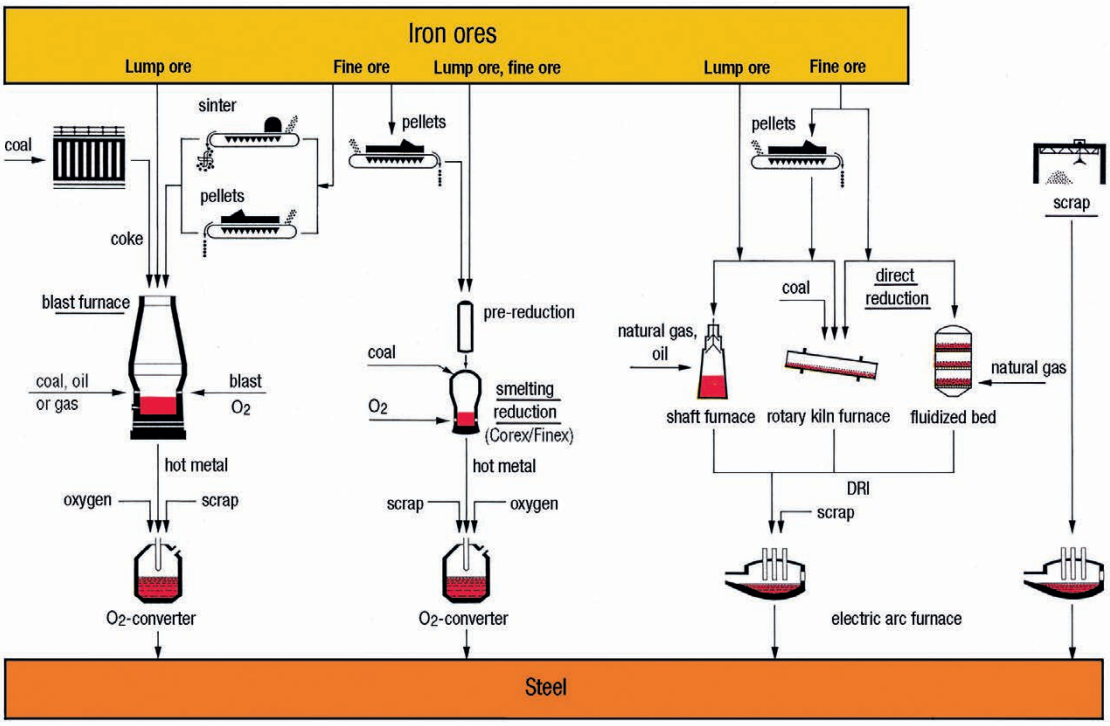

Figure 1.3: Overview of major steel production technologies [1].

Smelting reduction processes produce hot metals from iron ores avoiding the use of coke as a raw material. The overall production process is split in two units: first, iron ore is heated and reduced to an extent of 90 % by gases, mainly CO and H_2, delivered from the second unit [7]. The produced metallic foam is then fed to the second unit, where the solid material is molten, fueled by partial combustion of coal. Commercially available technologies of this type are Corex® and Finex® processes. The separation of reduction and melting of the iron ore allows for the usage of a broad range of coal qualities; produced raw iron qualities are comparable to blast furnace pig iron. In smelting reduction processes large quantities of off-gas with comparatively low heating value are produced, to a great extent local reuse of these waste gases is responsible for the environmental successful implementation of this technology [1].

Direct reduction of iron ore is limited to processing of high-grade ores (e.g. 68 % iron and 27 % gangue). Iron oxides are reduced to the metallic form in the solid state using natural gas as the main fuel that is partially converted to carbon monoxide and hydrogen in the process. At operating temperatures below 1050 °C iron oxides are directly reduced by the gaseous reducing agents, leaving a sponge-like iron structure with considerable contents of gangue residue ($3 - 6$ %) that is mainly used as a feedstock for steel production in electric arc furnaces [1].

1.1 The blast furnace process

As discussed in the previous chapter, iron production is mainly done via the blast furnace process; alternative processes such as DRI or SR are of minor importance. This is also due to the fact, that deep knowledge was achieved during the long history of the blast furnace process. The eldest known blast furnace dates back to the 1st century BC and was operated in China. In Europe (Lapphyttan, Sweden), first blast furnaces are dated back to the medieval times in between 1150 and 1350. It is not clear, whether the knowledge of iron production was brought from China to Europe or was invented independently. In the early furnaces iron ore was heated in simple clay ovens using large specific amounts of charcoal (about $100\,^{\mathrm{kg\,charcoal}}/_{\mathrm{kg\,iron}}$ [12], compare today: $0.4\,^{\mathrm{kg\,coke}}/_{\mathrm{kg\,iron}}$ [2]). Since the early 17th century, by reaching higher temperatures, iron smiths were able to directly produce molten iron [13].

The quality of raw iron was significantly increased in the 18th century. While the direct usage of coal in the blast furnace resulted in iron of low quality (very brittle due to the sulfur contained in the coal, as discovered later), coal pretreatment in an oxygen-free environment released the sulfur content to the air, providing the sulfur-free fuel and reducing agent coke. Therefore, expensive charcoal could be replaced by coal as a primary resource, reducing progressive deforestation of woods and, as wood has become a strategic raw material in Europe, also the cost of iron production was decreased drastically. By implementing a batch process and using coke instead of charcoal, iron production in the blast furnace arrived at the technology that is used today (first true blast furnace utilizing coke: 1735 in Britain [14]). Later on, the trend to reduce production costs was put forward by increasing the scales in which iron was produced.

By invention of the Bessemer Converter in 1856, mass production of steel from carbon-saturated raw iron was possible in an efficient way, increasing the productivity by a factor of 70 [14]: Liquid pig iron is fed to the converter, where by injection of air the carbon contained in the liquid iron is oxidized and removed as CO and CO_2, leaving an ideal input-material for the steel reforming process [15].

From the viewpoint of general process characteristics, the blast furnace represents a continuously operated counter-current flow reactor that is fed on the top alternately with coke, iron-bearing materials and flux, forming a layered structure. Following gravitational forces, the burden slowly moves downwards, thereby being subjected to physical and chemical processes at continuously rising temperatures. The shape of the shaft promotes this movement of solid matter. The boundary of a blast furnace is made of steel with cooling systems and special refractory lining and is either self-supporting or mounted on a special construction framework. In the so-called *cohesive zone* iron oxide and gangue are molten. Below this zone, coke is the only material remaining solid, forming a supporting pillar. Molten raw iron and slag trickle through the cokebed towards the bottom of the blast furnace and are collected in the crucible, being alternately drained via different tapping holes. Therefore, metallurgical coke needs to comply with certain requirements such as conditioned particle sizes and stability against mechanical stresses to retain a bed that is permeable for liquid iron and slag as well as ascending gases [2, 3]. In the center of the shaft a cone-shaped coke structure, the so-called *dead man* is built up. The coke in the dead man is continuously renewed and provides for the dissolution of carbon in liquid metal.

The pig iron is saturated with approx. $4.5\,\%_{\mathrm{w/w}}$ carbon dissolved from the coke bed, resulting in a decrease of the melting point of iron from 1534 °C to 1150 °C due to the eutectic composition (Fe−Fe_3C phase diagram). Blast furnace slag consists of nonmetallic

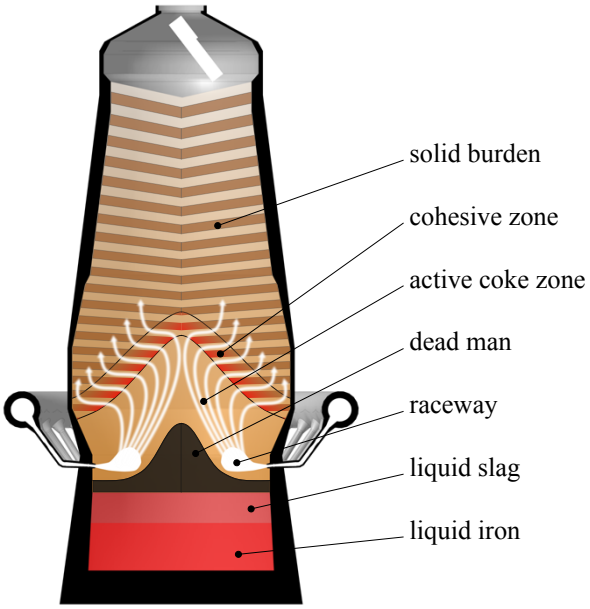

Figure 1.4: Overview of zones and gas flow in the blast furnace.

substances resulting from gangue and flux, mainly being composed of silicates, aluminosilicates and calcium-alumina-silicates [12]. The slag phase also takes the role to absorb much of the sulfur content as well as other undesired elements from charged materials.

Just above the hearth crucible, hot blast as well as additional reducing agents and fuels are injected via circumferentially arranged tuyères. The blast is in principle heated air, often increased in oxygen content to enhance the furnace productivity. It is injected at very high velocities and often elevated pressures, consequently forming a cavity in the cokebed, the so-called *raceway*, that will be discussed in more detail in chapter 1.2.

Injected fuels react with the introduced oxygen. Heat of combustion reactions deliver part of the heat required for warming and melting the burden materials as well as heat for endothermic reduction reactions. Eventually, reducing gases CO and H_2 are formed which ascend through the stack, thereby extracting oxygen from the ores. Excess gas is withdrawn at the furnace top, cleaned and reused in the integrated steel plant e.g. for heating purposes.

The principle of the iron oxide reduction reaction can be written as [3]:

$$FeO_n \longrightarrow Fe + nO \qquad |R\,1|$$

While iron oxides are reduced to raw iron, reducing agents are oxidized:

$$nO + n(C,\, H_2,\, CO) \longrightarrow n(C,\, H_2,\, CO)O \qquad |R\,2|$$

As a general understanding of the blast furnace process, several stages of iron oxide reduction are reported. In the upper zones, relatively low temperatures below 1000 °C are present. In this region, reduction of iron oxides mainly takes place via CO:

$$3Fe_2O_3 + CO \longrightarrow 2Fe_3O_4 + CO_2 \qquad \text{(at temperatures above 500 °C)} \qquad |R\,3|$$

$$Fe_3O_4 + CO \longrightarrow 3FeO + CO_2 \qquad (600 - 900\,°C) \qquad |R\,4|$$

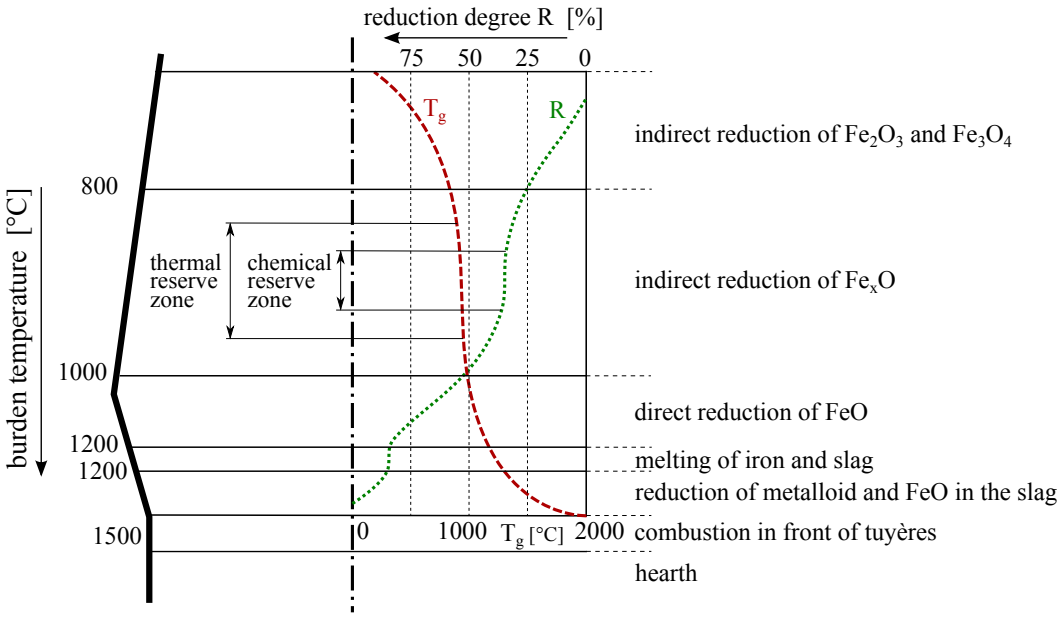

Figure 1.5: Temperature and reduction profiles in the blast furnace (adapted from [2]).

$$FeO + CO \longrightarrow Fe + CO_2 \qquad (900 - 1100\,°C) \qquad |R\,5|$$

The reduction step from hematite Fe_2O_3 to magnetite Fe_3O_4 (reaction R 3) proceeds fast and therefore plays a minor role in the overall rate of reduction [2]. R 3 and R 4 together with R 5 are called indirect reduction reactions.

Modern blast furnace operation often includes the injection of auxiliary reducing agents that are broken down according to the following general reaction equation:

$$C_nH_m + \frac{n}{2}\,O_2 \longrightarrow n\,CO + \frac{m}{2}\,H_2 \qquad |R\,6|$$

Hydrogen is formed as a product from combustion reactions and steam gasification of coke:

$$CH_4 + 1.5\,O_2 \longrightarrow CO + 2\,H_2O \qquad |R\,7|$$

$$H_2O + C \longrightarrow CO + H_2 \qquad |R\,8|$$

Therefore, iron oxide reduction reactions with H_2 as reaction partner take place [16], particularly at temperatures above 1000 °C [12]:

$$3Fe_2O_3 + H_2 \longrightarrow 2Fe_3O_4 + H_2O \qquad |R\,9|$$

$$Fe_3O_4 + H_2 \longrightarrow 3FeO + H_2O \qquad |R\,10|$$

$$FeO + H_2 \longrightarrow Fe + H_2O \qquad |R\,11|$$

Reactions R 3 to R 5 are exothermic, while the reduction with hydrogen, reactions R 9 to R 11, are of endothermic nature. In zones with elevated temperatures, besides indirect

reduction also reactions between liquid wustite FeO and solid carbon take place:

$$\mathrm{FeO + C \longrightarrow Fe + CO} \qquad |\mathrm{R\,12}|$$

This reaction is called *„direct reduction“*. In a typical blast furnace, approx. 35% of total ore reduction takes place via this route [12].

In the furnace, charged limestone is calcined to react with nonferrous oxides (mainly alumina and silica oxides) that is contained as gangue in the iron ore to be withdrawn as molten slag (in practice, slag is a much more complex compound, including various other ions such as Na, Mg and K):

$$\mathrm{CaCO_3 \longrightarrow CaO + CO_2} \qquad \text{(above 870 °C)} \qquad |\mathrm{R\,13}|$$

$$\mathrm{2\,CaO + Al_2O_3 + SiO_2 \longrightarrow Ca_2Al_2SiO_7} \qquad |\mathrm{R\,14}|$$

Also unwanted sulfur that is mainly charged via coke reacts with calcium oxide and is bound chemically to avoid dissolution in pig iron:

$$\mathrm{S + CaO + C \longrightarrow CaS + CO} \qquad |\mathrm{R\,15}|$$

1.2 Tuyère, raceway zone

Hot blast is injected into blast furnaces via up to 42 [1] circumferentially arranged tuyères. The high injection velocity clears a cavity in the coke bed in front of each of the tuyères. The bottom of this cavity is formed by a firm region of lump coke, while the top boundary is rather loosely packed, leaving space for the hot blast to emerge into the coke bed. Coke particles released from the upper boundary continually fall into the cavity, being consumed via combustion reactions with the often oxygen-enriched hot blast. Of interest is the shape of the raceway concerning e.g. its length, determining the penetration depth of auxiliary reducing agents into the coke bed. The raceway shape is influenced by injection characteristics (velocities, temperature and gas pressures) as well as by injection of alternative reducing agents and mechanical loads by burden [17, 18]. Furthermore, size and shape of the raceway cavity are also affected by hysteresis phenomena [19].

Due to the hostile conditions in the raceway zone (high temperatures and gas velocities) as well as spatially restricted access to the cavity (small tuyère cross-sectional area), experimental investigation at working blast furnaces poses a significant technical challenge [20]. Of special interest are the size and location of the cavity and raceway formation dynamics at different operating conditions considering blast and fuel injection rates. Experimental techniques to study raceway formation partly relies on the examination of stopped reactors, where porosity profiles can be determined by probing through the tuyères [21, 22].

Raceway shapes in active furnaces were more recently studied applying microwave measurement techniques, delivering the raceway depth and therefore the reach of injected blast [23, 24]. This measurement concept is based on the interaction of electromagnetic radiation with the various matter and phases occurring in the blast furnace, changing the polarization and pattern of wave modulation in characteristic ways. The advantage of using microwaves is the possibility to penetrate dust and fumes and is therefore well fitted for usage in such environments. Radar technology can be used in a similar manner and is also regularly applied on the stock level of blast furnaces, giving data for burden distributions.

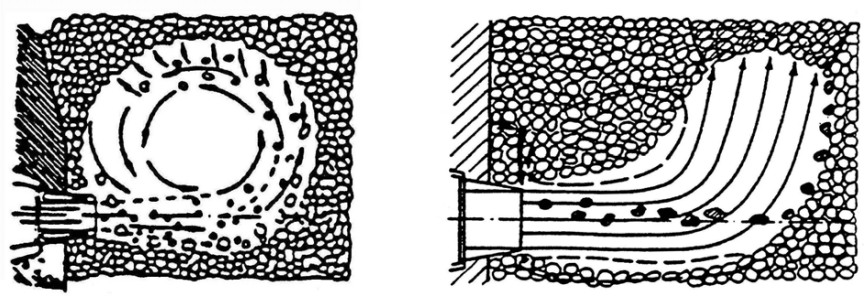

Figure 1.6: Reported main possibilities for raceway formation in the context of coke particle movement. Left: Circulation of coke particles, right: Raceway directed upwards, no coke recirculation [17].

Two basic possibilities of coke movement in the injection zone are reported: At specific operating conditions, a certain flow regime with rapidly hurtling coke particles is formed in the raceway that features circulating movement of coke particles in the cavity, driven by the injected blast [20, 25]. By breaking up coagulates, this motion provides for low particle attrition rates, therefore improving coke reactivity – however, this comes at the cost of higher rates of mechanical coke breakup. Cold model experiments [18, 26] showed a circulating movement of tracer particles. Near the upper boundary of the tuyère nose, coke particles from the coke bed enter the stream of hot blast. The particles are rapidly transported towards the tip of the raceway cavity, where particles move upwards; at the top of the raceway, coke particles move in the lateral direction towards the tuyère, and finally after descending vertically re-enter the jet of hot blast (see the illustration on the left side in fig. 1.6).

A circulating movement of coke particles was also reported from experimental observation of an operating blast furnace using an endoscope in a water-cooled tuyère probe (purged with nitrogen to avoid contamination of the tip glass) in combination with a high speed camera at 3000 $^{\text{frames}}/_{\text{s}}$ [25]. It was found that much more coke enters the raceway zone than can be combusted via the amount of oxygen injected, calculated based on combustion/gasification stoichiometry. It was concluded that a circulating coke movement in the tuyère zone is responsible for residence times high enough to consume the coke; the amount of coke recirculated depends on the blast rate.

However, contrary to the above explained circulating movement forming a rather spherical raceway, also upwards penetrating cavities (see fig. 1.6, right side) without any recirculation was reported [27]. Again, the combination of water-cooled endoscope and high-speed imaging technology was used on a working blast furnace. It was found that directly in front of the tuyère coke dropped into the blast jet and was accelerated towards the center of the furnace, where the coke was deposited and combusted.

Hilton and Cleary [20] examined the raceway formation by means of coupled Discrete Element and Navier–Stokes numerical simulations, concluding that the dynamics of cavity development is strongly influenced by particle shape and blast inlet velocity. Above a critical inlet gas velocity that also depends on the coke bed pressure [20, 28], the flow regime of solid coke particles in the raceway zone showed a transition from static to circulating.

Besides coke, also alternative reducing agents and fuels injected via lances in the tuyères are consumed to a great extent in the raceway zone [29]. The locally concentrated release of conversion products (mainly CO_2 and H_2O) results in the maximum CO_2 concentrations found in the blast furnace (see fig. 1.7). The gases are transported to

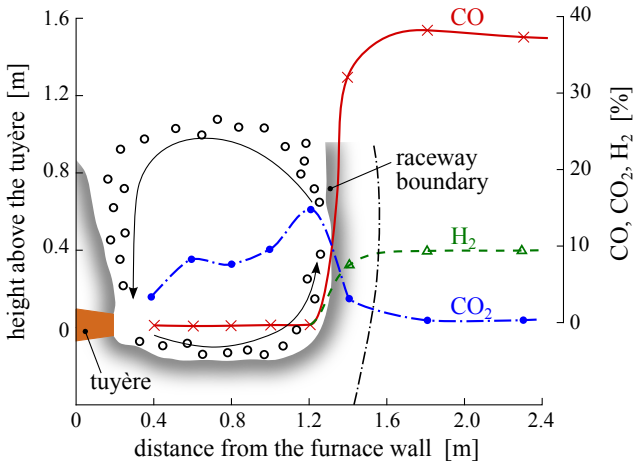

Figure 1.7: Exemplary gas-phase species profiles in the vicinity of the tuyère opening (adapted from [2]).

the inner zones of the blast furnace and move through the porous structure of the coke bed, also passing liquid raw iron and iron oxides. CO_2 further reacts with coke via the Boudouard reaction to form CO. Consequently, coke is consumed in the raceway zone, causing the whole bed of burden to move downwards continuously [30]. The raceways are of major importance for stable operation of the whole blast furnace, because the hot blast is distributed into the coke bed in these regions [31]. Furthermore, injection of alternative fuels and reducing agents have to be well-designed to provide for efficient utilization of the carbon carriers.

1.3 Injection of auxiliary reducing agents

First attempts to decrease coke rates by usage of auxiliary reducing agents date back to the 1950s. The aim of these efforts is to increase the blast furnace performance and productivity at concurrent reduction of coke consumption. Furthermore, the reduction of coke rates directly lowers the environmental impact of iron production facilities. In general, the overall demand of reducing agents was drastically reduced since 1950 by a number of measures increasing the process productivity such as:

- Ore pretreatment, enhancing the reducibility as well as pre-reduction, reduction of gangue concentrations
- Increase of blast temperature and therefore lowering the demand for heat supply via coke combustion
- Oxygen-enrichment of hot blast
- Increased top pressure
- Improved burden distribution
- Improved coke qualities

The average specific consumption of reducing agents in blast furnaces in Germany is shown in figure 1.8. The injection of oil was first tested in the 60s of the last century, coal injection was practiced since 1985 and has increased considerably since its introduction.

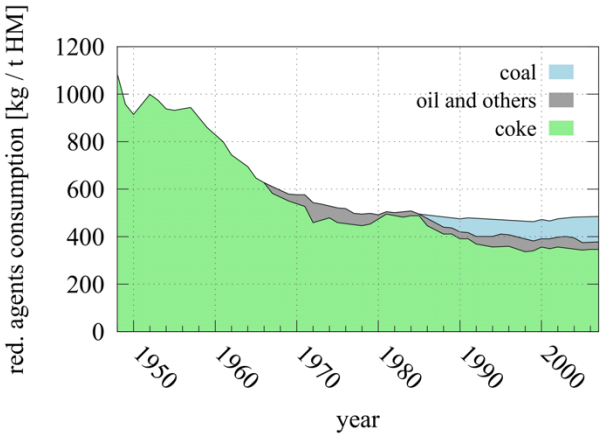

Figure 1.8: Average specific consumption of reducing agents in blast furnaces operated in Germany (data source: [34]).

The main auxiliary reducing agents used are oil and coal, injected at the tuyère level (called *direct injection*), but in principle a wide variety of materials might be used such as tar, oil residues, natural gas, coke oven gas, plastics and even biomass (e.g. charcoal in Brazil [32]).

Auxiliary reduction materials are partly oxidized in the raceway zone to provide heat as well as reducing agents (CO and H_2) for iron oxide reduction. However, up to now there is no detailed understanding about the limits to which coke rates can be decreased. The coke/ore ratio has to be above certain limits to assure permeability of the coke bed for gases as well as liquid iron and slag phase [33]. Also, coke charging rates have to be set high enough to ensure that the coke in the dead man is continuously renewed, assuring carburization of iron and consequently lowering the melting temperature; otherwise the blast furnace process would be changed fundamentally [2].

By direct injection of hydrocarbons or coal, the temperature in the raceway zone decreases due to the heat of pyrolysis (breaking of C-H bonds) as compared to combustion of coke that arrives at the raceway preheated to temperatures of about 1400 –1500 °C. The extent of temperature decrease depends on the injected material as well as the injection rates. Therefore, to provide for the required temperature levels to achieve stable furnace operation, injection is usually combined with oxygen-enrichment [1, 32].

1.3.1 Oil

By direct injection of liquid hydrocarbons, also the availability of hydrogen in the blast furnace is increased, allowing for enhanced ore reduction through hydrogen reduction (reactions R 9 through R 11), as the rate of ore reduction by H_2 is higher than by CO [10, 32]. Hydrogen is more effective, because the H_2 regeneration reaction R 8 is less endothermic and proceeds at higher rates than CO formation through the Boudouard reaction. Also, hydrogen and steam diffusion in the pores of iron oxide pellets is faster as compared to the diffusion of carbon monoxide and -dioxide, further promoting the effective reaction rates ([11], see also chapter 3.6.1).

The injection of liquid hydrocarbons can be achieved at rates of up to $130\,^{\mathrm{kg}}/_{\mathrm{t_{hm}}}$ if additional oxygen enrichment at levels of $7 - 9\,\%$ is applied [1]. Up to 1.2 tons of coke can be replaced per ton of heavy fuel oil [35, 36]. Concerning operating costs of the blast furnace, the oil price shows large fluctuations, stating a reason for varying feeding rates reported in figure 1.8.

Important for successful utilization of oil is the atomization forming a very small droplet regime. Otherwise, residuals of unburnt fuel may leave the oxidizing zone near the tuyères, being later on transformed to carbon black. The soot freight in the ascending gas might cause clogging of the voids in the coke bed or, if leaving the blast furnace with the top gas, be carried over to the gas-cleaning system and discharged in the cleaning water [32]. Finally, the effective fuel utilization is reduced by soot formation. Therefore, great emphasis is laid on proper atomization devices (e.g. using two-fluid nozzles assisted by pressurized steam). The installation of a dual lance configuration allows for a higher degree of oil combustion in the raceway zone.

1.3.2 Coal

The most commonly used auxiliary reducing agent is coal, as can be seen in fig. 1.8. This is also due to the fact that Pulverized Coal Injection (PCI) is quite effective to reduce coke consumption: 1 kg coal can replace $0.85 - 0.95$ kg coke [11, 37]. Most efficient utilization is achieved, if injected coal dust is fully gasified in the raceway zone. Similar to the case of oil utilization, unreacted coal leaving the raceway cavity may cause clogging of the voids in the coke bed, causing problems related to the gas flow distribution, decreasing the reduction efficiency and therefore blast furnace productivity.

Gasification characteristics of the inserted coal play an important role. Coals with low content of volatiles are preferred, as these types exhibit a lower tendency to caking. Therefore, coals with higher carbon content are favored; these coals also have a higher efficiency in replacing coke [12]. The theoretical maximum coal injection rates via tuyères is thought to be $270\,^{\mathrm{kg}}/_{\mathrm{t_{hm}}}$ [1] based on thermochemical estimations and considering the supporting function of the coke bed.

1.3.3 Plastics

In 2011, approx. 280 million tons of plastics were produced worldwide [38], and the ever increasing demand for plastics results in an average annual increase of production rates of approx. 9 % [11]. At the end of life of plastic products, environmental issues concerning the further treatment of the waste material arise. Currently most of the waste plastics are being deposited in landfills, inducing problematic stability issues, as leaching of toxic elements from the polymers can occur [11]. Further ways to treat waste plastics are:

Combustion Besides deposition, a part is utilized thermally in combustion facilities to produce electricity. Proper gas cleaning systems have to be installed to avoid the release of pollutants such as dioxins and furans. Energetic utilization is only considered a sensible way of plastics disposal, if processes to chemically recover the material are unavailable or economically inefficient [39].

Recycling A better way of waste plastics treatment is to apply recycling technologies, i.e. plastics are melted and transformed to new products. For this purpose, the input material has to follow stringent quality criteria. This is the case only for around 20 % of collected waste plastics [40].

Chemical recycling Another method to treat waste plastics is to operate processes that break down the polymers into smaller molecules and use these as a feedstock to produce new petrochemicals or plastics [39]. The utilization of plastics in blast furnaces acts in such a way, as pyrolysis products finally yield CO and H_2 for the reduction of iron oxide (reaction R 6). Besides chemical recycling in the blast furnace, also the energetic content is recovered and used for heating purposes.

In principle, waste plastics can be utilized in various zones of blast-furnace based iron production [11]:

- Carbonization by blending of coal in the coking plant
- Charging on top of the blast furnace with the burden. This is considered to increase unwanted tar fractions in the top gas, as pyrolysis takes place in the upper zones of the shaft [41].
- Gasification outside the blast furnace and injection of the pyrolysis products at tuyère level
- Direct injection of solid plastic matter through the tuyères

The injection of solid plastic particles via tuyères is investigated in this work. Commercial utilization of waste plastics as auxiliary reducing agents in blast furnaces is practiced only in few blast furnaces in Japan (since 1996) and Europe [11]. The goal of plastics injection is to reduce coke rates. Savings might be as high as in the case of coal injection [42]. The injection of 1 kg plastics can replace about 1.3 kg of PCI coal or about 1 kg of heavy fuel oil [11].

The quality of the feedstock (coke, waste plastics) has a major impact on the stability of the blast furnace process as well on the raw iron quality. Plastics have considerable energy content with calorific values between coal and oil [43]. Important parameters that influence the usage of auxiliary fuels in blast furnaces are physical properties, chemical composition, heating values and the concentration of non-ferrous metals and inorganics [44, 45]. The concentration of certain impurities in the feedstock is of special interest. Chlorine that is mainly contained in polyvinyl chloride (PVC) may corrode the blast furnace refractory lining and cause fouling and chemical corrosion in the gas treatment system. Therefore, PVC is typically separated from the feed stream applying e.g. gravitational methods, although processes to remove chlorine from plastic wastes are available [11, 41, 42] (typically chlorine content in feed $< 2\,\%$ [46]). Non-ferrous metals that are in particular contained in automotive shredder fractions tend to reduce the quality of raw iron (e.g. copper causes brittle steel characteristics). Also other heavy metals such as lead and zinc are found problematic in the blast furnace process. Zinc builds up a circular flow in the furnace shaft and reduces process economics as specific rates of reducing agents increase [3]. Lead has a lower evaporation pressure and therefore accumulates in the bottom of the furnace, lowering the productivity [11]. Hence, feedstock has to undergo a number of preparation steps to ensure that quality requirements are met.

The method of plastic preparation influences the conversion characteristics in the raceway. Generally, consumption of agglomerates is at lower rates as compared to shredder fractions. Gasification and combustion efficiency was reported to be higher at finer particle sizes [11]. Large particles are considered to circulate in the raceway cavity while fine particles are expected to leave the raceway with ascending gases. Principally, the location of particle utilization by gasification or combustion varies with particle size. The combustion of coarse waste plastics is located deep in the raceway, but still proceeds effectively [47]. Plastic particles do not disintegrate as compared to PCI (break up of coal particles due to rapid heating) – this is considered to be a reason for high combustion and gasification efficiency inside the raceway. Tar fractions from plastics pyrolysis are broken down fast, so no problem in gas cleaning systems for top-gas treatment is to be expected. Due to the high temperatures above 2000 °C organic chlorine compounds are destroyed and the reducing conditions in the furnace inhibit the ocurrence of dioxin formation [46].

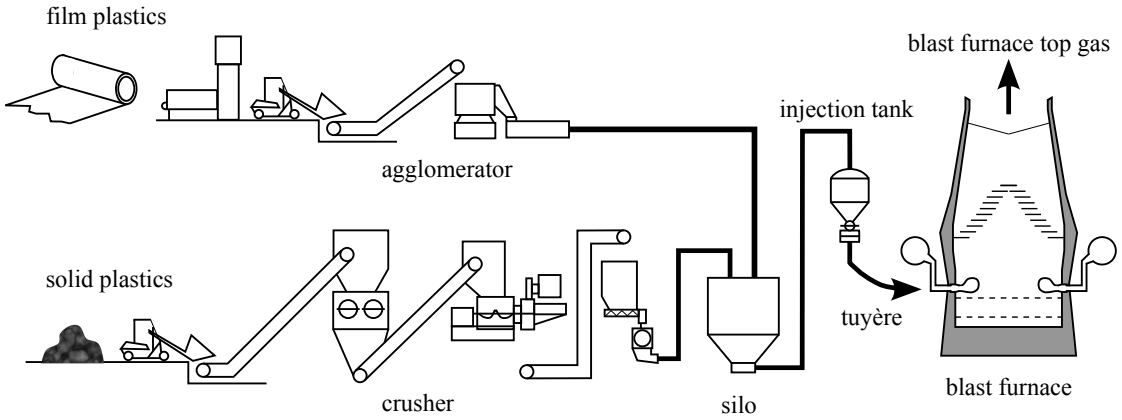

Figure 1.9: Schematic illustration of plastics preparation for blast furnace injection (adapted from [47]).

Massive injection of plastic particles is possible if injectants are charged with proper particle size distributions and preparation methods (crushed vs. agglomerated). However, at high injection rates an issue concerning the clogging of the coke bed arises: Even though plastics for injection typically have a low ash content, the melting point of ashes originating from waste plastics was reported to be rather high (about 1750 °C), resulting in the fact that deterioration of the furnace permeability may occur [48].

Of the injected plastics, approx. 63 % is utilized chemically for reduction of iron oxides, 37 % contribute to heating of the furnace [46]. Therefore, in terms of efficiency, the utilization of waste plastics in the blast furnace process is favorable as compared to combustion in waste incineration plants.

1.3.4 Natural gas

Compared to other types of alternative reducing agents, the injection of natural gas requires little capital investment to equip blast furnaces with pressure equalization and gas distribution systems but still offers the option to considerably decrease coke consumption. Higher hydrogen supply rates with gas contribute to increase indirect iron oxide reduction and tend to decrease direct coke reduction rates and therefore coke consumption [10]. Coke replacement ratios were reported to be in the range of $0.9 - 1.15\,\mathrm{kg_{gas}/kg_{coke}}$ [36, 49].

The applicability of natural gas injection strongly depends on the current gas price, again economics determine the attractiveness of this alternative reducing agent. Natural gas injection rates increased in North America since the 1990s [35] and might still gain significance considering the current situation on the gas market. Due to the exploitation of shale gas sources, average gas injection rates in blast furnaces in North America increased from $20\,\mathrm{kg/t_{hm}}$ in 2009 to $60\,\mathrm{kg/t_{hm}}$ in 2013 [50].

Natural gas injection rates in blast furnaces are typically in the range of $40-110\,\mathrm{kg_{gas}/t_{hm}}$, injection rates of up to $155\,\mathrm{kg/t_{hm}}$ were reported [10]. Higher rates of natural gas injection are considered to cause problems due to strong local cooling effects, soot formation and increase of slag viscosity. Apart from economic considerations, today the suppression of CO_2 emission with top gas also plays an important role [51]. The high specific hydrogen content in natural gas causes a decrease of the carbon dioxide content emitted with the blast furnace top gas.

1.4 CO_2 Emissions

On a global scale, in the manufacturing sector iron and steel industry is responsible for about 27 % of the carbon dioxide emissions, representing $4 - 5$ % of total CO_2 emissions [11, 52]. This is due to the fact, that steel production strongly depends on fossil fuels as the main energy source. Half of the CO_2 emissions of an integrated steel plant originates from the operation of the blast furnace and its associated processes [52]. Steel producing industry attempts to reduce the emission of greenhouse gases, not least because of the general agreement of European and non-EU governments to tackle global warming problematics.

A reduction of CO_2 emissions by 6.5 % was reported, when the specific PCI rate was increased from 16 to 116 $^{kg}/_{thm}$ [53]. Due to the increased rates of hydrogen introduced by injection of waste plastics, the CO_2 content in blast furnace topgas is reduced by about 27 % as compared to operation by coal and coke alone [11, 54], carbon dioxide being replaced by hydrogen and steam. Also, the energy consumption is decreased as the regeneration of H_2 from steam gasification of coke is less endothermic than the Boudouard reaction and direct iron oxide reduction. The emission reduction potentials of some major thermoplastics used for injection is shown in figure 1.10. Differences between the material types are caused by varying plastic properties, i.e. mainly the carbon and hydrogen content as well as calorific value [11, 55].

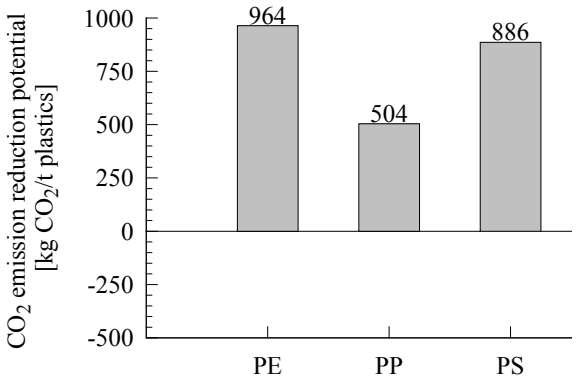

Figure 1.10: CO_2 reduction potential [55].

1.5 Thesis outline

The present thesis is structured starting with an introduction of the blast furnace process, also addressing the injection of alternative reducing agents (Chapter 1). Chapter 2 summarizes some background information on numerical simulation, focusing on computational fluid dynamics and presenting basic approaches to model the processes occurring in the blast furnace. The mathematical models that were implemented to study the specific physical phenomena in the vicinity of blast furnace tuyères are presented in chapter 3. This section also includes a description of the applied dual-grid approach allowing to investigate occurring multiphase transport phenomena and inter-phase energy and mass exchange. The developed model was applied to a number of experimental setups to validate model predictions against real-world experimental data (Chapter 4).

Finally, Chapter 5 reports the application of the validated simulation tool to the actual blast furnace process. Parameters such as the tuyère diameter, hot blast properties and

rates of alternative reductants for injection were varied to examine the sensitivity of local gas-phase and coke properties in the furnace on the operating and boundary conditions. The overall conclusions from the current research study as well as recommendations for further work are summarized in chapters 6 and 7.

2 Theory

In the following chapters, the basic principles of numeric simulation are summarized. Emphasis is laid on the presentation of modeling approaches for physical phenomena that occur in the blast furnace process.

2.1 Conservation equations

The basic knowledge to describe the flow of fluids mathematically was laid a long time ago. The equations describing the motion of frictionless moving fluids were already found in 1755 by Leonhard Euler, the more general Navier-Stokes equations describing the motion of viscous Newtonian fluids date back to 1827. Further important mathematical models are the Arrhenius-approach describing the rate of chemical reactions (1855), the description of shear stresses in a moving fluid (e.g.: shear-stress-tensor of Newtonian fluids, 1682), Fourier's law of conductive heat transport (1822) and Fick's diffusion law (1855) [56]. These mathematical models are employed in a number of balance equations in numerical simulation models, the conservation equations of species, energy and momentum are based on these principles.

In the field of fluid mechanics, mass, momentum and energy are referred to as *conserved quantities*, i. e. in a closed system these quantities are not produced nor consumed but converted by numerous physical processes. The fundament of numerical simulations applying finite volume methods are therefore conservation equations that are based on following principles:

- Conservation of mass (continuity equation)
- Conservation of momentum (Navier-Stokes equations)
- Conservation of energy

In their differential form, these laws form a coupled set of partial differential equations that thoroughly describes the characteristics of real fluids.

Essential for the validity of this approach is the assumption, that the flowing fluid can be treated as a continuum. This means, that the mean free path length $\mathcal{L}$ of e.g. the gas molecules motion in the case of a gas flow is much lower than the smallest length scales that appear in the fluid flow, l_f. If the nature of the fluid flow is turbulent, the smallest length scale is defined by the size of the smallest eddies, the so-called *Kolmogorov* scale η [57]. A dimensionless number defined in this context is the *Knudsen* number:

$$Kn = \frac{\mathcal{L}}{l_f} \qquad |2.1|$$

To satisfy the criterion of continuum fluid motion, it is necessary that $Kn \ll 1$. If the *Kolmogorov* length scale is used to define the *Knudsen*-number, we obtain [56]:

$$Kn = \frac{\mathcal{L}}{\eta} \approx \frac{Ma}{Re^{1/4}} \qquad |2.2|$$

with the *Mach* number

$$Ma = \frac{v}{a} \qquad |2.3|$$

and the *Reynolds* number

$$Re = \frac{\rho\, v\, l}{\mu} \qquad |2.4|$$

In most industrial apparatuses, the *Mach* number is small, while the *Reynolds* number is high (turbulent flows) – therefore, the criterion of a low *Knudsen* number is fulfilled.

The general conservation equation of an extensive quantity in its differential form is shown in equation 2.5 (vectorial notation, in the following also the component notation will be used).

$$\underbrace{\frac{\partial \Phi}{\partial t}}_{\text{storage term}} = - \underbrace{\nabla(\mathbf{v}\Phi)}_{\text{convective term}} - \underbrace{\nabla \mathbf{J}_\Phi}_{\text{molecular transport}} + \underbrace{S_\Phi}_{\text{source term}} \qquad |2.5|$$

An *extensive* quantity depends on the amount of the considered matter in the examined control volume (e.g. energy), while *intensive* quantities do not depend on the amount of fluid that is transported. Well-known examples for this latter class of quantities are density, fluid velocity, temperature and pressure. The relation between an intensive quantity ϕ and its corresponding extensive quantity Φ is given by [58]:

$$\Phi = \int^{V_{CV}} \rho\phi \, \mathrm{d}V \qquad |2.6|$$

The terms in equ. 2.5 can be interpreted as follows:

Storage term: The storage term describes the change of the quantity in time in a control volume at a fixed position.

Convective term: Rate of change due to fluid motion with respect to the surface of the control volume. This term is also called *advective flux*.

Molecular transport: The molecular transport term is – depending on the quantity under consideration – called *heat conduction*, *species diffusion* or *viscous friction*. While the aforementioned convective term is calculated directly from the known variable vector (e.g. the velocity vector field), for the calculation of the diffusive flux additional laws are needed that depend on experimental data or correlations originating in the kinetic theory of gases.

The vector of the molecular flux $\mathbf{J}$ is generally written as a linear function of the gradient of Φ and a proportionality factor Γ_Φ (molecular transport coefficient):

$$\mathbf{J}_\Phi = \Gamma_\Phi \nabla \Phi \qquad |2.7|$$

Examples of dependence of the diffusive flux on the corresponding gradient are the *Fourier* law for heat conduction and *Fick*'s law of species diffusion. In general, the molecular transport coefficient is a property that depends on the conditions present, such as pressure and temperature [57].

Source term: In general, also source terms occur in the conservation equations. These terms account for conversion processes that take place in the control volume, such as the formation or destruction of species due to chemical reactions and heat release due to heat of reaction. While the above mentioned convective and molecular transport terms are evaluated on a *per-surface-rate* (specific to surface area of the control volume), source terms are calculated volume-specific (per m^3 control volume).

Generally, the formulation of the conservation equations can be done in two ways. In the description of dynamic systems, a widely used approach is the *Lagrangian* formulation. The conservation equation for the quantity under consideration is written for an element that moves along its path in space. The elements are often treated as rigid bodies. Therefore, the control mass can be easily defined. The conservation quantities are defined with respect to a coordinate system that moves analog with the element. This means, that the convective terms in the conservation equations disappear. In the *Eulerian* method the balance equations for a control volume are set up with respect to a coordinate system that is fixed in space.

The two approaches to set up the conservation equations are coupled via the total derivative $\frac{\mathrm{D}}{\mathrm{D}t}$ for a fluid element that follows the flow [59]:

$$\frac{\mathrm{D}\phi}{\mathrm{D}t} = \frac{\partial\phi}{\partial t} + v_x\frac{\partial\phi}{\partial x} + v_y\frac{\partial\phi}{\partial y} + v_z\frac{\partial\phi}{\partial z} = \frac{\partial\phi}{\partial t} + \mathbf{v}\cdot\nabla\phi \qquad |2.8|$$

The variation of the quantity ϕ is the sum of the change in time on a fixed position $\frac{\partial\phi}{\partial t}$ (*Eulerian* form) and the variation due to the movement of the coordinate system $\mathbf{v}\cdot\nabla\phi$ (*Lagrangian* form). In the following, the *Eulerian* form will be used. The equations are written in component notation, where $x_{i=1,2,3}$ are cartesian coordinates and v_i are the cartesian components of the velocity vector.

Mass balance In the field of fluid mechanics, the conservation of the total mass in a control volume is a fundamental condition. The balance equation is derived from the general conservation equation 2.5 by setting $\phi = 1$ in equation 2.6:

$$\underbrace{\frac{\partial\rho}{\partial t}}_{\text{storage term}} + \underbrace{\frac{\partial}{\partial x_j}(\rho v_j)}_{\text{convective term}} = \underbrace{S_M}_{\text{source term}} \qquad |2.9|$$

The time rate of mass change in the control volume is a result of convective flux through the boundaries of the control volume as well as a mass source term on the right side. In a technical system, the mass source in the fluid represents e.g. the release of pyrolysis products from a coal particle passing the control volume. In this balance, the total mass does not encounter diffusive transport, as this would result in motion relative to the convective velocity [57].

Species balance If the fluid system to be modeled consists of more than one component and the concentration distribution of these species has to be considered (this is the case, if combustion processes occur), an additional species conservation equation has to be implemented ($\phi = Y_n$):

$$\underbrace{\frac{\partial}{\partial t}(\rho Y_n)}_{\text{storage term}} + \underbrace{\frac{\partial}{\partial x_j}(\rho Y_n v_j)}_{\text{convective Term}} = \underbrace{\frac{\partial}{\partial x_j}\left(D_{n,m}\frac{\partial(\rho Y_n)}{\partial x_j}\right)}_{\text{species diffusion}} + \underbrace{S_n}_{\text{source term}} \qquad |2.10|$$

As individual species are tracked, also chemical reactions can be modeled by specifying proper source terms S_n for educt and product species that are present in chemical reactions.
The diffusive species transport in the fluid mixture is calculated on the basis of the diffusion coefficient $D_{n,m}$. In turbulent flows (and usage of RANS turbulence models, see chapter 2.3), the influence of the molecular diffusion is insignificant and can be neglected, as the equivalent turbulent diffusion term is several orders of magnitude higher.

Momentum balance Setting $\phi = \mathbf{v}$ in equations 2.5 and 2.6 yields the momentum balance:

$$\underbrace{\frac{\partial}{\partial t}(\rho v_i)}_{\text{storage term}} + \underbrace{\frac{\partial}{\partial x_j}(\rho v_i v_j)}_{\text{convective term}} = \underbrace{-\frac{\partial p}{\partial x_j} + \frac{\partial \tau_{ij}}{\partial x_j}}_{\text{surface forces}} + \underbrace{\rho f_i}_{\text{volumetric forces}} + \underbrace{S_F}_{\text{source term}} \qquad |2.11|$$

In the momentum balance, the counterpart of diffusive transport is represented by *surface forces* (transport of momentum due to pressure and viscous friction). To end up with a closed set of partial differential equations, all quantities in the conservation equations need to be expressed in terms of velocity and density. Therefore, the shear stress tensor τ_{ij} has to be replaced by a proper expression. Fluids often exhibit Newtonian behavior [56, 58] and Stokes' law is valid:

$$\tau_{ij} = \underbrace{\mu\left[\frac{\partial v_i}{\partial x_j} + \frac{\partial v_j}{\partial x_i}\right]}_{\text{incompressible}} - \underbrace{\frac{2}{3}\mu\frac{\partial v_i}{\partial x_i}\delta_{ij}}_{\text{compressible}} \qquad |2.12|$$

The last term in equ. 2.12 cancels out, if the fluid can be considered incompressible ($Ma \ll 1$) [59]. Volumetric forces act on the fluid element due to impacts such as gravitation, centrifugal and Coriolis forces. These are implemented as source terms on the right side of the equation. Further source terms S_F might be present, if the flow regime includes dispersed particles with different velocity (drag) or if the fluid passes a porous bed. In this case, the source terms represent the interaction between particles or porous media and the moving continuous fluid.
The set of equations 2.11 and 2.12 are called *Navier-Stokes equations.*

Energy balance In a system that includes chemical reactions, energy is present in different types that can be converted into each other by a broad range of physical processes. The so-called *internal energy* is temperature-dependent and includes the kinetic energy of the movement of smallest fluid elements (e.g. gas molecules), chemical bond energies etc. The internal energy is not calculated as an absolute value, but is specified with respect to a reference temperature T_{ref}.
The *kinetic energy* includes macroscopic motion in the fluid flow that plays an important role in turbulent flows. Many turbulence models are based on the calculation of a *turbulent kinetic energy* that is often introduced by a separate conservation equation (see section 2.3). Another type of energy is the potential energy, induced by a gravitational field or as a result of an electric field acting on a charged fluid element.

Equation 2.13 represents energy conservation, written in terms of the specific enthalpy h:

$$\underbrace{\frac{\partial}{\partial t}(\rho h)}_{\text{storage term}} + \underbrace{\frac{\partial}{\partial x_j}(\rho h v_j)}_{\text{convective term}} = \underbrace{\frac{\mathrm{D}p}{\mathrm{D}t}}_{\substack{\text{source due to} \\ \text{pressure forces}}} + \underbrace{\frac{\partial}{\partial x_j}\left(\lambda \frac{\partial T}{\partial x_j}\right)}_{\text{diffusive transport}} + \underbrace{\frac{\partial}{\partial x_j}(v_i \tau_{ij})}_{\substack{\text{source due to} \\ \text{viscous dissipation}}} + \\ + \underbrace{\sum_{n=1}^{N} \frac{\partial}{\partial x_j}\left[D_{n,m} h_n \frac{\partial(\rho Y_n)}{\partial x_j}\right]}_{\text{transport due to species diffusion}} + \underbrace{S_E}_{\text{source term}} \qquad |2.13|$$

The diffusion term in the energy balance describes the transport of energy due to heat conduction (*Fourier's* law). In industrial applications, the contribution of pressure forces to energy transformation can be neglected. This is also true for the source term due to viscous dissipation.
The enthalpy h_n of a component is calculated by integrating the specific heat capacity in the range of the reference temperature and the temperature in the control volume (no phase change):

$$h_n = \int_{T_{ref,j}}^{T} c_{p,n}\,\mathrm{d}T \qquad |2.14|$$

The specific enthalpy of the mixture is calculated by mass-weighted summation over all components:

$$h = \sum_{n=1}^{N} Y_n h_n \qquad |2.15|$$

The heat of material conversions (chemical reactions, phase transition of dispersed particles or droplets, etc.) is accounted for by the last term in equation 2.13. This source term also includes contributions to the fluid temperature due to radiation interaction as well as energy transfer to or from particles or droplets.

Thermodynamic relation To solve the set of conservation equations, a relation is necessary that describes the correlation between the thermodynamic variables of state (temperature, pressure, density and specific heat capacity). If intermolecular forces in the fluid can be neglected, the ideal gas equation can be used [56]:

$$p = \rho R_m T \sum_{n=1}^{N} \frac{Y_n}{M_n} \qquad |2.16|$$

Furthermore, in most industrial applications the assumption that the fluid behaves *thermally perfect* can be applied [56]. This means, that the specific heat capacity can be expressed as a function of the fluid temperature $c_p = c_p(T)$, while the pressure dependence can be neglected.

2.2 Discretization

The governing conservation equations build a system of partial differential equations that can be solved *analytically* only for a very limited number of special cases. If industrial applications are to be modeled, the model setup tends to be very complex (turbulence effects, complex geometries etc.), therefore the direct solution of the equations is not feasible. The strategy usually applied using the methods of CFD is to discretize the mathematical model in the computational domain. This results in a set of algebraic equations that approximates the original differential system and is to be solved using computers. The discretized equations are applied to small control volumina that are generated by spatial discretization of the considered flow domain. The results of the computations represent data fields for the considered transport quantities at discrete positions in space and time. The accuracy of the results strongly depends on the quality of the applied discretization algorithms [58].

The simplest method to discretize a flow domain is to use so-called *structured grids*. Here, a structured, i.e. regular grid of nodes is applied to represent the geometric features. This results in a regular matrix describing the flow problem. Very efficient solution routines can be applied to solve such types of problems. However, in real industrial apparatuses geometries are usually too complex to be described by a structured grid. The necessary flexibility is provided by using unstructured grid elements (see fig. 2.1, right sketch). This grid type also offers the opportunity to introduce zones with higher spatial resolution (e.g. regions with large gradients of flow variables) and continuous decrease of resolution towards zones where gradients are expected to be low. Using unstructured grid topologies, the resulting matrix of the algebraic system has no regular diagonal structure, therefore the solution procedure is slowed down as compared to fully structured grids.

In this work, a combination of structured an unstructured hexahedral volume elements is used to describe the geometric layout of considered validation cases and the blast furnace geometry.

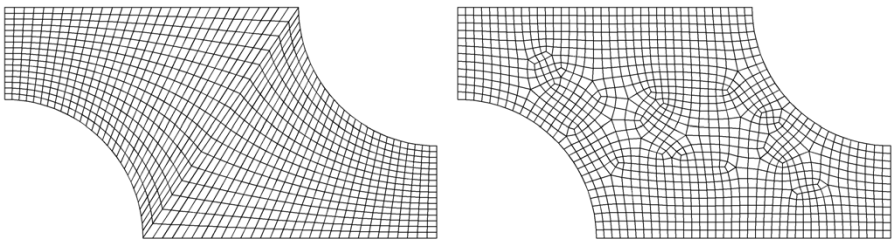

Figure 2.1: Illustration of methods for spatial discretization (adapted from [58]). Left: Structured, right: Unstructured grid.

2.3 Turbulence modeling

The majority of flows appearing in industrial apparatuses exhibit turbulent behavior [60]. In comparison to laminar flow regimes, turbulent flows feature some special characteristics [58]:

- Turbulent flows are highly time-dependent. At a fixed position, the plot of fluid velocity vs. time appears to show a directed base flow superimposed by chaotic fluctuations in all three spatial dimensions.

- Lots of swirling motions are present in turbulent flows.
- Turbulence increases the mixing rate of conservation quantities – this contribution is commonly referred to as *turbulent diffusion*.
- Due to increased (momentum-) diffusion, velocity gradients are damped more strongly as compared to laminar flows. This dissipative process results in an increased apparent viscosity.
- In turbulent flows the appearing structures show a broad bandwidth in terms of length- and time scales. This results in high computational demands to model the turbulent behavior directly.

The characteristics of turbulent flows are beneficial for certain types of processes, e.g. the speed of chemical reactions is increased due to higher mixing rates as compared to laminar flow regimes. On the other hand, increased dissipative momentum transport results in higher specific power consumption, e.g. at turbulent flows in piping systems [58].

In general, several methods with different complexity are available to predict the characteristics of turbulent flows [58], the most important amongst them are listed in the following:

Correlations This very useful method describes turbulent properties of a flow system based on a low number of characteristic parameters and is very often applied in engineering tasks. Popular examples for such correlations are the calculation of drag coefficients of particles in a fluid flow as a function of the particle Reynolds number, $c_w = f(Re)$, or the well known Nusselt number to characterize heterogeneous heat transfer as a function of Reynolds and Prandtl number, e.g. $Nu = C \cdot Re^m \cdot Pr^n$.

Such correlations are readily available for standard cases but usually cannot be applied to complex geometries. Therefore, more general approaches for the description of turbulence effects in flow systems to be implemented in CFD models were developed in the last decades. An overview for these modeling approaches is given in the following.

Direct Numeric Simulation (DNS) Using DNS, the three-dimensional, unsteady Navier-Stokes equations (see equ. 2.11 and 2.12) are solved directly for the turbulent flow, i.e. without averaging or approximation of turbulent fluctuations. Apart from errors due to spatial and temporal discretization, no further modeling uncertainties are introduced by this method.

The idea behind this approach is to use a sufficiently fine computational grid to resolve even the smallest turbulent eddies. In an industrial apparatus, the size of the largest eddies is in the order of the available channel width, represented by the characteristic length l. Dissipation of turbulent kinetic energy by turbulence effects takes place on the smallest length scales (Kolmogoroff length scale η). Therefore, distances between computational nodes have to be such that these structures are resolved properly. Using an equidistant grid, $\frac{l}{\eta}$ grid points have to be implemented in every direction. According to the stability criterion proposed by Courant et al. [61], afforded time discretization depends on local flow conditions *and* grid resolution. Overall, the resulting computational demand is proportional to Re^3 [58].

Consequently, the application of direct numerical simulation is limited to flow systems with relatively low Reynolds numbers and therefore, in general, cannot be used for industrial apparatuses.

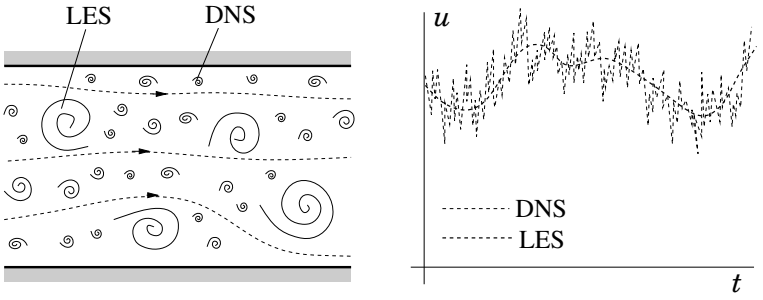

Figure 2.2: Turbulent flow. Left: Schematic sketch of eddies of different length scales; right: Temporal evolution of velocity at a fixed position [58].

Large Eddy Simulation (LES) With this approach, large eddies are resolved directly, while flow structures that are smaller than a certain length scale Δ are modeled via so-called *small scale turbulence models* (see fig. 2.2). Therefore, the Navier-Stokes equations are filtered to this length scale and small eddies are approximated by models. The resulting computational grid is coarser than in the case of DNS, but still rather fine. Furthermore, the nature of this modeling approach is inherent unsteady and temporal discretization of the governing conservation equations has to be applied. Consequently, the computational demand of LES is considerably higher than setups incorporating the below mentioned RANS-models.

Reynolds-Averaged Navier Stokes equations (RANS) DNS and LES are usually computationally too demanding to be used for industrial applications of CFD. This is especially true for cases that include submodels for phenomena such as radiation and/or chemical reactions. Therefore, in engineering applications usually RANS-averaging is applied [62].
The idea of RANS-models is based on averaging of time variations of the transport quantities. A general transport quantity ϕ is represented as the sum of the time-averaged value $\overline{\phi}$ and its temporal fluctuation ϕ':

$$\phi\left(x_i,t\right)=\overline{\phi}\left(x_i\right)+\phi'\left(x_i,t\right) \qquad \text{with} \qquad \overline{\phi}\left(x_i\right)=\lim_{\Delta t\to\infty}\frac{1}{\triangle t}\int_0^{\triangle t}\phi\left(x_{i,t}\right)\mathrm{d}t \quad |2.17|$$

From the definition of the mean value in equation 2.17 follows, that $\overline{\phi'}=0$. Applying this expression to the Navier-Stokes equations (equ. 2.11 and 2.12), linear terms are replaced by the mean value. For non-linear terms, additional expressions are introduced to the equations, e.g. for a quadratic term:

$$\overline{v_i\phi}=\overline{\left(\overline{v_i}+v_i'\right)\left(\overline{\phi}+\phi'\right)}=\overline{v_i}\overline{\phi}+\overline{v_i'\phi'} \quad |2.18|$$

The last term in equation 2.18 represents the turbulent scalar transport of the general quantity ϕ that in general does not vanish. In the case of the momentum equation, the turbulent scalar transport is called *Reynolds stress* ($\tau_{ij,\,turb}$ in equation 2.19).

$$\frac{\partial}{\partial t}\left(\rho\overline{v}_i\right) + \frac{\partial}{\partial x_j}\left(\rho\overline{v_i}\overline{v_j} + \underbrace{\rho\overline{v_i'v_j'}}_{\tau_{ij,\,turb}}\right) = -\frac{\partial\overline{p}}{\partial x_j} + \frac{\partial}{\partial x_j}\underbrace{\mu\left(\frac{\partial\overline{v_i}}{\partial x_j} + \frac{\partial\overline{v_j}}{\partial x_i}\right) - \frac{2}{3}\mu\frac{\partial\overline{v_i}}{\partial x_j}\delta_{ij}}_{\text{Newtonian shear stress } \tau_{ij}} \qquad |2.19|$$

The obtained equation set states more variables than equations. To close the set of Reynolds-averaged equations, additional laws have to be introduced to calculate the elements of the tensor of Reynolds stresses, $\tau_{ij,\,turb}$. In literature, this fact is usually referred to as „closure problem".
The so-called *turbulence models* basically calculate turbulent scalar fluxes and Reynolds stresses from the mean values applying various kinds of approximations. A very common type of turbulence models is based on the concept of *eddy viscosities* that assume the Reynolds-stress tensor exhibits a similar impact on the flow as the Newtonian shear stress tensor (see equ. 2.12). This approach gives the following definition of the Reynolds stresses [58]:

$$-\rho\overline{v_i'v_j'} = \tau_{ij,\,turb} = \mu_t\left(\frac{\partial\overline{v_i}}{\partial x_j} + \frac{\partial\overline{v_j}}{\partial x_i}\right) - \frac{2}{3}\rho\delta_{ij}k \qquad |2.20|$$

The term k in equation 2.20 represents the turbulent kinetic energy that is defined by:

$$k = \frac{1}{2}\left|\overline{v_i'v_i'}\right| = \frac{1}{2}\left(\overline{v_x'v_x'} + \overline{v_y'v_y'} + \overline{v_z'v_z'}\right) \qquad |2.21|$$

The *turbulent viscosity* μ_t is a system quantity and therefore cannot be implemented as a material property (as compared to the *molecular viscosity* μ). A large number of models for the calculation of μ_t is available in literature. The choice of a turbulence model also depends on the complexity of the model that influences the computational demands of the simulation (hardware resources, time for solution process). E.g. the demand to solve for the 5-equation RSM-model is considerably higher than for simpler one- or two-equation models [63]. However, none of the models is capable to model the nature of turbulence exactly, the accuracy of each model depends on the present flow conditions and also on the geometric setup [64]. Large differences are found in the ability to predict spreading rates of planar and axis-symmetric jets [63].
The group of k-ϵ-models is due to good stability, robustness and comparable low computational demands and at the same time good accuracy very often applied in modeling of industrial processes [65]. The *standard k-ϵ model*, implemented by Launder, B. E. and Spalding, D. B. [66], is applicable to modeling tasks in systems involving combustion processes [67, 68]. Two transport equations are introduced to the simulation setup: for turbulent kinetic energy k and its dissipation rate ϵ, derivation of these equations can be found in the literature (e.g. [58]). An improved k-ϵ model was introduced by Shih et al. [69]: the so-called *realizable k-ϵ model*. The term *realizable* means, that certain physics of the nature of turbulent flows are considered by introduction of mathematical constraints. Furthermore, a new approach to calculate turbulent viscosity is introduced and an alternative transport equation for the dissipation rate ϵ was derived. This model is more reliable in the prediction of decay rates of turbulent round free jets and is also expected to yield good results for flows including recirculation zones and is therefore applied in this study [12, 69].

2.4 Chemical reaction modeling

The basic principle for the mathematical description of interactions between molecules (reactants) to form products is to set up chemical reactions [70]. The actual rate of a reaction is influenced by a wide number of parameters such as educts and reactants concentrations, temperature, pressure and potentially the presence of catalysts or other phases. The reaction rate is to be expressed by a mathematical model, accounting for these conditions. Generally, a reaction can be written as follows:

$$\mathrm{aA} + \mathrm{bB} + \cdots \rightleftharpoons \mathrm{xX} + \mathrm{yY} + \cdots \qquad |\mathrm{R}\,16|$$

This macroscopic (*global*) reaction can be divided into a set of reactions on a microscopic level (*elementary reactions*) that define a reaction mechanism. The mechanism of an overall reaction, e.g. the oxidation of CO to form CO_2, is usually determined experimentally.

In the case of an irreversible elementary reaction

$$\mathrm{aA} + \mathrm{bB} \longrightarrow \mathrm{xX} + \mathrm{yY} \qquad |\mathrm{R}\,17|$$

the commonly adopted structure of the rate law is:

$$r = k\,[A]^a\,[B]^b\ . \qquad |2.22|$$

The factor k is independent of reactant and product concentrations, but describes the dependency of the reaction rate on system temperature, pressure and medium properties. As long as the considered reaction is elementary, the stoichiometric coefficients are to be used as powers for the concentration values. The orders of global reactions have to be defined based on experimental observation and usually differ from the stoichiometric coefficients [71].

In 1884, the Dutch chemist J.H. van 't Hoff presented an empirical rate law describing the temperature-dependence of chemical reactions. He stated, that the reaction rate can be modeled using an exponential expression:

$$k = Ae^{-\frac{E_a}{R\cdot T}} \qquad |2.23|$$

The physical interpretation for the validity of this model was given later by the Swedish chemist *S. Arrhenius*, and the expression was named after him [71]. In its basic form, the pre-exponential factor (*frequency factor*) A and activation energy E_a are temperature-independent model parameters. An often used variation of the Arrhenius equation considers a pre-exponential factor that changes with temperature. This provides for an applicability of the rate law for a wider temperature range:

$$k = A'T^m e^{-\frac{E_a}{R\cdot T}} \qquad |2.24|$$

In principle, even if a reaction mechanism is able to describe the overall macroscopic reaction progress, it is not possible to confirm that a set of reactions correctly describes the real reaction progress *in detail* - the uncertainty remains, that the reaction might take place via intermediate steps. Thus, the current approach to set up chemical kinetic models is to concentrate on elementary steps in the mechanism that have the largest influence on the overall reaction kinetics. This reaction is the so-called *rate-determining step* of the mechanism [71].

2.5 Radiation

Radiation describes the energy transport via electromagnetic waves. In combustion processes, thermal radiation wavelengths to be considered are in the range of 0.1 to 100 μm [70] (compare visible light: $0.38-0.76\,\mu$m, infrared radiation: $1\,\mu\text{m}-1\,\text{mm}$). Heat transport due to radiation plays a major role in facilities involving combustion and gasification reactions [72, 73].

In the context of computational fluid dynamics, heat transport by conduction induces the transport of thermal energy between adjacent discrete control volumina via the cell boundary. Contrary to this, characteristic for heat transfer by radiation is its long range effect: A fluid element exchanges heat with all cells and with the boundaries defining the computational domain. This results in a mathematical model that, in general, cannot be solved analytically. A number of model approaches were developed to deal with radiative heat transfer in computational fluid dynamics, accounting for the radiative properties of the fluid under consideration. These properties include absorptive, emissive and refractive characteristics of the gas species and – if present – solid or liquid particles (e.g. ash particles, soot or liquid sprays). Due to these characteristics, radiative transfer is coupled to the other conservation equations such as energy equation and species balances [70].

In CFD, energy transfer by radiation is considered via introduction of an additional conservation equation that calculates the radiation intensity I. In general, radiation intensity varies within the wavelength spectrum and is also inhomogeneously distributed regarding spatial directions. Considering these dependencies, the incoming intensity to a surface element $\mathrm{d}A$ is given by (dihedral angle Θ, angle range $\mathrm{d}\Omega$, wavelength interval $\mathrm{d}\nu$):

$$I_\nu = \frac{\dot{Q}_{rad}}{\mathrm{d}\nu\,\mathrm{d}A\,\cos\Theta\,\mathrm{d}\Omega} \qquad |2.25|$$

In a finite volume element, incident radiation is subjected to change due to absorption, refraction and emission as the electromagnetic waves pass the fluid. Impact on the radiation intensity depends on local gas temperature and composition as well as solid particles or liquid sprays concentration, if dispersed phases are present. The conservation equation, integrated throughout the wavelength spectrum, can be written as [65]:

$$\frac{\mathrm{d}I\left(\mathbf{r},\mathbf{s}\right)}{\mathrm{d}s} + \left(a+\sigma_s\right) I\left(\mathbf{r},\mathbf{s}\right) = a\frac{\sigma T^4}{\pi} + \frac{\sigma_s}{4\pi}\int_0^{4\pi} I\left(\mathbf{r},\mathbf{s}'\right)\Phi\left(\mathbf{s}\cdot\mathbf{s}'\right)\mathrm{d}\Omega \qquad |2.26|$$

Equation 2.26 fulfills the conservation of radiation intensity at the position $\mathbf{r}$ in the direction of the vector $\mathbf{s}$ and is derived applying the laws of Kirchhoff and Stefan-Boltzmann. This balance already includes a simplification: Characteristic properties such as the absorption coefficient a are considered independent of the wavelength. The first term accumulates the change of radiation intensity along the path length $\mathrm{d}\mathbf{s}$. In the second term, refraction is implemented, similar to absorption (coefficients σ_s and a), as an intensity sink. On the right hand side of the equation, the first term describes the contribution to radiation intensity due to temperature dependent emission using the law of Stefan and Boltzmann. Finally, in the last term the intensity increase due to incident radiation is integrated for all spatial directions.

The phase function $\Phi(\mathbf{s} \cdot \mathbf{s}')$ can be used to model anisotropic refraction behavior. If refraction is considered diffuse, i.e. identical in all spatial directions, then $\Phi(\mathbf{s} \cdot \mathbf{s}') \equiv 1$, therefore:

$$\frac{\mathrm{d}I(\mathbf{r},\mathbf{s})}{\mathrm{d}s} + (a+\sigma_s)\, I(\mathbf{r},\mathbf{s}) = a\frac{\sigma T^4}{\pi} + \frac{\sigma_s}{4\pi}\int_0^{4\pi} I\left(\mathbf{r},\mathbf{s}'\right)\mathrm{d}\Omega \qquad |2.27|$$

In the numerical model, the source term in the energy equation due to radiation (last term in equ. 2.13) is computed by integration of intensity change in the considered discrete volume element.

3 Mathematical Model

In this chapter, the approaches to describe physical processes that occur in the blast furnace by means of mathematical expressions and their implementation into the current CFD model are summarized. The CFD simulations were carried out using the framework of the commercially available solver code ANSYS FLUENT®, version 6.3.26 [74].

An important feature of the FLUENT code is the possibility to enhance the features of the standard solver with new models by utilizing compiled user defined functions (UDF's, libraries written in C programming language), which can be linked dynamically to predefined solver interfaces. Using this possibility, empirical correlations as well as theoretical approaches describing the blast furnace process were implemented.

3.1 Dual-grid method

In the work-flow of CFD modeling, usually the considered computational domain is implemented and discretized spatially to solve the governing conservation equations, resulting in data fields describing one set of fluid conditions or conditions in stagnant solid zones in the domain. In the case of the blast furnace, solid raw material (iron ore, coke, flux) is fed to the top of the shaft. These solids slowly move downwards; iron ore is reduced by reducing agents present in the furnace and is transformed to molten raw iron, coke is also subjected to heterogeneous reactions.

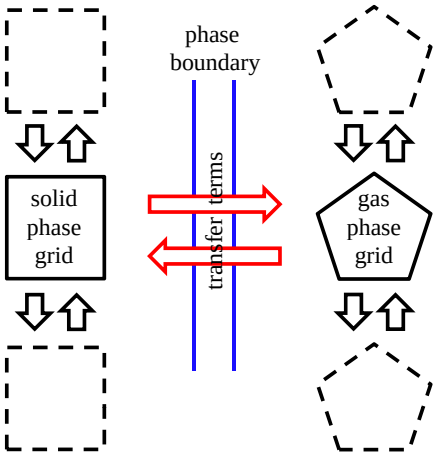

Figure 3.1: Schematic illustration of coupling terms implemented for the dual-grid method.

In the dual-grid approach, conservation equations are solved for both, solid (i.e. coke bed) and gas phase. The general conservation equation of an extensive quantity in its differential form can be written as given in equation 2.5. The dual grid model was set up by implementing source terms (last term in equ. 2.5) in the conservation equations describing the physical processes, i.e. heat sources in the case of heat transfer between solid and gas phase (see fig. 3.1). By implementing the dual grid method and therefore

solving for the fluid as well as solid data fields, the driving forces for transfer processes between the occurring phases can be calculated in the model.

The implementation of the dual grid model has been validated for a number of heat transfer problems in porous media of different types in a wide range of operating conditions (stationary solid phase) as well as for heterogeneous and homogeneous chemical reactions (moving solid bed). The validation procedure was structured such, that different experimental setups from literature were implemented in CFD with increasing complexity of the physical processes, starting at simple heat transfer problems between gas and solid phases. The simulation results were compared to the measured data to analyze the model performance [75, 76, 77, 78, 79, 80, 81].

3.2 Thermal conductivity in fixed beds

An important thermodynamic property in processes including heat flux is the thermal conductivity of the considered material. In the case of a blast furnace, intense interaction between solid coke and injected hot blast takes place. Due to the oxygen contained in the blast, very high reactivity occurs in the region around the tuyères. By the onset of heterogeneous coke combustion as well as oxidation of inserted fuels, temperatures are increased to up to 2200 °C [2]. The heat is transported to zones around the tuyères by convective transport via the gases as well as by heat conduction in the coke bed. To be able to successfully model the blast furnace process, these transport phenomena have to be taken into account.

Direct computation of thermal conductivity in fixed beds can be done by solving the Laplace equation for heat transport in and around single particles in the bed [82]. This means, that the exact geometry of every single particle in the coke bed needs to be known and the fluid flow around the particles has to be computed. Due to the resulting very high computational expense as well as the impossibility to define the coke bed in every detail, this approach is not feasible for industrial applications. Therefore, the apparent conductivity of the coke bed is estimated by calculation of the effective thermal conductivity using models from literature that are compatible to the porous medium approach which was adopted to represent the cokebed.

In general, thermal conductivity of fixed beds can be expressed in terms of solid material conductivity λ_p, conductivity of the fluid λ_f and the bed porosity ε. Besides these primary parameters, according to the operating conditions, a number of secondary parameters needs to be considered that account for effects due to particle radiation (especially important at higher temperatures), pressure (Smoluchowski-effect), structure of the packed bed or particle deformation due to mechanical load [82]. In the dual-grid method, the effective thermal conductivity is calculated by implementing the model of Zehner, Bauer and Schlünder [83, 84, 85, 86], which is also recommended for practical use in industrial applications [82, 87].

3.3 Turbulence

The gas flow in the vicinity of tuyères of blast furnaces features a dominating round free jet that is introduced by the injected hot blast and by injection of additional substances via injection lances. To properly model the decay rates of gas velocity as well as mixing processes that are heavily influenced by turbulence, an adequate turbulence model has to be applied. Jordan et al. [88] conducted a number of experiments for turbulent free jets utilizing laser doppler anometry for velocity measurements. Velocity profiles along the jet

axis as well as in the radial direction were measured and compared to CFD simulations involving various kinds of turbulence models. According to this work, the SST-kω model and the realizable k-ϵ model performed best considering the length and spreading rate of the free jets. The realizable k-ϵ model is widely used in industrial applications including chemical reactions [67, 68] and therefore is adopted in the present model setup.

3.4 Heterogeneous heat transfer

Due to temperature differences between solid and fluid phase in the blast furnace, heterogeneous heat transfer takes place. In the model, heat flow rates are calculated using a classical approach based on the dimensionless Nusselt number Nu. A variety of expressions correlating Reynolds number Re and Prandtl number Pr, accounting for different flow regimes, is available.

Here, the expression of Gnielinski [89, 90], applicable to heat transfer at fixed bed conditions is used to compute the required heat transfer coefficient α. In the correlation, the Reynolds number accounts for the effect of fluid dynamics on the boundary layer thickness. Gnielinski introduced the following definition for Re, to be used in a fixed bed of spheres with porosity ε, using the particle diameter d_p as the characteristic length:

$$Re_\varepsilon = \frac{v\, d_p}{\nu\, \varepsilon} \qquad |3.1|$$

Laminar (Nu_l), turbulent (Nu_t) and particle (Nu_p) Nusselt numbers are calculated as:

$$\begin{aligned} Nu_l &= 0.664 \cdot \sqrt{Re_\varepsilon} \cdot \sqrt[3]{Pr} \\ Nu_t &= \frac{0.037 \cdot Re_\varepsilon^{0.8} \cdot Pr}{1 + 2.443 \cdot Re_\varepsilon^{-0.1} \cdot \left(Pr^{2/3} - 1\right)} \\ Nu_p &= 2 + \sqrt{Nu_l^2 + Nu_t^2} \end{aligned} \qquad |3.2|$$

Heat transfer coefficients are higher for particles in a fixed bed as compared to single particles immersed in a fluid flow. Gnielinski introduced a shape factor f_a to be used with the single-particle Nusselt number Nu_p:

$$Nu_{bed} = f_a \cdot Nu_p \quad , \qquad |3.3|$$

where for a fixed bed of uniformly sized spheres f_a is calculated as:

$$f_a = 1 + 1.5 \cdot (1 - \varepsilon) \quad . \qquad |3.4|$$

Finally, the specific heterogeneous heat transfer rates α are calculated from the Nusselt number:

$$Nu_{bed} = \frac{\alpha \cdot d_p}{\lambda} \qquad \text{and} \qquad \dot{Q} = \alpha \cdot A_p \cdot \Delta T \quad . \qquad |3.5|$$

3.5 Homogeneous reactions

A prerequisite for successful computation of reactions in the gas-phase is the implementation of a suitable reaction model. In the current model, the *Eddy Dissipation Concept* based on the work of Magnussen [91] was used. This model accounts for the influence of turbulent mixing processes on the reaction kinetics: Reactions are considered to take place in the finest structures of turbulent eddies. It is assumed, that educt species need

to be mixed on these smallest length scales of the turbulent flow before an actual chemical reaction can proceed. The fluid in a cell volume is therefore split into reacting and non-reacting fractions. The reacting part is modeled as a perfectly stirred reactor that is fed with fluid from the non-reacting part of the cell volume. Residence times in the reactor are estimated from turbulence quantities.

In the CFD model, gas-phase combustion and gasification reactions were modeled using a mechanism of global reactions based on Arrhenius-type reaction kinetics, considering 10 gas mixture components (O_2, N_2, CH_4, H_2, CO, CO_2, H_2O, gaseous fuel oil $C_{19}H_{30}$, soot C_s, coal volatiles $CH_{2.65}N_{0.07}O_{0.21}$) in a set of reactions [74, 92] (R 18 - R 29):

$$2\,CH_4 + 4\,O_2 \longrightarrow 2\,CO_2 + 4\,H_2O \qquad |R\,18|$$

$$2\,CO + O_2 \longrightarrow 2\,CO_2 \qquad |R\,19|$$

$$2\,CO_2 \longrightarrow 2\,CO + O_2 \qquad |R\,20|$$

$$2\,H_2 + O_2 \longrightarrow 2\,H_2O \qquad |R\,21|$$

$$CO + H_2O \longleftrightarrow CO_2 + H_2 \qquad |R\,22|$$

$$CH_4 \longleftrightarrow C_s + 2\,H_2 \qquad |R\,23|$$

$$C_{19}H_{30} + 17\,O_2 \longrightarrow 19\,CO + 15\,H_2O \qquad |R\,24|$$

$$C_{19}H_{30} + 6\,O_2 \longrightarrow H_2 + 7\,CH_4 + 12\,CO \qquad |R\,25|$$

$$C_{19}H_{30} \longrightarrow 0.13\,C_s + 3\,H_2 + 6\,CH_4 \qquad |R\,26|$$

$$CH_{2.65}N_{0.07}O_{0.21} + 1.56\ O_2 \longrightarrow CO_2 + 1.33\ H_2O + 0.033\ N_2 \qquad |R\,27|$$

$$CH_{2.65}N_{0.07}O_{0.21} + 0.4\ O_2 \longrightarrow CO + 1.33\ H_2 + 0.033\ N_2 \qquad |R\,28|$$

$$CH_{2.65}N_{0.07}O_{0.21} \longrightarrow C_s + CO + 1.33\ H_2 + 0.033\ N_2 \qquad |R\,29|$$

Most important reactions in the mechanism include e.g. the homogeneous Boudouard reaction (R 20) and the homogeneous water-gas shift reaction (R 22).

The consumption of fuel oil vapor is computed via two competing combustion reactions (R 24 and R 25). An additional pyrolysis reaction is implemented that accounts for destruction of injected heavy oil due to high temperatures (reaction R 26, kinetic parameters as given by Kok and Gundogar [93]). In this pathway of oil consumption, carbon is released from oil as soot (C_s). An analog setup was implemented to describe the conversion of volatiles released from injected pulverized coal (reactions R 27 to R 29).

Another source for soot in the model is from homogeneous decomposition of CH_4. Methane is the most stable hydrocarbon, non-catalytic decomposition of CH_4 starts at

temperatures above 1000 K. In the model the rate of methane decomposition is calculated using the kinetic data from Abbas and Daud [94].

The complexity of the chemical reaction mechanism greatly influences the computational effort:

- Additional gas-phase species require additional transport equations to be solved,
- and the stiffness of the equation system to be solved during chemistry integration is increased by adding more reaction equations, as the range of chemical time scales is widened.

By using the presented global reaction mechanism, extensive full-scale studies of industrial applications can be carried out. To speed up integration of the chemical reaction terms, reaction kinetics were integrated using in-situ adaptive tabulation of reaction rates in the multi-dimensional reaction domain [74].

3.6 Heterogeneous coke reactions

In the blast furnace process, coke is fed as fuel and as carbon-carrier. While the feed materials in the shaft furnace proceed downwards, besides direct reduction of ore, coke is also subjected to heterogeneous reactions with the counter-current gas flow. The coke gasification reactions produce gas species that interact with the iron ore and therefore contribute to secondary ore reduction.

In the current modeling approach, heterogeneous reactions are modeled using kinetic expressions. This allows for a much more accurate description as opposed to setups assuming e.g. local chemical equilibrium [95]. Furthermore, coke particles are treated accounting for their inner porous structure and therefore the contribution of heterogeneous reactions that take place on the inner surface. However, the attempt to calculate reaction rates accounting for the variety of physical and chemical processes and interactions strongly increases the model complexity.

The general reaction scheme that takes place on the particle level can be considered as a series of processes [3]:

- Diffusion of gaseous educt species through the boundary layer towards the outer particle surface,
- gas diffusion in the particle pores towards actual reaction sites and
- heterogeneous chemical reactions at the actual reaction site.

Effective reaction rates (i.e. the rates of conversion that are observed on a macroscopic scale) are influenced by these steps depending on the conditions such as e.g. gas/particle temperature levels (see fig. 3.2, left). This results in characteristic educt species profiles throughout the particle and the surrounding boundary layer for the different temperature regimes as shown in the right sketch of figure 3.2.

3.6.1 Effective heterogeneous reaction rates

Chemically controlled regime

At low temperatures and small particle dimensions, conversion rates are limited by the intrinsic kinetics of chemical reactions because diffusion processes are much faster than chemical kinetics. In this regime, the concentration of educt species is nearly constant

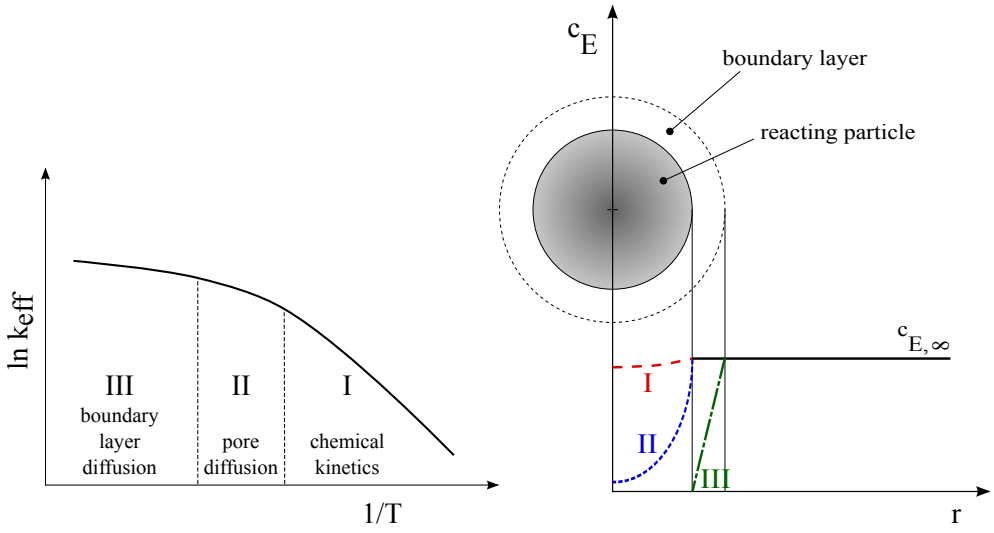

Figure 3.2: Left: Temperature-dependence of effective heterogeneous reaction rates. Right: Schematic illustration of educt concentration profiles in different temperature zones.

throughout the particle, the entire inner surface of the porous particle is subjected to chemical reactions (fig. 3.2, right). The overall reaction rate is determined by the intrinsic reaction rate that is mainly given by the characteristics of the particle material and the considered reaction partners – therefore, this range is called the *chemical regime*.

The majority of kinetic expressions for oxidation and gasification of carbonaceous substances is based on the theory of *active centers* that assumes that chemical reactions between gas molecules and solid surfaces take place at energetically favored positions [96]. These locations are e.g. irregularities on the surface such as embedded heteroatoms, disturbances in the grid structure or edges formed by carbon layers. It is assumed, that an educt molecule is adsorbed to the solid surface before the chemical reaction takes place. After the reaction, the product molecule is released to the gas phase.

Accordingly, the reaction kinetics of the considered solid phase strongly depends on the characteristics of the active sites and therefore on the considered material. Intrinsic reaction kinetics need to be implemented and validated for the used solid matter.

Pore diffusion

While most chemical reactions rates increase exponentially with temperature (modeled using e.g. Arrhenius-type kinetics, equ. 2.23), rates of gas diffusion increase in the order of $T^{1.75}$ (see equ. 3.11). Therefore, as with increasing temperature the chemical reaction rate reaches the rate of species transport, educt concentration levels in the particle pores decline. The resulting concentration profile in the particle has the effect that only a part of the inner particle surface is involved in the chemical reaction [96]. The partial utilization of the inner surface can be modeled by the introduction of an effectiveness factor γ [97]. This approach allows for the estimation of the degree of pores that is utilized in the considered heterogeneous reaction and therefore the decrease of the overall reaction rate due to pore diffusion:

$$\gamma \equiv \frac{\text{reaction rate accounting for diffusion}}{\text{intrinsic reaction rate}}$$

The effectiveness factor is a function of educt concentration in the particle pores and the intrinsic reaction rate and can be expressed by the Thiele-modulus ψ. The Thiele-modulus accounts for the partial utilization of the available inner particle surface by integration of local reaction rates throughout the particle volume [95]. For a spherical porous particle, γ is estimated as [97]:

$$\gamma = \frac{1}{\psi}\left(\frac{1}{\tanh\psi} - \frac{1}{\psi}\right) \qquad |3.6|$$

with the Thiele modulus given by [96]:

$$\psi = \frac{d_p}{2} \cdot \sqrt{\frac{1+\nu}{2} \cdot \frac{k \cdot \rho_p \cdot c_{ed,S}^{\nu-1}}{D_{eff}}} \quad , \qquad |3.7|$$

where the effective diffusion coefficient D_{eff} is used. D_{eff} is calculated accounting for increased resistance against the movement of gas molecules due to blocking effects inside the pore structures (Knudsen diffusion coefficient for species i, $D_{K,i}$) [98]:

$$D_{K,i} = \frac{d_p}{3}\sqrt{\frac{8RT}{\pi M_i}}\frac{\varepsilon_p}{\tau} \qquad |3.8|$$

In equation 3.8, the particle porosity ε_p represents the void fraction of a single particle, while the pore tortuosity τ accounts for the labyrinth structure of the pores that desires the molecules to travel a longer distance to reach to the same particle radii [96].

$$D_{eff} = \frac{1}{\frac{1}{D_{i,m}} + \frac{1}{D_{K,i}}} \qquad |3.9|$$

The diffusion coefficient of a gas species in the bulk depends on operating conditions such as temperature and pressure (increasing with temperature, inversely proportional to pressure). The model setup involves a number of gas components. Reactants are assumed to be subjected to diffusive transport in the gas mixture. So, the problem to solve is the calculation of $D_{i,m}$ – that is the diffusion of species i in the gas mixture m (multicomponent gas diffusion, Stefan-Maxwell-diffusion [99]). Multicomponent diffusion coefficients are calculated starting from the computation of the coefficients for binary diffusion, i.e. the diffusion of the considered species in each of the mixture components and proper combination of these diffusivities. In this work, the multicomponent diffusion coefficient is calculated based on the relationship of Wilke [100]:

$$D_{i,m} = \frac{1}{\sum\limits_{j=1,\, j\neq i}^{N} \frac{x_j}{D_{i,j}}} \quad , \qquad |3.10|$$

where the binary diffusion coefficients $D_{i,j}$ are calculated following the correlation of Fuller et al. [101]:

$$D_{i,j} = \frac{0.00143 \cdot T^{1.75}\sqrt{\frac{1}{M_i} + \frac{1}{M_j}}}{p\sqrt{2}\left(\sqrt[3]{V_i} + \sqrt[3]{V_j}\right)^2} \cdot 10^{-4} \quad . \qquad |3.11|$$

In this expression, V_i and $\mathrm{V_j}$ represent the sum of group contributions for diffusion volumes [82].

Boundary layer diffusion

The bulk of the gas phase is connected to the solid particle surface via an interface, the boundary layer. Prior to a heterogeneous reaction it is necessary that the involved gas component passes this gas layer to reach the solid particle surface. The resistance to mass transfer through this interface causes a concentration gradient between bulk and surface. The concentrations on both sides of the interface are related to each other by thermodynamic laws and are usually expressed in terms of thermodynamic equilibrium [99]. In general, this diffusion problem is solved by computation of a mass transfer coefficient. This coefficient can be calculated using an empirical equation that correlates fluid properties and operating conditions to the mass transfer coefficient [99]. Basis for the estimation methods is the kinetic gas theory [82].

The mass transfer coefficient k_c is defined as the ratio of species flux to concentration difference. In real applications including flow around the particle, due to physical processes at the interface caused e.g. by convection or turbulence, the mass transfer coefficient is much larger as it would be observed by the concentration difference alone. In practice, correlations are used to account for these flow effects.

For dilute systems, the general expression for the transfer rate of species i via the interface can be written as:

$$\dot{N}_i = k_c A \left(x_i - x_{i,S}\right) \qquad |3.12|$$

The diffusion problem in this work is related to adsorption of gas components on a solid surface (coke) prior to gasification reactions. The diffusion problem is considered uni-directional – the expression for the diffusion rate can therefore be written as:

$$\dot{N}_i = \frac{D_{i,m} p}{RT\delta_c} A \left(x_i - x_{i,S}\right) \qquad |3.13|$$

The film thickness δ_c depends on the hydrodynamics and transport properties in the system and is expressed in terms of Reynolds and Schmidt number.

The fixed bed has very complex geometric properties – theoretical correlations for mass transfer coefficients are not available. Correlations are therefore obtained empirically by fitting experimental findings [99]. Due to the analogy between heat and mass transfer, a variety of expressions correlating Re and Sc to obtain the Sherwood-number Sh is available. The correlation of Petrovic and Thodos [102] was used to account for the transfer conditions of fluid flow in a fixed bed of solid particles:

$$Sh = \frac{k_c d_p}{D_{i,m}} = f\left(Re, Sc\right) = \frac{0.357}{\varepsilon} Re^{0.641} Sc^{1/3} \qquad |3.14|$$

The Reynolds number is calculated accounting for the non-sphericity of coke particles [99]), using the specific surface area $a = \frac{6(1-\varepsilon)}{d_p}$ in the coke bed:

$$Re = \frac{v\,\rho}{\mu\,\Psi\,a} \qquad |3.15|$$

The definition of the Sherwood-Number (equ. 3.14) is rearranged to give the surface specific mass transfer rate for species i:

$$k_{c,i} = \frac{0.357}{\varepsilon} Re^{0.641} Sc^{1/3} \frac{D_{i,m}}{d_p} \qquad |3.16|$$

For the calculation of diffusion coefficients (equ. 3.10) as well as thermodynamic properties used in the correlations, the temperature in the boundary layer surrounding the coke surface is calculated as the arithmetic mean from particle and gas-phase bulk temperature:

$$T_m = \frac{T_f + T_p}{2} \qquad |3.17|$$

At very high temperatures, the transport of educts from the bulk flow surrounding the solid particle through the boundary layer towards the particle's outer surface forms the limiting step.

Effective heterogeneous reaction rate

Finally, the effective heterogeneous reaction rate for each of the considered reaction equations is calculated accounting for the above mentioned transport mechanisms and intrinsic reaction rate k_{reac} as a series of resistances [95]:

$$k_{eff} = \frac{1}{\frac{1}{k_{c,i} \cdot A_{coke} \cdot c_i^{1-\nu}} + \frac{1}{\gamma \cdot k_{reac}}} \qquad |3.18|$$

Using this approach the effective reaction rate can be calculated for a wide temperature range, accounting for limitation of heterogeneous reactions by intrinsic reaction rates at lower operating temperature (zone I), limitation by pore diffusion at intermediate temperatures (zone II) and boundary layer diffusion at high temperatures (zone III) (see figure 3.2).

3.6.2 Considered heterogeneous reactions

A set of heterogeneous gasification reactions was implemented to model the coke utilization with various reaction partners. The most important aspects in gasification of solid carbonaceous fuels can be described by four heterogeneous reactions [103, 104, 105, 106], summarized in table 3.1. In this set, coke oxidation is by far the most exothermic reaction, while Boudouard and water-gas shift reactions are endothermic. The methanation reaction is slightly endothermic and plays a minor role at conditions present in the blast furnace process.

Table 3.1: Heterogeneous coke reactions implemented in the reaction system.

reaction	reaction equation	ΔH
Combustion	$C + O_2 \xrightarrow{k_{O_2}} CO_2$	$-393.5\,\mathrm{kJ/mol}$
Boudouard	$C + CO_2 \xrightarrow{k_{CO_2}} 2\,CO$	$172.5\,\mathrm{kJ/mol}$
Water-gas shift	$C + H_2O \xrightarrow{k_{H_2O}} CO + H_2$	$131.3\,\mathrm{kJ/mol}$
Methanation	$C + H_2 \xleftrightarrow{k_{H_2}} CH_4$	$-74.9\,\mathrm{kJ/mol}$

In the developed model, coke reactions are rewritten as proposed by Blasi [107] to properly represent oxygen and hydrogen contained in the coke matrix, as given by the elementary analysis. Furthermore, coke is modeled dry. This assumption is considered appropriate for the current conditions, as the upper boundary of the simulation domain

that also defines the interface of coke intake is located at a level where temperatures are high at sufficiently long residence times to ensure that any moisture contained in the coke has been evaporated.

Coke combustion: Injected hot blast contains oxygen that reacts with coke forming the boundary of the raceway as well as particles passing the raceway cavity. This exothermic reaction releases heat that is utilized by endothermic gasification reactions as well as for the reduction of iron oxides.

$$\mathrm{CH_xO_y(s)} + (\frac{\mathrm{x}}{4} - \frac{\mathrm{y}}{2})\,\mathrm{O_2} \xrightarrow{k_{O_2}} \mathrm{CO_2} + \frac{\mathrm{x}}{2}\,\mathrm{H_2O} \qquad |\mathrm{R\,30}|$$

Reaction kinetics for this equation were adopted from Rumpel [96]. The reaction data originate from the regression of thermogravimetric experiments using coke obtained from various carbon carriers such as wood and bituminous coal:

$$k_{coke,\,O_2} = 3.8 \cdot 10^7 \cdot e^{-\frac{150500}{R \cdot T_{coke}}} \quad \left[\mathrm{mol_{coke}/kg_{coke}{\cdot}s\,(m^3/mol_{O_2})^{\nu}}\right] \qquad |3.19|$$

This expression for the intrinsic reaction rate is used together with the diffusion models presented in section 3.6.1 to calculate effective heterogeneous reaction rates. The resulting reaction rates are shown in figure 3.3. For the blast furnace simulation runs, burning rates of coke are expressed in terms of the volumetric coke consumption as:

$$S_{coke,\,O_2} = -k_{O_2,\,eff} \cdot M_{coke} \cdot (1-\varepsilon) \cdot \rho_{coke} \cdot c_{O_2}^{\nu} \quad \left[\mathrm{kg_{coke}/m^3{\cdot}s}\right] \qquad |3.20|$$

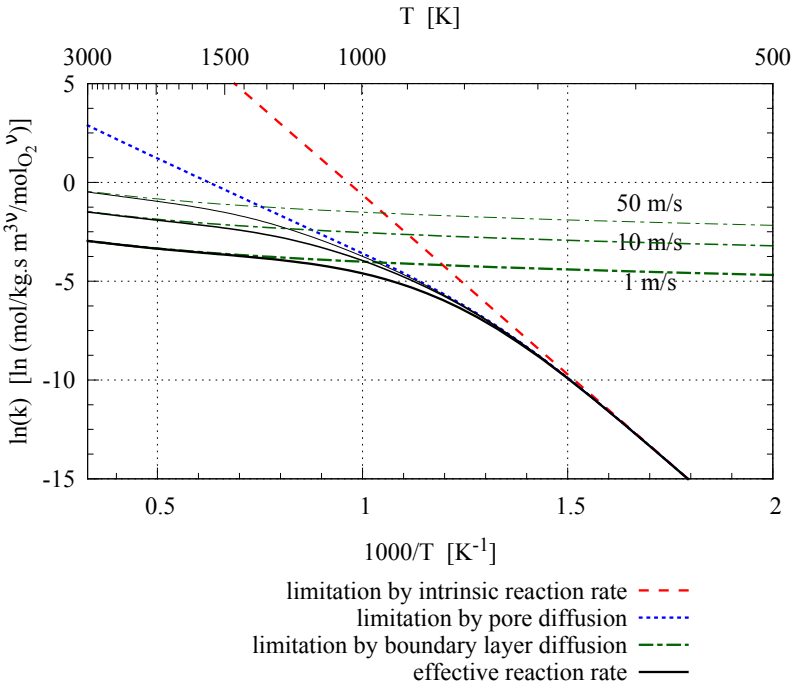

Figure 3.3: Rate of coke oxidation as function of temperature at various gas-solid relative velocities. Operating conditions as at the raceway boundary in the blast furnace: gas velocities 1 m/s, 10 m/s and 50 m/s, $p = 5.1$ bar, $d_p = 21$ mm, $\varepsilon = 0.8$, gas mixture: 15.2 $\%_{v/v}$ H_2O, 10.4 $\%_{v/v}$ CO_2, 4.9 $\%_{v/v}$ O_2, balance N_2.

Boudouard reaction: At elevated temperatures, coke also reacts with other gas components such as carbon dioxide, water vapor and hydrogen. The proper description of these gasification reactions is even more important than in the case of oxidation, because intrinsic reaction rates are typically significantly lower, consequently the rate limiting step is depicted by the combination of reaction kinetics and diffusion processes.
The most important heterogeneous reaction of blast furnace coke is the gasification with CO_2 to form CO that is subsequently utilized for indirect iron oxide reduction.

$$\mathrm{CH_xO_y(s) + CO_2 \xrightarrow{k_{CO_2}} 2\,CO + yH_2O + (\frac{x}{2}-y)\,H_2O} \qquad |\mathrm{R\,31}|$$

The Boudouard reaction is highly endothermic (see ΔH in tab. 3.1) and is at standard conditions thermodynamically hindered due to the higher Gibbs enthalpy of the reaction products. As the reaction proceeds, the entropy in the system is increased ($\Delta S_{298,\,Boud} = 180\,^{\mathrm{J}}/_{\mathrm{mol\cdot K}} > 0$), resulting in a decrease of the Gibbs-enthalpy difference $\Delta G = \Delta H - T \cdot \Delta S$ at higher temperatures. Accordingly, the reaction is exergonic at temperatures above 700 °C and the equilibrium of the reaction is shifted to the product side.
With increasing pressure levels, the reaction rate declines due to the stoichiometry of the reaction equation (2 mol of gas produced, 1 mol consumed; Le Chatelier's principle), as illustrated in figure 3.4:

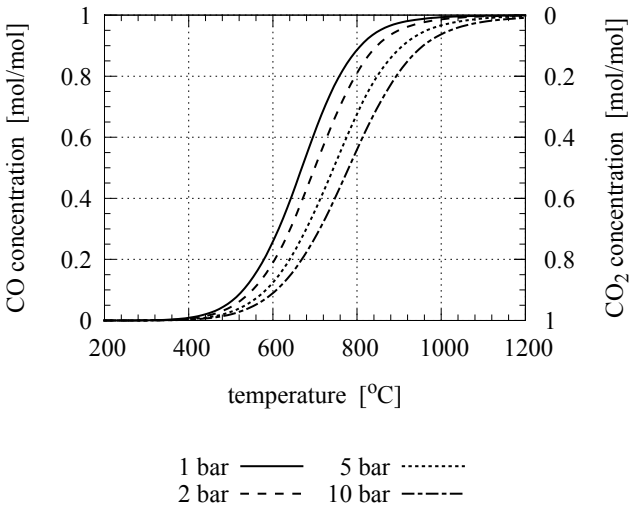

Figure 3.4: Equilibrium gas-phase concentration profile of Boudouard reaction at varying temperature and pressure (initial conditions: $n_C = n_{CO_2} = n_{CO} = 1\ mol$).

Kinetic rate expression used in this work (coke from bituminous coal, [96]):

$$k_{coke,\,CO_2} = 2.7 \cdot 10^5 \cdot e^{-\frac{185200}{R \cdot T_{coke}}} \quad \left[\mathrm{mol_{coke}/kg_{coke}\cdot s\,(m^3/mol_{CO_2})^{\nu}}\right] \qquad |3.21|$$

Definition of the source term in the simulation model:

$$S_{coke,\,CO_2} = -k_{coke,\,boud,\,eff} \cdot M_{coke} \cdot (1-\varepsilon) \cdot \rho_{coke} \cdot c_{CO_2}^{\nu} \quad \left[\mathrm{kg_{coke}/m^3\cdot s}\right] \qquad |3.22|$$

The resulting reaction rates at conditions near the raceway-boundary of the blast

furnace are shown in figure 3.5. In comparison with the oxidation reaction, the intrinsic rate of CO_2 gasification is low, therefore the overall reaction rate is limited by reaction kinetics in a wider temperature range.

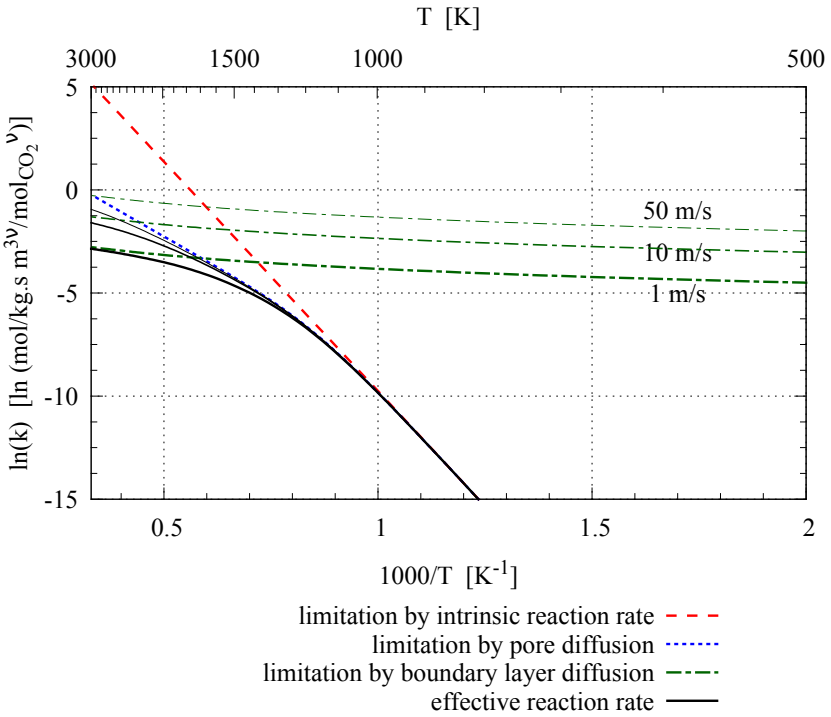

Figure 3.5: Rate of Boudouard reaction as a function of temperature at various gas-solid relative velocities. Operating conditions as at the raceway boundary in the blast furnace: gas velocities 1 m/s, 10 m/s and 50 m/s, $p = 5.1$ bar, $d_p = 21$ mm, $\varepsilon = 0.8$, gas mixture: 15.2 $\%_{v/v}$ H_2O, 10.4 $\%_{v/v}$ CO_2, 4.9 $\%_{v/v}$ O_2, balance N_2.

Heterogeneous water-gas shift: At equal temperature and partial pressure of gasification agent, steam gasification proceeds several times faster than CO_2–gasification [105, 108].

$$\mathrm{CH_xO_y(s) + (1{-}y)\,H_2O \xrightarrow{k_{H_2O}} CO + (1 + \frac{x}{2}{-}y)\,H_2} \qquad |\mathrm{R\,32}|$$

The coke consumption by reaction with water vapor is calculated using a model of Hobbs et al. [109], where the reaction rate is expressed with respect to the particle surface $A_{coke} = \frac{6}{d_p \rho_p}$:

$$k_{coke,\,H_2O} = 3.42 \cdot T_{coke} \cdot e^{-\frac{129700}{R \cdot T_{coke}}} \quad [\mathrm{mol_{coke}/m^2_{coke}{\cdot}s m^3/mol_{H_2O}}] \qquad |3.23|$$

Coke source terms are therefore computed as:

$$S_{coke,\,H_2O} = -k_{coke,\,H_2O,\,eff} \cdot M_{coke} \cdot (1-\varepsilon) \cdot \rho_{coke} \cdot c_{H_2O} \cdot A_{coke} \quad [\mathrm{kg_{coke}/m^3{\cdot}s}] \quad |3.24|$$

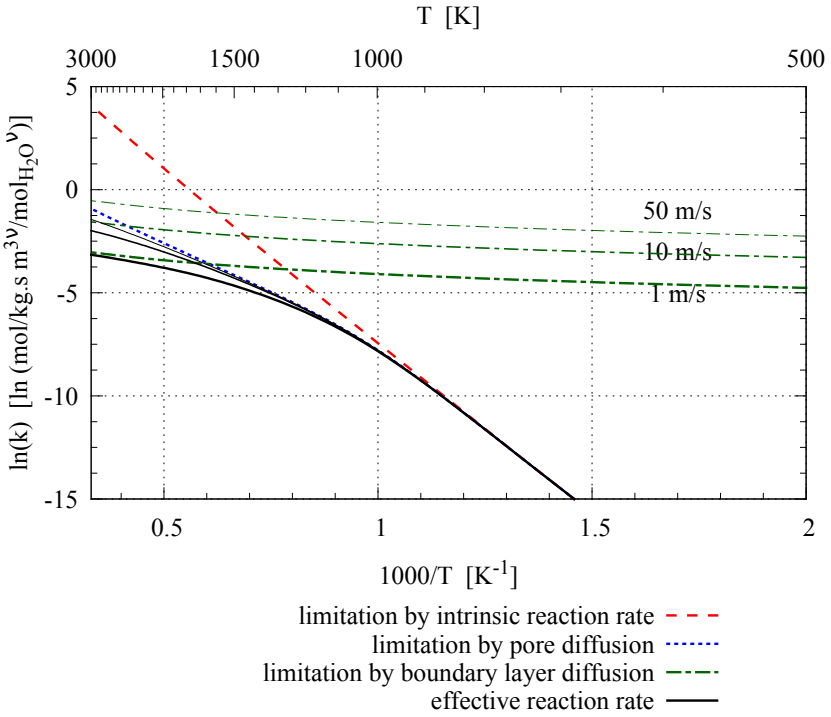

Figure 3.6: Rate of water-gas shift reaction as function of temperature at various gas-solid relative velocities. Operating conditions as at the raceway boundary in the blast furnace: gas velocities 1 m/s, 10 m/s and 50 m/s, $p = 5.1$ bar, $d_p = 21$ mm, $\varepsilon = 0.8$, gas mixture: 15.2 $\%_{v/v}$ H_2O, 10.4 $\%_{v/v}$ CO_2, 4.9 $\%_{v/v}$ O_2, balance N_2.

The equilibrium gas-phase composition for initially equal moles of C, H_2O, H_2 and CO is shown in figure 3.7:

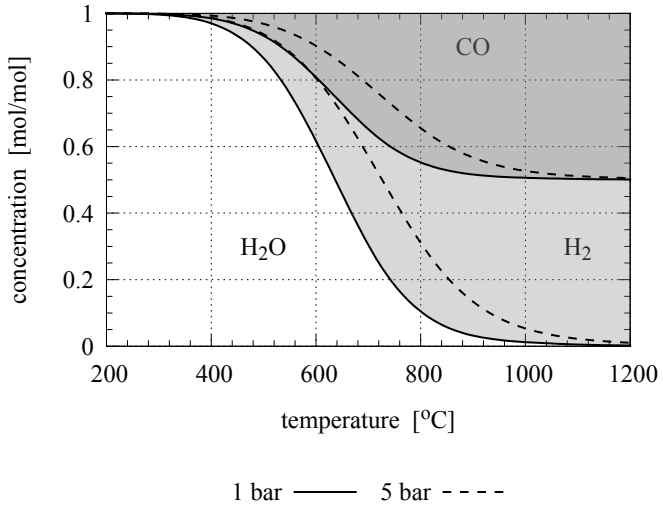

Figure 3.7: Equilibrium gas-phase concentration profile of heterogeneous water-gas shift reaction varying temperature and pressure (initial conditions: $n_C = n_{H_2O} = n_{CO} = n_{H_2} = 1\ mol$).

Heterogeneous methane formation:

$$\mathrm{CH_xO_y(s)} + (2 + \mathrm{y} - \frac{\mathrm{x}}{2})\,\mathrm{H_2} \xrightarrow{k_{H_2}} \mathrm{CH_4} + \mathrm{y}\,\mathrm{H_2O} \qquad |\mathrm{R}\,33|$$

The gasification of coke by hydrogen to produce methane is implemented based on the approach of Hobbs et al. [109] using the kinetic data as given by Tepper [95].

$$k_{coke,\,H_2} = 0.00342 \cdot T_{coke} \cdot e^{-\frac{129700}{R \cdot T_{coke}}} \quad [\mathrm{mol_{coke}/m^2_{coke}{\cdot}s m^3/mol_{H_2}}] \qquad |3.25|$$

$$S_{coke,\,H_2} = -k_{coke,\,H_2,\,eff} \cdot M_{coke} \cdot (1-\varepsilon) \cdot \rho_{coke} \cdot c_{H_2} \cdot A_{coke} \quad [\mathrm{kg_{coke}/m^3{\cdot}s}] \qquad |3.26|$$

Heat of heterogeneous reactions: The heat of reactions ΔH_r are computed from standard state enthalpy differences at local coke temperatures using polynomial expressions available for thermophysical properties (Shomate equations, [110]) to calculate enthalpy differences relative to standard conditions.

$$\Delta H_r = \sum \Delta H^{T_g}_{i,\,prod} - \sum \Delta H^{T_g}_{i,\,ed} \qquad |3.27|$$

The standard enthalpy of formation of solid coke was calculated from the tabulated values of gas species involved in the combustion reaction using the lower heat of combustion of coke given from experimental examination (see tab. 5.3).

In the blast furnace, coke size varies from 3 mm to 30 mm near the raceway boundary and further away, respectively [19]. However, the particle size represents a critical parameter to successfully model raceway conditions, as it directly influences the length of educt species diffusion paths. The reasonable choice of a mean diameter was reported to offer a promising approach to model the blast furnace process [19], thereby avoiding the introduction of computationally very expensive population balance models to thoroughly describe particle shrinking effects.

3.7 Reduction of iron oxides

The simulation domain considered is restricted to the lower part of the blast furnace, where the reduction of iron oxide is reported to be finished and liquid hot metal as well as slag is present (see e.g. [2, 3, 12, 30]). Therefore, the reduction reactions of the liquid phase are not included in the model. If in future work the simulation domain is to be extended towards the stack, this functionality can be added by introducing species and heat source terms in the governing conservation equations.

3.8 Simulation of solid flow

The flow of solids charged to the blast furnace has considerable influence on the operating characteristics. The loading of iron ore and coke on top of the bed and the bulk flow in shaft, raceway and hearth zone determine the operation stability to a great extent [29, 111]. While the burden descends driven by gravity, coke is gasified and iron ores are reduced. The ore is molten in the cohesion zone, below this region coke remains as the only solid material, allowing for liquid raw iron and slag to move downwards,

countercurrent to hot blast moving towards the top of the furnace. The flow of solids in a blast furnace is mainly driven by melting of iron ore and conversion of coke in the raceway zone.

For simulation of the flow of solid matter in a blast furnace, several approaches of problem formulations can be defined [29]:

Continuum multiphase approach The so-called Euler-granular method is commonly implemented for flow simulation of gas and granular solids [112]. Solid and fluid media are treated as continuous, fully interpenetrating with separate conservation equations. This approach makes use of the kinetic theory of gases to describe inter-phase exchange coefficients between gas or liquid and granular materials. Several model setups reported in the literature use this approach to model flow of solids in iron blast furnaces [28, 113, 114, 115].

Discrete approach Direct computation of the movement of each of the particles present in a two-phase flow is called „discrete element method“. In this approach Newton's law of motion is integrated for every single particle present in the simulation domain. This offers the possibility to evaluate trajectories as well as forces acting on the particulate matter and delivers significant input to a deep understanding of processes on a microscopic level. However, this output comes to a tremendous computational effort [20]. This is especially true, if a wide range of velocities is present in the process to be modeled – this is the case when a blast furnace is considered: very high velocities are found near the tuyères, whereas the movement of burden in the stack is very slow. Furthermore, due to still restricted computational resources the number of particles that can be modeled is limited and therefore simplifications and assumptions have to be made to model real-world blast furnace flow problems. Several authors have tested model setups coupling the computation of solid particles using the methods of DEM with finite volume solvers (CFD) [20, 116, 117, 118, 119, 120].

Viscous flow model Simplified modeling techniques are based on the representation of the coke bed as continuous, single-phase fluids with modified viscosity to account for the characteristic behavior of moving beds of particles [121, 122]. A big advantage of this approach is the considerably lower computational demand as compared to the above mentioned multiphase-models, as computations can be performed for steady-state conditions, avoiding computationally very demanding time-discretization of the conservation equations. If the shape of the dead-man zone in the blast furnace is prescribed, the motion of the moving solid's bed can also be modeled using a viscosity-model adopting the Newtonian approach [122]. Friction between particles is described by introducing a fictive solid viscosity. The resulting viscosity model can be used in the Navier-Stokes equations. This approach offers the big advantage that the flow field of solid matter can be calculated using a finite volume solver.

The currently implemented model represents solid flux via the viscous flow approach, including the ability to describe the driving forces (coke consumption in the raceway zone and by heterogeneous gasification reactions). Viscosity is expressed using correlations for Bingham media. Various authors [121, 123, 124] state the possibility to model the movement of a bed of solids as a viscous fluid with properties of so-called „Bingham“ media. The viscous properties are described by two parameters: yield viscosity μ_0 and yield stress τ_0. These parameters were determined experimentally for various solid matters (glass beads, quartz sand, silica spheres, alumina balls, soy beans, millet, coal and salt)

by Nogami and Yagi [121]. Parameters for coal particles were used in the present study ($\mu_0 = 1230\,\mathrm{Pas}$, $\tau_0 = 1.14\,\mathrm{Pa}$). As coke particles are usually larger than the length scale of roughness of the furnace rigid walls, the usually applied no-slip boundary condition for solid velocities is not valid [122]. Actually, partial slip of solids at the furnace insulation material is possible. Consequently, in the simulation a slip boundary is applied at walls.

3.9 Raceway cavity

The size and shape of the cavity, formed by hot blast injected through the tuyères, determines the traveling distance of injected fuels prior to impact on the coke bed and therefore states an important boundary condition. In the current simulation framework emphasis is laid on chemical reactions in the raceway cavity and in the surrounding coke bed. To limit computational demands to an affordable level, the model assumes a constant raceway shape that is taken from literature.

3.9.1 Raceway size

The size of the raceway is calculated depending on actual tuyère blast furnace operating conditions. In literature, a number of correlations to estimate the raceway size is available [31, 125], most of which are reported to fail in predicting raceway cavity sizes at actual blast furnace conditions [19].

In this work, a one-dimensional model proposed by Gupta and Rudolph [19] was used to describe the effect of tuyère and hearth diameter, blast momentum, coke size and density, bed height and void fraction of the undisturbed bed, also introducing raceway hysteresis phenomena. The model was developed based on a force balance equation for the raceway zone accounting for particle friction in the cokebed. Friction effects are of importance: Actual raceway size in operating blast furnaces is shown to belong to the decreasing velocity part of the hysteresis curve [19], the sign of friction forces in the force balance has to be set accordingly. The model was validated using literature data from full blast furnace operation. Parameters that were used as input to the model calculations are summarized in table 3.2.

Table 3.2: Properties of blast furnace coke particles, applied for the computation of raceway size.

property	value		ref.
particle density	1100	$\mathrm{kg/m^3}$	**voest**alpine
particle size	25	mm	**voest**alpine
particle shape factor	0.7	–	[19]
angle of particle-particle friction	43.3	°	[19]
coke bed porosity	0.5	–	[19]
upward facing fraction of raceway envelope	0.8	–	[19]
coke bed height (max. fill level)	26	m	**voest**alpine, BF A
hearth diameter	12	m	**voest**alpine, BF A

The impact of hot blast momentum on the raceway size of blast furnace A, operated by **voest**alpine Stahl GmbH in Linz, as calculated applying this model is shown in figure 3.8. The chart compares the response of the cavity size for varying inner tuyère diameter at a constant hot blast rate to the case of constant blast velocity (i.e. blast injection rates

increase with tuyère diameter). In the case of a constant blast rate, blast momentum increases with decreasing tuyère diameter, therefore the penetration depth of hot blast is enhanced and cavity volume is estimated to increase by a factor of approx. 2.8 as the tuyère diameter is decreased from 160 to 130 mm.

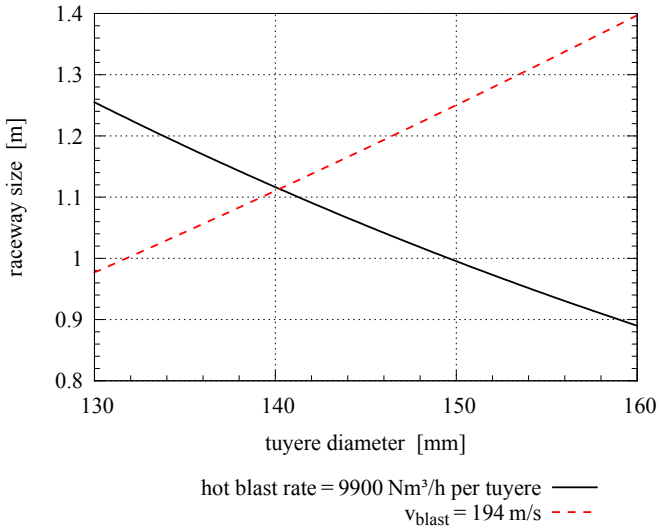

Figure 3.8: Influence of tuyère diameter on the raceway size. Blast conditions: 1220 °C, 5.1 bar, 24.9 %$_v$ O_2, 2.5 %$_v$ H_2O, balance N_2.

3.9.2 Raceway shape

Generally, the shape of the raceway cavity is defined by the porosity distribution in the vicinity of the tuyère opening. The porosity profile from literature [113] as implemented in the current model assembly is shown in figure 3.9.

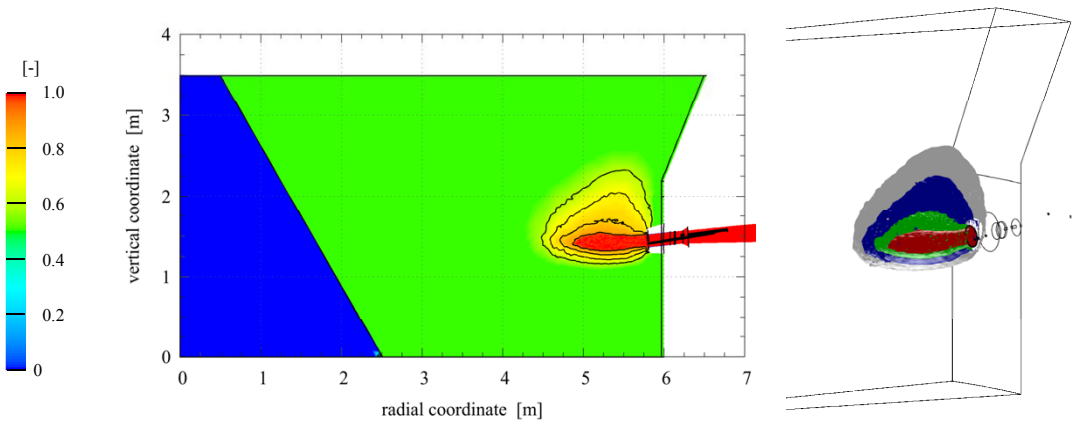

Figure 3.9: Shape of raceway cavity implemented in the CFD-model.

Due to the fact that the model applied to compute the raceway size is one-dimensional, the result is an average raceway diameter for a spherical raceway. This parameter is used to scale the raceway shape published by Zhou [113]. Measurements of the coke bed voidage at stopped blast furnaces and hot model experiments showed that the local porosity varied near the boundary of the raceway cavity and approached 0.5 further

away [19]. Therefore, the porosity in far-field of raceway was implemented applying a void fraction of $\varepsilon = 0.5$.

3.10 Injection of alternative reducing agents

Industrial processes often include solid particles, liquid sprays or even gas bubbles, dispersed in a fluid to increase the specific surface of the injected substance [70]. Furthermore, in many cases these dispersed phases interact with the surrounding continuous fluid, e.g. heterogeneous heat transfer processes, species release due to pyrolysis or drying processes and heterogeneous chemical reactions.

Two basic approaches are available to model such multiphase flow problems:

Euler-Euler approach In the concept of Eulerian modeling of multiphase flow domains, each phase is treated as a continuous fluid. The momentum equation is solved for each of the phases in an Eulerian frame of reference, including phase interactions estimated using drag laws. This model is not applicable to steady-state CFD simulations.

Lagrangian approach If the volume concentration of the secondary phase is low (typically below $12\,\%_{\mathrm{v/v}}$), dispersed particles (solid particles, droplets or bubbles) can be modeled applying a tracking scheme in the Lagrangian frame of reference, i.e. the balance boundaries move along with the particle. In this approach the movement of particles in the computational domain is calculated by integrating balance equations (momentum, heat and species balance) for parcels that are representative for a high number of particles, so much less particles are tracked numerically than are actually present in the spray or particle flow and computational demands can be limited to affordable levels [58]. On their way, particles pass the discrete volume elements where the fluid phase is solved in an Eulerian frame of reference. Exchange terms between dispersed and continuous phase are modeled by implementing mathematical expressions. Particle tracks are calculated at specific intervals of continuous-phase iterations to update the source terms.

In the current model setup, the Lagrangian modeling approach was identified as the proper method due to the high flexibility of the solver code to introduce user-defined subroutines concerning e.g. heat and mass transfer and interaction with solid coke bed while at the same time the computational demand is low as compared to full Euler-Euler simulations.

Trajectories of injected particles are calculated based on the particle momentum balance:

$$\frac{\mathrm{d}\mathbf{v}_p}{\mathrm{d}t} = F_D\left(\mathbf{v}_f - \mathbf{v}_p\right) + \frac{\mathbf{g}\left(\rho_p - \rho_f\right)}{\rho_p} + \mathbf{F}_p \qquad |3.28|$$

The drag force per particle mass is calculated based on the drag coefficient C_D that accounts for the particle Reynolds number Re_p:

$$F_D = \frac{18\mu}{\rho_p d_p^2}\frac{c_D Re_p}{24} \qquad Re_p = \frac{\rho_f d_p \left|\mathbf{v}_f - \mathbf{v}_p\right|}{\mu} \qquad |3.29|$$

The drag coefficient is calculated for the entire range of Re_p applying the correlation given by Haider and Levenspiel [126]:

$$c_D = \frac{24}{Re_{sph}} \left(1 + b_1 Re_{sph}^{b_2}\right) + \frac{b_3 Re_{sph}}{b_4 + Re_{sph}} \quad , \tag{3.30}$$

using the parameters:

$$\begin{aligned} b_1 &= e^{2.3288 - 6.4581\varphi + 2.4486\varphi^2} \\ b_2 &= 0.0964 + 0.5565\varphi \\ b_3 &= e^{4.905 - 13.8944\varphi + 18.4222\varphi^2 - 10.2599\varphi^3} \\ b_4 &= e^{1.4681 + 12.2584\varphi - 20.7322\varphi^2 + 15.8855\varphi^3} \end{aligned} \tag{3.31}$$

The shape factor φ accounts for the impact of non-sphericity of injected particles on the particle drag and is used to express experimental data [127] available for the plastic particles injected into the blast furnace raceway (see tab. 3.4).

The heat balance for the tracked discrete particle is calculated as [74]:

$$m_p c_p \frac{dT}{dt} = \alpha A_p \left(T_f - T_p\right) + \frac{dm_p}{dt} h_{fg} + a A_p \sigma \left(T_R^4 - T_p^4\right) \quad . \tag{3.32}$$

3.10.1 Liquid hydrocarbons

The application of a Lagrangian approach to track injected oil droplets allows for a drastic reduction of computational efforts as compared to full resolution of the liquid atomization process using e.g. volume of fluid (VOF) approaches. However, as a consequence, the initial droplet size distribution of injected heavy fuel oil has to be defined as a model parameter.

Due to experimental difficulties the size distribution resulting from atomization cannot be measured directly at the operating blast furnace. Therefore, atomization efficiency was studied experimentally in a lab-scale cold model, featuring a tuyère in the length scale of 1 : 2 [128, 129]. Air was injected into the model raceway cavity with velocities in the range of 50 to 100 m/s at ambient conditions. The injected model fluids were chosen such, that the experimental conditions reproduced the governing set of dimensionless numbers describing atomization processes estimated for blast furnace conditions (considering Ohnesorge, Weber and Reynolds number). Optical accessibility of the zone in front of the injection lances was provided by realization of the cold model as a transparent PMMA box. Experimental measurement techniques included Laser Doppler Anemometry (LDA), Particle Image Velocimetry (PIV) and high speed imaging to estimate droplet velocities, size distributions as well as the angle of the spray cone at various operating conditions. An image of the experimental setup is shown in figure 3.10. The right diagram shows an example of measured droplet velocities in the lab scale blast jet.

In addition to these experimental observations, detailed modeling studies have been performed to study the high-velocity breakup of liquid jets using the VOF approach in comparison with experimental results [130].

The liquid fuel injected into blast furnace A consists of a mixture of hydrocarbons containing 10 $\%_{w/w}$ water (see tab. 3.3), being preheated to 280 °C prior to injection. To account for the presence of the two species in the liquid mixture, a multicomponent droplet evaporation model was applied that computes release rates of the components based on the estimation of their temperature dependent vapor pressures [131]. Oxidation and thermal degradation of released oil vapor are assumed to take place in the gas phase

Table 3.3: Physical and chemical properties of injected liquid fuel.

parameter	value
ultimate analysis	88 $\%_{w/w}$ C, 12 $\%_{w/w}$ H
water content	10 $\%_{w/w}$

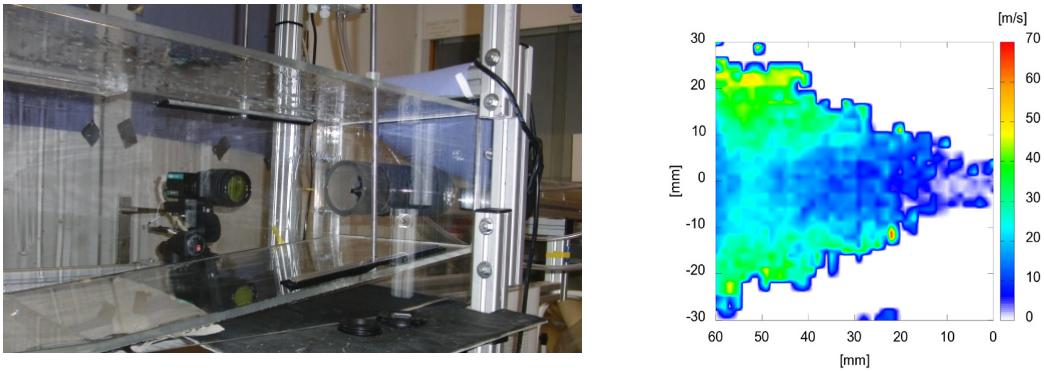

Figure 3.10: Experimental investigation of fuel oil atomization. Left: experimental setup, Right: exemplary result from PIV measurement (droplet velocity magnitude in the blast jet) [129].

only, corresponding reactions are included in the reaction mechanism (R 18 - R 26).

The width of the droplet size distribution was described applying the Rosin-Rammler function. This distribution was originally developed for the characterization of size distributions of coal dust, but is also widely applied for droplet sprays [132]. The two empirical parameters in this correlation are the mean droplet size $\bar{d}$ and the spread parameter n. The mean size of the oil spray was estimated using the correlation proposed by Paloposki and Hakala [133] who experimentally studied the injection of residual fuel oil into a cold model raceway:

$$\bar{d} = 147 \cdot \dot{m}_{oil}^{0.186} \quad , \tag{3.33}$$

giving a mean droplet size of approx. 100 µm as an average for the blast furnace injection conditions studied in this work (see chapter 5).

The spread parameter was set following Slaby [12], giving the distribution function:

$$Y = 1 - e^{-\left(\frac{d}{\bar{d}}\right)^n} = 1 - e^{-\left(\frac{d}{100}\right)^{4.5}} \tag{3.34}$$

The resulting Rosin Rammler distribution is shown in figure 3.11. In the CFD-model, the continuous size distribution is approximated using 6 size bins, as detailed in the histogram, according to experimental observation the angle of the spray cone was set to 20°.

3.10.2 Natural gas

The conversion behavior of natural gas was studied as representative for gaseous reducing agents. In the model, the fluid representing natural gas was considerably simplified in terms of composition, being implemented as pure methane. This molecule is already included in the list of component species and incorporated in the set of homogeneous and heterogeneous reactions.

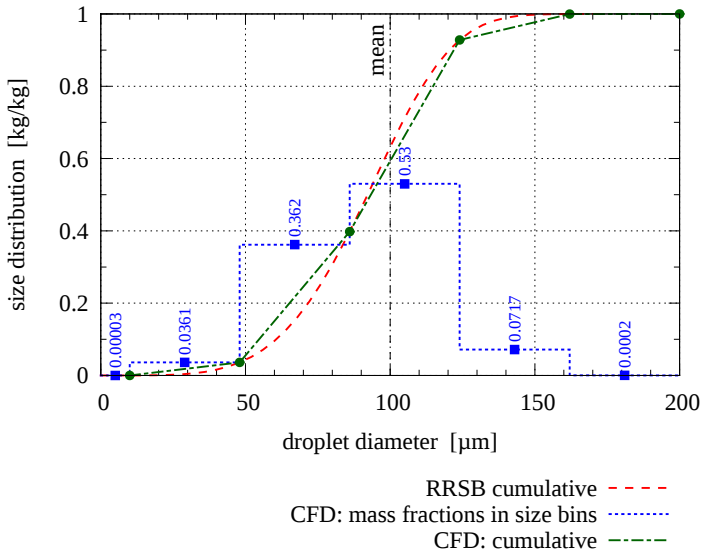

Figure 3.11: Fuel oil droplet size distribution: Rosin-Rammler distribution and distribution as implemented in the CFD-model.

3.10.3 Plastic particles

Experimental investigation of plastic particle thermolysis at raceway conditions showed that non-isothermal behavior of the particles is to be expected. This is due to the fact that heat transfer rates are very high (high relative velocities and intense radiative heat transfer) and thermal conductivity of the highly porous material is rather low (see thermophysical data given in table 3.4).

Table 3.4: Physical and chemical properties of injected plastic particles.

parameter	value
mean equivalent diameter [range]	$7.5\,[6-8\,]$mm
sphericity	0.5
aspect ratio	$0.55-0.75$
mean particle density	$< 1100\,\mathrm{kg/m^3}$
particle porosity	$0.35-0.70$
ultimate analysis	$71\,\%_{\mathrm{w/w}}$ C, $10\,\%_{\mathrm{w/w}}$ H, $12\,\%_{\mathrm{w/w}}$ O, $7\,\%_{\mathrm{w/w}}$ ash, traces of Cl and F
thermal conductivity	$0.1\,\mathrm{W/m{\cdot}K}$
mean specific heat capacity	$600\,\mathrm{J/kg{\cdot}K}$
optical emmisivity	0.9

In the experiments [134], plastic particles were heated by laser pulses to achieve heat transfer rates high enough. Each pulse resulted in the release of pyrolysis products from the surface of the particles that rapidly ignited. The core temperature of the particles, measured by a thermocouple positioned in the center, remained constant. This is also confirmed by estimation of the dimensionless Biot-number Bi, calculated as [135]:

$$Bi = \frac{\alpha \cdot d_p}{\lambda_p \cdot 2} \qquad |3.35|$$

Table 3.5: Model for Plastic pyrolysis.

step no.	reaction step	description
1	$C \longrightarrow CH_4$	release of methane, if hydrogen is present
2	$C \longrightarrow CO$	if oxygen is present
3	$H \longrightarrow H_2O$	if oxygen still present
4	$C \longrightarrow C_s$	soot formation, consumption of residual carbon
5	$H \longrightarrow H_2$	if hydrogen still available
6	$O \longrightarrow O_2$	if oxygen still available

The Biot-number compares the convective heat transfer towards the particle surface to thermal conductivity in internal particle structures. At high Biot-numbers, spatial temperature gradients near the particle surface are very high, so over time the core temperature remains nearly constant. This thermal behavior of particles is called *thermally thick* [136]. In the case of plastic injection into blast furnace raceways, it was found that $Bi > 15$ in the zone where the particle shell reached gasification temperature. Accordingly, the implementation in the CFD code assumes that the temperature in the center of the particle remains at initial values, while heat transferred to the particle surface is utilized to heating of the particle shell. As gasification temperatures are reached (in the range of 300 °C, according to thermogravimetric analysis [127]), incoming heat is consumed by plastic pyrolysis, resulting in the release of thermolysis products. No direct combustion reaction on the surface is considered, as oxygen from the continuous phase is assumed to be swept away from the particle as thermolysis proceeds [137]. Convective and conductive heat transfer towards the particle surface is modeled applying common dimensionless Nusselt correlations valid for single particles (equ. 3.2).

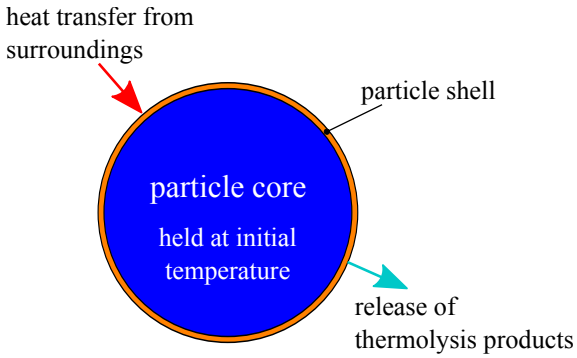

Figure 3.12: Schematic illustration of plastic particle gasification model.

Plastic pyrolysis is modeled following an approach that was developed for biomass gasification in combustion systems [138], as implemented for plastic pyrolysis at raceway conditions by Jordan et al. [127] (see table 3.5). Plastic material is assumed to consist of C, H and O only. Ash content as well as heavy metal, Cl, F, P, S and other pollutants are neglected. The pyrolysis products are released as gas compounds (H_2, CO, CH_4, H_2O, O_2 and soot). Combustion of the pyrolysis products and therefore the release of heat of reactions takes place in the gas phase. The reactivity of char from plastics pyrolysis in the solution-loss-reaction was reported to be higher than that of char derived from coal [47]. Therefore it is assumed that char from plastics, deposited in the coke bed, is readily consumed in the blast furnace.

In the model, plastic particles that are not fully consumed before the edge of raceway is reached also interact with the coke bed. In accordance with experimental findings applying high-speed imaging of the raceway zone [139], plastic particles that have passed the raceway cavity and hit the coke lumps surrounding the raceway are modeled to be reflected considering the local porosity value.

Figure 3.13 shows the size distribution of the injected plastic particle mixture. The material for the sieve analysis was sampled from the injection point at BF A (fig. 3.14), because sizes change during transport from storage hopper to the tip of the injection lance due to particle breakup and/or coagulation.

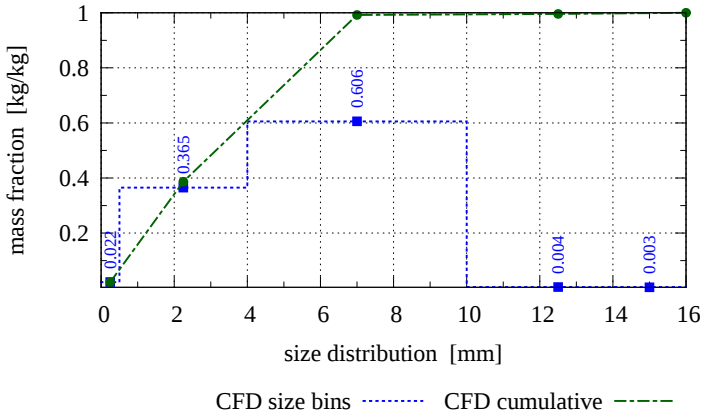

Figure 3.13: Plastic particle size distribution from sieving analysis, implemented in the CFD-model.

Figure 3.14: Processed waste plastics for injection into the blast furnace.

3.10.4 Pulverized coal

Similar to plastics and liquid hydrocarbons, pulverized coal utilization is modeled applying the discrete particle model and Lagrangian tracking schemes. Base models for coal combustion are available in the standard solver routines. The overall process of coal combustion includes the evaporation of moisture that is contained in the coal, devolatilization and finally the utilization of residual char by heterogeneous reactions [140]. The ash contained in virgin coal is not modeled, therefore after completion of heterogeneous reactions the particle stream is deleted from the computational domain. The size of coal particles is approximated applying the size distribution by Rosin-Rammler.

In this work coal conversion is modeled in a sequence of processes:

Coal particle heating The first sequence in modeling the combustion of pulverized coal represents a preheating step, i.e. particle temperature increases by heat that is transferred from the surroundings. Convective and radiative heat transfer rates to the particle are integrated, solving for the rate of particle temperature change (equ. 3.32). In this phase particles are considered inert in terms of mass transfer until a certain particle temperature level is reached.
The Nusselt number correlation given by Ranz and Marshall [141, 142] is applied to compute the heat transfer coefficient between continuous and discontinuous phase:

$$Nu = \frac{\alpha\, d_p}{\lambda_f} = 2.0 + 0.6 \cdot Re_p^{1/2} \cdot Pr^{1/3} \qquad |3.36|$$

This correlation is valid in the range of particle Reynolds numbers $0 < Re_p < 200$ and continuous phase Prandtl number $0 < Pr < 250$ and is therefore applicable to conditions in the tuyères and raceways of blast furnaces. In the model, the internal temperature profile of the coal particles is not computed explicitly, but rather a constant temperature throughout the particles is assumed. The validity of this approach can be proven by evaluation of the Biot Number (equ. 3.35).
In general, thermophysical properties of coals change during thermal utilization. However, in combustion processes, the thermal conductivity can be considered constant, as due to the high heating rates in the range of $10^4 - 10^5\,\mathrm{K/s}$ coal bonds are presumed to be frozen [143], therefore thermal conductivity and specific heat capacity remains at conditions that represent values at room temperature.

Drying / Devolatilization As the particle temperature exceeds the fictive vaporization temperature T_{vap}, onset of moisture release and discharge of volatile compounds to the gas phase is modeled. The release rate of particle mass is estimated by evaluating the rate of heat transfer to the particle, accounting for heat sink due to latent heat of evaporation.
Considering drying, the driving force for the mass transfer of water from the coal particle to the gas phase is evaluated based on the computation of the difference of the H_2O partial pressure on the particle surface to the partial pressure in the surrounding fluid phase [74]. In analogy to heat transfer, the mass transfer coefficient k_c is retrieved from the Sherwood number, evaluating the diffusion coefficient $D_{i,m}$ of the considered component in the gas mixture:

$$Sh = \frac{k_c\, d_p}{D_{i,m}} = 2.0 + 0.6 \cdot Re_p^{1/2} \cdot Sc^{1/3} \qquad |3.37|$$

Devolatilization is modeled applying a two competing rates model to compute the release of volatile coal compounds to the surrounding fluid phase (fig. 3.15). Two kinetic expressions and volatile yields are implemented, describing thermal disintegration at different temperature ranges.

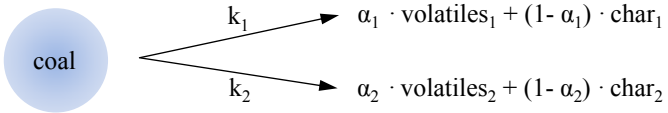

Figure 3.15: General layout of devolatilization scheme of injected coal.

In the model it is assumed that volatile species released at different heating rates are identical, the same approach is applied to describe the remaining char fractions (i.e.: $\text{volatiles}_1 \equiv \text{volatiles}_2$ and $\text{char}_1 \equiv \text{char}_2$). By this simplification only a minor impact on the computed coal burnout ratios is to be expected [144]. Temperature dependence of devolatilization rates are implemented as Arrhenius-type reaction kinetics (equ. 2.23) [144, 145]:

$$A_1 = 3.7 \cdot 10^5 \,{}^1/_\text{s} \quad E_1 = 18000\,\text{K}$$
$$A_2 = 1.46 \cdot 10^{13} \,{}^1/_\text{s} \quad E_2 = 30189\,\text{K}$$

Yield factors α_1 and α_2 depend on the conditions at thermal coal utilization, such as the type of coal, heating rates, temperature levels etc. At high heating rates, as also obtained at injection into the blast furnace, the mass fraction of coal that is released with volatiles increases. Volatile yields are specified based on the volatile content that is available from proximate coal analysis. The actual yield is estimated incorporating the enhancement due to high heat transfer rates at high temperatures as proposed by Shen et al. [146]:

α_1 set as volatile yield from proximate analysis
α_2 calculated from α_1 according to $\alpha_2 = 1.25\,\alpha_1^2 + 0.92\,\alpha_1$

During devolatilization, swelling of particles may occur as volatiles also form inside the solid particle, causing inflation. This can be described by introduction of a swelling coefficient that relates the particle diameter to the fraction of volatiles released. The swelling index strongly correlates to the heating rate. However, according to the results of Gale et al. [147] regarding coal utilization at heating rates in the range of $10^5\,{}^\text{K}/_\text{s}$ this index is set to unity.
Combustion of volatiles is modeled to take place in the gas phase by including an oxidation reaction yielding CO_2 (reaction R 27) and partial combustion to form CO and H_2 (reaction R 28). A further reaction describing the thermal destruction of volatiles in the absence of oxygen was introduced to the set of reactions (reaction R 29).
The particle emissivity is expected to change during the release of volatiles [146]. This variation of the particle absorption coefficient a has a large impact on the particle heat balance (equ. 3.32). A user-defined subroutine was implemented that introduces a variable absorption coefficient, following the suggestions given by Shen et al. [146]: Particle emissivity changes linearly with respect to the fraction of volatiles released, where the emission factor of the virgin coal particle is set to unity ($a_{coal} = 1$) and the emissivity of the char remaining after volatiles release decreases to a value of $a_{char} = 0.6$ (char absorption coefficient as in [148]).

Combustion / Gasification The last step in utilization of pulverized coal involves the consumption of residual char that remains in the particulate phase after volatile components were released. This sequence represents an important episode in the live-span of injected coal particles, since devolatilization takes place in a relatively short time period and consequently the burnout rate in the raceway cavity is strongly determined by the conversion behavior of chars due to heterogeneous reactions.
The onset of heterogeneous reactions is modeled to take place after the release of volatiles is finished, owing to the flow of volatiles that tend to sweep the surrounding gas away from the particle surface and oxygen therein cannot reach the particle surface. Furthermore, the combustion of volatiles requires high stoichiometric oxygen

demands, therefore the ambient fluid in close proximity to the particles tends to be oxygen depleted. Additionally, char oxidation is slower than combustion of volatiles because coal particles are small and O_2 molecules have to be transported towards the particle surface. Still, char oxidation is reported to contribute the major part of heat of reaction from coal injection [11]. The particle diameter is modeled to remain constant. Consequently the particle density decreases during utilization and the particle porosity increases accordingly.
A set of heterogeneous reactions was implemented as wall particle reactions, considering reactant bulk diffusion through the particle boundary layer. In these reactions, composition of remaining char was simplified and modeled as pure carbon. Intrinsic Arrhenius-type reaction kinetics for oxidation of residual char from coal combustion as proposed by Gibb [149] were implemented:

$$\beta\,C + O_2 \longrightarrow 2\,(\beta{-}1\,)\,CO + (2{-}\beta)\,CO_2 \quad A = 497\,\mathrm{kg/m^2s} \quad E_a = 7.101 \cdot 10^7\,\mathrm{J/kmol} \qquad |R\,34|$$

In this mechanism, char oxidation is evaluated introducing a variable to estimate the share of reaction towards CO and CO_2 based on the char particle temperature:

$$\frac{2(\beta-1)}{2-\beta} = A_S \cdot e^{-\frac{T_S}{T_p}} \qquad A_S = 2500 \qquad T_S = 6240\,\mathrm{K}$$

Two additional gas-char reactions were implemented, namely steam and CO_2 gasification. These reactions are of high importance in the blast furnace and therefore are considered in the model. Gasification of residual char is the slowest of the steps, therefore it continues outside the raceway cavity if gasification agents are still available and temperatures are sufficiently high. Reaction kinetic data were adopted from [146]:

$$C + CO_2 \longrightarrow 2\,CO \quad A = 20230\,\mathrm{m/s{\cdot}K} \quad E_a = 3.304 \cdot 10^8\,\mathrm{J/kmol} \qquad |R\,35|$$

$$C + H_2O \longrightarrow CO + H_2 \quad A = 606.9\,\mathrm{m/s{\cdot}K} \quad E_a = 2.697 \cdot 10^8\,\mathrm{J/kmol} \qquad |R\,36|$$

An effectiveness factor η that reflects the utilization characteristics of the coal type is used for each reaction. The kinetic reaction rate is multiplied by this dimensionless correction factor. The effectiveness factor therefore represents a model parameter that is to be set in order to adapt the model to the examined coal type and to account for coal characteristics that are not introduced explicitly. Values applied in this model to successfully compute particle burnout ratios (see validation results in chapter 4.4) are summarized in table 3.6.

Table 3.6: Effectiveness factors applied in heterogeneous char reactions model.

char reaction		η
oxidation	R 34	0.6
CO_2 gasification	R 35	0.7
H_2O gasification	R 36	0.6

3.11 Time discretization

Spatial discretization of conservation equations is common in CFD simulations, where the finite volume approach is applied to compute the fluid motion in a computational domain. If the data fields also vary in time, additionally to spatial discretization also time-discretization is necessary to properly describe the flow phenomena.

In this work the movement of the coke bed is modeled by approximating the particulate flow as a continuous fluid with a porous structure introducing the raceway cavity (see chapter 3.8). Consequently, the Navier-Stokes equations are solved to estimate the particulate flow rather than computing the movement of each and every single coke particle and its interactions with neighboring particles as applied in discrete element modeling. DEM has to be solved applying time discretization, while it is possible to neglect the time derivative when solving for fluid flow by Navier-Stokes equations. Furthermore, liquids such as hot metal and slag phases are not considered. The volume of fluid approach that is applicable to introduce liquid phases would require time-resolved conservation equations.

In the current model no time discretization is applied, i.e. the flow properties are expected to remain constant with respect to time. Due to the residence time and flow conditions in the blast furnace raceway cavity this approach is considered valid [150]. This is also possible as the raceway shape is defined as a boundary condition that does not change with progress of the iterative solution, no raceway hysteresis is considered. The steady-state solution of coke and gas flow results in a drastic reduction of computational demand as compared to time resolved computation, allowing for the implementation of detailed chemical reaction schemes to model the feed conversion.

Contrary to gas and coke phase, injected alternative reducing agents are introduced applying discrete particle models. In this approach the change of droplet and particle properties during time of flight is integrated along particle trajectories applying time discretization of the particle heat, mass and momentum balance (e.g. equations 3.32 and 3.28). Heat, momentum and mass sources are computed for the continuous phase to introduce heterogeneous interaction. The source terms are updated periodically in the solution procedure by computing particle tracks.

3.12 Parallel considerations

In the blast furnace process, a vast number of physical processes take place that need to be accounted for in a numerical model. The mathematical model needs to include quantities and their transport equations describing the flow field (velocities, density, turbulence quantities), temperature, radiation as well as chemical species. This results in a large set of discretized differential equations to be solved iteratively by the solver routines and therefore a considerably high need of computational resources, increasing the calculation time.

The solution process can be sped up by splitting the calculation to several CPUs. This is done by dividing the computational domain and simultaneous computation of partial flow problems on each of the processors. By splitting the flow domain, the number of grid elements to be solved per CPU decreases and therefore results are available earlier [151]. The computing nodes performing the calculations need to exchange data via the processor interfaces to ensure consistent results throughout the whole computational domain. As the speed of data transfer is limited by available hardware resources, the time to solve the problem does not decrease linearly with increasing number of CPUs,

but rather a decay in performance increase is found.

The current implementation of the DualGrid-method (as explained in chapter 3.1) solves for solid and gas phase in the blast furnace in separate grid zones, communication between these zones is done by implementing a region mapping algorithm via storing the cell addresses of corresponding fluid and solid domain cells in a user-defined data field. In the user-defined solver subroutines for heterogeneous transfer processes the stored values are used for indirect addressing using pointer structures.

Calculations were performed on Intel® Core™ i7-3770 processors with a clock rate of 3.40 GHz, 8 MB cache and 32 GB DDR3 at 1600 MHz main memory, equipped with a 36 GB solid state disk. Typically, a converged run was achieved after approx. two weeks real time if fourfold parallelization was applied.

3.13 Solution Procedure

An iterative solution procedure is applied to numerically solve for the unknowns such as flow, species concentration and temperature fields. An overview of a typical calculation sequence of the governing equations for steady-state simulations is shown in figure 3.16.

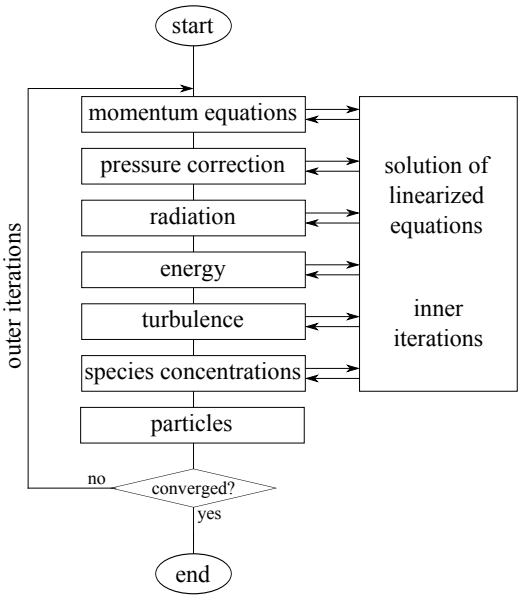

Figure 3.16: Diagram of typical solution procedure.

A typical work flow of starting a new simulation run addressing the conversion of alternative reducing agents in the raceway applying the developed model from scratch is based on stepwise introduction of model functionality and balance equations. This allows to minimize the computational efforts to achieve a converged solution and also to avoid stability problems arising from conditions that might be computed as intermediary results during the iterative solution procedure. For example, large temperature fluctuations typically appear when starting the solution of a temperature-dependent flow problem by means of CFD. The calculation of e.g. chemical reactions in such an early stage of the solution process would be very demanding and also unreasonable because conversion rates at such unrealistic conditions would not reflect the actual situation in a blast furnace.

So, after initialization of data fields with reasonable numbers that are close to expected values, first the flow of hot blast and coke is computed, applying first order discretization

of the momentum equation without considering the impact of spatially variable temperature profiles. After a converged solution was obtained for this *cold* flow, species balances are introduced to compute the composition. In this step also the energy equation is activated as the local temperature is needed to to compute fluid properties such as the gas density that is computed from the ideal gas equation, evaluating the mean molecular weight of the gas mixture. Then the far-field energy transfer by radiation is introduced by activating the radiation model. At this stage all components are still rendered inert, no chemical reaction rates are computed.

In the next step, the modules for homogeneous and heterogeneous reactions are activated. In order to dampen the impact of reaction rates on local species concentration and temperature values and therefore to maintain simulation stability, up to this point hot blast is modeled as pure nitrogen. Changing the boundary condition for hot blast injection from N_2 to the actually considered hot blast composition including O_2 and H_2O results in a continuous increase of oxygen partial pressure in the iteration progress. A smooth onset of oxidation reactions and therefore heat release provides for fast convergence and stable iteration loops.

The activation of the module for injection of alternative reducing agents adds further source terms in the discrete volume elements, reflecting the release of e.g. moisture, volatiles and consumption or release of gas-phase species due to heterogeneous reactions.

To obtain the final converged simulation results, the discretization scheme applied to compute the facet-values of quantities from cell-centered values is to be changed from first to second order to increase the simulation accuracy.

For simulation runs that aim at new operating conditions an already available converged solution can be used as a starting point. New settings, e.g. in terms of hot blast composition are to be defined via the boundary conditions and iteration can be continued.

In this work the history of simulation convergence is monitored by definition of a number of parameters that reflect important process characteristics, for example the average temperature or gas velocity in the raceway cavity. These are computed in every iteration loop. Exemplary plots of various integral type monitor parameters are shown in figure 3.17. In this run the rate of pulverized alternative reducing agent injection were increased, resulting in a reduction of temperatures and changes in gas composition in the raceway.

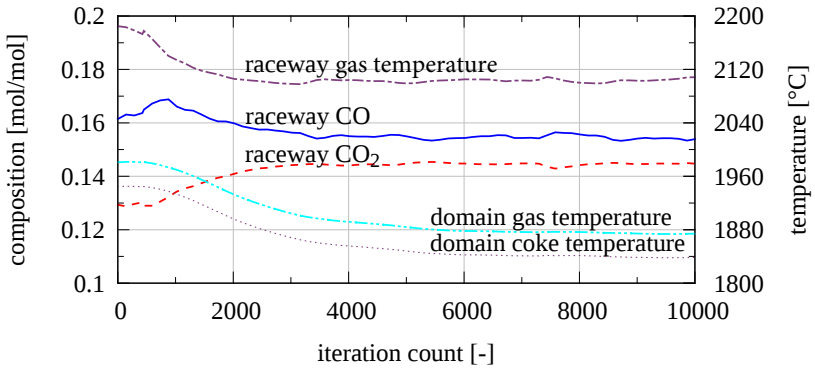

Figure 3.17: Exemplary plot of parameters vs. iteration number to monitor simulation convergence.

4 Model Validation

The implementation of the dual grid model has been validated for a number of heat transfer problems in porous media of different types in a wide range of operating conditions as well as for heterogeneous and homogeneous chemical reactions, see table 4.1. The validation procedure was structured such, that various experimental setups from literature were implemented in distinct CFD models with increasing complexity of the physical processes, starting at simple heat transfer problems between gas and solid phases. The simulation results were compared to available measured data to analyze the model performance.

Table 4.1: Overview of validation cases applied for the Dual-Grid model.

validation case	temp. range	solid matter	solids structure	reactivity	ref. exp.
closed system with respect to mass transfer, gas flow: natural convection	$< 1250\,^{\circ}\mathrm{C}$	graphite pebbles	bed of spheres	inert	[152]
open system gas flow: forced flow through fixed bed	$20 - 100\,^{\circ}\mathrm{C}$	ceramic pebbles	bed of spheres	inert	[82]
porous burner: open system	$< 1500\,^{\circ}\mathrm{C}$	SiC, Al	foam matrix, bed of Al spheres	homogeneous	[153]
continuous coke gasification	$< 1100\,^{\circ}\mathrm{C}$	charcoal	coke bed	homogeneous heterogeneous	[154]
gasification of metallurgical coke (NSC test)	$1000 - 1100\,^{\circ}\mathrm{C}$	metall-urgical coke	coke bed	homogeneous heterogeneous	[155]
pulverized coal combustion and gasification	$> 1100\,^{\circ}\mathrm{C}$	coal	particles	homogeneous heterogeneous	[156, 157]

4.1 Heat transfer

4.1.1 Heat transfer in a closed system at high temperatures

A first benchmark to test the implemented submodel for heterogeneous heat transfer and heat conduction in a fixed bed of particles was applied for an experiment simulating

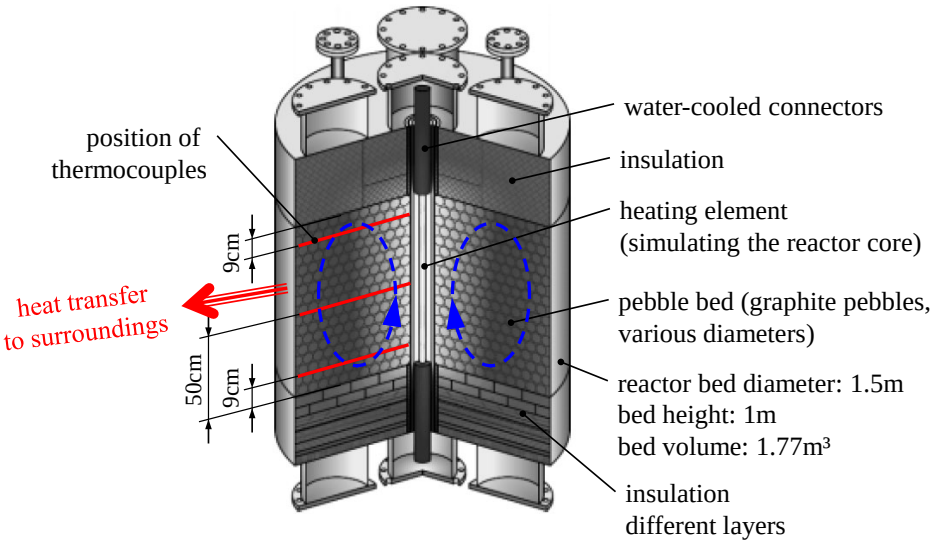

Figure 4.1: Overview of heat conduction experiment (adapted from [152]).

the decay heat removal from modular gas-cooled nuclear reactors at accidental conditions [152]. In these experiments the temperature field in a cylindrical bed of spherical graphite pebbles was measured, while in the center of the bed an electrically powered heating element simulated the reactor core to be cooled. In the experiments, heat was transported from the center of the heating element to the reactor wall via natural gas convection, heat conduction in the pebble bed and radiation. Measurement instrumentation included a number of thermocouples to resolve radial temperature profiles 9 cm above and below the bottom and top of the cylindrical bed, respectively, as well as in the vertical center (see figure 4.1).

The experiments were run at two power rates (10 kW and 30 kW), using two kinds of cooling fluids (He and N_2) and two pebble diameters (30 mm and 60 mm). The temperatures measured were in a range starting close to room temperature and up to 1250 °C.

Model setup

In the CFD model a wedge of the cylindrical reactor and the various insulating materials was implemented, applying rotary symmetry conditions on the cutting planes. The boundary conditions for the simulations were set as summarized in figure 4.2.

The porosity in the pebble bed was initialized to a value of $\varepsilon_\infty = 0.41$. However, in the vicinity of a solid wall the stochastic behavior of a bed of spheres is disturbed, a bed of perfect spheres even exhibits oscillatory behavior [82]. Therefore porosity needs to be expressed as a function of the distance to the wall, x. An empirical correlation that satisfactorily describes the increase of the void fraction in the packing near a wall for ground material, given by Giese [158], was implemented (R... radius of the reactor):

$$\varepsilon(x) = \varepsilon_\infty \cdot \left(1 + 1.36 \cdot e^{-5 \cdot \frac{R-x}{d_p}}\right) \qquad |4.1|$$

The resulting void fraction distribution along the radial coordinate is shown in figure 4.3.

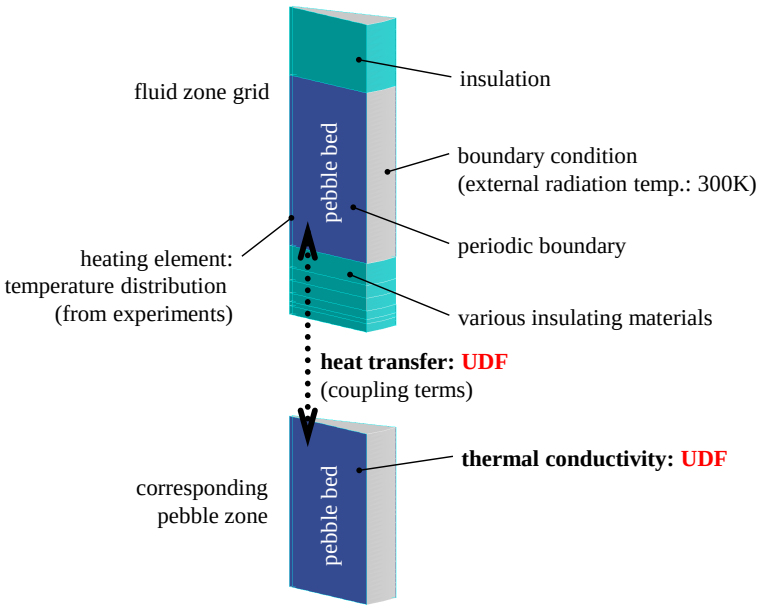

Figure 4.2: Boundary conditions set in the CFD model

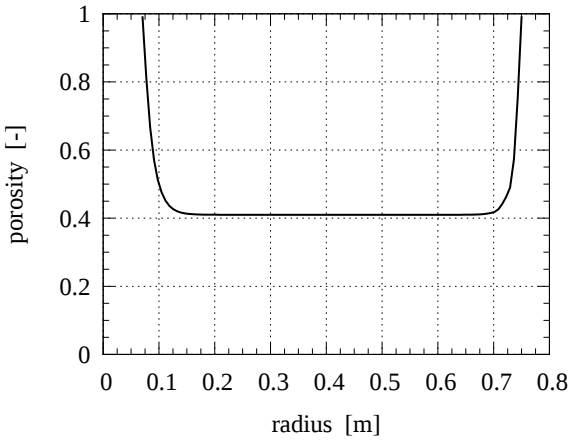

Figure 4.3: Porosity distribution in pebble bed.

Simulation results

CFD simulations were run for the above mentioned operating conditions considering He and N_2 as cooling gas and heating power rates. For validation purposes, the measured temperature profiles were compared to simulation results.

The calculated temperature field in the packed bed for the experimental run with 10 kW heating power and N_2 as operating gas is presented in figure 4.4. The left part of the sketch shows the temperature of the graphite pebbles, the right part the values calculated for gas phase temperature. The heat source located in the center and heat losses to surroundings (cooling purpose) are responsible for the temperature variation in the reactor.

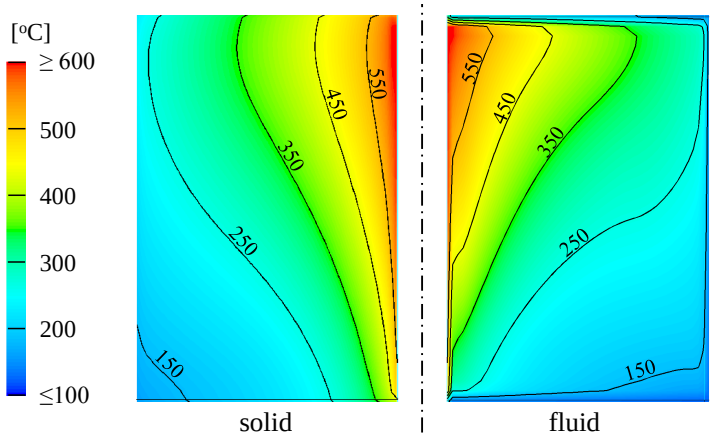

Figure 4.4: Temperature field in the region of the pebble bed. Left: Temperature of graphite pebbles, right: Gas temperature. Heating power: 10 kW, gas: N_2, 60 mm pebbles.

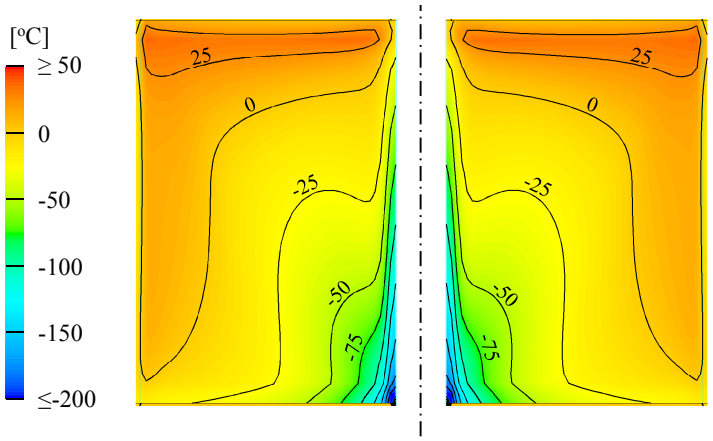

Figure 4.5: Temperature field in the region of the pebble bed: Temperature difference $\Delta T = T_{gas} - T_{solid}$. Heating power: 10 kW, gas: N_2, 60 mm pebbles.

Gas density varies inversely proportional with gas temperature, inducing gas motion in the voids of the packed bed through natural convection, see figure 4.6.

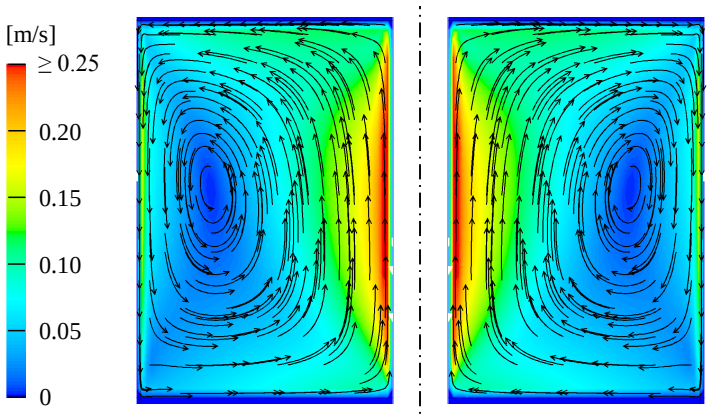

Figure 4.6: Gas flow field in the voids of the pebble bed.

Heat is transported by gas convection to the upper region of the fixed bed where the gas is deflected towards the reactor walls. Here, heat is transferred from the hot gases to the cooler graphite pebbles, increasing the desired cooling rates and widening the zone with higher bed temperatures. The comparison of simulation results to temperature readings at different operating conditions is shown in figures 4.7 and 4.8.

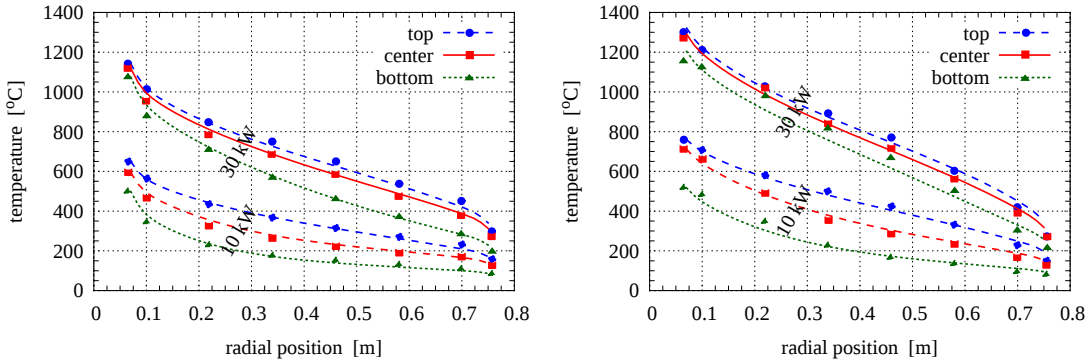

Figure 4.7: N_2 as cooling gas at heating rates 10 kW and 30 kW. Pebble diameter left: 60 mm, right: 30 mm. Symbols: Experimental data, lines: Simulation results.

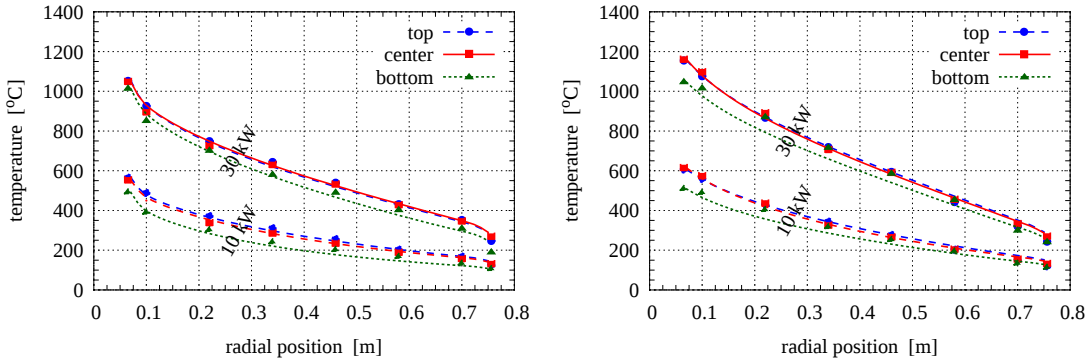

Figure 4.8: He as cooling gas at heating rates 10 kW and 30 kW. Pebble diameter left: 60 mm, right: 30 mm. Symbols: Experimental data, lines: Simulation results.

The variation of the type of cooling gas allows to examine the impact of thermal conductivity of the fluid on the heat transport ($\lambda_{He} \cong 6 \cdot \lambda_{N_2}$). Also, specific heat of He is considerably larger than that of N_2 ($cp_{He} \cong 5 \cdot cp_{N_2}$), but of course the density of helium is much lower than that of nitrogen ($\rho_{N_2} \cong 7 \cdot \rho_{He}$), so on the basis of equal gas velocities convective transport of sensible heat using He is about 70 % as compared to N_2.

In general, excellent agreement between experimental values and simulation results was found, effects of various conditions were reproduced properly. A prerequisite for satisfactory model performance at the current operating conditions is to account for secondary effects in heat conduction processes (solid radiation, radiative heat transfer between pebbles, see chapter 3.2). The simulation results show poor agreement with experimental values if important physical processes are not included in the model, see e.g. results without heterogeneous heat transfer or solid radiation in figure 4.9. The implementation of a complex model that addresses the relevant features is essential to

properly describe heat transfer and transport procresses of fluid flow in a packed bed of particles. This is even more important if extreme conditions, e.g. high temperatures, are present.

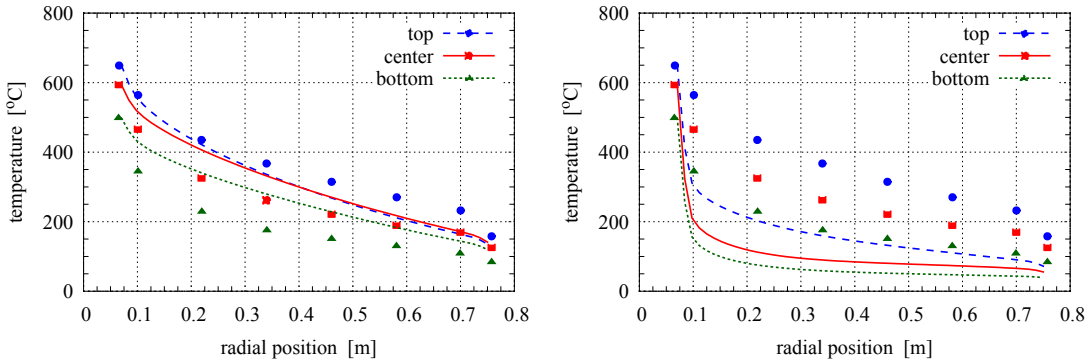

Figure 4.9: N_2 as cooling gas at 10 kW heating rate, pebble diameter 60 mm. Left: No heterogeneous heat transfer, right: No solid radiation. Symbols: Experimental data, lines: Simulation results.

4.1.2 Low temperature heat transport

In the previous chapter the simulation of a closed system with respect to mass flow was presented. In the next step, the model was applied to a system including mass transfer via the system boundaries. A simple experimental setup was considered as validation case: Air at a temperature of 21.5 °C enters a steam-heated tube with a packed bed of mono-disperse ceramic pebbles [159] (see figure 4.10).

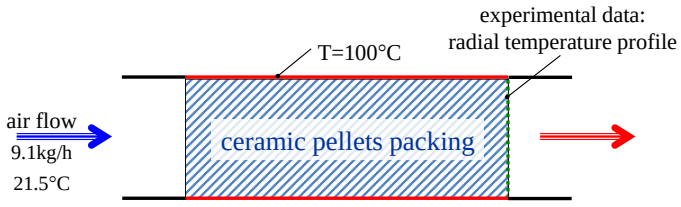

Figure 4.10: Setup and boundary conditions (experimental setup by Dixon [159]).

As the air flow enters the heater section, heat is transferred from the ceramic pebbles to the gas flow, cooling the spheres. Heat transport from the pipe wall towards the center of the pipe mainly takes place via conduction in the solid material.

Comparison of temperature readings at the end of the packed bed to the simulation results (see figure 4.11) showed good agreement between experiment and calculations.

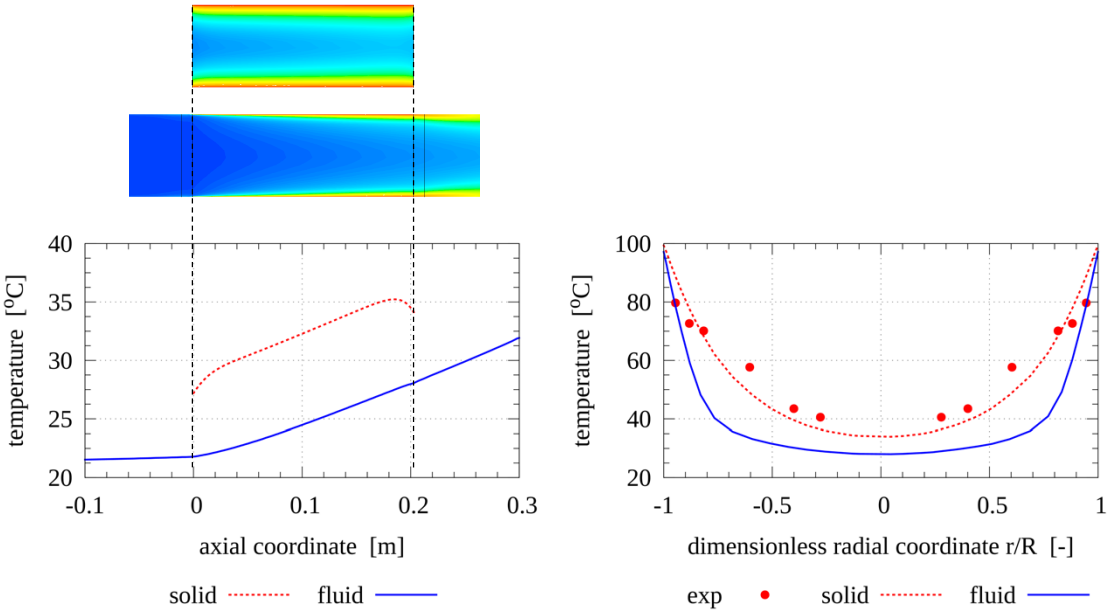

Figure 4.11: Temperature profiles, heat transport in an open system with respect to mass flow. Symbols: Experimental data, lines: Simulation results.

4.2 Gas-phase combustion, inert solid phase

Apart from heat transfer processes, a wide number of heterogeneous and homogeneous reactions take place in a blast furnace. Following the strategy of stepwise implementation of a full blast furnace model including validation of each step, a submodel predicting simplified homogeneous gas-phase combustion was implemented. A proper combustion system including gas flow and heat conduction by inert solid material was found to be represented by a porous burner setup (fig. 4.12).

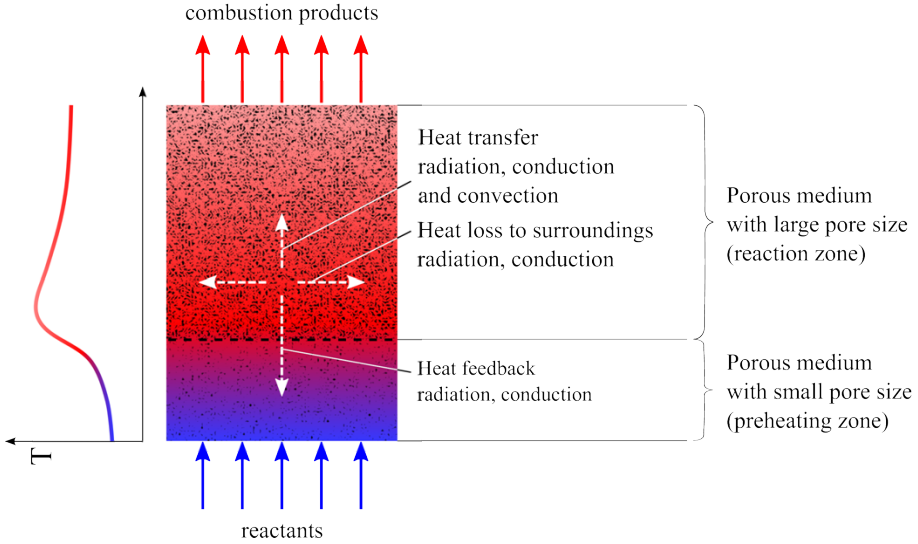

Figure 4.12: Porous burner: Setup and qualitative illustration of heat fluxes and temperature profile along the center line.

In porous medium combustion, a mixture of gaseous fuel and oxidizer first enters a

preheating zone. This zone is composed of an inert porous structure with relatively small pore sizes assuring that any flames are quenched. This happens through intense heat exchange in the turbulent flame zone at small characteristic diameters of hollow spaces in the porous medium. The flame is quenched if the timescale of thermal relaxation is smaller than that of chemical reaction [160]. The characteristics of flame propagation in a porous medium can be described by introduction of the modified Péclet-number [161]:

$$Pe = Re \cdot Pr = \frac{S_L \, d_m \, c_p \, \rho}{\lambda_f} \qquad |4.2|$$

This dimensionless number computes the ratio between advective and diffusive transport, in this case applied for heat transport. Experimental observation of porous burner systems by Trimis and Durst [162] has shown that the limit of flame propagation is at $Pe = 65$, at lower Péclet-numbers flames are quenched. The preheating zone therefore is to be designed such, that with the applied fuel mixture and therefore the resulting laminar flame speed S_L the condition $Pe < 65$ is fulfilled.

At the position where the flame front should be located, a different porous medium with larger pore size ($Pe \geq 65$) is realized. Here, the actual oxidation of combustible gas constituents starts. The highly developed inner surface of the porous medium leads to very efficient heat transfer between gas and solid, so combustion temperature in the porous burner is controlled via the porous medium temperature [161, 163].

In the current work, the burner setup of Durst and Trimis [153, 164] was adopted. In the experiments the burner was fueled with methane (excess air coefficient 1.5) at a rate of 2 kW thermal power. The preheating zone was realized as a fixed bed of alumina spheres (d_p = 5 mm), combustion was located in a silicon carbide foam (10 pores per inch, 86 % void fraction).

Simulation setup

An overview of the implemented computational domain is shown in figure 4.13. The fuel/oxidizer mixture enters the fluid zone at the inlet on the left, is heated in the preheating zone (heat transfer modeling via the dual-grid model) and then enters the combustion zone. Computation of the temperature field and accordingly heat conduction in the porous structures is done in the grid zone holding the solid material.

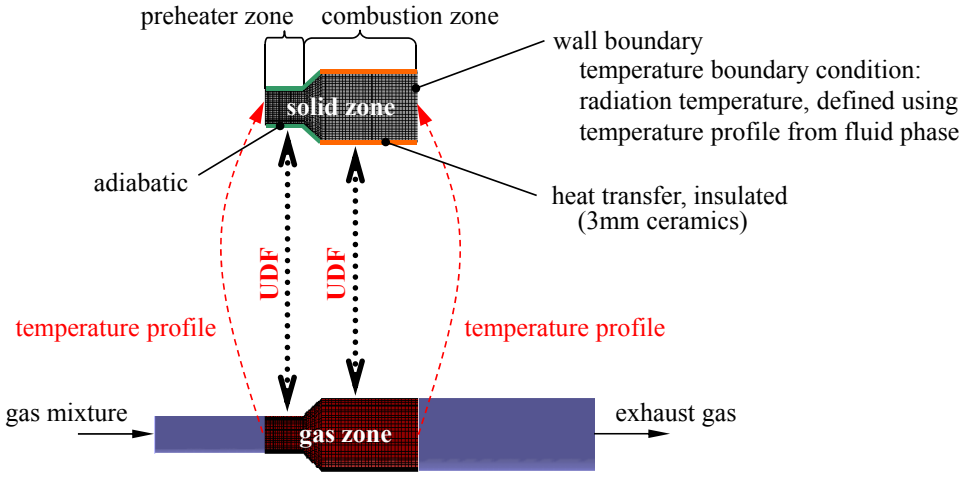

Figure 4.13: Computational domain implemented in the CFD model.

Gas combustion was modeled using a simple two-step methane mechanism considering 7 species (CH_4, O_2, CO, H_2, H_2O, CO_2, N_2):

$$CH_4 + 1.5\,O_2 \longrightarrow CO_2 + 2\,H_2O \qquad |R\,37|$$

$$2\,CO + O_2 \longrightarrow 2\,CO_2 \qquad |R\,38|$$

Reaction kinetics were integrated considering turbulence effects by applying the Eddy Dissipation Concept based on Magnussen and Hjertager [165] along with in-situ adaptive tabulation of reaction rates in the multi-dimensional reaction domain. The convective heat exchange between SiC-foam and gas flow was calculated using $Nu = 0.146 \cdot Re^{0.96}$, applicable to foam structures [166]. Effective thermal conductivity of the porous structure was calculated based on the Zehner-Bauer-Schlünder model [83, 84, 85] with the modifications proposed by Hsu et al. [167] to account for the ceramic foam.

A constant thermal conductivity $\lambda_s = 237\,\mathrm{W/m{\cdot}K}$ of alumina spheres was applied, conductivity of solid silica carbide was calculated accounting for the local solid temperature:

$$\lambda_s = -2.08 \cdot 10^{-7} \cdot T^3 + 7.24 \cdot 10^{-4} \cdot T^2 - 0.88 \cdot T + 437$$

Simulation results

Figure 4.14 presents the temperature profile along the center line of the burner setup. The dual-grid model is able to reproduce the heating phase of the gas mixture in the preheater: Heat is transferred from the combustion zone to the preheating region via conduction in the solid phase, where it is passed via convective heat transfer to the gas phase. The base for computation of heat transfer rates is the temperature difference between gas mixture and solid foam structure. Good agreement between experimental and calculated position of the flame front was found.

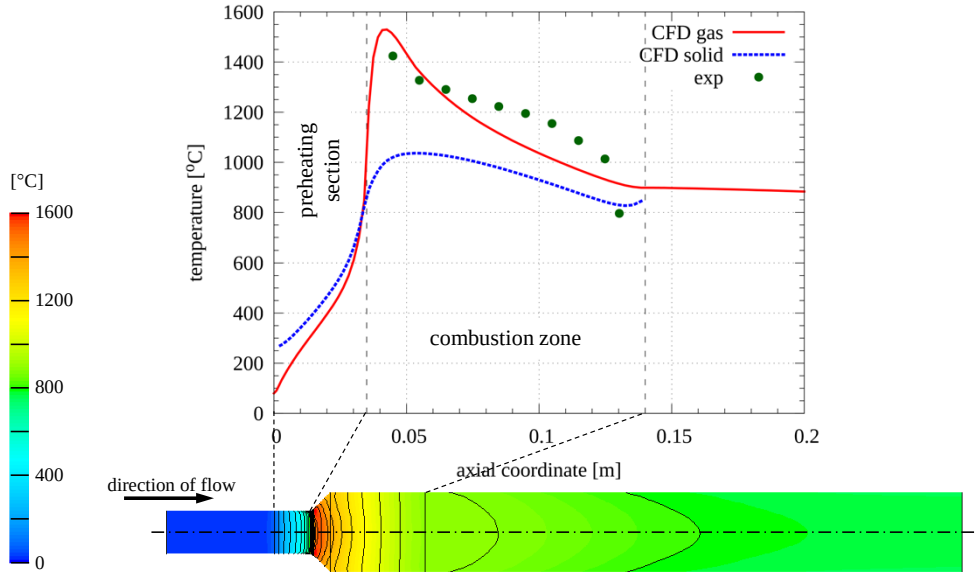

Figure 4.14: Temperature profile along burner axis.

Accordingly, species concentration profiles clearly state the onset of oxidation reactions (see figure 4.15). Reaction products CO_2 and H_2O are formed, as well as the

intermediate combustion product CO. The simplified chemistry model heavily overpredicts CO-emissions (experimentally observed values: typically $< 10\,\mathrm{ppm_v}$). However, the model predictions according to CO burnout can be improved by using a more detailed reaction set including radical components [60, 168].

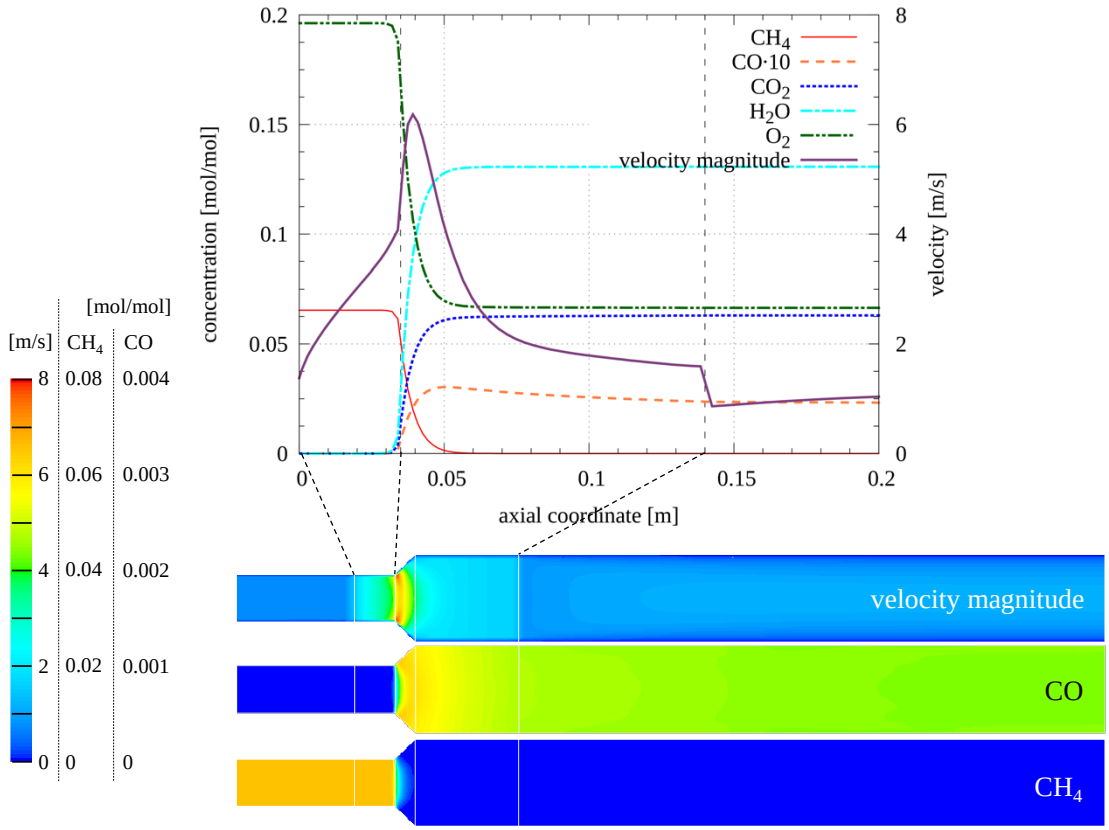

Figure 4.15: Species and velocity evolution along burner axis.

4.3 Heterogeneous reaction setup

4.3.1 Continuous coke gasification

The implementation of the module for heterogeneous coke reactions was first tested against published experimental data comprising a fixed bed reactor for wood char gasification in continuous operation mode [154], see figure 4.16. Continuous operation is important if it comes to the representation of the setup in a CFD-model: by continuous operation mode, steady-state operating characteristics are achieved and thus it is not necessary to apply time-discretization of the conservation equations, drastically reducing the computational demand.

In the experiments coke was prepared by pyrolysis of wood chips at 750 °C for 1 h. Therefore, in the presented gasification model it is not necessary to consider the drying process, solids are assumed to be free of moisture. The experimental reactor is fed with coke particles from top (feed rate $28\,\mathrm{g/min}$, ultimate analysis: $89.8\,\%_{\mathrm{w/w}}$ C, $2.2\,\%_{\mathrm{w/w}}$ H, $6.1\,\%_{\mathrm{w/w}}$ O, $0.1\,\%_{\mathrm{w/w}}$ N). The reacting gas was produced by propane flames located above the coke bed (gas conditions prior to coke bed: 1020 °C, $30\,\%_{\mathrm{v/v}}$ H_2O, $8\,\%_{\mathrm{v/v}}$ CO_2, $2.7\,\%_{\mathrm{v/v}}$ O_2, $59.3\,\%_{\mathrm{v/v}}$ N_2, feed rate $226\,\mathrm{L_{STP}/min}$). Instrumentation included sampling

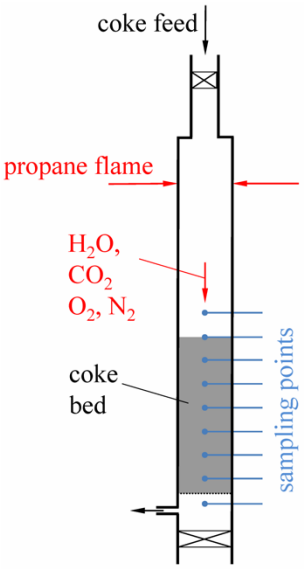

Figure 4.16: Sketch of the continuous fixed-bed reactor used in the experimental work of Steene et al. [154].

and measuring probes in 10 cm intervals along the fixed bed, allowing for determination of temperature and species concentration profiles in the reactor [154].

Simulation setup

A set of heterogeneous gasification reactions was implemented to model the coke utilization. The reaction equations and intrinsic kinetics are summarized in table 4.2. The parameters in the kinetic expressions are valid for coke from wood pyrolysis, as charcoal of this type was used in the experiments that were adopted for model validation [154].

Table 4.2: Intrinsic kinetics of heterogeneous reactions applied for coke from wood chips. Reaction order ν, stoichiometric coefficients $x = 0.292$, $y = 0.0085$.

reaction	ν	ref.
$CH_xO_y + (x/4 - y/2)\,O_2 \longrightarrow CO_2 + x/2\,H_2O$ $k_{coke,O_2} = 4.8 \cdot 10^9 \cdot e^{-\frac{16731}{T_s}}$ $\left[\mathrm{mol_{coke}/kg_{coke}{\cdot}s\,(m^3/mol_{O_2})^{\nu}}\right]$	0.59	[96]
$CH_xO_y + CO_2 \longrightarrow 2\,CO + y\,H_2O + (x/2 - y)\,H_2$ $k_{coke,CO_2} = 2.7 \cdot 10^5 \cdot e^{-\frac{185200}{R \cdot T_s}}$ $\left[\mathrm{mol_{coke}/kg_{coke}{\cdot}s\,(m^3/mol_{CO_2})^{\nu}}\right]$	0.13	[96]
$CH_xO_y + (1 - y)\,H_2O \longrightarrow CO + (1 + x/2 - y)\,H_2$ $k_{coke,H_2O} = 3.42 \cdot T_{coke} \cdot e^{-\frac{15600}{T_{coke}}}$ $\left[\mathrm{mol_{coke}/m^2_{coke}{\cdot}s\,m^3/mol_{H_2O}}\right]$	1	[109]
$CH_xO_y + (2 + y - x/2)\,H_2 \longrightarrow CH_4 + y\,H_2O$ $k_{coke,H_2} = 0.00342 \cdot T_{coke} \cdot e^{-\frac{15600}{T_{coke}}}$ $\left[\mathrm{mol_{coke}/m^2_{coke}{\cdot}s\,m^3/mol_{H_2}}\right]$	1	[95]

Coke particles were modeled accounting for size reduction by gasification applying a shrinking particle approach, modeled by implementing a user-defined scalar that is bound

to the mass flux of the coke bed. Particles were assumed spherically and initialized with a diameter of 5 mm.

Simulation results

The left diagram in figure 4.17 shows the calculated profiles of coke consumption due to heterogeneous reactions. Near the surface of the coke bed, steep gradients are found due to the onset of coke oxidation. This reaction is strongly exothermic and therefore delivers heat as well as additional gasification agents for the gasification reactions including CO_2 and H_2O as educts. The latter reactions also contribute to the release of H_2 that is subsequently consumed by the methanation reaction, however, at comparatively low reaction rates (according to the low a frequency factor in this reaction, see table 4.2). The released gaseous reaction products are also subjected to the homogeneous reaction mechanism.

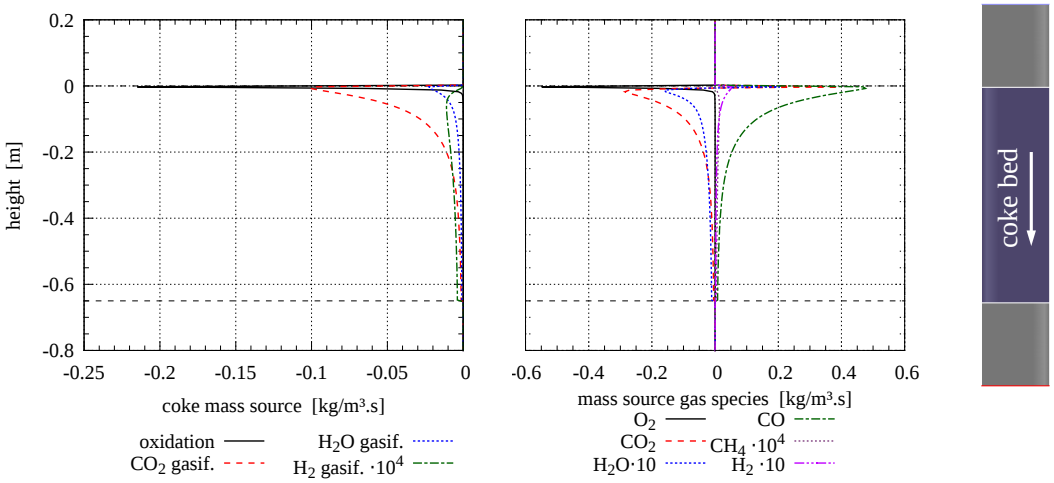

Figure 4.17: Simulation results: Source terms due to heterogeneous reactions. Left: Coke sources, right: Sources of gas components in gas phase.

The trend of O_2 concentration in the gas phase reproduces the above mentioned occurrence of the combustion reaction as the content of oxygen rapidly drops (see figure 4.18), also a distinct peak in gas-phase temperature is predicted. Further downstream heat is consumed by endothermic gasification reactions. The concentrations of CO as well as H_2 rapidly increase in the upper region of the bed. In accordance to the experiments it was found that this is the most reactive zone, as approx. 80 % of the final values of the species concentrations are reached after 10 cm.

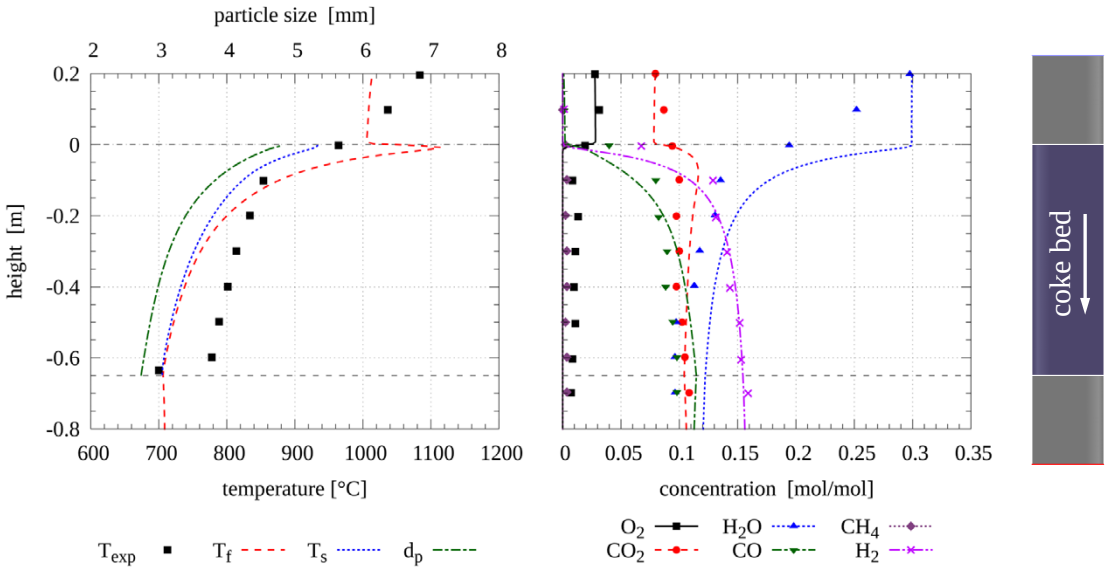

Figure 4.18: Profiles along reactor height. Left: Temperature profiles, right: Gas components concentration profiles. Points: Experimental data, lines: Simulation results.

4.3.2 Reactivity of metallurgical coke

A method that since its introduction in the 1970s achieved common practice in the iron industry was invented by the Nippon Steel Corporation (NSC), Japan. The experiment was designed to indirectly characterize the connection between chemical reactions of coke with CO_2 and the remaining physical strength of coke particles after this reaction in the blast furnace. It has also been adopted as an international standard to characterize metallurgical coke in terms of reactivity (Coke Reactivity Index, CRI) and mechanical stability (Coke Strength after Reaction, CSR) [169, 170]. The NSC test is designed to measure the solution-loss reaction, i.e. the reaction of carbon dioxide with solid coke to produce carbon monoxide.

In the standardized routine 200 g coke in the size range of $19 - 21.4$ mm are exposed to carbon dioxide at a temperature of 1100 °C for 2 h. Afterwards, the weight loss of coke is evaluated, giving the value for the CRI. The remaining material is used in the second part of the experiment: After cooling down to room temperature, coke particles are subjected to mechanic stresses in a tumbling drum. CSR is defined as the mass fraction of particles held by a sieve with 10 mm screen opening after tumbling [171, 172]. Consequently, in this testing procedure coke to be used in the blast furnace process is characterized in terms of reactivity as well as its resistance against mechanical loads, two very important parameters responsible for stable and efficient operation of the blast furnace.

The general setup of an NSC experiment and the implementation in the CFD-model for validation purposes is shown in figure 4.19. The prepared coke is placed on a tray inside the oven and is heated to the desired gasification temperature. Gas moves through the voids of the coke bed from bottom to the top, heterogeneous reactions take place on the surfaces as well as in the pore structures of the coke particles, consuming the gasification agents and releasing the gasification products that are withdrawn on the top of the oven.

Results of an exemplary run are shown in figure 4.20. During preheating to the desired temperatures, the coke bed is purged with nitrogen. After reaching the temperature

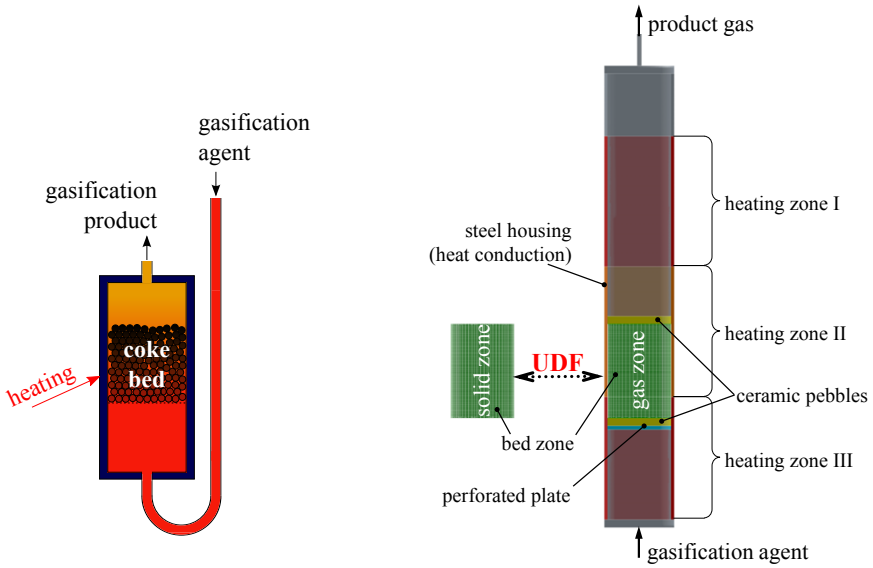

Figure 4.19: NSC-experiment. Left: General setup of NSC setup, right: Implementation in the CFD model.

level the injection gas is switched to the gasification agent under consideration. The original layout of the experiment considers the estimation of global coke consumption rates. However, in the conducted experiments also the composition of the exhaust gas was measured using mass spectroscopy. The resulting concentration profiles are very valuable for validation purposes.

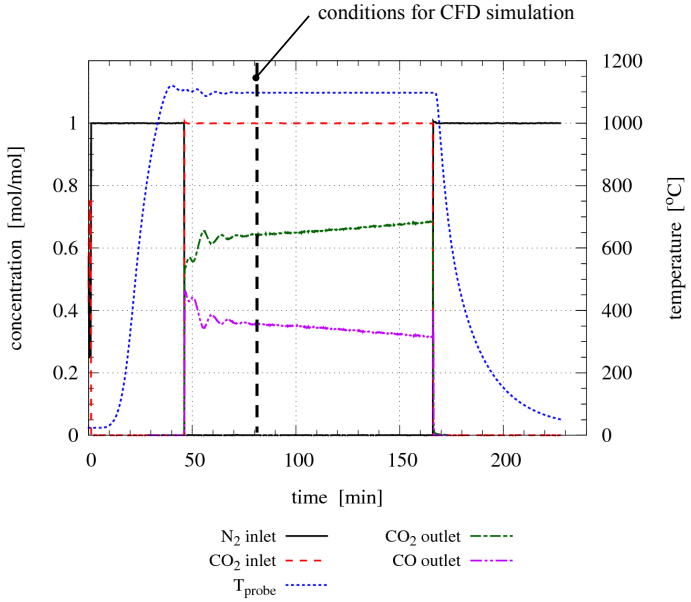

Figure 4.20: Experimental data of a typical NSC run with pure CO_2 as gasification agent.

Simulation results for the case applying standard conditions (1100 °C, pure CO_2 as gasification agent) are shown in figures 4.21 and 4.22. The gasification agent enters the coke bed at the bottom and ascends through the voids in the bed towards the exit at the top of the reactor. The model incorporates the influence of reactant partial

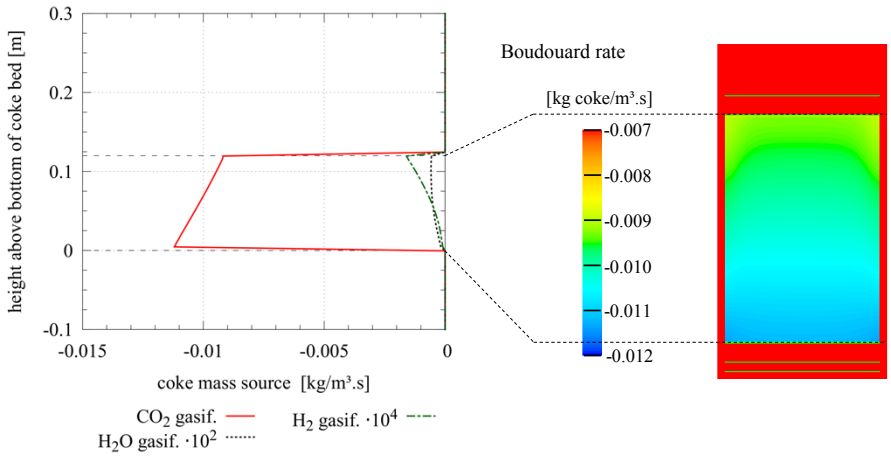

Figure 4.21: Results of CFD-simulation for NSC standard test: Heterogeneous reaction rates.

pressures on the reaction rates, therefore the rate of the solution loss reaction follows the gradients in the CO_2 concentration profile, highest rates appear near the bottom of the coke bed. The coke used in the experiments contains small amounts of hydrogen and oxygen, being released as heterogeneous CO_2 gasification proceeds (coke ultimate analysis: 86 $\%_{w/w}$ C, 1.5 $\%_{w/w}$ O, 1 $\%_{w/w}$ N, 0.17 $\%_{w/w}$ H, 0.6 $\%_{w/w}$ S, balance ash). This results in the occurrence of steam gasification and heterogeneous methane formation, however at low rates due to low reactant partial pressures.

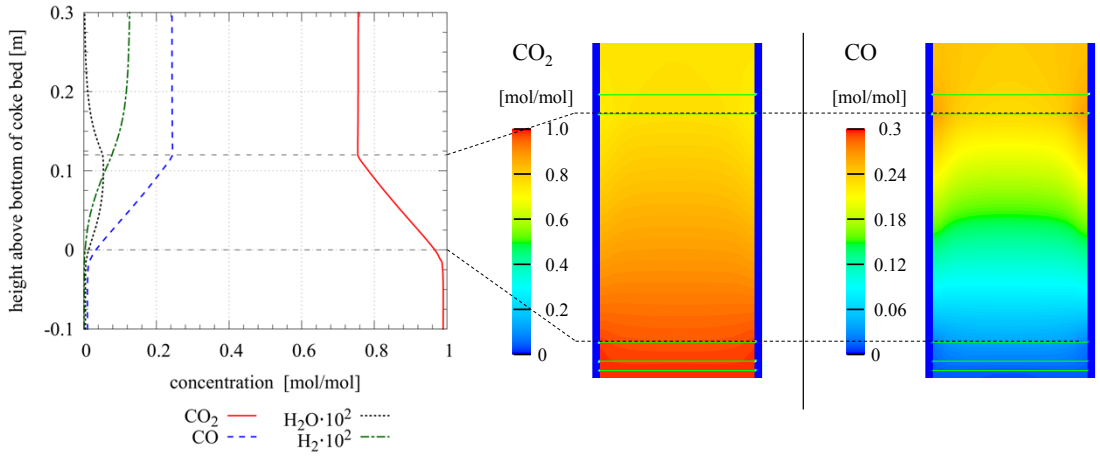

Figure 4.22: Results of CFD-simulation for NSC standard test: Mole fractions of gas species.

Finally, gasification products leave the coke bed, ascending towards the reactor exit. Besides heterogeneous reactions, also the set of homogeneous gas-phase reactions is solved, accounting for the changes in gas composition in the freeboard zone (e.g. water-gas-shift reaction figure 4.22).

Apart from the standard routine, additional experimental work was conducted, varying the operating conditions concerning temperature, coke particle sizes and composition of the gasification agent. Experimental conditions are summarized in table 4.3.

Calculated rates of coke depletion due to CO_2 gasification for the range of experimental conditions are shown in figure 4.23. Significant differences (approx. factor 5) between

Table 4.3: List of experiments and operating conditions. Gas flow applied to all experiments: $5\,l_{STP}/min$.

exp. no.	T [°C]	d_p [mm]	$CO_{2,\,inlet}$ [$\%_{v/v}$]	$N_{2,\,inlet}$ [$\%_{v/v}$]
1	1100	$19 - 21.4\,mm$	100	0
2	1100		25	75
3	1000		100	0
4	1000		50	50
5	1100	$8 - 10\,mm$	100	0

gasification rates for the conditions studied were found. Highest reactivity appears for the case with smaller coke particles (exp. 5), being precipitated by higher specific surface of the particles as well as diffusion issues inside the solid particles: smaller particle sizes allow for shorter diffusion distances of reaction educts in internal pore structures to the actual reaction sites. Consequently, a larger fraction of the inner particle surface is involved in heterogeneous reactions, increasing the overall rates of reaction.

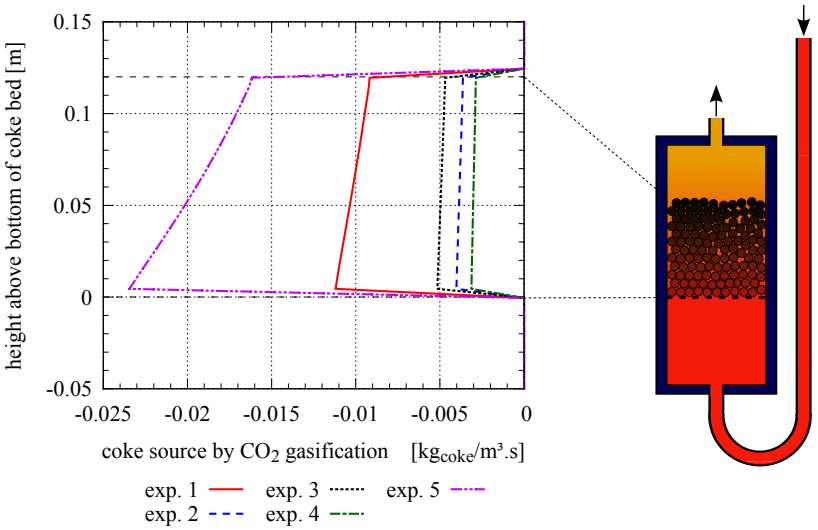

Figure 4.23: Vertical profile of coke consumption rates due to the solution loss reaction, experimental conditions as listed in table 4.3.

The rates of boundary layer and pore diffusion, intrinsic reaction rates and the resulting effective reaction rates for the experiments no. 2 and 5 are shown in figure 4.24. At low temperatures, the limiting factor for the overall reaction rate is given by intrinsic reaction rates of CO_2 with solid coke. With increasing temperature, this rate increases exponentially, while the rate of boundary layer diffusion increases only in the order of $T^{1.75}$ (see equ. 3.11). Therefore, at high temperatures the concentration of educts inside coke particles declines and the diffusive transport of educt species through the boundary layer towards the particle surface becomes the rate limiting step. At intermediate temperatures, the diffusion of educts inside porous particle structures plays an important role, while at low and very high temperatures the effective reaction rate asymptotically approaches the intrinsic and the rate of boundary layer diffusion, respectively. As carbon dioxide is consumed, CO is released into the voids of the coke bed (see fig. 4.25).

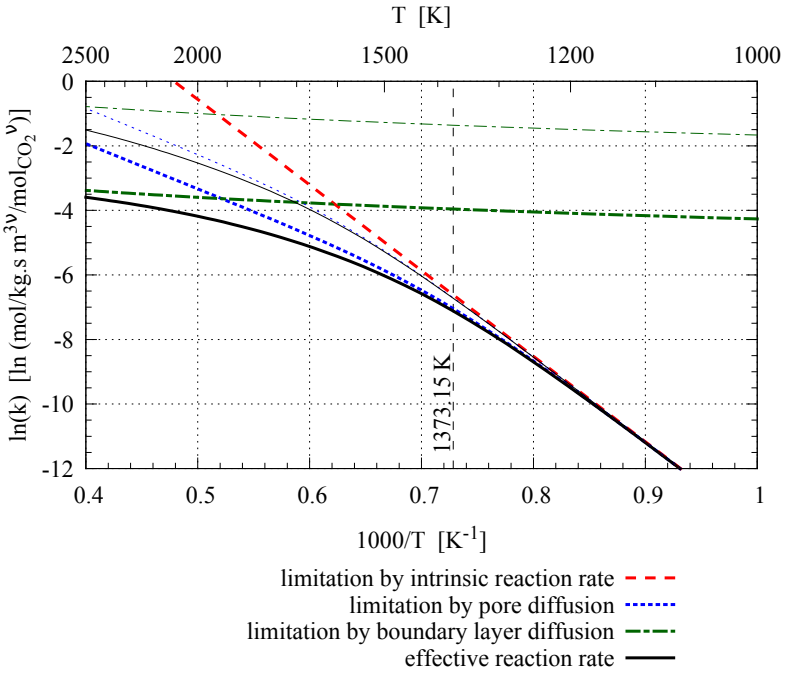

Figure 4.24: Reaction rates at mean concentration in the coke bed. Bold lines: exp. 2, thin lines: exp. 5.

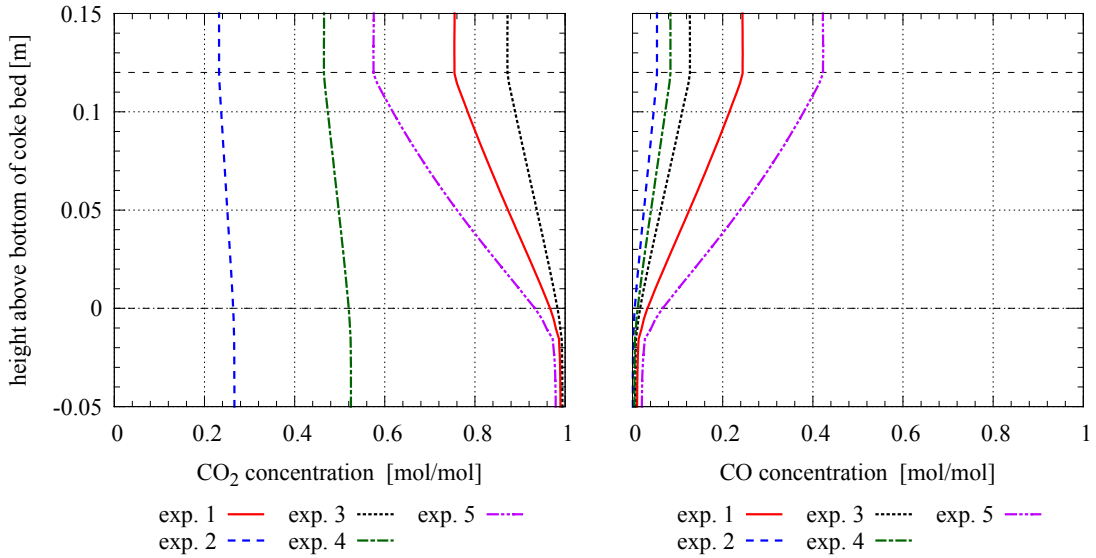

Figure 4.25: Profiles of CO_2 and CO mole fractions along the coke bed.

The comparison of product gas compositions for the various experimental runs to the simulation results is shown in figure 4.26. Good agreement was found for the range of parameter variation, indicating that the model setup is able to capture and reproduce the main physical processes involved in CO_2-gasification of coke, such as boundary-layer diffusion, pore diffusion and the influence of intrinsic reaction kinetics.

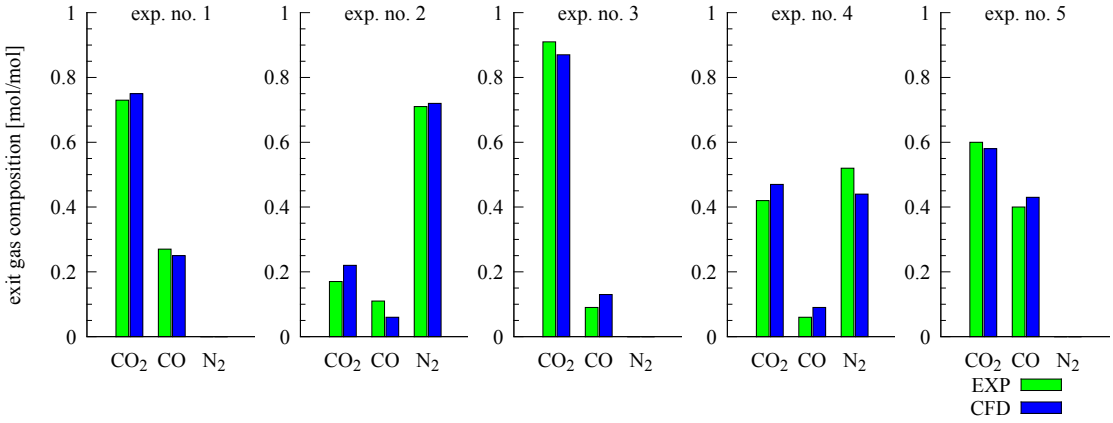

Figure 4.26: NSC validation results, exit gas composition.

4.4 Pulverized coal conversion

The model for conversion of coal was validated by implementing an experimental setup simulating the combustion of pulverized coal at raceway conditions [156] and comparison of CFD simulation results to the available experimental data available therein.

Experimental setup

The experimental setup represents a combustion test rig where pulverized coal is injected into a gas flow that resembles the hot blast of blast furnaces in the tuyère and raceway zone (experimental work: Shen et al. [156], see fig. 4.27). The gas flow is air, preheated to 1200 °C that is supplied at rates of 300 m^3_{STP}/h, resulting in a maximal hot blast velocity in the tuyère of approx. 140 m/s.

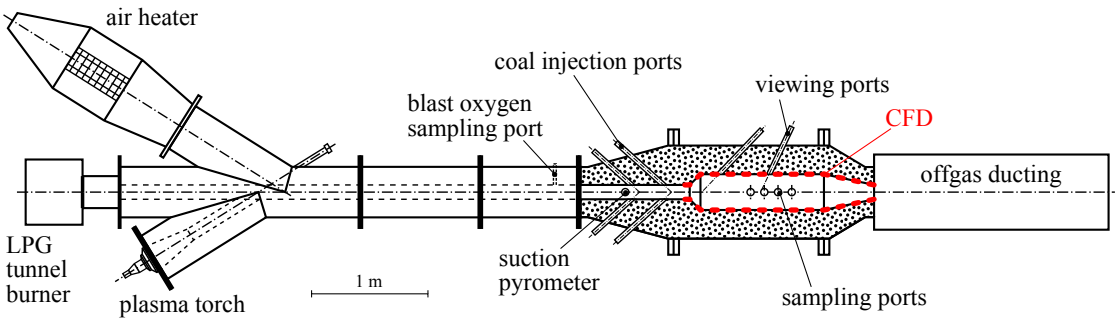

Figure 4.27: Experimental setup for validation of PCI model (adapted from [156]), highlighting the region observed by CFD simulation.

The published experimental data include the measurement of the coal burnout ratio in the center of the combustion chamber at an axial distance of 925 mm to the tip of the coal injection lance. In processes involving thermal utilization, e.g. combustion, the value of coal burnout represents an important parameter as it describes the degree of coal conversion that is achieved in a certain environment.

The burnout ratio of coal is defined from its ash balance as given by:

$$BO = \frac{1 - \frac{w_{a,0}}{w_a}}{1 - w_{a,0}} \quad , \qquad |4.3|$$

where $w_{a,0}$ represents the ash content in virgin coal and w_a the ash remaining in the coal at observation. Therefore, the burnout ratio is a measure for the fraction of organic coal mass that has been released due to devolatilization, combustion and gasification reactions.

Table 4.4: Coal data, source: Shen et al. [156].

coal		A	B	C	D
proximate analysis					
moisture	[kg/kg]	0.009	0.012	0.034	0.056
volatile matter	[kg/kg]	0.124	0.200	0.326	0.391
ash	[kg/kg]	0.080	0.097	0.092	0.027
fixed carbon	[kg/kg]	0.787	0.691	0.548	0.526
gross specific energy	[MJ/kg]	33.0	32.1	31.2	30.5
ultimate analysis					
C	[kg/kg]	0.913	0.891	0.847	0.794
H	[kg/kg]	0.040	0.047	0.056	0.056
N	[kg/kg]	0.019	0.017	0.021	0.015
S	[kg/kg]	0.005	0.004	0.0067	0.006
O	[kg/kg]	0.023	0.041	0.069	0.129
Rosin Rammler parameters					
$\bar{d}$	[µm]	30	39	51	53
n	[−]	0.97	1.05	1.03	1.17

Experimental conditions were varied in terms of coal type, coal feed rates and type of coal lance cooling gas (see table 4.5). In all experiments pure nitrogen was used as conveying gas for the pulverized coal. In the CFD model, particle size distributions of these coals were approximated applying the Rosin Rammler method (see fig. 4.28). The two parameters (mean diameter $\bar{d}$ and spread parameter n) were determined by regression of published data [156]. In one of the experiments methane was used as cooling gas in the outer ring of the coaxial coal lance. In this variation, the ratio of C/H feed via the coal injection lance was kept constant by increasing the coal rate.

Table 4.5: PCI model validation: Experimental runs [156].

experiment no.		1	2	3	4	5
coal						
type		A	B	C	D	C
feed rate	[kg/h]	31.6	25.2	22.9	28.3	26.9
cooling gas						
type	[kg/kg]	air	air	air	air	methane
feed rate	[m^3_{STP}/h]			3.2		2.8
C/H	[mol/mol]	1.97	1.64	1.37	1.34	1.37

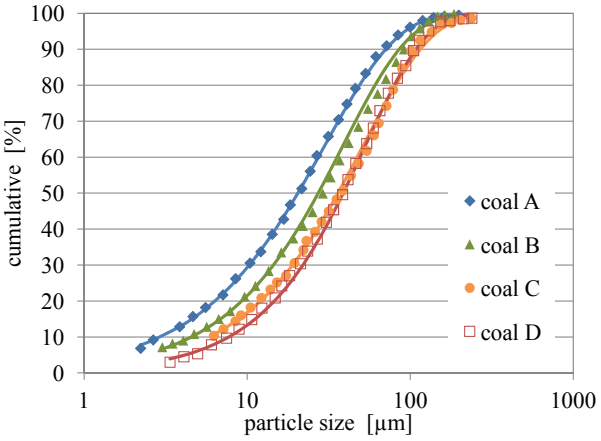

Figure 4.28: PCI model validation: Size distribution of pulverized coals used in the experiments by Shen et al. [156]. Points denote experimental data, lines show data regression applying the Rosin-Rammler method.

CFD simulation

The geometric representation of the experimental setup in the CFD model is shown in figure 4.29. The computational domain starts at the tuyère zone, 10 cm prior to the tip of the coal injection lance and ends at the exit of the combustion chamber. The geometry includes a detailed representation of tuyère geometry, combustion chamber and coal lance. In the experiments a co-axial lance was used where coal was injected with nitrogen as conveying gas. The annular gap was flushed with a cooling gas to prevent the coal pipe from overheating in order to avoid the formation of depositions in the coal lance. The lance was inclined downwards at an angle of 6°, the lance tip was positioned in the center of the tuyère cross-section.

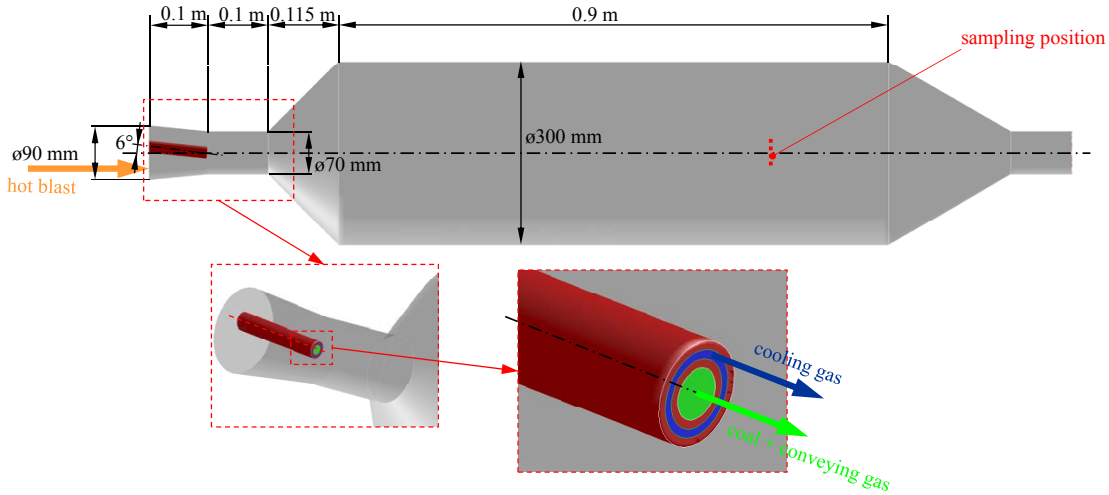

Figure 4.29: Implementation of experimental setup in a CFD model.

As shown in figure 4.30, the hot blast reaches its maximal velocity in the tuyère. The gas jet enters the combustion chamber and extends for a distance of approx. 1 m along the center line into the chamber. A large-scale recirculating gas flow is induced that forms a backflow region around the central coal flame. The gas leaves the combustion chamber

through the exit cross-section. Due to the combustion products from coal utilization the gas mole flow increases, resulting in an increased exit gas velocity.

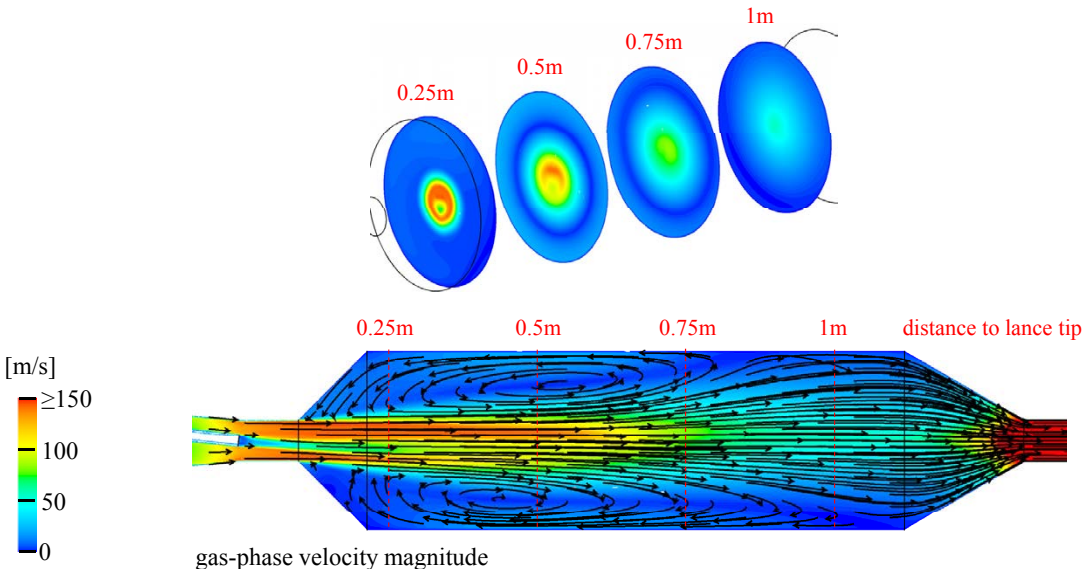

Figure 4.30: Validation of PCI model: Contours and path-lines of gas velocity on the symmetry plane of the combustion test rig.

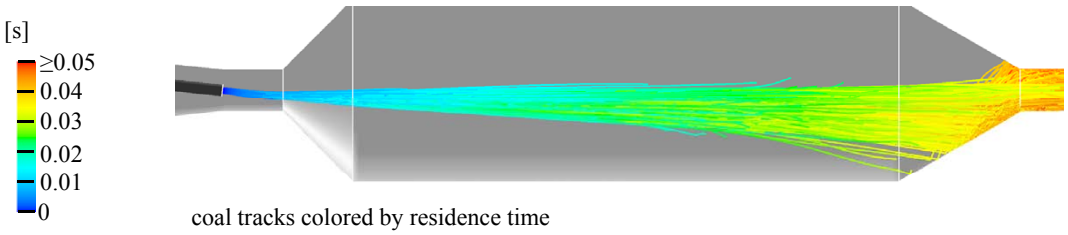

Figure 4.31: Validation of PCI model: Tracks of coal particles injected into the combustion test rig.

Injected coal particles tend to initially follow the direction of the injection lance but due to momentum transfer during the time of flight the direction is altered to resemble the gas flow (see particle tracks in figure 4.31). The coal rapidly passes the combustion chamber in approx. 30 ms, being accelerated by the hot blast flow. Particles that reach the back of the combustion chamber in a region outside the exit cross section hit the wall near the chamber exit. The evaluation of the spatial distribution of the mass-weighted average burnout coefficient computed for all particles that passed the corresponding fluid cell is shown in figure 4.32. Coal conversion is more complete in the boundary regions of the coal plume due to the oxygen supply from the surrounding blast flow. Here, oxidation rates are higher, consequently temperatures and therefore heat supply for endothermic gasification reactions is higher.

The computed temperature field is shown in figure 4.33. Right in front of the coal injection lance gas phase temperatures remain low in the core of the coal plume due to the consumption of heat by coal drying and the endothermic nature of volatiles release. Drying takes place very close to the coal injection lance tip and is finished right within the tuyère zone (fig. 4.34).

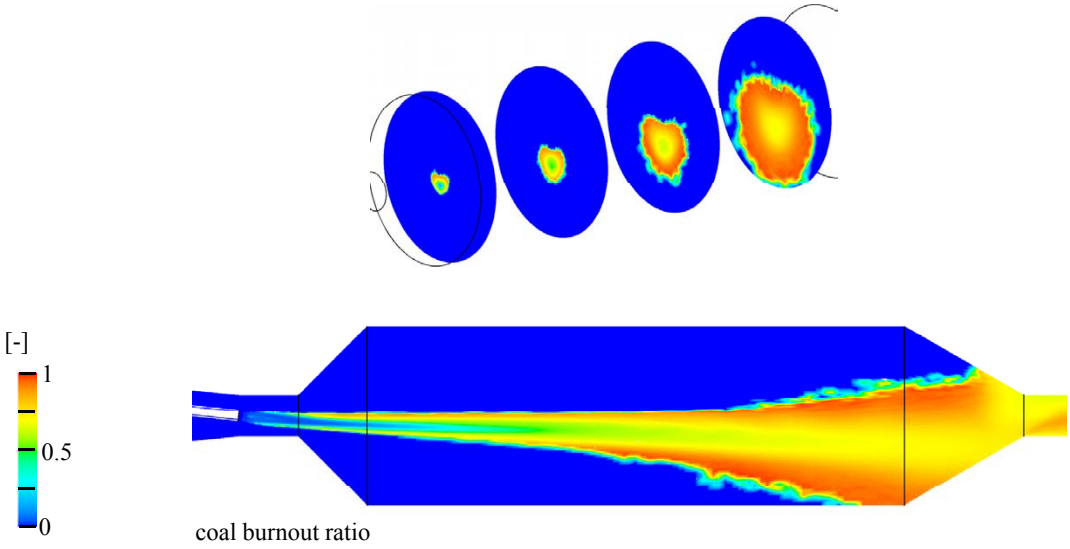

Figure 4.32: Validation of PCI model: Contours of coal burnout ratio.

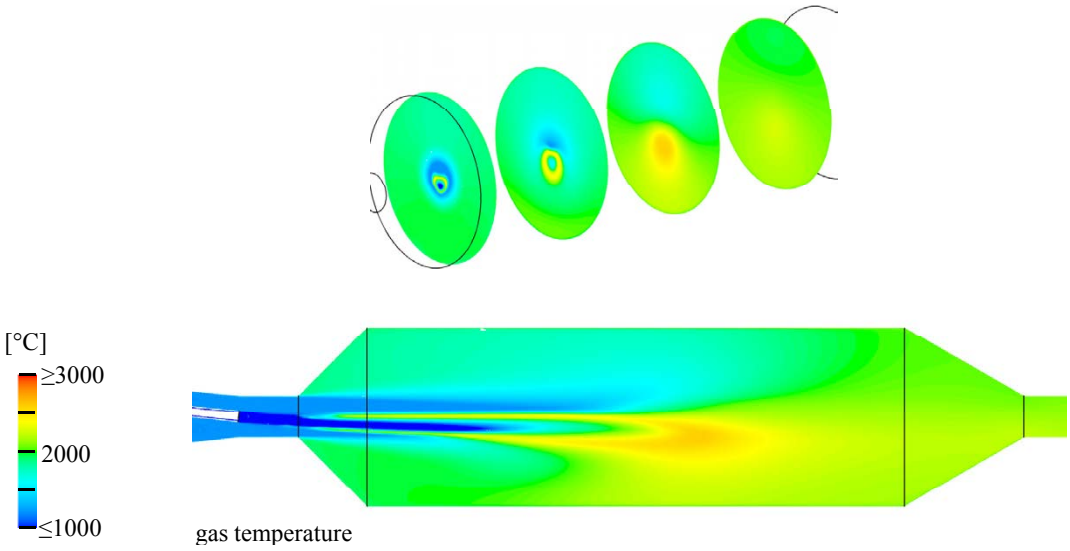

Figure 4.33: Validation of PCI model: Contours of gas-phase temperature.

Also, due to the utilization of inert nitrogen as conveying gas no oxygen is introduced directly to this region. O_2 that is mixed from the hot blast co-flow into the coal flame is rapidly consumed by combustion reactions of released volatiles, forming an oxygen-depleted core zone (fig. 4.35). Maximal rates of devolatilization are located in the core of the coal plume, extending into the combustion chamber to a distance of approx. 0.5 m from the lance tip. In this zone heat is transferred from the flame front to the particles by radiation.

The onset of combustion reactions in the gas phase as well as heterogeneous char oxidation is responsible for the delivery of heat of reactions, increasing gas and particle temperatures. Combustion products CO_2 and H_2O are released. Steam and carbon dioxide are also consumed by gasification reactions of char particles (negative source terms in figure 4.34), resulting in the release of CO and H_2. Rates of gasification reactions are highest where CO_2 partial pressures are high, and also temperatures are high to supply the heat for these endothermic reactions. Char gasification continues all the way

to the chamber exit. On the average, char particles are not fully consumed within the residence time in the reaction chamber.

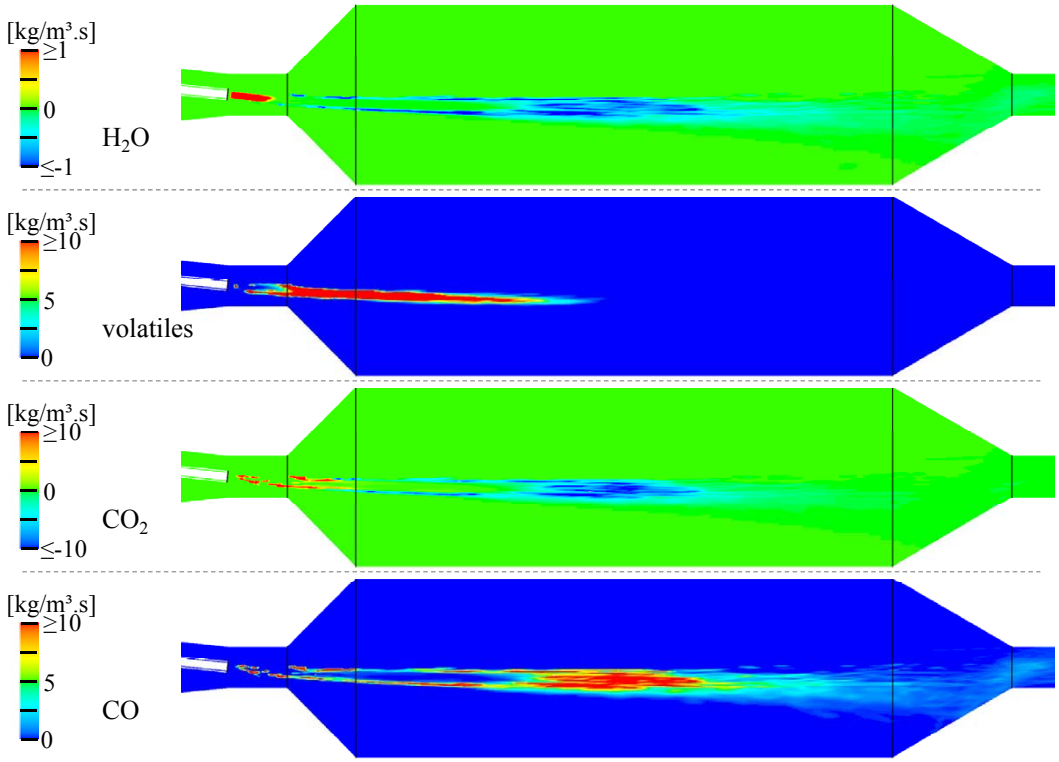

Figure 4.34: Contours of species mass source terms to the gas phase.

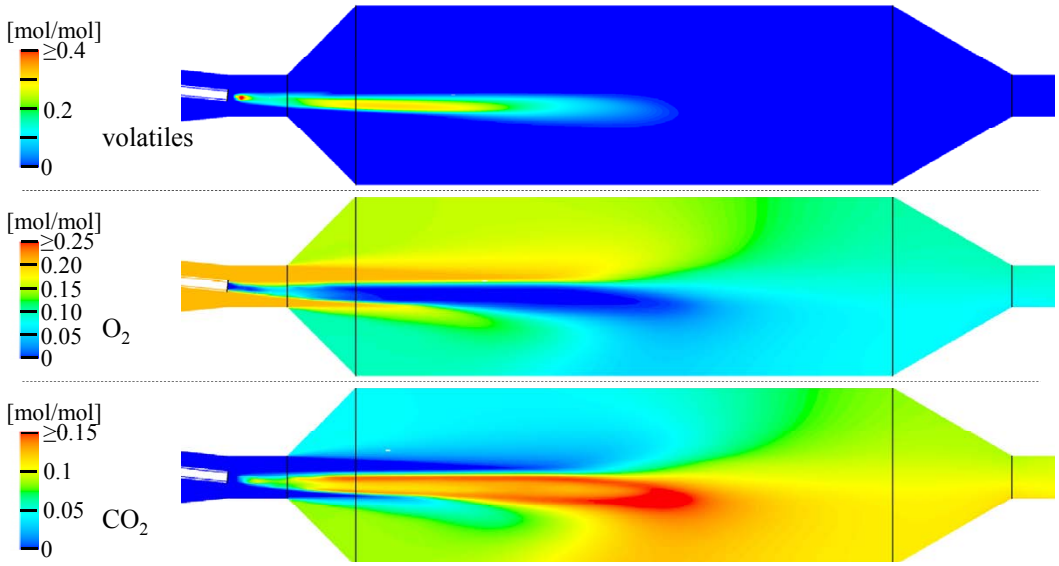

Figure 4.35: Contours of concentration distribution of major gas constituents.

The lapse of characteristic particle properties with residence time is shown in figure 4.36. In this diagram the fate of particles is shown in terms of mass-weighted averages with respect to time. After a short preheating phase, water is released from the virgin coal at a very early stage. Thermal decomposition starts after further increase of the coal particle temperature to approx. 450 °C, the char fraction modeled as a remnant increases due to devolatilization.

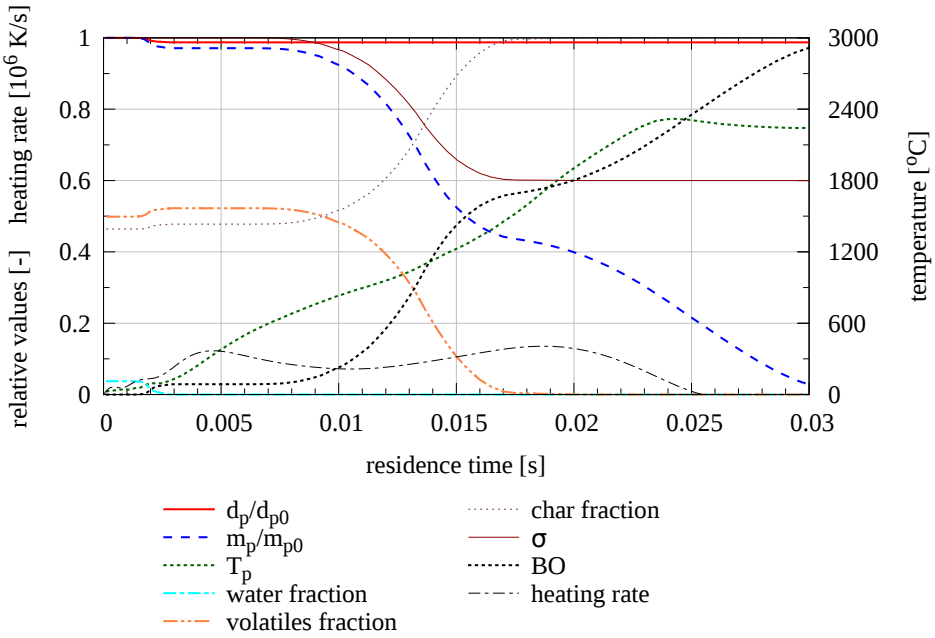

Figure 4.36: Particle properties vs residence time.

The model setup for pulverized coal injection is validated in terms of coal utilization. Experimental burnout ratios of coal collected at the position indicated in figure 4.29 are compared to values calculated by the CFD model, results are summarized in figure 4.37. The calculated average time of flight of coal particles prior to passing the sample point is 30 ms. In general good qualitative and quantitative agreement between experimental data and burnout ratios predicted by the model is achieved.

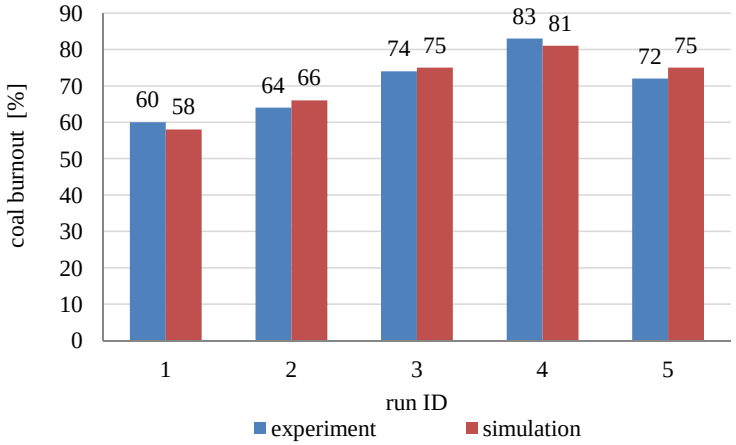

Figure 4.37: Comparison of measured and calculated coal burnout ratios.

5 Blast Furnace Simulation

The blast furnace studied is the largest unit of its type in Austria. It is operated by **voest**alpine Stahl GmbH in Linz. This furnace is arranged with equipment allowing for the utilization of a wide range of alternative reducing agents including natural gas, processed waste plastics, heavy fuel oil and tar, pulverized coal etc. The furnace features a hearth diameter of 12 m and has a working volume of approx. 3125 m^3, allowing for a hot metal production rate of up to 8800 t_{hm}/d. 320000 m^3_{STP}/h hot blast is injected at a temperature of about 1200 °C and a gauge pressure of 4.2 bar via 32 circumferentially arranged tuyères. Auxiliary reducing agents are fed directly into the hot blast flow via retractable lances positioned in the tuyères. The atomization of liquid hydrocarbons is done using a coaxial steam-cooled lance. The newly installed system for pulverized coal injection (startup in March 2015) utilizes inert nitrogen as fluid for pneumatic transport.

Figure 5.1: Blast furnace *A*, operated by **voest**alpine Stahl GmbH in Linz. Lower part of the blast furnace, showing bustle pipe and air distribution manifold [173].

An overview of the computational domain implemented in the CFD model is shown in figure 5.2. The geometry is restricted to the lower part of the blast furnace, starting from an elevation of 1.5 m below the blast injection level and extending to 2 m above. The geometry also includes the bustle pipe, in order to properly describe the flow conditions of hot blast when entering the hearth zone of the blast furnace.

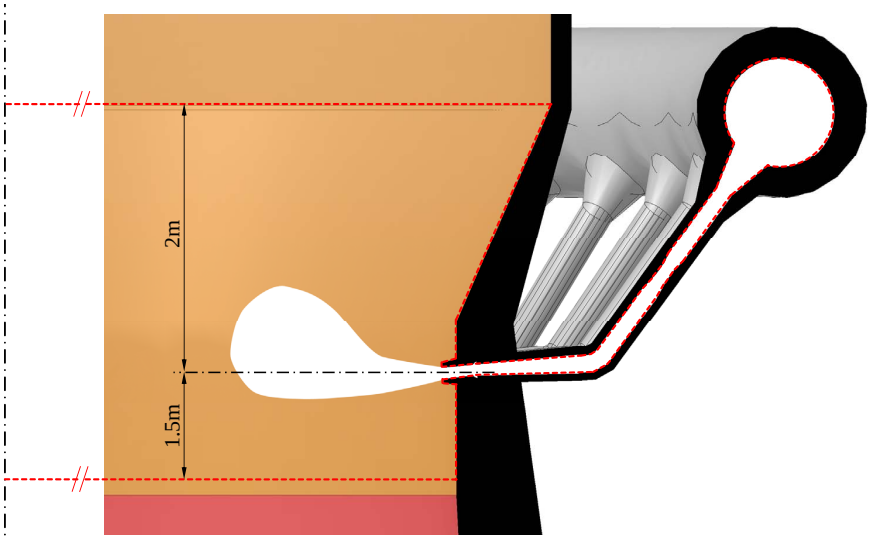

Figure 5.2: Simulation domain, highlighted by the dashed line.

The model compilation is applied to a section of the blast furnace, comprising a segment of the shaft including one tuyère for hot blast injection. Periodic boundary conditions are applied to the radial surfaces to link corresponding data structures on either side. By applying this approach, it is assumed that the conditions in the furnace are repeated periodically in the tangential direction with each tuyère element. The main purpose and big advantage of this strategy is to limit computational efforts to affordable levels by drastically reducing the number of discrete volume elements. The three-dimensional shape of the implemented computational domain is shown in figure 5.3, also highlighting the lances for injection of alternative reducing agents.

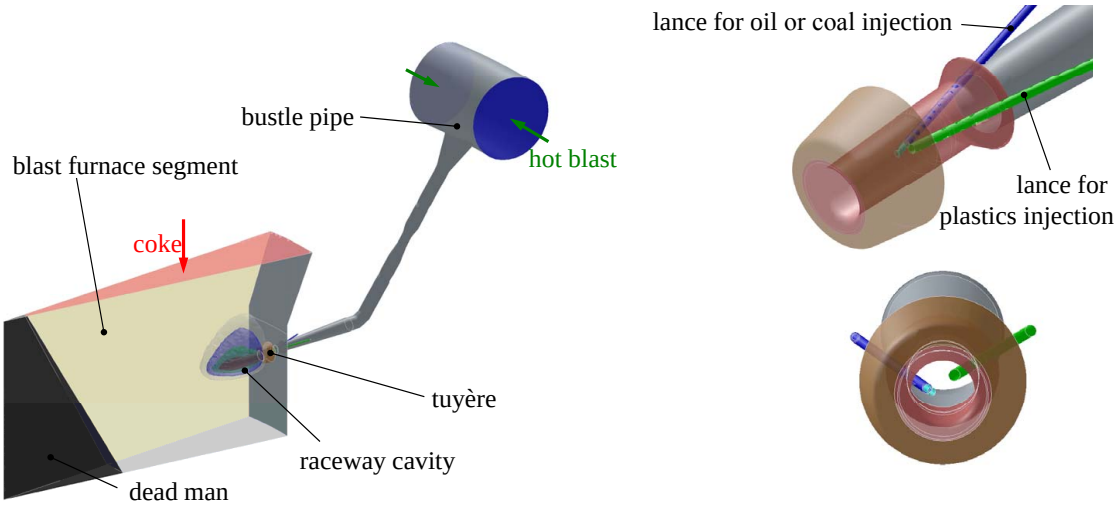

Figure 5.3: Geometry of simulation domain, detail: Tuyère and lances for injection. Left: isometric, right: front view.

The computational grid was built using the geometry pre-processor GAMBIT® [74]. This software tool provides a special 3d CAD-environment to set up the geometric features in the simulation domain and also offers the functionality for spatial volume

discretization. The grid was built from structured and unstructured hexahedral volume elements, gradually increasing the size of grid elements with increasing distance from the tuyère opening. Highest resolution was applied in the tuyère zone to spatially resolve the injection lances (average edge length of discrete volumes: 5.5 mm). The average spatial resolution in the raceway cavity is 18 mm. Towards the dead man zone in the center of the blast furnace (see fig. 5.3), the gradients of data fields decrease, allowing for coarser mesh sizes (gradual change, average in coke bed zone: 36 mm, dead man: 68 mm).

Additionally to this base geometry the model also includes geometry variations, featuring several positions of injection lance tips and inner tuyère diameters. The grid was implemented such that in the solver environment certain elements can be activated or removed from the model. Consequently, the simulation of geometry variations is possible by changing boundary conditions in the flow solver without the need for geometry preparation in a new preprocessing step. This is very efficient, because the study of a new situation, e.g. the injection of pulverized coal or liquid hydrocarbons only (plastics lance removed), can be done by changing the boundary description and continuation of iteration loops without the need to start the simulation from scratch as outlined in chapter 3.13.

5.1 Boundary conditions

The blast furnace modeling study was structured such that a case setup with certain geometry aspects and operating conditions was defined as a reference case. Alternative reducing agents considered in this baseline case are waste plastic particles and liquid hydrocarbons (modeled as heavy fuel oil). In the following, boundary conditions are given with respect to the simulation domain. As in the real-world blast furnace the particular types of auxiliary reducing agents are not introduced via each tuyère, herein rates of injection are therefore given as absolute values rather than specific values relative to the hot metal production rate.

Hot blast In the model the supply of hot blast is defined via a mass flow inlet boundary at bustle pipe level (see figure 5.3). Reference conditions of hot blast are given in table 5.1.

Table 5.1: Baseline case: Hot blast injection conditions.

hot blast rate	9900	$m^3_{STP}/h \cdot tuyère$
temperature	1220	°C
O_2 content (dry basis)	27.4	$\%_{v/v}$
H_2O load	5	g/m^3_{STP}
tuyère diameter	140	mm

The tuyère diameter evaluated in the reference case is 140 mm. The boundary condition for the energy equation is implemented such that the tuyère wall temperature is set to a fixed temperature of 250 °C to compute for local heat transfer rates from the hot blast to the cooling system.

Alternative reducing agents Characteristic properties and rates of alternative reducing agent injection are given in table 5.2. In the model, the ash introduced with the waste plastics is not considered - injection rates are corrected correspondingly.

Table 5.2: Baseline operating conditions: Alternative reducing agents supply.

reducing agent	liquid hydrocarbons	waste plastics
feed rate	700 $^{kg}/_{h \cdot tuyère}$	800 $^{kg}/_{h \cdot tuyère}$
lower heating value	36.5 $^{MW}/_{kg}$	32.1 $^{MW}/_{kg}$
temperature	280 °C	30 °C
composition	79 $\%_{w/w}$ C, 11 $\%_{w/w}$ H, 10 $\%_{w/w}$ H_2O	71.5 $\%_{w/w}$ C, 7.4 $\%_{w/w}$ H, 13.9 $\%_{w/w}$ O , 7.2 $\%_{w/w}$ ash
supporting gas type	steam	air
purpose	cooling gas	transport fluid
supply rate	70 $^{m^3_{STP}}/_{h \cdot tuyère}$	200 $^{m^3_{STP}}/_{h \cdot tuyère}$
temperature	170 °C	30 °C

Coke The elemental composition of metallurgical coke is important to properly model the conversion characteristics. The results of the ultimate analysis of coke fed to blast furnace *A* is listed in table 5.3. Coke particles are modeled with a diameter of 25 mm that remains constant throughout the simulation domain. A spatially variable coke bed porosity is applied to introduce the raceway cavity (see chapter 3.9). A mass-flow inlet boundary condition is used to describe the coke flow entering the simulation domain from the furnace shaft zone. The outflow of unused coke towards the furnace hearth on the bottom is described applying a pressure outlet boundary.

Table 5.3: Ultimate analysis of metallurgical coke as used in the blast furnace.

feed rate	4.4	$^{t}/_{h \cdot tuyère}$
lower heating value	36.1	$^{MW}/_{kg}$
composition		
C	86	$\%_{w/w}$
H	0.17	$\%_{w/w}$
N	1.0	$\%_{w/w}$
S	0.6	$\%_{w/w}$
O	1.5	$\%_{w/w}$
ash	10.73	$\%_{w/w}$

Dead man The so-called *dead man*, a characteristic zone in the center of the blast furnace hearth, is modeled as conical structure with a fixed geometry. In the model the temperature of this stagnant zone of the coke bed is fixed to 1400 °C, it is furthermore modeled impenetrable for gas flow.

5.2 Baseline case simulation results

In the following sections simulation results for the full blast furnace geometry applying reference case boundary conditions are discussed.

5.2.1 Flow field variables

In a blast furnace the characteristics of gas-solids flow play an important role [114]. Hot blast is injected at high velocities reaching up to 200 m/s in the tuyère. After leaving the tuyère, due to the high inertia of the gas jet the blast first follows the tuyère center line. As the gas impinges on the coke bed at the boundary of the raceway cavity, the direction of the gas flow changes towards the gradient of the porosity profile owing to the exerted pressure drop. Gas velocity rapidly decreases due to the increasing cross-sectional area available for the gas flow as the gas expands into the coke bed (see figure 5.4 and 5.5).

The current model setup also includes a description of inter-phase momentum transfer. The high gas inertia results in acceleration of coke particles that enter the raceway cavity from top, transporting them towards the center of the furnace shaft. During the short residence time of coke in the void in front of the tuyère, coke particles are not fully consumed by heterogeneous reactions. This results in a circulating movement of coke in this region (compare coke path lines, as shown in fig. 5.4 d). This behavior of solids flow was also proposed by experimental observations through inspection windows in an operating blast furnace using optical instrumentation (high speed imaging) [25]. The movement of solid matter contributes to heat transport in the raceway zone by convection of sensible heat with the hot coke particles.

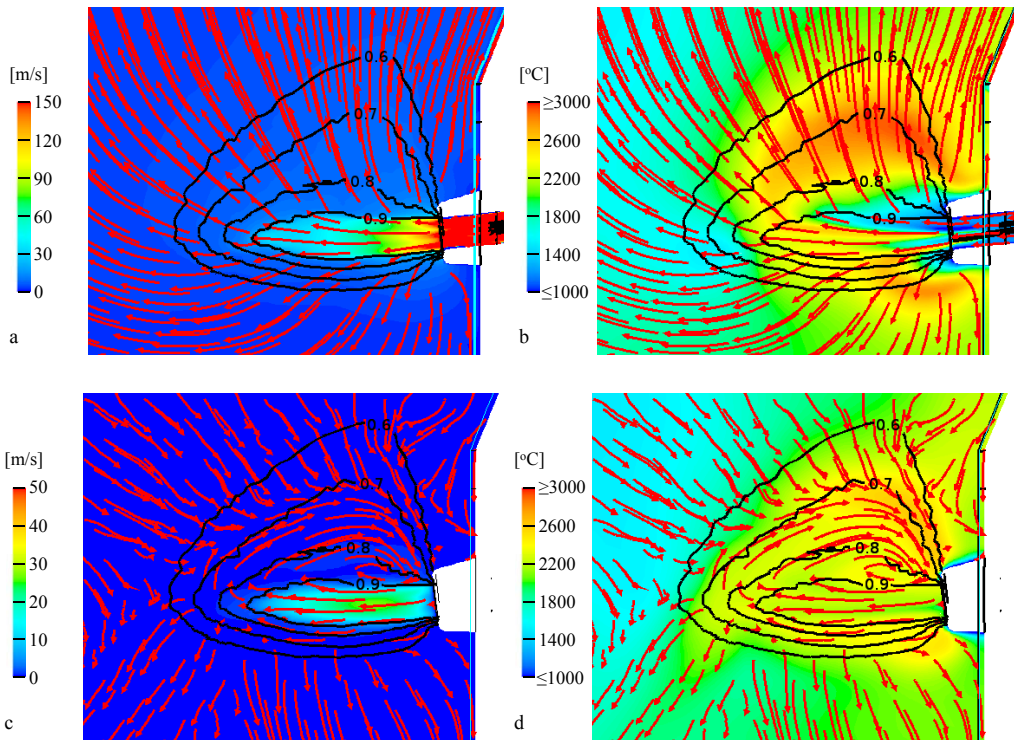

Figure 5.4: Flow and temperature field near the tuyère. Top: Gas-phase flow path lines and contours of velocity magnitude (a) and temperature (b). Bottom: Path lines of coke movement and contours of coke velocity (c) and temperature (d). Black lines represent iso-values of coke bed porosity.

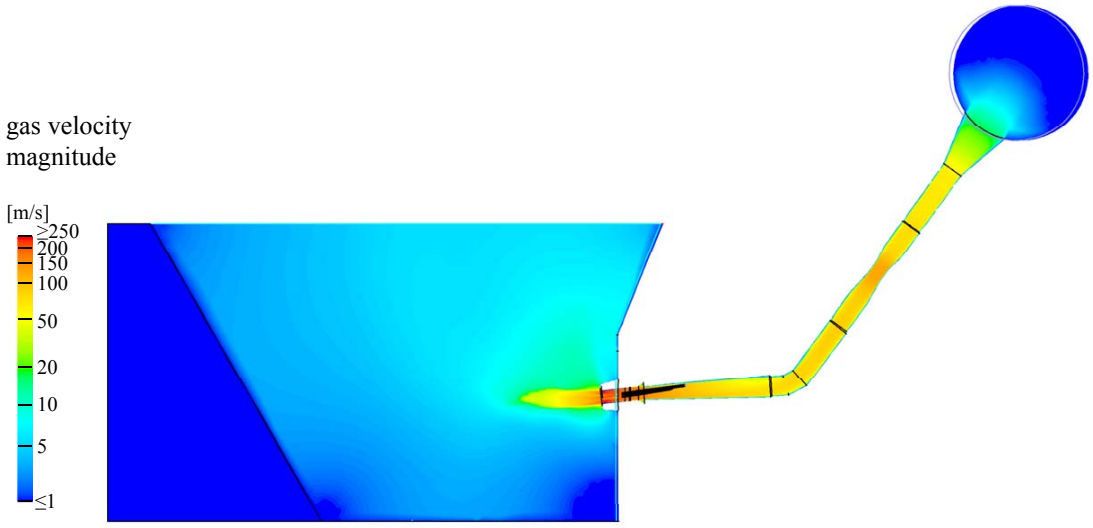

Figure 5.5: Profile of the gas flow velocity magnitude, logarithmic scale.

In the simulation, the static absolute pressure at the exit of the domain is fixed at 4.6 bar_a. Figure 5.6 shows the static pressure relative to this absolute value. The static pressure decrease of hot blast moving from the tip of the tuyère towards the exit boundary was calculated to be approx. 0.3 bar.

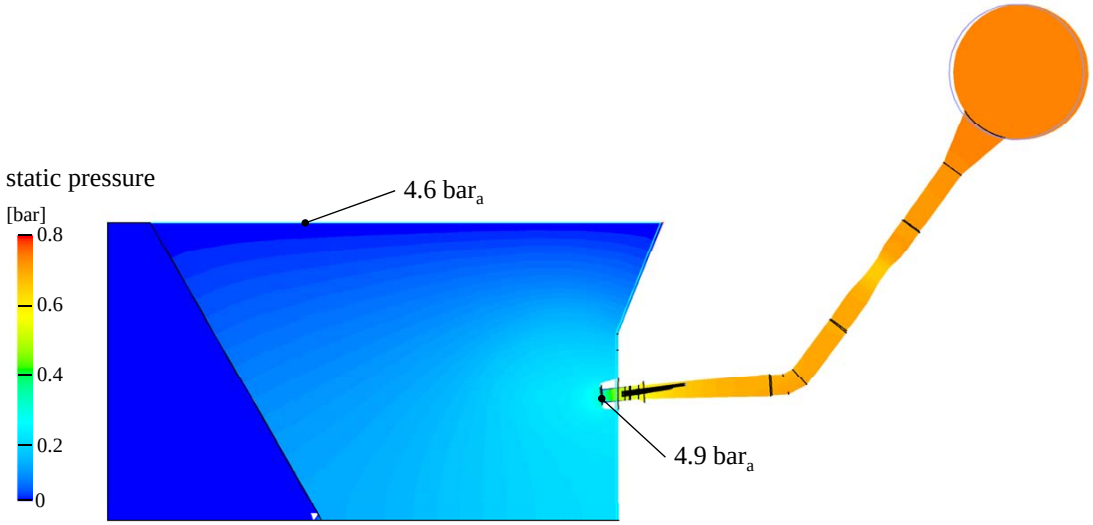

Figure 5.6: Profile of static pressure, relative to exit pressure (4.6 bar_a).

5.2.2 Liquid hydrocarbons

The lance for injection of heavy fuel oil is realized as a two fluid co-axial lance. Oil is injected via the inner pipe, the coaxially arranged outer pipe is charged with cooling gas to protect the inner pipe from high hot blast temperatures. Blast furnace *A* is usually operated using steam as cooling agent. In the base-case geometry setup studied in this work the tips of injection lances are positioned in a distance of approx. 25 cm to the tuyère opening (fig. 5.7).

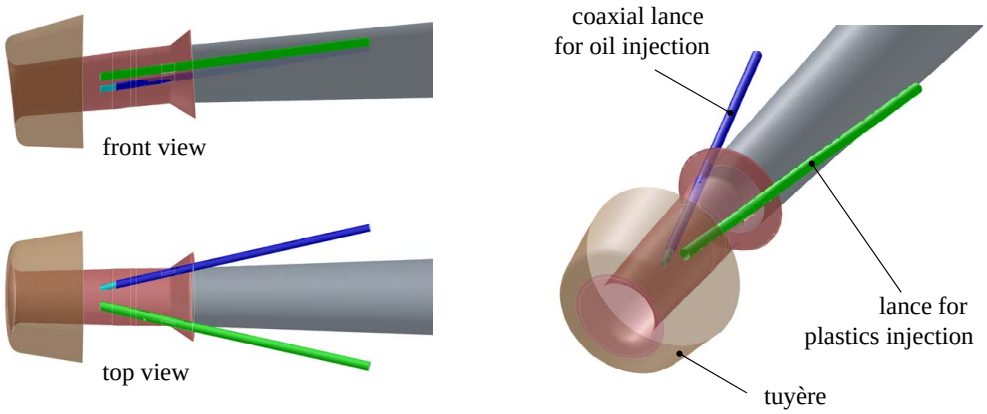

Figure 5.7: Configuration of injection lances studied in the baseline setup.

A narrow spray cone with an opening angle of approx. 15 ° results from oil injection, the tracks of oil droplets are shown in figure 5.8. Due to the small droplets originating from fierce conditions during oil atomization (mean droplet size approx. 100 µm, as discussed in chapter 3.10.1) as well as high relative velocities between oil droplets and hot blast and high blast temperatures, heat transfer from hot blast to the fuel oil spray is very intense. Consequently, fuel oil droplets are readily evaporated in the core of the raceway cavity, oil vapor is released to the gas phase in this zone.

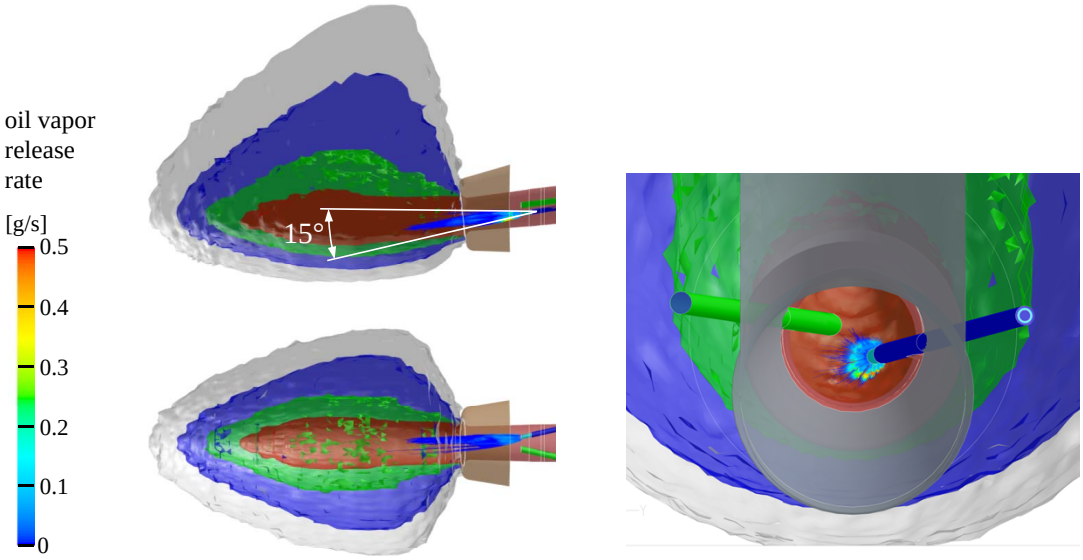

Figure 5.8: Injection of liquid hydrocarbons. Left: Droplet trajectories of injected alternative reducing agents, colored by mass release rates (Top: Side view, bottom: Top view); Right: View into raceway, in tuyère direction.

The left diagram in figure 5.9 shows the evolution of characteristic droplet properties during the droplet flight time. Water contained in the fuel oil is fully evaporated right inside the tuyère. After the water is released, droplet temperatures increase until the higher vapor pressure levels of hydrocarbons are reached, starting the thermolysis of liquid fuel and therefore release of the hydrocarbons to the gas phase (see fig. 5.9). Relative velocities between droplets and hot blast reach values in the range of 80 m/s in a distance of 1 to approx. 8 cm from the nozzle tip. Maximal traveling distances prior

to full evaporation of droplets with an initial droplet diameter of 140 µm are found to be 35 cm, corresponding to a comparatively short residence time in the range of 7 ms.

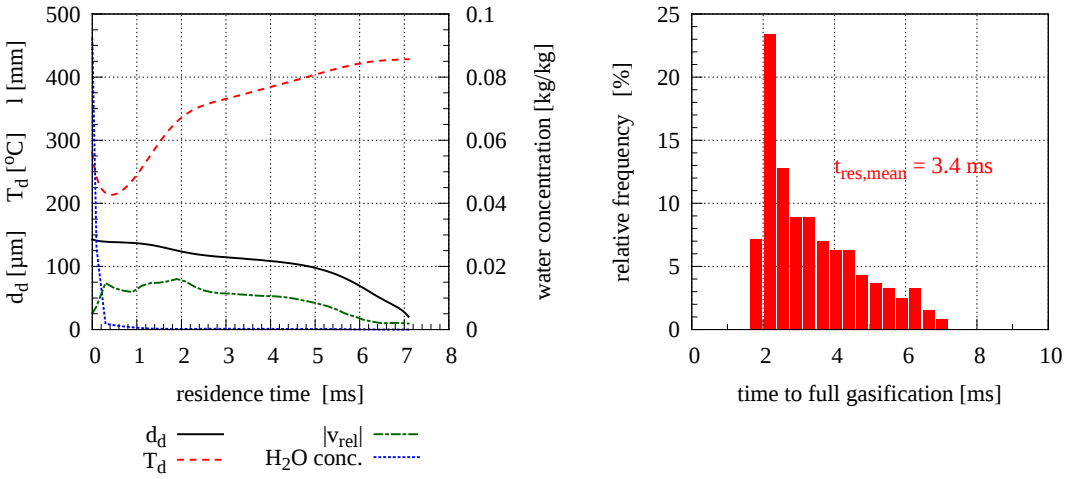

Figure 5.9: Left: Sliding mean values of oil droplet properties vs. residence time. Right: Residence time histogram of droplets with $d_{d,\,ini} = 140\,\mu m$.

5.2.3 Waste plastic particles

Waste plastics are injected via a lance that resembles a simple tube, using pressurized air as conveying gas (200 m^3_{STP}/h, resulting in velocities of approx. 27 m/s). Waste plastics are injected in size ranges much larger than the droplets originating from fuel oil injection, the mean particle size is 7 mm (see chapter 3.10.3), therefore longer residence times and a thermal behavior different to that of fuel oil are to be expected.

The tracks of injected waste plastic particles, colored by the rate of thermolysis, are shown in figure 5.10. According to the simulation results, plastic particles do not reach the inner wall of the tuyère, therefore the formation of depositions is not expected.

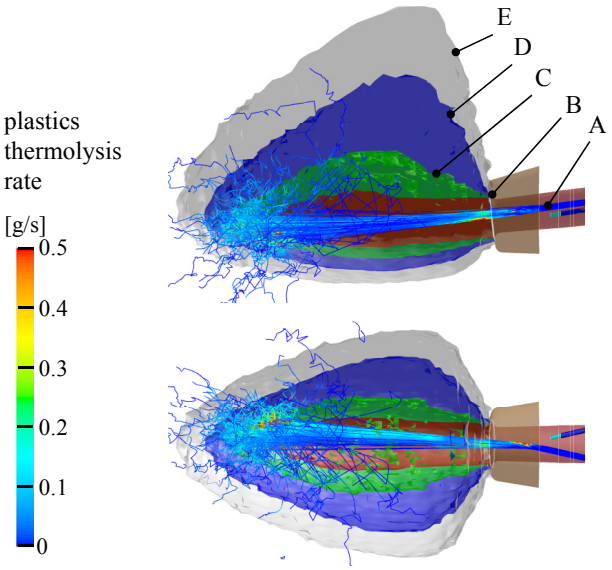

Figure 5.10: Trajectories of injected waste plastics, colored by mass release rates. Top: Side view, bottom: Top view.

It was found that the majority of injected plastic particles is not fully gasified during the short time of flight before the edge of the raceway cavity is reached. This is in accordance with experimental findings for plastics utilization in environments simulating blast furnace conditions [134]. Consequently, in addition to interaction of injected fuels with the gas phase in terms of heat, mass and momentum transfer, plastic particles are also modeled to exchange momentum with the solid coke bed. Plastic particles that have passed the raceway cavity and hit the coke lumps surrounding the raceway are modeled to be reflected considering the local porosity value (compare resulting particle tracks in fig. 5.10).

Figures 5.11 and 5.12 show the profiles of plastic particle parameters, plotted vs. residence time. As a large number of particle parcels are tracked in the simulation domain and turbulent stochastic tracking schemes are applied, in order to be able to show the trends, numerical data were post-processed by computation of sliding mean values in terms of particle residence time.

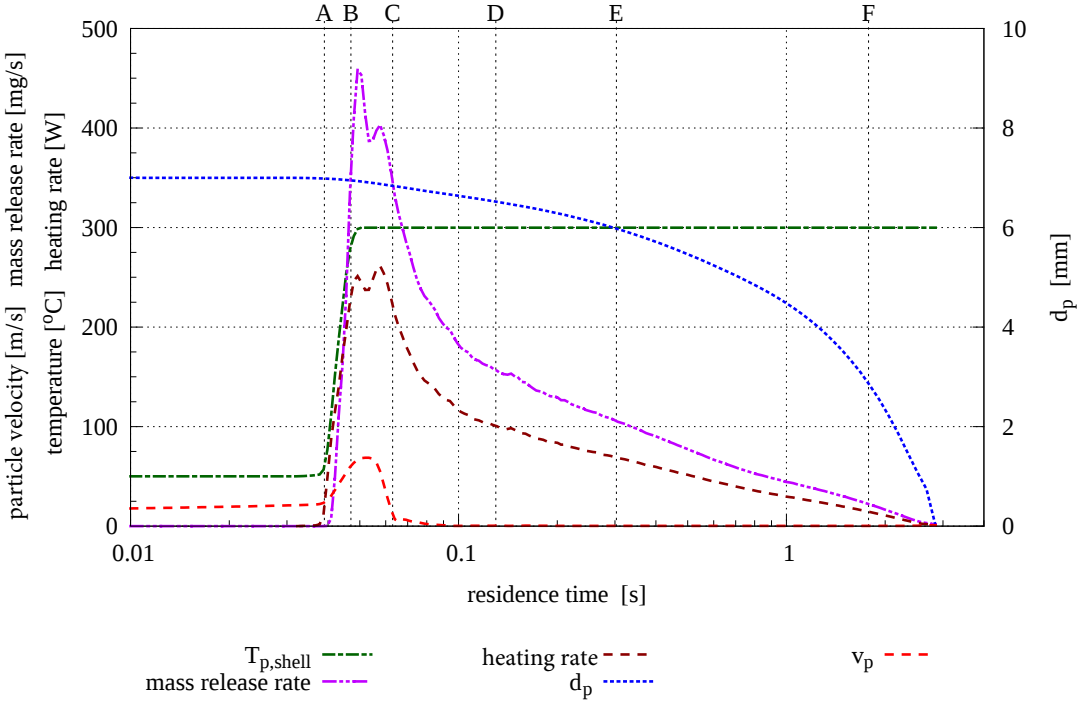

Figure 5.11: Plastic particle properties with $d_{p,ini} = 7\,\mathrm{mm}$. Upper-case letters refer to particle location (see fig. 5.10).

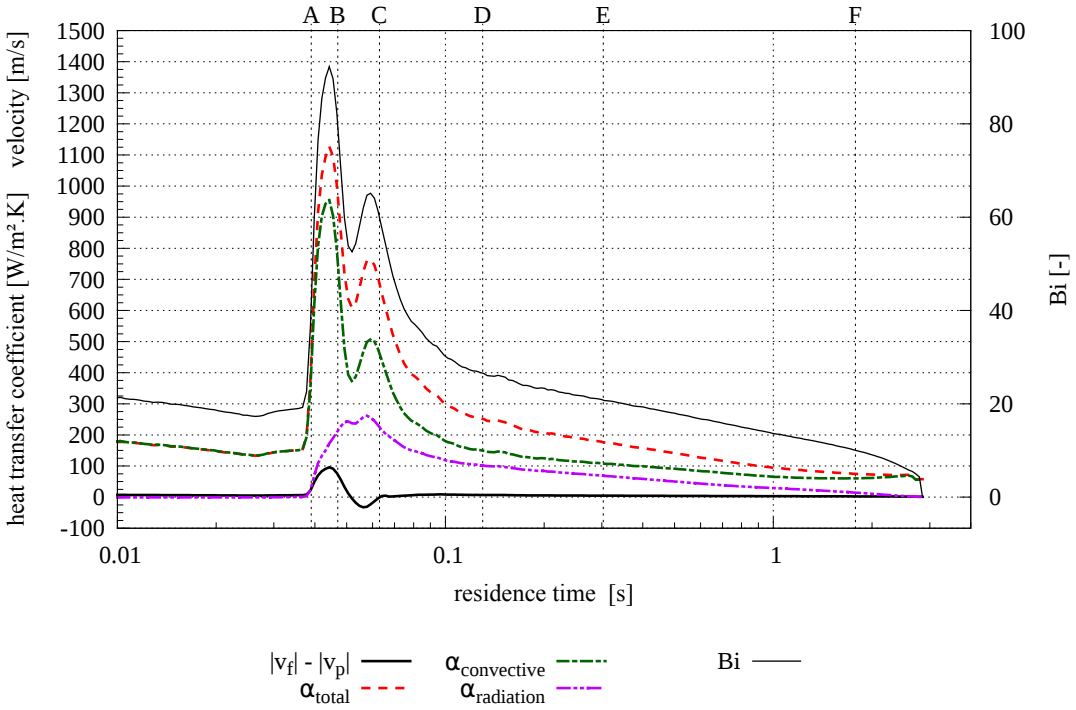

Figure 5.12: Characteristics of heat transfer to plastic particles with initial diameter $d_{p,ini} = 7\,\text{mm}$. Upper-case letters refer to particle location (see fig. 5.10).

The letters near the top border of these diagrams refer to certain locations in the blast furnace (also noted in fig. 5.10):

A *Tip of injection lance*
In the simulation, plastic particles are initialized at the inlet to the plastics lance, i.e. the junction of the flexible tube for plastics transport towards the furnace and the tube. In the lance the temperature difference between the conveying gas and particles is low. Particles are practically not heated during this phase. After 37 ms the particles reach the tip of the injection lance and enter the hot blast flow in the tuyère. Here conditions change drastically, relative velocities between particles (approx. 20 m/s) and by-passing hot blast (in the range of 200 m/s) are high. The particles are accelerated towards the center of the blast furnace. Due to intense heat transfer the temperature of the particle shell increases and the release of particle mass by onset of thermolysis reactions starts shortly after leaving the lance.

B *Tuyère opening*
At this point particles leave the tuyère and enter the raceway cavity. As shown in figure 5.10, the majority of the plastic particles follows the main direction of the hot blast flow, rapidly passing the raceway in the core zone of the cavity. The highest temperatures in a blast furnace are located in the boundary of the raceway cavity, where a part of the coke is oxidized by oxygen introduced with the hot blast. Therefore, in the core of the raceway rates of heat transfer to the plastic particles and consequently also thermolysis rates reach maximal values. The intense far-field heat transfer by radiation from the raceway boundary notably contributes to the overall heat transfer rate (fig. 5.12). In the core of the raceway particles also reach

their maximal velocities in the range of 70 m/s. As gases pass into the coke bed and the cross-sectional area for the gas flow increases, gas flow velocities decrease. In this phase the sign of relative velocity between fluid and particle changes, particles are decelerated towards the raceway boundary. This fact explains the characteristic bimodal shape of heat transfer coefficients and associated quantities showing two distinct maxima.

C *Coke-bed voidage 80 %*
Already after 63 ms of time of flight particles leave the very core of the raceway cavity, at this point on the timeline the average particle passes the iso-value of coke bed voidage of 80 %. Gas velocities entering the coke bed decrease, collision of plastic particles with coke lumps also contributes to further reduction of particle speed. Heat transfer rates continuously decrease, increasing the time to full gasification of the particles.

D *Coke-bed voidage 75 %*

E *Coke-bed voidage 70 %*

F *Coke-bed voidage 60 %*

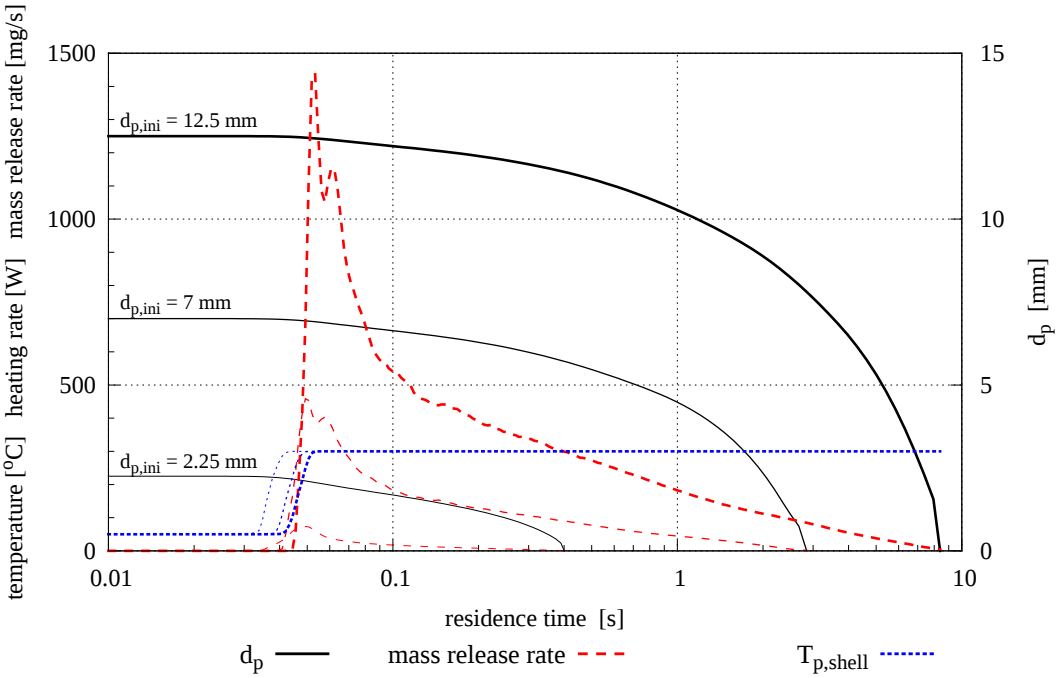

Figure 5.13: Plastic particle characteristics vs. residence time, comparison of particles with varying initial equivalence diameter. Thin lines: $d_{p,ini} = 2.25\,\mathrm{mm}$, medium lines: $d_{p,ini} = 7\,\mathrm{mm}$, bold lines: $d_{p,ini} = 12.5\,\mathrm{mm}$.

Contrary to the oil spray utilization, practically no plastic pyrolysis takes place in the tuyère close to the tip of the injection lance. According to the simulation results, 95 % of injected plastic mass is released in the raceway zone (i.e. porosity value > 0.5), as shown in the left diagram in figure 5.14. The majority of the plastic thermolysis is observed in a coke bed voidage range of 0.6 to 0.8. The remaining 5 % are released in the surroundings

of the raceway cavity, in the undisturbed coke bed. Highest volume specific gasification rates are found in the core of the raceway cavity, with a distinct decay towards the edge (fig. 5.14, right diagram). Residence times of plastic particles prior to full gasification are in the range of several seconds (see fig. 5.15).

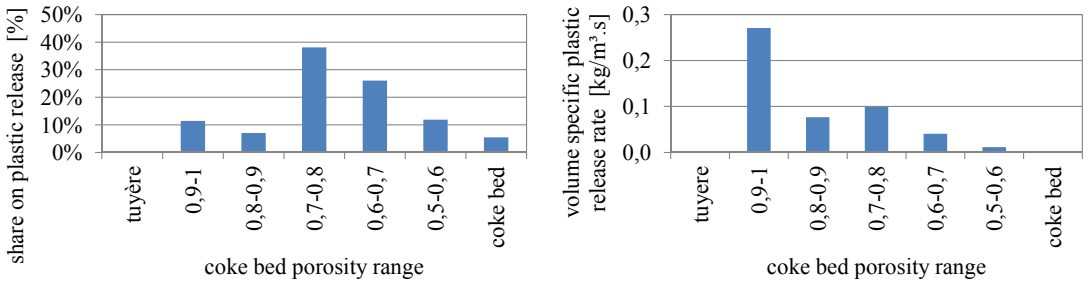

Figure 5.14: Location of plastics thermolysis with respect to porosity zones. Left: Integral gasification rate, right: Volume specific gasification.

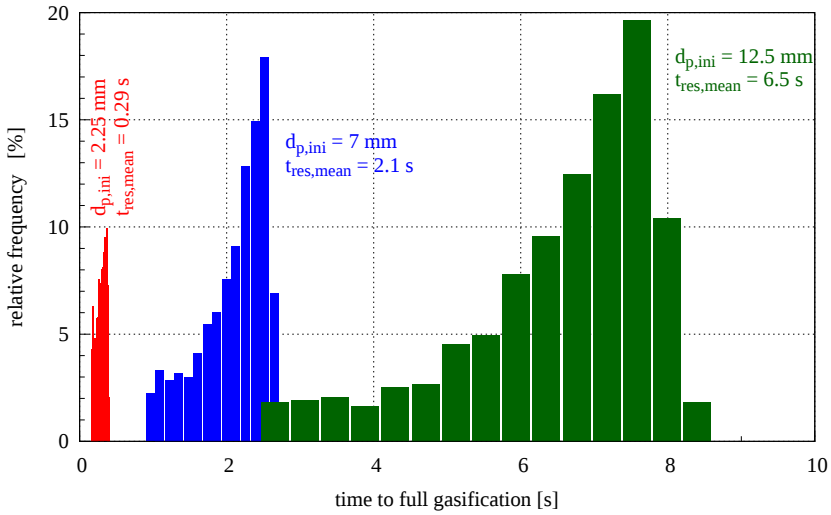

Figure 5.15: Plastic particle residence time histogram, comparison of particles with various initial equivalence diameters.

In flow direction, the inner diameter of the tuyère decreases. This geometry constraint, together with an increase of the gas flow rate due to evaporation of injected material, the release of combustion products and heat of reaction, accounts for an acceleration of the gas inside the tuyère and consequently to an increased specific heat flux through the inner surface of the tuyère (see figures 5.16 and 5.17). Towards the tip of the tuyère, the specific heat flux increases due to the exposure to the high-temperature zone of the raceway and far-field energy transfer by radiation. Right at the tuyère tip the thermal load is highest where hot blast leaves the tuyère and expands into the furnace hearth.

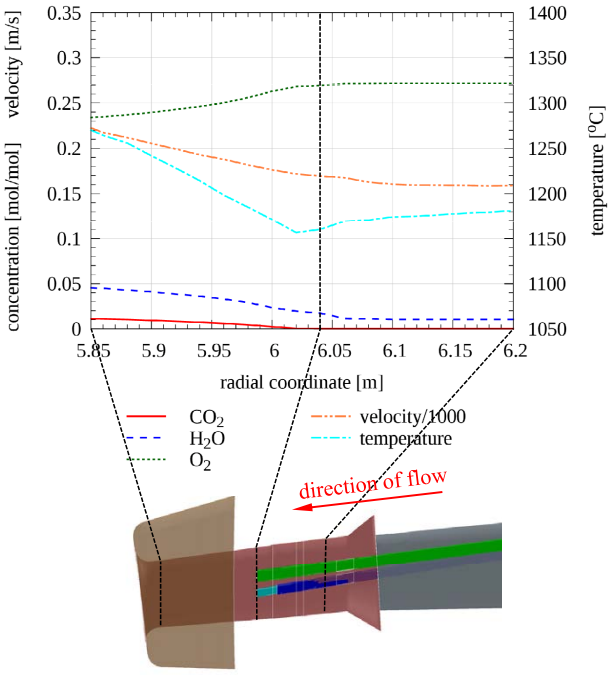

Figure 5.16: Profiles of cross-sectional average of flow and concentration variables in the tuyère.

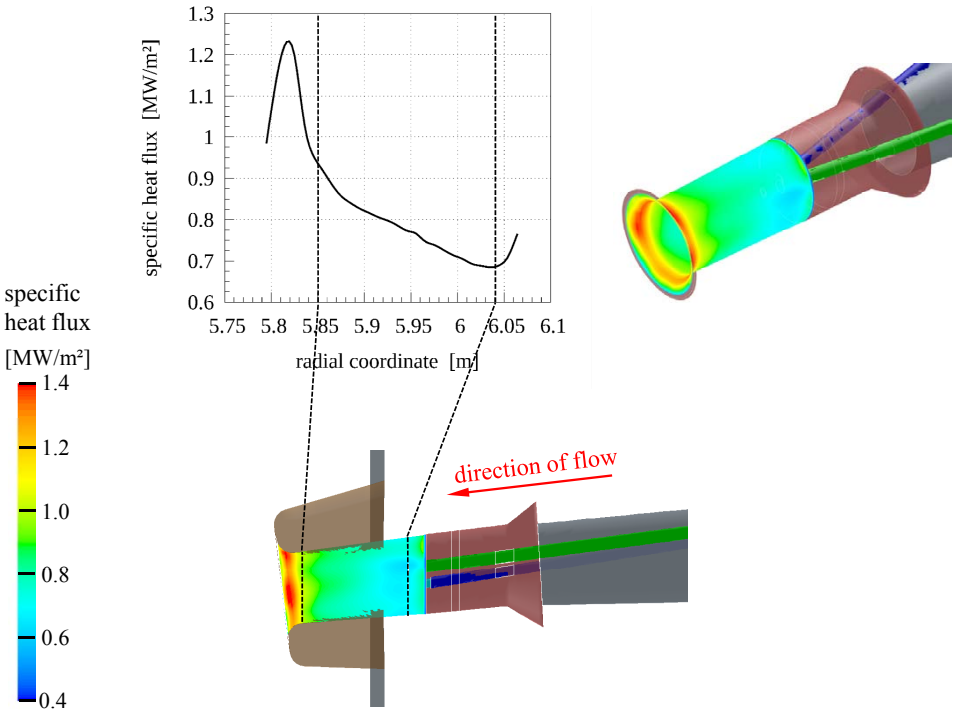

Figure 5.17: Heat flux through inner surface of tuyère.

5.2.4 Conditions in the raceway

In the modeling study the injected hot blast is oxygen-enriched air (27.4 $\%_{v/v}$ O_2), preheated to 1220 °C at a pressure of 4.2 bar_g. In front of the tuyère, due to high velocities and therefore high turbulent mixing rates of reactants, oxygen is rapidly consumed by oxidation of oil vapor and plastics decay products as well as solid coke (see oxygen concentration profile in fig. 5.18). Carbon dioxide and water vapor are released as combustion products, together with heat of reactions. Therefore, in this region temperatures increase and reach maximal values to be found in a blast furnace (fig. 5.22). The combustion reactions provide the heat required for the processes in the blast furnace, e.g. melting of ores and endothermic reactions. Towards the outer zones of the raceway cavity, the partial pressure of CO_2 increases. Due to the presence of CO_2 and H_2O at high temperatures, gasification of coke is facilitated (fig. 5.19). As these endothermic heterogeneous reactions proceed, CO and H_2 are released. In the furnace shaft these gas components are key agents for indirect reduction of iron oxides to produce hot metal.

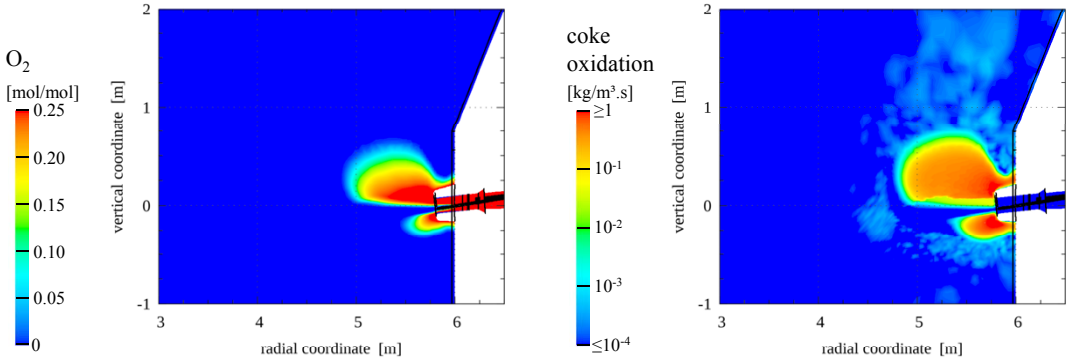

Figure 5.18: Left: Contours of O_2 mole fraction. Right: Specific coke oxidation rate.

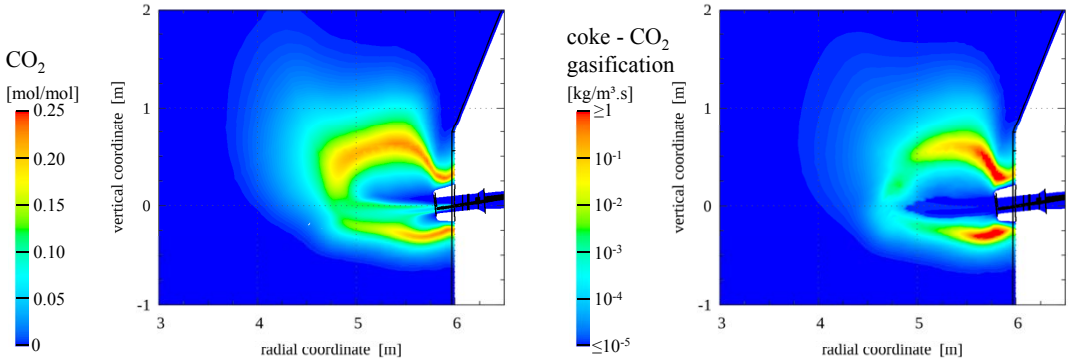

Figure 5.19: Left: Contours of CO_2 mole fraction. Right: Specific coke Bououard reaction rate.

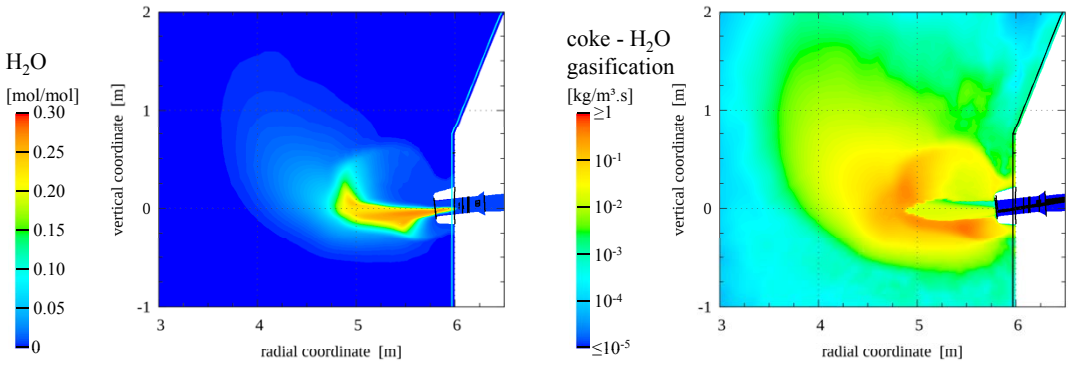

Figure 5.20: Left: Contours of H_2O mole fraction. Right: Specific coke steam gasification rate.

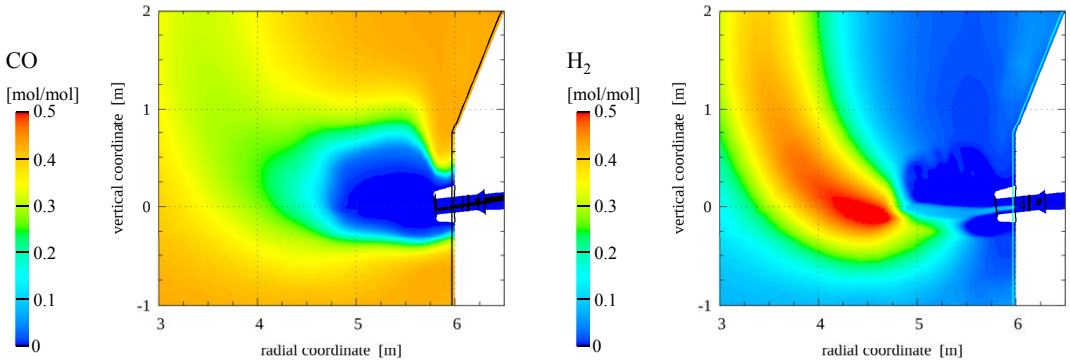

Figure 5.21: Left: Contours of CO mole fraction. Right: Contours of H_2 mole fraction.

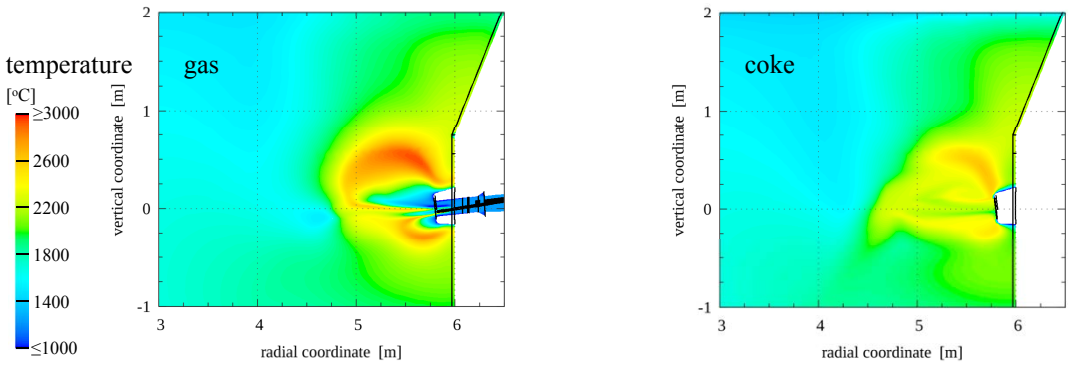

Figure 5.22: Contours of temperature fields.

Due to the energy demand for oil evaporation and plastics gasification, temperatures are decreased locally (fig. 5.22), and the direct injection of reducing agents tends to decrease adiabatic raceway temperatures [11]. Highest temperatures are found in the upper part of the raceway envelope, where lower impact rates of injected materials occur and therefore oxygen partial pressures are high.

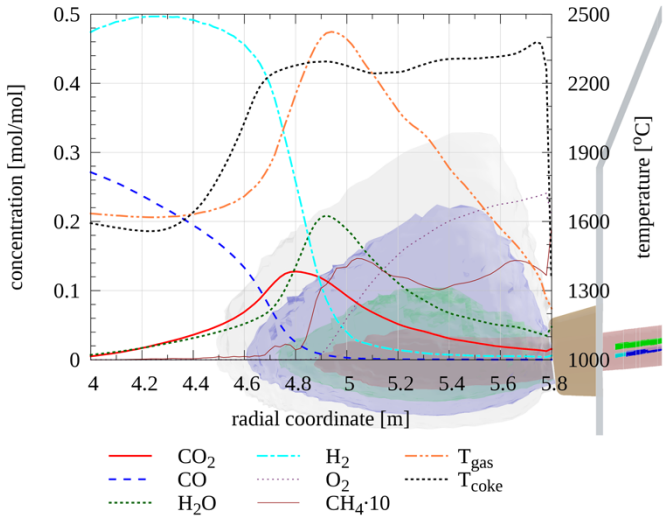

Figure 5.23: Radial gas phase composition and temperature profiles in the blast furnace on tuyère level.

Figure 5.23 shows the profiles of gas species concentrations, gas and coke temperatures on a radial coordinate on tuyère level, also highlighting tuyère opening and shape of the raceway cavity. The profile of the concentration of the combustion products CO_2 and H_2O shows distinct maxima near the edge of the raceway cavity. Further downstream, these species are reduced to CO and H_2 by heterogeneous reactions with coke. The temperature of the gas flow follows the trend of release of combustion products and endothermic gasification reactions. Due to its higher heat capacity and the characteristic circulating flow pattern of coke, the average temperature of coke particles shows less variability in the raceway cavity. In the surrounding bed the coke temperature decreases to levels in the range of 1600 °C. Computed average raceway conditions are summarized in table 5.4.

Table 5.4: Reference case simulation results: Average conditions in raceway cavity.

property		value	
temperature			
	gas	2309	°C
	coke	2194	°C
major gas component fractions			
	O_2	3.6	$\%_{v/v}$
	CO_2	10.2	$\%_{v/v}$
	H_2O	3.0	$\%_{v/v}$
	CO	16.1	$\%_{v/v}$
	H_2	9.0	$\%_{v/v}$

Spatial distribution of data fields in the raceway were also examined by integration of averages on surfaces of constant porosity as explained in figure 5.24. Void fraction decreases from the raceway center towards the undisturbed coke bed. Consequently, in the diagrams shown in figure 5.25, the right end of the abscissa represents the situation in the raceway cavity, while the left part shows conditions in the surrounding coke bed.

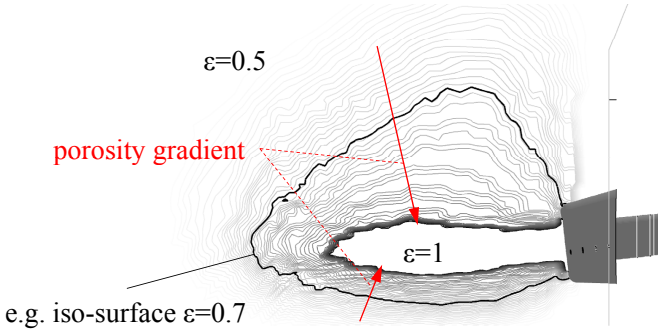

Figure 5.24: Iso-surfaces of coke bed porosity for data evaluation.

Volume-specific rates of coke consumption are shown in the left diagram in figure 5.25. Next to the tuyère opening, owing to high oxygen partial pressures, the major route of coke consumption takes place via oxidation. In porosity ranges down to approx. 0.8, steam is already available from injection with hot blast and also from fuel oil oxidation (see also fig. 5.20). In this zone, the rate of consumption via steam gasification is higher than CO_2 gasification, but still much lower than coke oxidation. Right in front of the tuyère, approx. 50 % of overall specific coke consumption takes place via oxidation, the share of steam and CO_2 gasification are in the range of 25 %. Further away, at decreasing coke bed porosities, coke is primarily consumed by the heterogeneous Boudouard reaction. In the raceway core more heat is released from exothermic combustion than consumed by gasification. The situation reverses in the raceway boundary (fig. 5.25, right diagram).

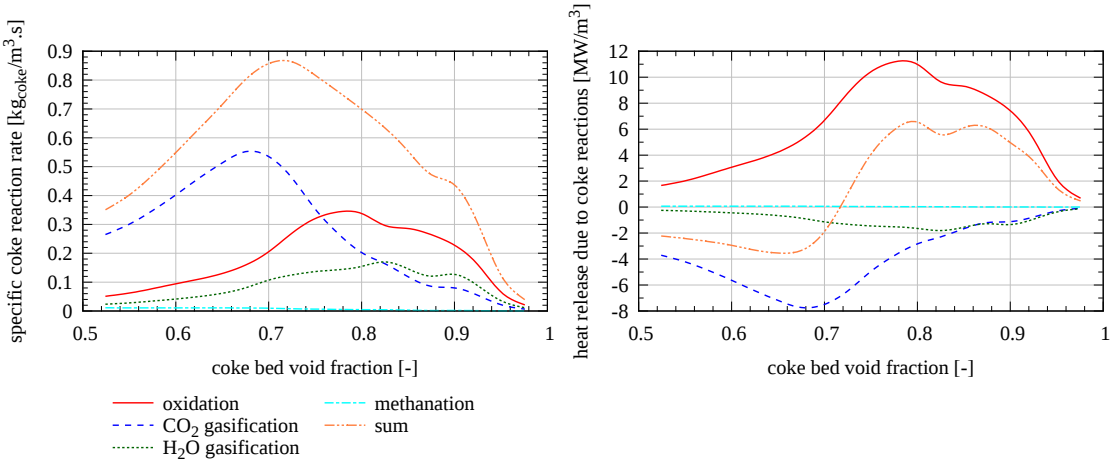

Figure 5.25: Coke conversion profiles in raceway cavity as a function of coke bed void fraction, area-weighted averages. Left: Specific rates of coke consumption due to heterogeneous reactions. Right: Release of heat due to coke reactions.

In figure 5.26 the profiles of release rates of major gas species are shown. Carbon monoxide is also released close to the tuyère opening due to coke steam gasification.

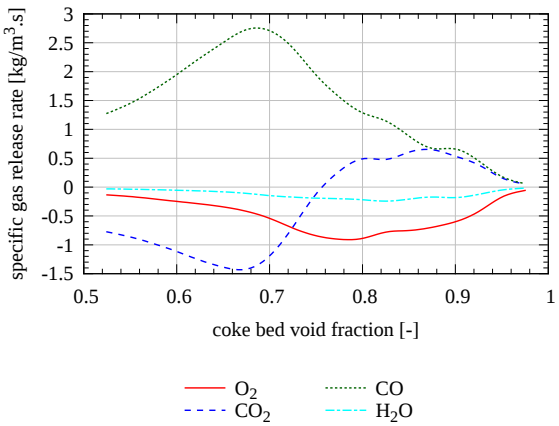

Figure 5.26: Specific release rates of gas components due to coke reactions.

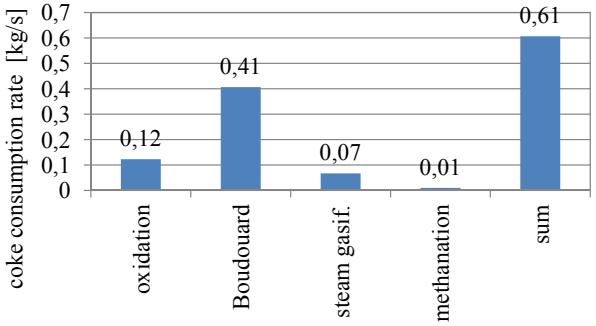

Figure 5.27: Integral coke consumption in raceway cavity ($\varepsilon > 0.5$) to coke reactions.

According to the modeling results, approx. 0.6 kg/s coke are consumed in the raceway zone, of which the major routes refer to oxidation (20 %) and CO_2 gasification (67 %), as shown in figure 5.27.

5.3 Variation of operating conditions

The developed model setup was applied to various conditions to study the variability of injectant utilization efficiency. A univariate analysis method was applied to investigate the effect of a certain parameter on the conditions in the raceway zone, while the other parameters were kept at the baseline operating level. A summary of cases investigated is given in table 5.5. The simulation runs were grouped according to the varied parameter, discussion of the simulation results in the next sections refers to the case identifiers given in the table.

Table 5.5: Matrix of investigated cases. Flow rates are given for the simulation domain (one tuyère segment).

hot blast conditions						alternative reducing agents: plastics lance		alternative reducing agents: oil/gas/coal lance						variation - groups								
tuyère diameter [mm]	air flow rate [$m^3_{STP,dry}/h$]	O_2 enrichment [m^3_{STP}/h]	total flow, dry [m^3_{STP}/h]	moisture [$g_{H_2O}/m^3_{STP,dry}$]	temperature [°C]	waste plastics rate [kg/h]	Δl lance [cm]	fuel oil rate [kg/h]	water content in oil [$\%_{w/w}$]	lance cooling gas type	natural gas rate [m^3_{STP}/h]	pulverized coal rate [kg/h]	Δl lance [cm]	tuyère diameter A	plastics/oil injection rates B	lance length C	hot blast H_2O load D	hot blast O_2 enrichment E	hot blast temperature F	oil lance cooling gas type G	oil water content H	reducing agent type I
140	9000	813	9813	5	1220	800	0	700	10	steam	0	0	0	base								
150	9000	813	9813	5	1220	800	0	700	10	steam	0	0	0	A1								
160	9000	813	9813	5	1220	800	0	700	10	steam	0	0	0	A2								
140	9000	813	9813	5	1220	0	0	1200	10	steam	0	0	0		B1							
140	9000	813	9813	5	1220	400	0	950	10	steam	0	0	0		B2							
140	9000	813	9813	5	1220	1150	0	500	10	steam	0	0	0		B3							
140	9000	813	9813	5	1220	800	13	700	10	steam	0	0	13			C1						
140	9000	813	9813	5	1220	800	18	700	10	steam	0	0	18			C2						
140	9000	813	9813	5	1220	800	23	700	10	steam	0	0	23			C3						
140	9000	813	9813	10	1220	800	0	700	10	steam	0	0	0				D1					
140	9000	813	9813	20	1220	800	0	700	10	steam	0	0	0				D2					
140	9000	813	9813	30	1220	800	0	700	10	steam	0	0	0				D3					
140	9094	719	9813	5	1220	800	0	700	10	steam	0	0	0					E1				
140	9047	766	9813	5	1220	800	0	700	10	steam	0	0	0					E2				
140	8953	859	9813	5	1220	800	0	700	10	steam	0	0	0					E3				
140	8906	906	9813	5	1220	800	0	700	10	steam	0	0	0					E4				
140	9000	813	9813	5	1100	800	0	700	10	steam	0	0	0						F1			
140	9000	813	9813	5	1150	800	0	700	10	steam	0	0	0						F2			
140	9000	813	9813	5	1200	800	0	700	10	steam	0	0	0						F3			
140	9000	813	9813	5	1250	800	0	700	10	steam	0	0	0						F4			
140	9000	813	9813	5	1300	800	0	700	10	steam	0	0	0						F5			
140	9000	813	9813	5	1220	800	0	700	10	air	0	0	0							G1		
140	9000	813	9813	5	1220	800	0	700	10	N_2	0	0	0							G2		
140	9000	813	9813	5	1220	800	0	665	5	steam	0	0	0								H1	
140	9000	813	9813	5	1220	800	0	735	15	steam	0	0	0								H2	
140	9000	813	9813	5	1220	800	0	0	–	–	1100	0	0									I1
140	9000	813	9813	5	1220	800	0	0	–	–	0	689	0									I2

5.3.1 A - Tuyère diameter

To obtain stable furnace operation and successful feed utilization, deep penetration of hot blast into the coke bed is desired. As discussed in section 3.9, the diameter of the tuyères directly correlates to the hot blast momentum and consequently to the size of the raceway cavity. The impact of the inner tuyère diameter on heterogeneous coke reactions and utilization of injected alternative reducing agents was studied by conducting simulation runs with varying tuyère geometry while the hot blast rate was kept constant at the value given in table 5.1.

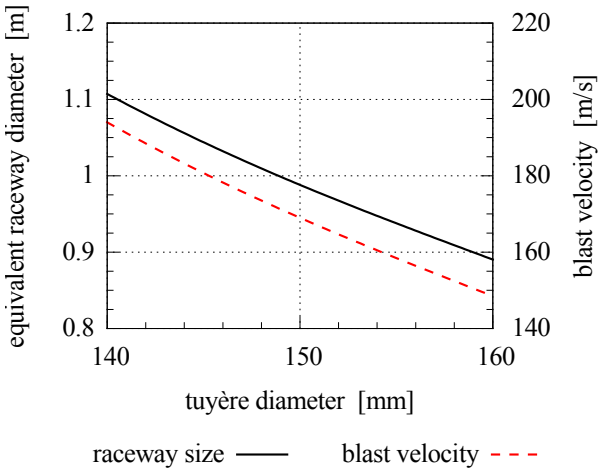

Figure 5.28: Variation of raceway size with respect to tuyère diameter. Hot blast rate per tuyère: 9900 $m^3_{STP}/h \cdot tuyère$ at 1220 °C, pressure level 4.2 bar_g, oxygen enrichment to 27.4 $\%_{v/v}$ O_2.

Table 5.6: Tuyère diameter variation: Impact on raceway volume.

case ID	tuyère diameter [mm]	raceway volume [m^3]
base	140	0.71
A1	150	0.51
A2	160	0.37

As summarized in table 5.6, in the range of parameter variation the volume of the raceway cavity decreases by a factor of approx. 1.9. Accordingly, the residence time of hot blast and therefore the time available for conversion of injected feed decreases, resulting in a shift of gas-phase species concentration profiles. Oxygen is consumed in regions closer to the tuyère tip, the CO_2-peak is shifted (see fig. 5.29).

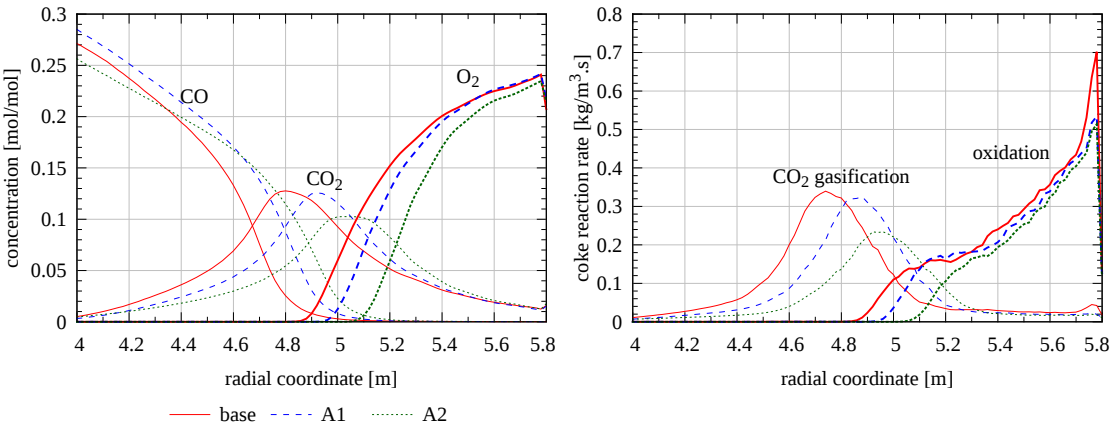

Figure 5.29: Tuyère diameter variation. Radial profile on tuyère level, left: O_2, CO_2 and CO concentration. Right: Coke consumption by oxidation and Boudouard reaction.

The situation for the conversion of steam to H_2 via heterogeneous reactions is quite similar, as shown in figure 5.30. The volume of the raceway cavity is larger if a smaller tuyère is installed, as expected a deeper penetration of hot blast into the coke bed is achieved, see e.g. coke utilization by heterogeneous water-gas shift reaction in the right diagram of figure 5.30.

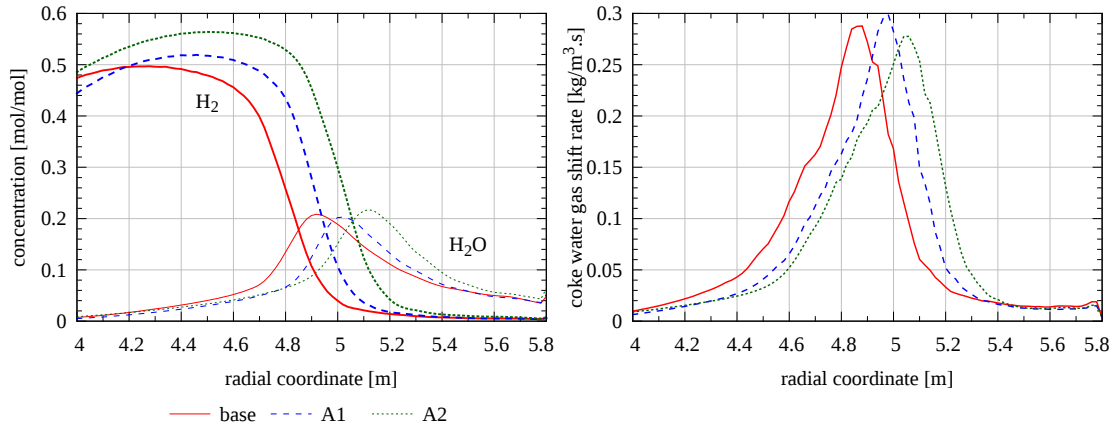

Figure 5.30: Tuyère diameter variation. Radial profile on tuyère level, left: H_2 and H_2O concentration, right: coke consumption by heterogeneous water-gas shift reaction.

Due to the decrease in blast velocity with increasing tuyère diameter, the total heat transfer rate through the tuyère wall and therefore tuyère cooling rates decline (fig. 5.31).

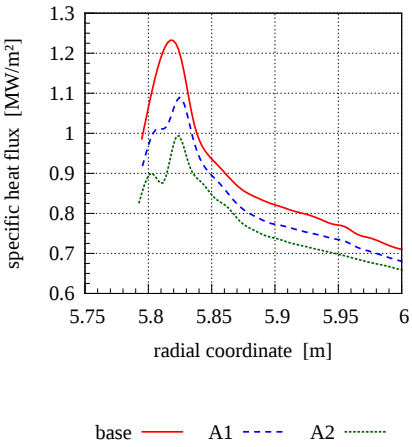

Figure 5.31: Profile of average specific heat flux through tuyère wall vs. radial coordinate.

5.3.2 B - Injection rates

In general, the input materials used for blast furnace operation strongly influence the cost of hot metal production [114]. In this context, higher flexibility in terms of fuel supply can contribute to economically improved blast furnace operation. The impact of various rates of material injection starting from fuel oil alone and increasing the share of waste plastics is discussed in the following (injection rates investigated are summarized in table 5.7).

Table 5.7: Alternative reductant injection rates under consideration.

case ID	fuel oil rate $^{kg}/_{h \cdot tuyère}$	plastics rate $^{kg}/_{h \cdot tuyère}$
B1	1200	0
B2	950	400
base	700	800
B3	500	1150

Due to the early release of injected liquid hydrocarbons to the gas phase by evaporation of the droplet spray, onset of oxidation reactions takes place in close proximity to the tuyère opening, as shown in the contour plot of oxygen concentration in figure 5.18. As the supply of plastics is increased at the expense of the oil rate, the rate of release of combustible thermolysis products is decreased and shifted towards the boundary of the raceway cavity. As a consequence, more oxygen is available in regions comprising a more closely packed coke bed, resulting in higher coke oxidation rates (fig. 5.32). The utilization of plastics is localized deeper in the coke bed as compared to injected fuel oil. Owing to the already decreased oxygen partial pressures in these regions, plastics are oxidized to a lower extent while gasification is favored and therefore increased amounts of char residues are formed in the region of the raceway boundary. These residues are reported to be highly reactive [47] and therefore are not expected to accumulate in the coke bed.

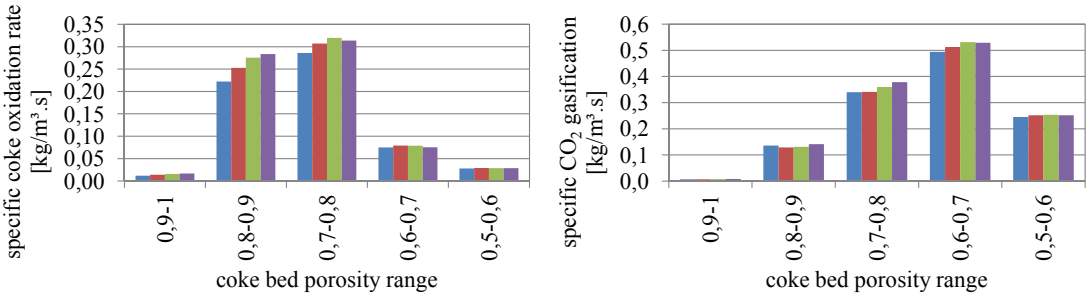

Figure 5.32: Volume specific rates of coke utilization. Left: coke oxidation, right: CO_2 gasification. Legend: B1, B2, base, B3.

Observing the operating conditions of case B1 (oil only operation) it can be seen that the overall rate of hydrogen feed into the blast furnace is higher as compared to the cases with plastics injection. This results in higher coke utilization by reactions with species involving hydrogen as a compound, e.g. steam gasification (see fig. 5.33).

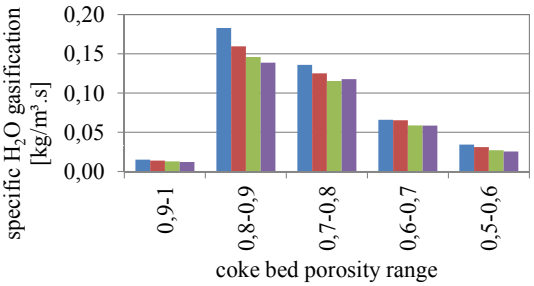

Figure 5.33: Volume specific rates of heterogeneous water-gas-shift reaction. Legend: B1, B2, base, B3.

Right in front of the tuyère opening velocities of injected hot blast are very high. This strongly contributes to the rates of convective heat transfer between gas and solid coke particles in the blast furnace, as shown in figure 5.34. In this zone the temperature of coke particles passing through the raceway boundary is higher than the local hot blast temperature as these particles are preheated from passing the oxidation zone. Furthermore, heat for gasification of injected oil and plastics is consumed from the gas. Consequently, in the raceway core heat is transferred from solid coke to the gas. Towards the edge of the raceway the situation reverses: Due to the onset of endothermic coke gasification reactions coke temperature decreases below the gas temperature. At higher temperatures also heterogeneous heat transfer by radiation gains significance (fig. 5.34, right diagram).

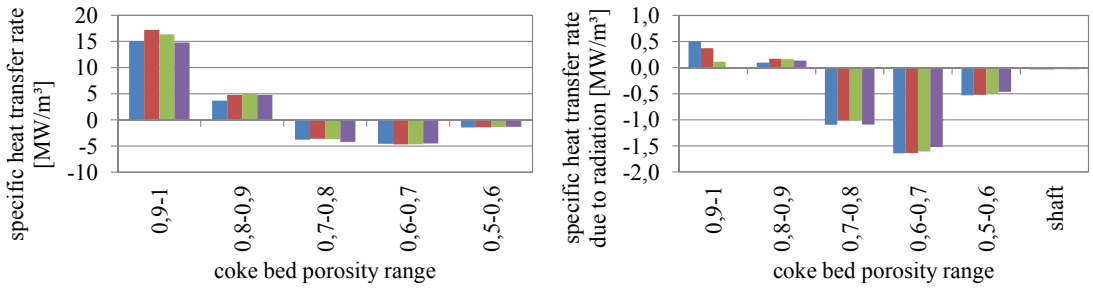

Figure 5.34: Heterogeneous heat transfer from solid coke to gas. Left: Overall heat transfer rate. Right: Heat transfer by radiation. Legend: B1, B2, base, B3.

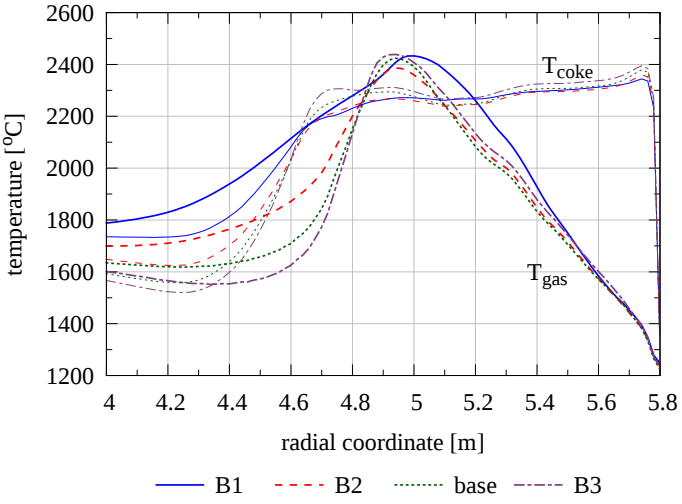

Figure 5.35: Radial profiles of gas and coke temperature.

The temperature profiles given in figure 5.35 reveal that with increasing plastics injection rates, the coke temperature slightly increases throughout the raceway cavity (more oxygen available for coke combustion) while at the raceway boundary the temperature of the gas flow considerably decreases due to locally increased plastics gasification rates.

Table 5.8: Mean residence time of injected reductants and average gas species concentrations in raceway cavity.

case ID	fuel oil $d_{d,ini} = 140\,\mu m$ [ms]	plastics $d_{p,ini} = 7\,mm$ [s]	O_2 [$\%_{v/v}$]	H_2O [$\%_{v/v}$]	H_2 [$\%_{v/v}$]
B1	4.6	-	3.18	3.69	11.02
B2	4.0	1.96	3.45	3.39	10.12
base	3.4	2.09	3.59	3.01	9.00
B3	2.8	2.08	3.57	2.90	9.54

The rates of reducing agent injection directly influence the gas-phase concentration field. The higher fraction of hydrogen contained in fuel oil as compared to plastics is responsible for the release of larger amounts of H_2O that is converted to H_2 by water gas shift reaction (see table 5.8).

Due to the earlier release of fuel oil thermolysis products to the gas phase oxidation and therefore release of heat of reaction starts earlier (right in the tuyère), consequently tuyère cooling rates are slightly higher at increased oil injection rates.

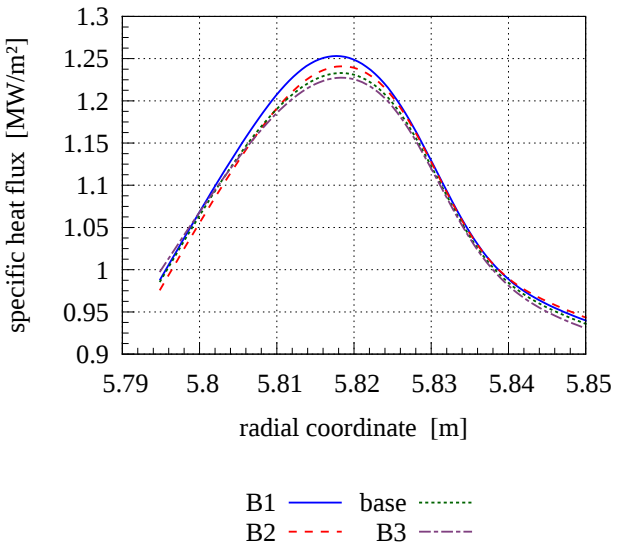

Figure 5.36: Injection rates variation: Specific total heat flux through tuyère inner wall.

5.3.3 C - Position of injection lance tips

The location of release of alternative reducing agents to the gas phase is determined by the position of lance tips. In the baseline setup, the lances for injection do not overlap each other (see fig. 5.7). Three additional geometry setups with deeper inserted lances as outlined in figure 5.37 were studied.

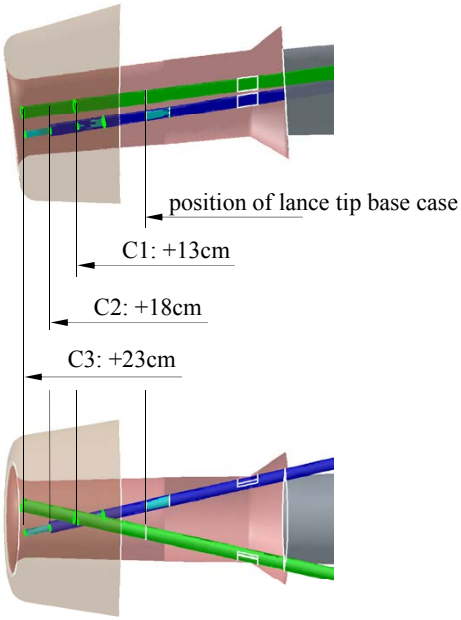

Figure 5.37: Side and top view of tuyère and lances, highlighting the range of lance tip position variation.

As the lance tips are shifted towards the opening of the tuyère, the release of fuel oil vapor to the gas phase is transferred into the raceway cavity (fig. 5.38). In the base case lance tips feature the largest distance to the tuyère opening. In this setup more than 99 % of the fuel oil is evaporated within the tuyère. In the variation cases, oil vapor release is already moved towards the coke bed but still evaporation is completed in the region with void fractions of 80 – 100 %.

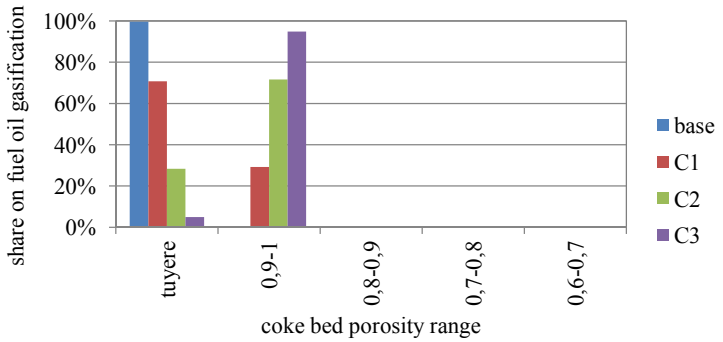

Figure 5.38: Location of fuel oil release, lance length variation.

Energy necessary to evaporate the fuel droplets is modeled to be provided by radiation (far-field energy transfer) as well as by convective and conductive heat transfer from the gas phase (locally). Therefore, at the point of fuel oil release a cooling impact is exerted on the gas flow until the combustion of volatiles overbalances this effect and temperature levels increase in the surroundings of the oil spray.

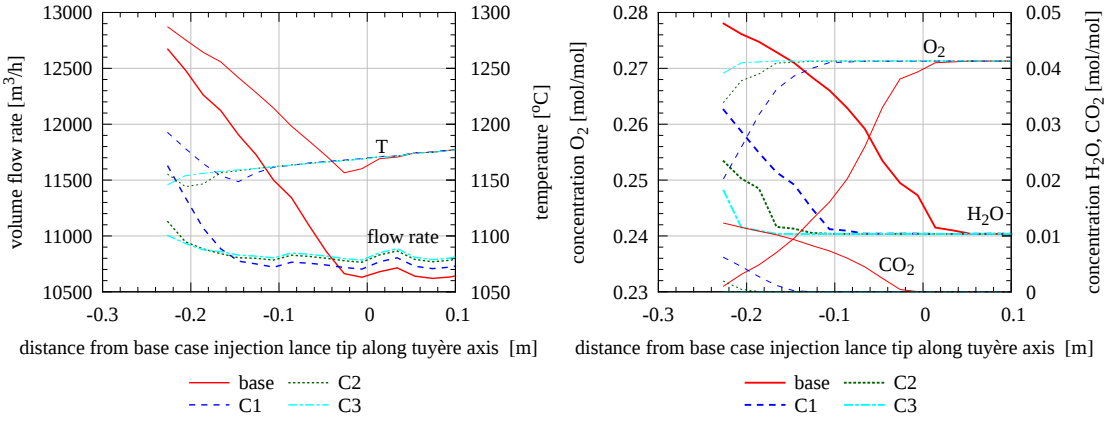

Figure 5.39: Variation of hot blast properties along the tuyère axis relative to base case lance tip position, cross-sectional averages.

Due to the variation of the proximity of the lance tip to the tuyère wall a variation of heat impact on the tuyère wall that stems from injected fuel oil was found. The cooling effect from oil pyrolysis on the one hand and heat release from oil vapor combustion on the other hand influence the heat transferred via the inner surface of the tuyère and therefore the cooling duty, as summarized in table 5.9.

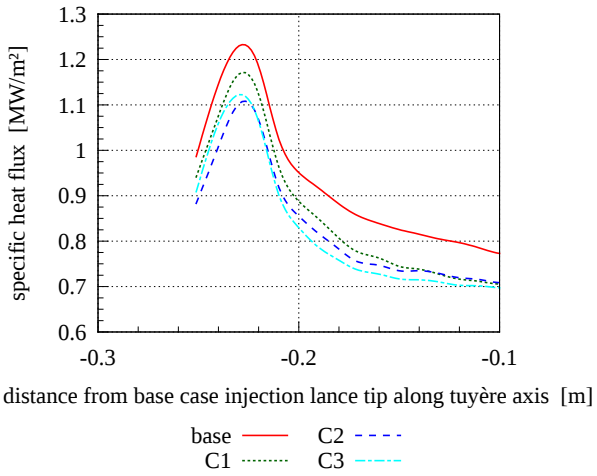

Figure 5.40: Lance length variation: Specific total heat flux through tuyère inner wall.

A plot of the gas phase temperature on a cutting plane between the oil and plastic injection lances is shown in figure 5.41. Volume-averaged gas temperature in the raceway reduces from 2310 °C at the base case to 2280 °C at case C3.

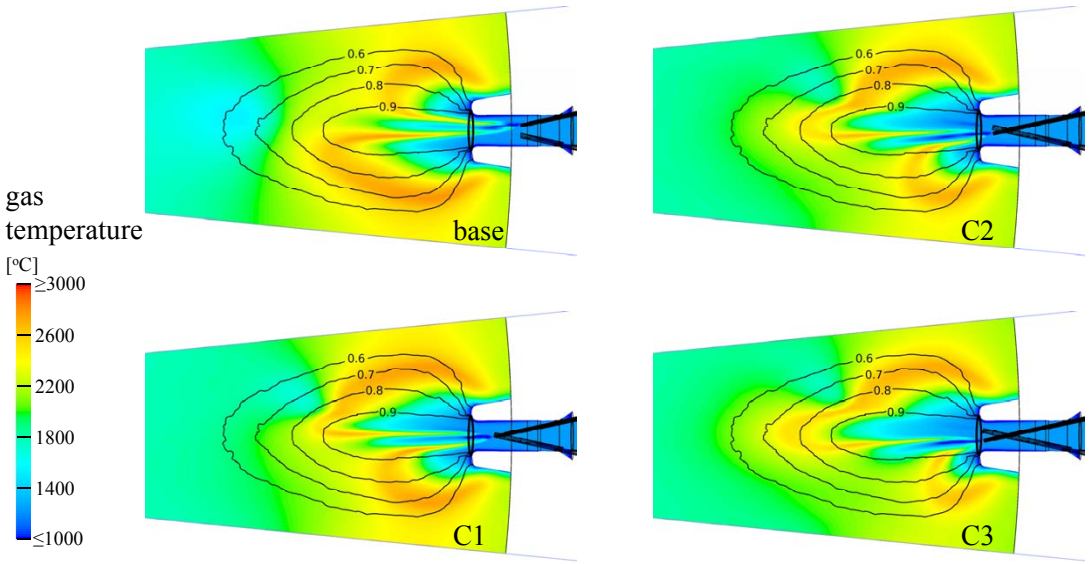

Figure 5.41: Gas temperature profiles, horizontal cut between injection lances.

In base case the distance from injection lance tips to the tuyère opening is largest, therefore oxygen is consumed earlier by released thermolysis products. Consequently, the release of H_2O and CO_2 takes place further upstream in the hot blast flow. This results in a slightly shifted CO_2 peak. In the cases with further retracted lances higher temperatures of gas phase as well as coke are calculated. This effect is restricted to the core of the raceway, the influence of injection lance position diminishes towards the undisturbed coke bed (fig. 5.42).

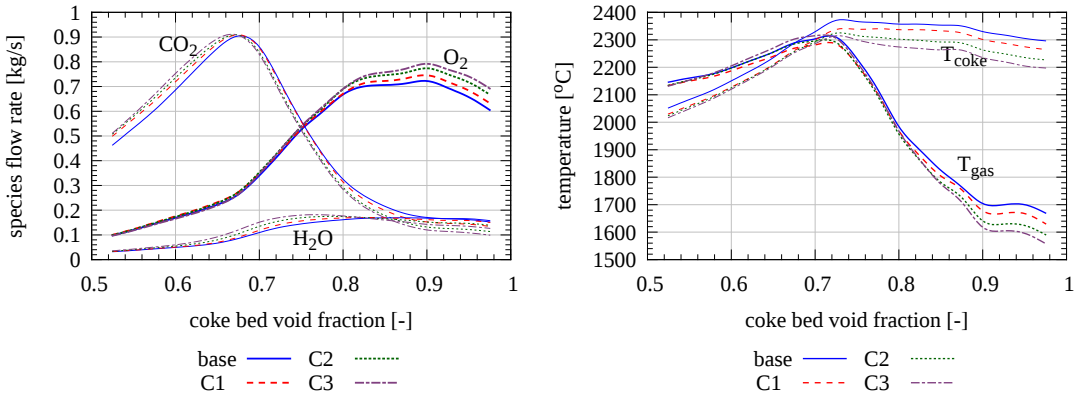

Figure 5.42: Left: Gas species flow rates. Right: Coke and gas temperature, plotted vs. coke bed void fraction.

The location of the release of the oil spray also has an impact on the mean droplet residence times as the gas temperatures in the surroundings of the spray vary. In case C3 the evaporating spray reaches very hot regions located near the boundary of the raceway cavity, therefore computed mean residence times are reduced significantly (table 5.9).

Table 5.9: Variation of lance tip position: Heat transfer via inner wall of tuyère, oil droplet and plastics residence times.

case ID	heat transfer rate [kW]	time to oil evaporation [ms]	time to plastics gasification [s]
base	116	3.40	2.09
C1	109	2.62	1.85
C2	107	3.00	1.89
C3	106	3.90	1.83

Due to the comparatively large initial diameter of injected waste plastics and therefore generally longer residence times of plastic particles, lance length only poses a minor impact on the position of plastics pyrolysis as compared to the sensitivity of fuel oil release (fig. 5.43). However, due to variation in gas-particle temperature differences in the cavity plastics residence times vary in the range of 8 % .

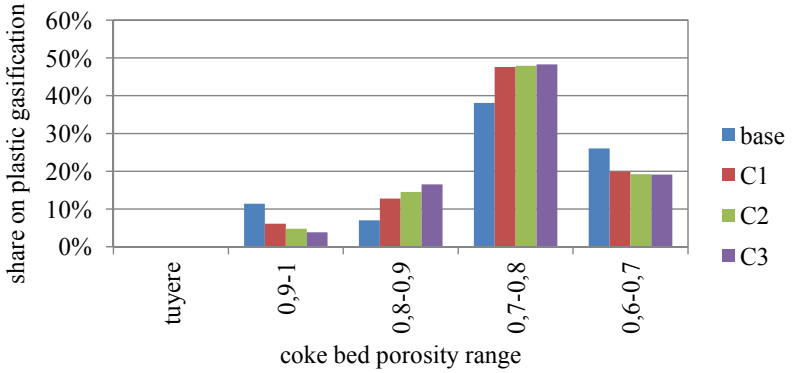

Figure 5.43: Location of plastics thermolysis, lance length variation.

5.3.4 Blast conditions

Effective utilization of alternative reducing agents requires changes in the blast furnace operation to compensate for the impact on changes in the raceway zone if injection is performed at high rates. For waste plastic rates of up to $10\,^{kg}/_{t_{hm}}$ it is not necessary to change anything [42]. At higher rates measures such as

- increasing the oxygen rates supplied with hot blast,
- higher blast temperatures and
- oxygen enrichment rates

are practicable measures to adjust the adiabatic raceway flame temperature.

These parameters were varied systematically from base case conditions (injection of $700\,^{kg}/_{h\cdot tuyère}$ fuel oil and $800\,^{kg}/_{h\cdot tuyère}$ waste plastics), the results are summarized in the following chapters.

5.3.4.1 D - Blast moisture

When operating a blast furnace, the H_2O load on hot blast varies according to weather conditions, being altered by temperature and relative humidity in the ambient air. Representative values for hot blast humidity for blast furnace *A* are given by $5\,^{g_{H_2O}}/_{m^3_{STP}}$ in the winter season, while increasing to approx. $30\,^{g_{H_2O}}/_{m^3_{STP}}$ during summer time. Base case operating conditions were evaluated at minimum H_2O load, so variation was done increasing the water fed by hot blast injection as summarized in table 5.10.

In this table also average raceway properties are listed. As more water is introduced with the hot blast, higher partial pressures of H_2O are available for the steam gasification of coke. The higher rates of this endothermic reaction is responsible for lower raceway temperatures and also for higher hydrogen concentrations. H_2 in the bosh gas is an effective agent for iron oxide reduction in the shaft zone. Due to its higher reactivity with iron oxide as compared to CO, raceway temperatures can be decreased [11].

If raceway temperatures are too high to obtain stable furnace operation, the injection of steam offers an efficient measure for controlling purposes. In contrast, lowering the blast moisture can also help to compensate the cooling effect of alternative reducing agent injection.

Table 5.10: Sensitivity of average raceway conditions on hot blast H_2O load.

case ID	H_2O load $[^{g_{H_2O}}/_{m^3_{STP}}]$	H_2O $[\%_{v/v}]$	H_2 $[\%_{v/v}]$	CO $[\%_{v/v}]$	CO_2 $[\%_{v/v}]$	T_{gas} [°C]	T_{coke} [°C]
base	5	3.01	9.00	16.1	10.2	2309	2194
D1	10	3.31	9.45	15.8	10.4	2293	2174
D2	20	3.73	9.90	15.4	10.7	2278	2156
D3	30	4.18	10.1	15.1	10.8	2265	2174

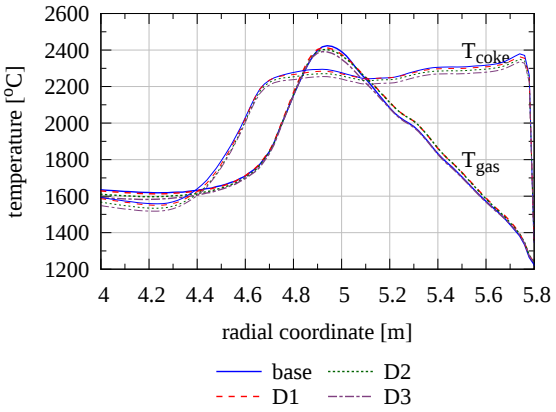

Figure 5.44: Radial profiles of coke and gas temperature on tuyère level at varying steam load on hot blast.

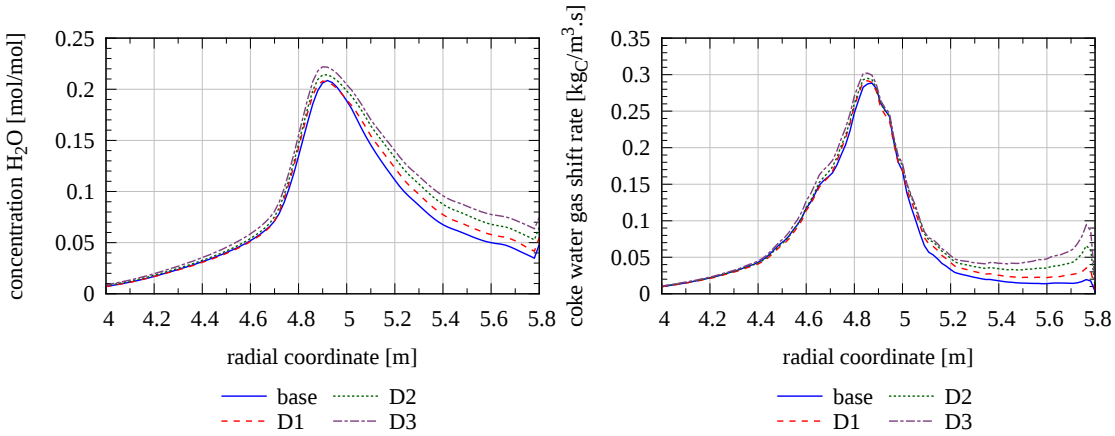

Figure 5.45: Radial profiles of H_2O concentration and steam gasification rate on tuyère level at varying steam load on hot blast.

5.3.4.2 E - Hot blast oxygen enrichment

At blast furnace *A* the rate of oxygen feed to the raceway is controlled by the grade of hot blast oxygen enrichment. In general, additional oxygen can also be provided by injection via the reducing agent lances. As more oxygen is available, a tendency towards higher combustion efficiency of injected materials in the raceway cavity is to be expected.

In the simulation setup boundary conditions are set such that the overall blast volume flow is the same as for the base case, i.e. the volume flow variation due to changing O_2 enrichment is compensated by adjusting the hot air rate accordingly. Consequently, the feed rate of N_2 is decreased, also decreasing the flow of inert gases through the coke bed and burden layers (see table 5.11).

Table 5.11: Boundary conditions for hot blast oxygen enrichment variation, flow rates are given per tuyère.

case ID	hot blast O_2 concentration [$\%_{v/v}$]	air flow rate (dry) [m^3_{STP}/h·tuyère]	O_2 enrichment [m^3_{STP}/h·tuyère]
E1	26.6	9094	719
E2	27.0	9047	766
base	27.4	9000	813
E3	27.8	8953	859
E4	28.2	8906	906

A summary of the computed average conditions in the raceway is given in table 5.12. Carbon monoxide and hydrogen volume fractions increase due to the lower rates of N_2 introduced with hot blast. Higher partial pressures of these reducing gases contribute to better reduction of iron oxides in the center of the furnace shaft.

Table 5.12: Sensitivity of average raceway conditions on hot blast O_2 concentration.

case ID	residence time fuel oil [ms]	residence time plastics [s]	H_2 [$\%_{v/v}$]	CO [$\%_{v/v}$]	T_{gas} [°C]	T_{coke} [°C]
E1	3.5	2.13	9.20	15.4	2279	2163
E2	3.5	2.08	9.60	15.7	2295	2179
base	3.4	2.09	9.00	16.1	2309	2194
E3	3.4	1.99	10.15	16.1	2320	2204
E4	3.3	1.97	10.23	16.5	2331	2215

Mean evaporation times of injected fuel oil tend to decrease as the oxygen enrichment rate is increased (from e.g. 3.5 ms at E1 to 3.3 ms at case E4 for droplets with an initial diameter of 140 µm). Heat transfer to the oil droplets increases slightly as more oxygen is available for combustion, but still an oxygen-depleted zone in the core of the oil spray exists (see fig. 5.46).

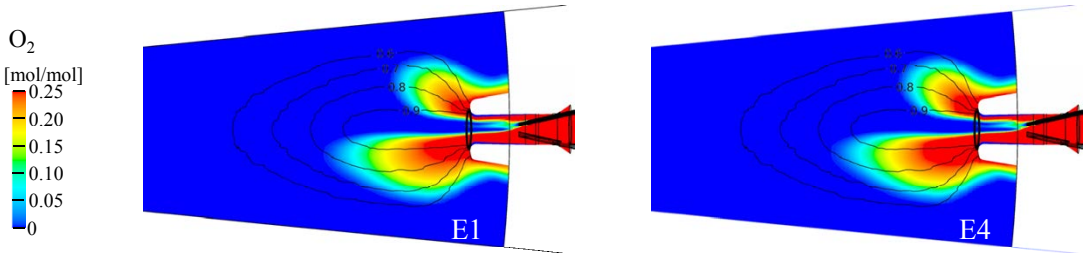

Figure 5.46: Contours of oxygen concentration, cut through oil injection lance.

Due to the increased partial pressure of oxygen available, the concentration of carbon dioxide in the boundary of the raceway increases (figure 5.47).

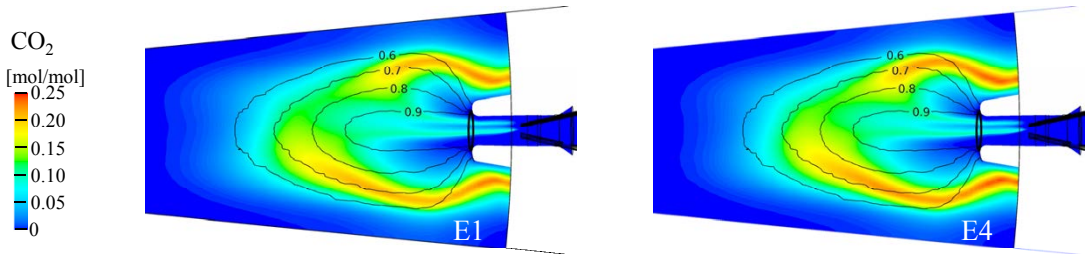

Figure 5.47: Contours of carbon dioxide concentration, cut through oil injection lance.

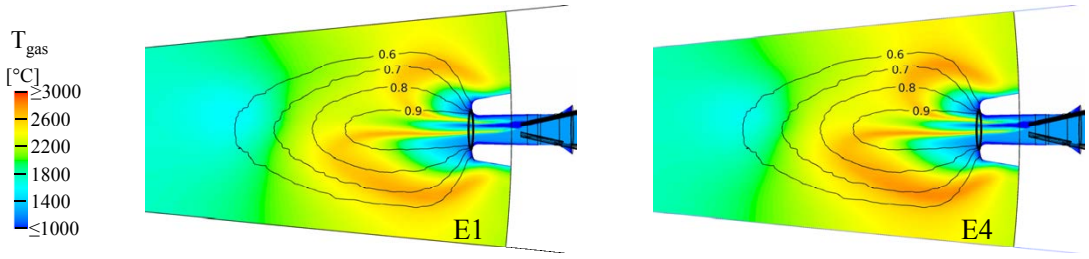

Figure 5.48: Contours of gas temperature, cut through oil injection lance.

Even though the blast rate is kept constant in the parameter variation, gas flow rate in the raceway increases as more coke is consumed by oxidation and CO_2 gasification. At blast furnace conditions a net increase of gas molecular flow rate is achieved. The average magnitude of the gas velocity vector in the raceway increases from 7.08 to 7.33 m/s, also contributing to an increase of the coke conversion rates.

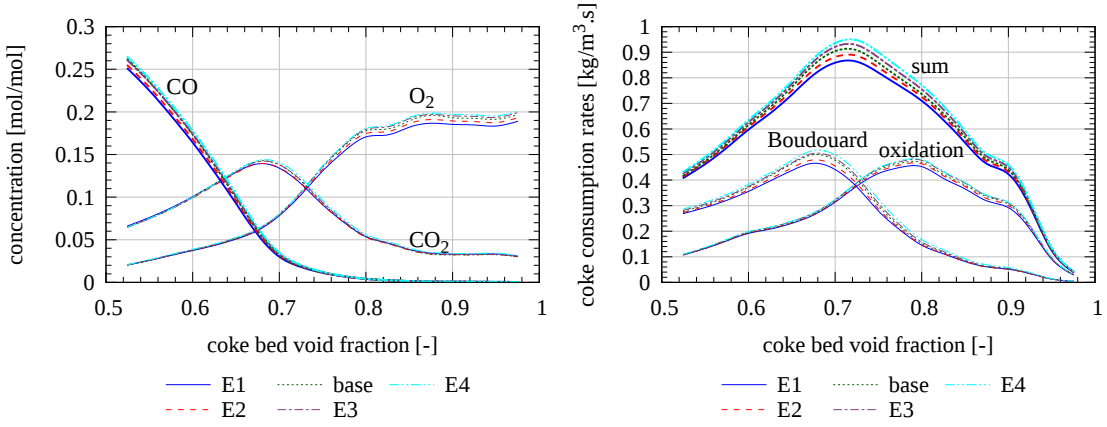

Figure 5.49: Concentration profiles and major coke consumption reaction rates in the raceway cavity, plotted vs. coke bed void fraction.

5.3.4.3 F - Blast temperature

In the simulation cases with varying hot blast temperature the total blast mass flow rate was kept at the baseline operation level, therefore with higher blast temperatures also an increase in gas velocity in the tuyère is achieved. This results in a slight increase of the raceway size that was not accounted for in the current simulation runs. Five cases were implemented with hot blast temperatures ranging from 1100 to 1300 °C (see table 5.13).

Table 5.13: Variation of hot blast temperature: Heat transfer via inner wall of tuyère, oil droplet and plastics residence times.

case ID	hot blast temperature [°C]	time to oil evaporation [ms]	time to plastics gasification [s]	tuyère cooling rate [kW]
F1	1100	3.68	1.58	102
F2	1150	3.67	1.57	109
F3	1200	3.56	1.54	114
F4	1250	3.41	1.52	120
F5	1300	3.23	1.46	127

As the preheating temperature of hot blast is increased from case F1 to F5, mean times for gasification of injected materials decrease in the range of 13 % for fuel oil and 8 % for plastics. As plastic particles are generally larger in initial sizes they are less affected by the conditions in the center of the raceway cavity, where blast preheating has the highest impact on local temperatures (see figure 5.50; for reasons of clarity in the diagrams only cases F1, F3 and F5 are shown – cases F2 and F4 follow the trends consistently).

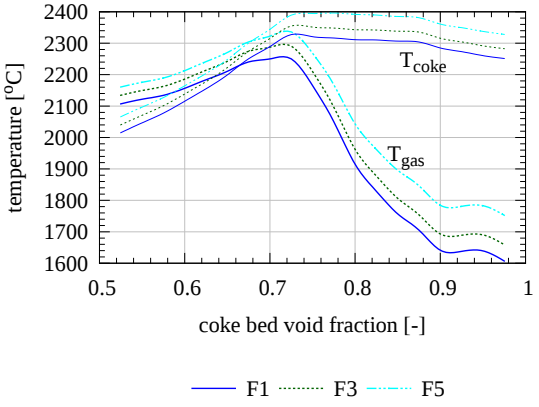

Figure 5.50: Gas and coke temperature profiles in the raceway cavity, plotted vs. coke bed void fraction.

Contrary to oil evaporation, the majority of plastics thermolysis takes place in regions with coke bed voidage less than 0.8 (fig. 5.51).

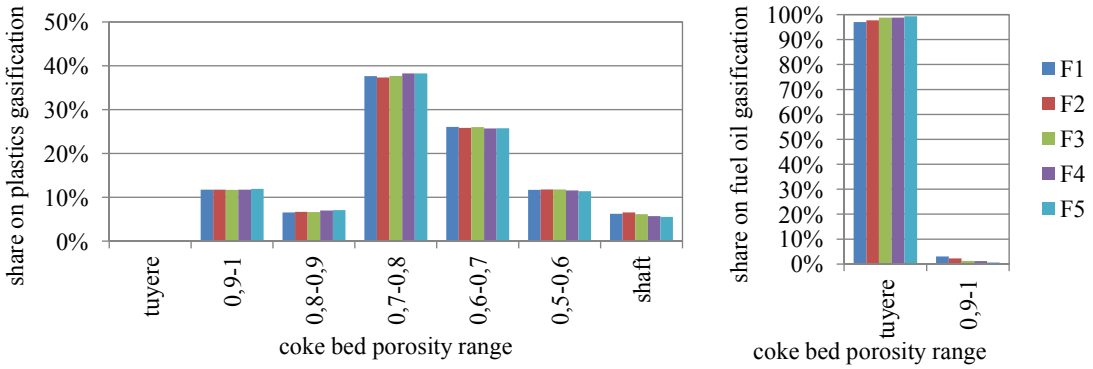

Figure 5.51: Location of plastics thermolysis.

Examining the computed temperature field, it was found that the blast preheating temperature has a strong impact on the heat capacity needed to temper the tuyère (figure 5.52).

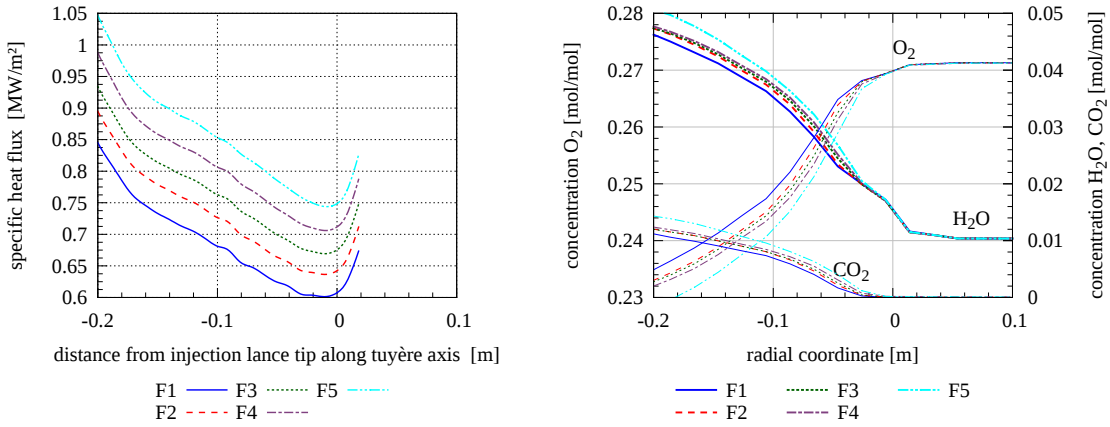

Figure 5.52: Conditions in the tuyère at varying hot blast temperature. Left: Heat flux through tuyère inner wall, right: Cross-sectional averages of gas species concentrations.

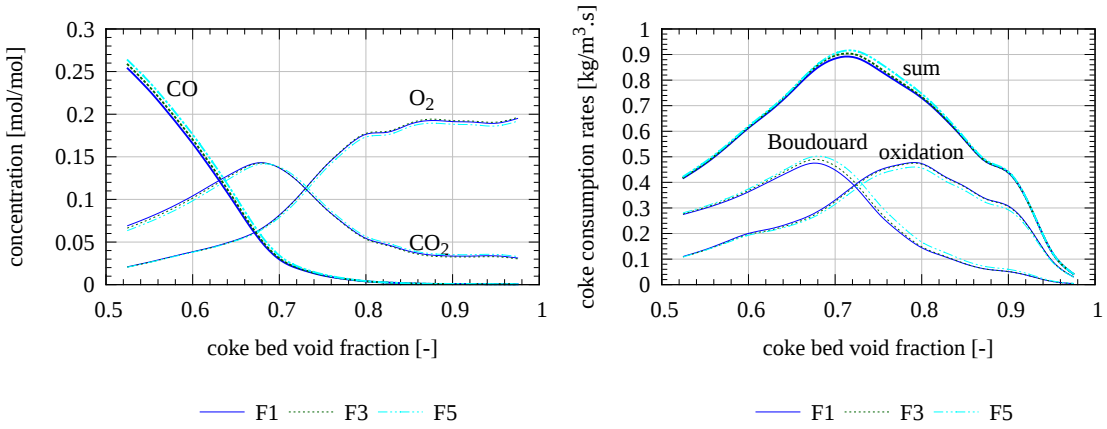

Figure 5.53: Concentration profiles and major coke consumption reaction rates in the raceway cavity, plotted vs. coke bed void fraction.

In the raceway, the coke oxidation reaction is located in the mass transfer controlled regime, the oxidation rate is largely determined by diffusion of O_2 towards the coke surface. Furthermore, the coke oxidation rates also decrease as more oxygen is consumed by more concentrated combustion of alternative reducing agents in a close proximity to the tuyère opening. As compared to the oxidation, the Boudouard reaction is more sensitive to the local temperature level and therefore kinetics still play a more important role (temperature dependence of effective reaction rates, discussed in chapter 3.6.2). At elevated blast temperatures, in the raceway cavity the rate of CO_2 gasification is higher due to higher temperatures delivering heat for reaction and providing for the necessary activation energy. Steam gasification reaction also proceeds at higher rates, contributing to the release of H_2 and CO.

Higher raceway temperatures offer the opportunity to increase injection rates and decrease coke rates. On an economic point of view, increasing the blast temperature was reported to be cheaper than oxygen enrichment to increase the adiabatic raceway flame temperature [11].

Table 5.14: Sensitivity of average raceway conditions to hot blast temperature.

case ID	T_{gas} [°C]	T_{coke} [°C]	O_2 [$\%_{v/v}$]	H_2O [$\%_{v/v}$]	CO_2 [$\%_{v/v}$]	CO [$\%_{v/v}$]
F1	2268	2217	3.57	3.18	10.5	15.5
F2	2284	2233	3.57	3.13	10.4	15.7
F3	2295	2245	3.59	3.11	10.3	15.9
F4	2309	2265	3.47	3.08	10.2	16.1
F5	2328	2285	3.43	3.02	10.1	16.4

5.3.5 G - Liquid hydrocarbon injection – cooling gas type

In blast furnace *A*, the lance for injection of fuel oil is realized as a coaxial lance. Preheated heavy fuel oil is fed in the core pipe, while the annular gap is flushed with a gas for cooling purposes. The baseline operation uses steam as cooling gas. Water vapor has a high heat capacity and in the furnace also the amount of hydrogen available for reduction reactions is increased.

In a sensitivity study the type of cooling gas was changed to air (case G1) and nitrogen (case G2) to evaluate the impact on the reducing agent utilization. The usage of pressurized air as cooling gas results in an additional oxygen feed of $9.3\,\mathrm{m^3_{STP}/h}$ (compare: O_2 introduced with hot blast $2703\,\mathrm{m^3_{STP}/h}$, of which $230\,\mathrm{m^3_{STP}/h}$ from oxygen enrichment; flow rates given per tuyère). Generally, in the core of the fuel oil injection spray oxygen is depleted rather fast. As the cooling gas type is changed to air, in this region some additional oxygen is available for combustion of fuel oil vapor. This results in slightly increased heat transfer rates to the oil droplets and consequently reduces the time for oil evaporation by approx. 5 % (see table 5.15). Furthermore, the computed average raceway temperature increases by approx. 10 °C.

Table 5.15: Variation of cooling gas type for fuel oil injection lance: Heat transfer via inner wall of tuyère, mean oil droplet and plastics residence times.

case ID	cooling gas type	mean time to oil evaporation [ms]	mean time to plastics gasification [s]	tuyère cooling rate [kW]	average raceway temperature [°C]
base	steam	3.39	2.09	116	2309
G1	air	3.22	2.05	117	2318
G2	N_2	3.39	2.05	117	2309

As compared to the impact on fuel oil release, the calculated mean time for plastics pyrolysis does not vary significantly. The change in conditions is restricted to regions in the spray cone of fuel oil and therefore does not impact the plastics tracks to a large extent, as these pass the tuyère zone rather fast. Also, the computed tuyère cooling rate is not much influenced by the type of cooling gas.

Figure 5.54 shows the radial profiles of steam concentration and its reaction with metallurgical coke. In the base case, the additional introduction of steam as applied for lance cooling purposes increases the H_2O partial pressure and contributes to increased steam gasification rates in the boundary of the raceway zone.

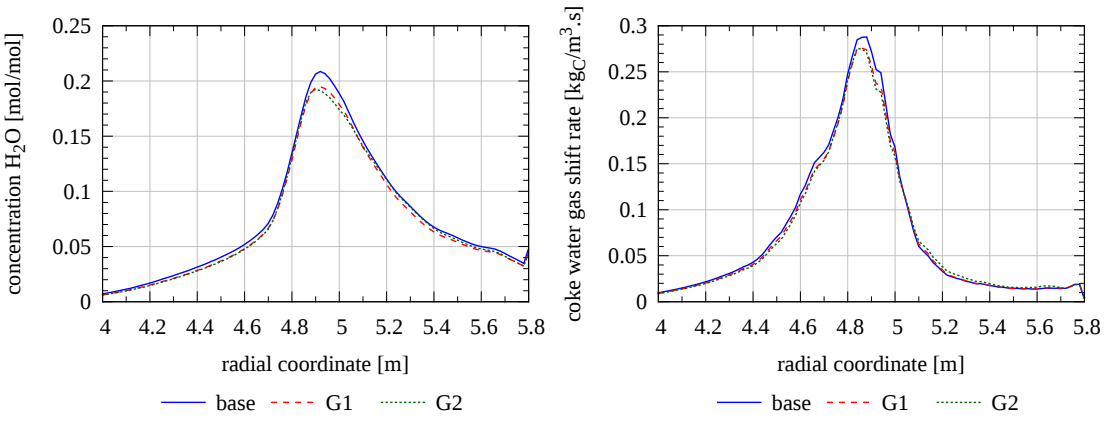

Figure 5.54: Steam concentration profiles and rate of water-gas shift reaction in the raceway cavity, plotted vs. coke bed void fraction.

5.3.6 H - Water content in liquid hydrocarbon mixture

Heavy fuel oil for injection into blast furnace *A* contains considerable amounts of water. At conditions studied in the base case a mass fraction of 10 % of water in hydrocarbons is applied. Parameter variation concerning this water feed was done as stated in table 5.16, in the simulation runs the rates of injected fuel oil was set consistently for all cases.

Table 5.16: Variation of water content in liquid hydrocarbons for injection. Cooling gas type for fuel oil injection lance: Heat transfer via inner wall of tuyère, mean oil droplet and plastics residence times.

case ID	water content in fuel oil mixture [$\%_{w/w}$]	mean time to oil evaporation [ms]	mean time to plastics gasification [s]	tuyère cooling rate [kW]
H1	5	3.08	2.00	117
base	10	3.39	2.09	116
H2	15	3.59	1.91	113

Table 5.17: Variation of water content in liquid hydrocarbons for injection. Cooling gas type for fuel oil injection lance: Average conditions in raceway cavity.

case ID	T_{gas} [°C]	T_{coke} [°C]	H_2O conc. [mol/mol]	CO conc. [mol/mol]
H1	2313	2197	2.91	16.3
base	2309	2194	3.01	16.1
H2	2304	2189	3.19	15.7

The driving force for release of mixture components from the spray droplets to the gas phase is calculated by evaluating the difference of partial pressure of the component on the droplet surface to the surrounding gas phase, incorporating the dependence of vaporization pressure on the droplet temperature (see also chapter 3.10.1). The evaporation pressure of water is higher than that of the hydrocarbon mixture, therefore water is released earlier to the gas phase. As a consequence, an increased H_2O partial pressure in droplet surroundings results in lower evaporation rates, and eventually in higher residence times. The cooling effect of additional water injection results in a decrease of the average raceway temperature in the order of 10 °C (table 5.17).

A decrease of water fraction in liquid hydrocarbons to 5 % results in a reduction of the mean droplet residence time by approx. 9 %. There is less need for water vaporization therefore reducing the latent heat of evaporation. Furthermore, the decrease of droplet temperature due to cooling limit temperature effects is less distinct (see figure 5.55). Mean plastic particle gasification times are affected to a minor extent (in the range of ±5 % with respect to the base case).

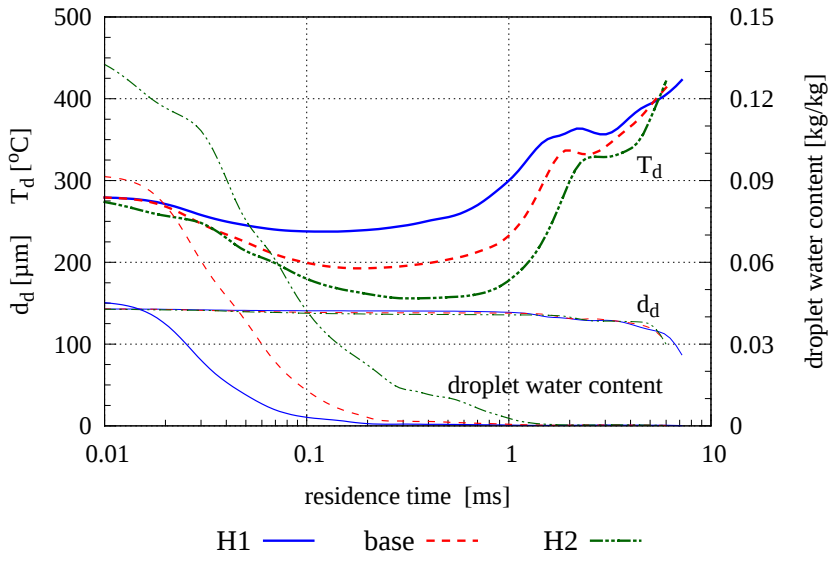

Figure 5.55: Sliding mean values of oil droplet temperature and diameter vs. residence time, initial droplet diameter $d_{d,\,ini} = 140\,\mu m$.

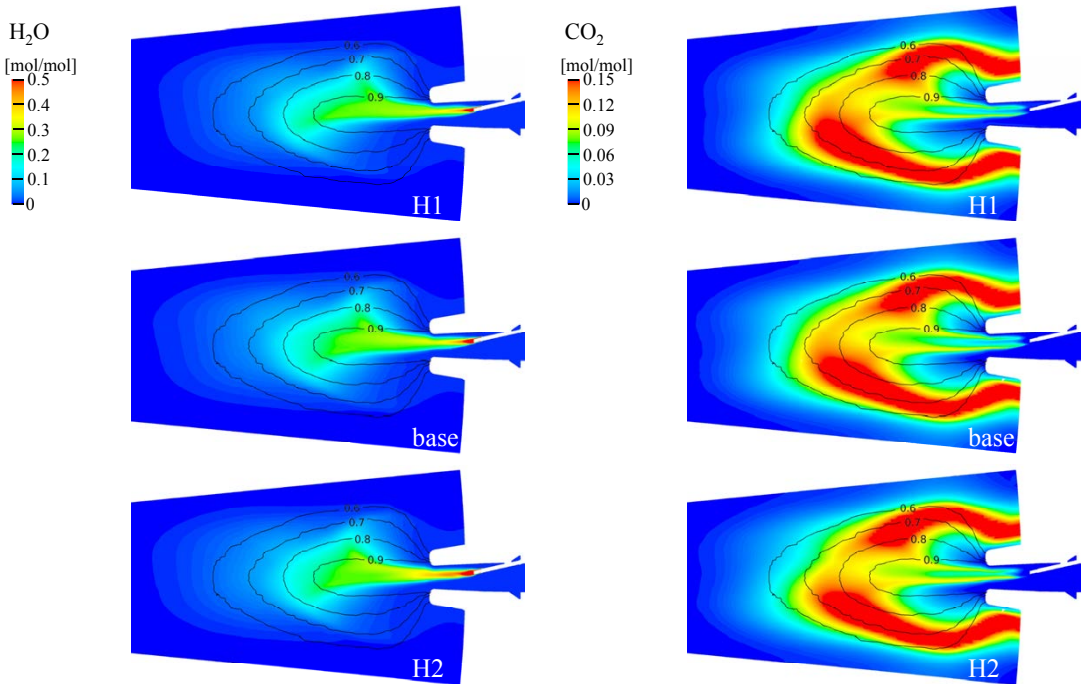

Figure 5.56: Evaluation of H_2O and CO_2 concentration, cut through oil injection lance.

5.3.7 I - Comparison of oil, gas and coal injection

This chapter aims at the comparison of the conversion behavior of different types of reducing agents, that also differ with respect to state of aggregation. Three cases were investigated, where the injection of 800 $^{kg}/_{h \cdot tuyère}$ waste plastics is combined with either

- 700 $^{kg}/_{h \cdot tuyère}$ heavy fuel oil (representing the reference case),
- 1040 $^{m^3_{STP}}/_{h \cdot tuyère}$ natural gas (case I1) or
- 689 $^{kg}/_{h \cdot tuyère}$ pulverized coal (case I2).

The individual rate of oil, gas and coal injection was set such, that the overall carbon input from alternative reducing agents was kept constant. As a consequence, due to varying composition of the materials studied, the hydrogen input varies as listed in table 5.18. This results in a variation of the C/H ratio of reductants, being highest for pulverized coal utilization and lowest for the case of natural gas injection. The values of element input rates in this table also include auxiliary streams such as air or nitrogen for plastics or coal conveying as well as steam for oil lance cooling purposes.

Table 5.18: Variation of alternative reducing agent type, in each case combined injection with 800 $^{kg}/_{h}$ waste plastics.

case ID	injectant type	overall element injection rates C [$^{mol}/_{s}$]	H [$^{mol}/_{s}$]	N [$^{mol}/_{s}$]	O [$^{mol}/_{s}$]	C/H [$^{mol}/_{mol}$]
base	waste plastics + heavy fuel oil	26.1	40.6	3.9	4.9	0.64
I1	waste plastics + natural gas	26.1	67.9	3.9	3.0	0.38
I2	waste plastics + pulverized coal	26.1	24.8	4.8	3.7	1.05
base, I1, I2	hot blast	0.0	1.5	17.6	6.8	

In the simulations, natural gas is simplified by treating it as a single species, namely pure CH_4. The properties of pulverized coal for injection under consideration are summarized in table 5.19. For the cases I1 and I2 the oil lance in the model is replaced by either a lance for natural gas injection or the PCI lance, respectively.

In the case of natural gas injection, a methane flame is formed on the tip of the injection lance that extends into the raceway cavity (see CH_4 concentration profile on a cutting plane through the oil/gas injection lance in figure 5.57). In the case of oil and coal injection the model also predicts the formation of CH_4 from pyrolysis products, therefore at a certain distance from the lance tip where thermolysis of oil volatiles takes place methane appears in the gas phase.

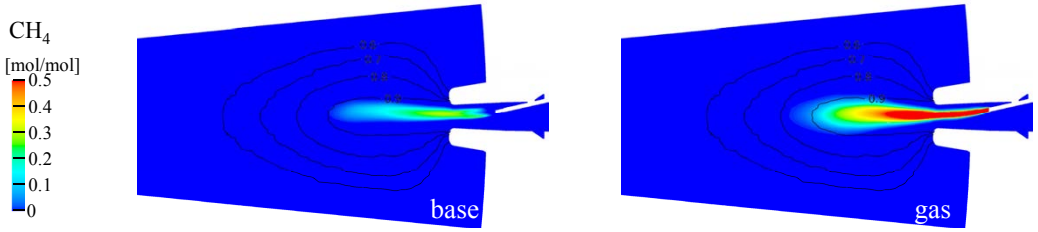

Figure 5.57: Contours of CH_4 concentration, cut through oil/gas injection lance.

Table 5.19: Physical and chemical properties of pulverized coal for injection. In the simulation, the ash content is neglected.

parameter	value
mean equivalent diameter	59 µm
Rosin Rammler spread parameter	1.14
mean particle density	1300 $^{kg}/_{m^3}$
ultimate analysis	80.8 $\%_{w/w}$ C
	4.44 $\%_{w/w}$ H
	5.55 $\%_{w/w}$ O
	1.51 $\%_{w/w}$ N
	6.70 $\%_{w/w}$ ash
	1.00 $\%_{w/w}$ water
thermal conductivity	0.26 $^{W}/_{m \cdot K}$
specific heat capacity	1500 $^{J}/_{kg \cdot K}$
lower heating value	32.7 $^{MW}/_{kg}$
conveying gas type	N_2
conveying gas flow rate	27 m^3_{STP}/h

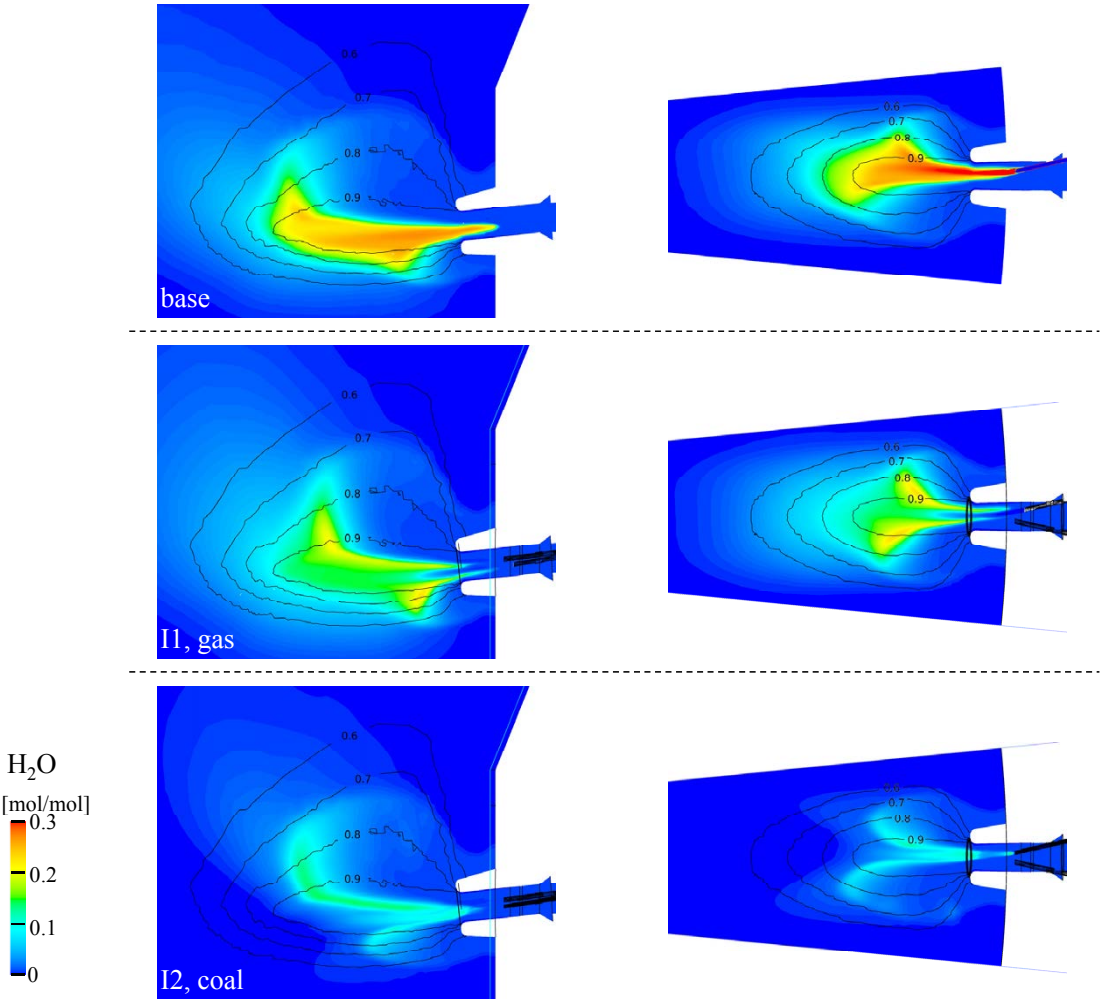

Figure 5.58: Contours of steam concentration. Left: Vertical cut through tuyère, right: Cut through oil/gas/coal injection lance.

The onset of oxidation reactions results in release of CO_2 and steam (see H_2O profiles in figure 5.58). In the base case a large fraction of the hydrogen input is introduced already oxidized as water in the oil mixture or steam for lance cooling (in total 1.96 mol/s H_2O). Consequently, in the oil injection case the H_2O concentration is high throughout the oil spray cone. Contrary to that, in the case utilizing natural gas, no steam additional to that introduced with hot blast is injected via the lances. The majority of H_2O results from methane combustion. Methane combustion starts early, oxygen is more readily consumed within the core of the raceway cavity. Due to the high availability of hydrogen, the steam flow rate through the raceway boundary exceeds that of oil injection (see trend of species flow rates integrated for iso-surfaces of coke bed void fractions in figure 5.59).

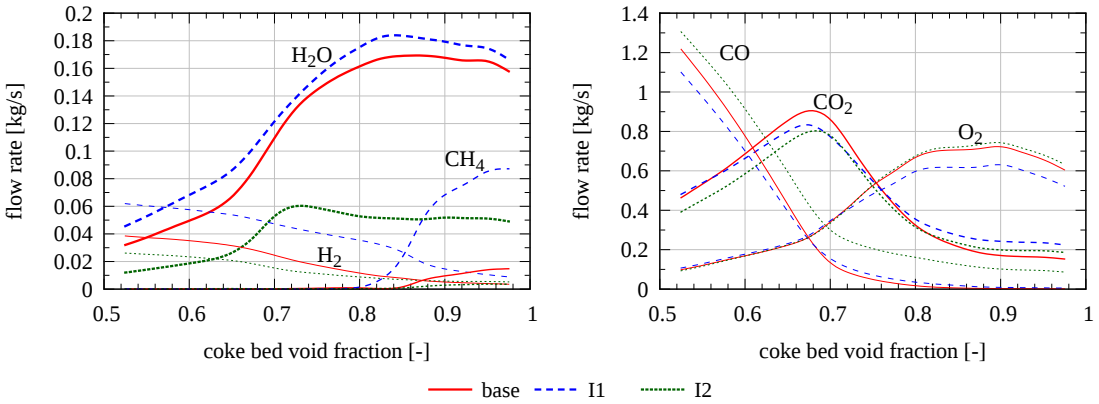

Figure 5.59: Species flow rate through raceway boundary with respect to coke bed void fraction.

As steam gets in contact with hot coke, heterogeneous steam gasification adds to the release of carbon monoxide and hydrogen. Highest rates of hydrogen release into the coke bed are calculated for the natural gas case. In the case of pulverized coal injection the availability of steam is lower as the used coal contains comparatively low amounts of hydrogen that is released with the volatiles. The PCI case discussed here introduces coal with 1 % moisture content, resulting in 0.11 mol/s H_2O feed. Coal drying is finished early, releasing water in the tuyère. Further downstream, steam is also produced from combustion of coal volatiles.

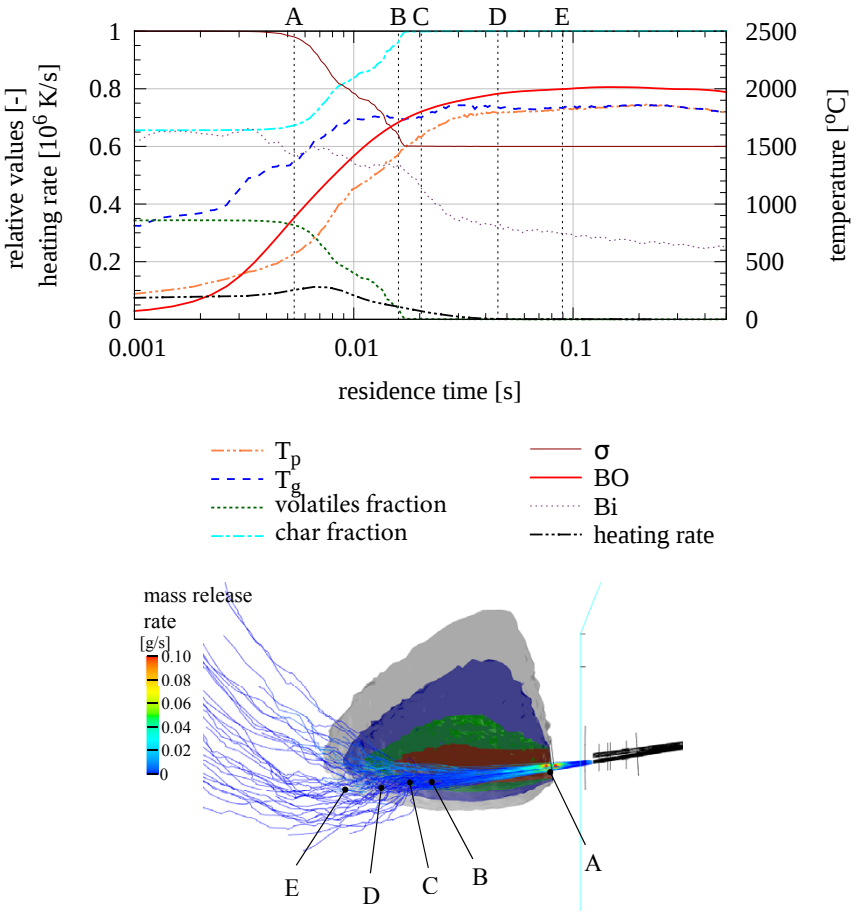

Figure 5.60: Evolution of mass-weighted coal particle properties vs. residence time in blast furnace raceway. Upper-case letters in the diagram refer to particle location.

As illustrated in figure 5.60, the release of volatiles from coal particles is finished after approx. 20 ms, in the core of the raceway cavity. Along with the release of volatiles the fraction of char remaining in the particle mass increases. The emissivity coefficient is modeled to decline as a function of the volatiles fraction. Average particle heating rates during devolatilization are in the range of 10^5 K/s, resulting in Biot numbers above 0.5 in the phase of rapid heating.

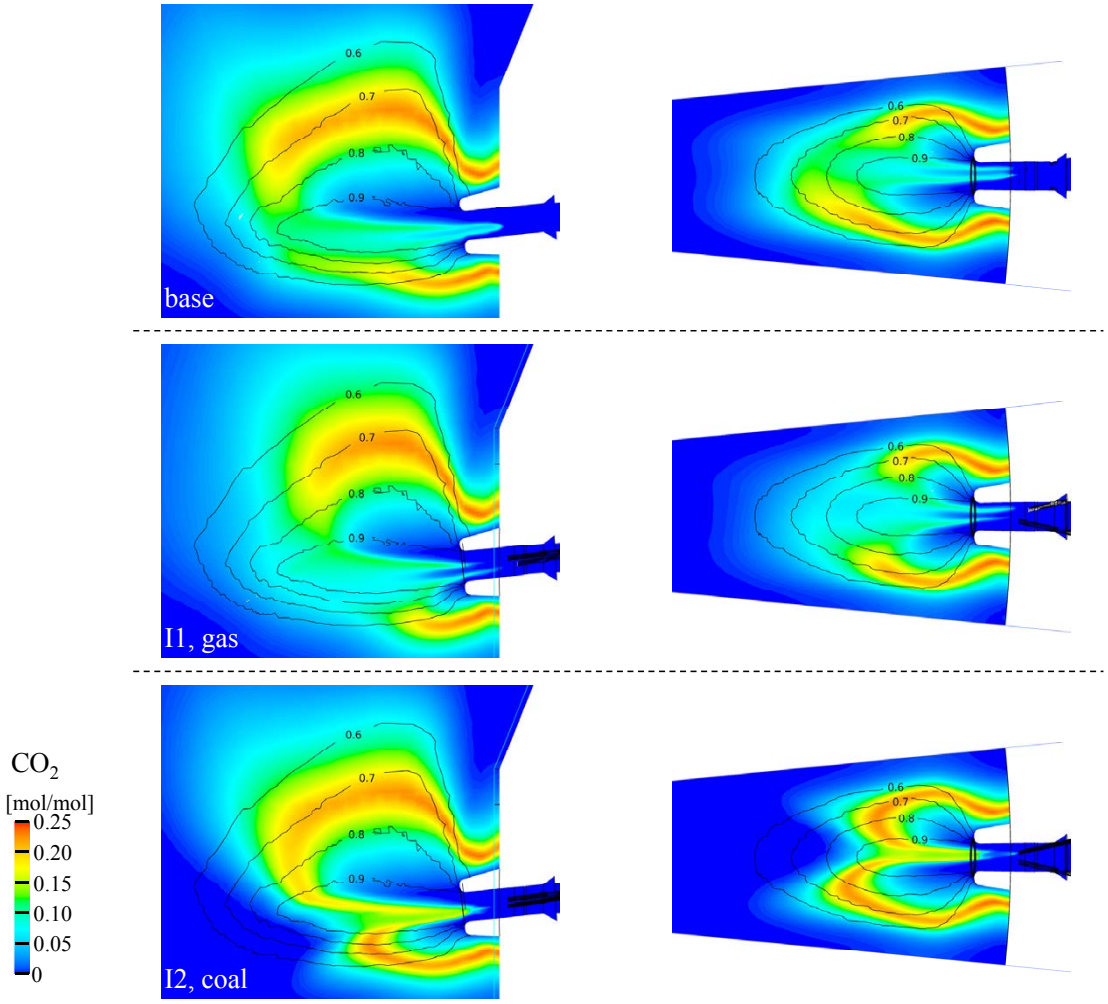

Figure 5.61: Contours of CO_2 concentration. Left: Vertical cut through tuyère, right: Cut through oil/gas/coal injection lance.

Volatiles are oxidized in the gas phase causing O_2 depletion in the region of the coal plume. Heterogeneous reactions of the remaining char are modeled to start after volatiles release is finished, starting oxidation as well as CO_2 and H_2O gasification in the core of the raceway cavity. Due to the high stoichiometric oxygen demand for volatiles oxidation, the availability of O_2 for heterogeneous char oxidation is limited and endothermic gasification reactions play a major role in overall coal utilization, releasing gaseous reducing agents CO and H_2 on the path of particle trajectories (see e.g. CO concentration in figure 5.62). In the tip of the raceway cavity, simulation results show a considerably higher concentration of carbon monoxide as compared to the other cases. This results from thermal decomposition of coal volatiles in the absence of oxygen, in the model introduced via reaction R 28.

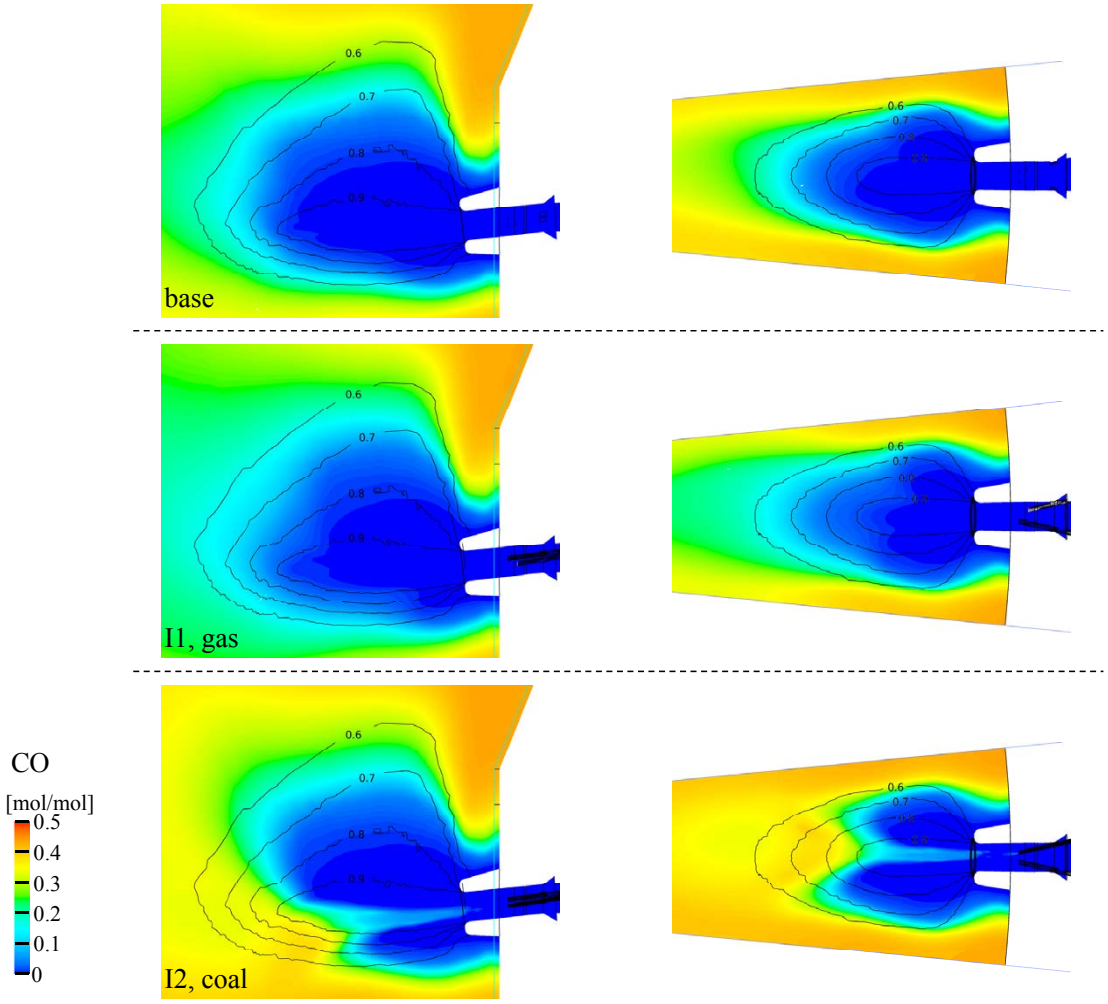

Figure 5.62: Contours of CO concentration. Left: Vertical cut through tuyère, right: Cut through oil/gas/coal injection lance.

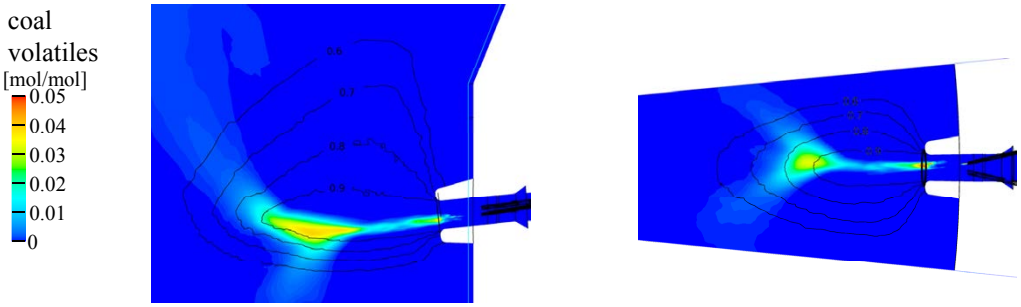

Figure 5.63: Contours of coal volatiles mole fraction. Left: Vertical cut through tuyère, right: Cut through oil/gas/coal injection lance.

The residence time of coal particles in the raceway cavity prior to entering the undisturbed coke bed is approx. 90 ms (see figure 5.60). The overall average coal conversion in the raceway zone (coke bed voidage > 0.5) for the operating conditions under consideration was calculated to be approx. 80 %. The size of coal particles exhibits a large impact on the conversion grade in the raceway, e.g. particles with an initial diameter of

30 µm are estimated to have a burnout ratio of 89 % at the raceway border, average coal particles with 59 µm are consumed to 70 % whereas only 58 % of the mass of particles with initially 90 µm is released within the raceway cavity (see figure 5.64).

After passing the raceway boundary the availability of reaction partners for char utilization (O_2, CO_2 and H_2O) is very low. Therefore, in the modeling study conversion rates decline as particles enter the undisturbed coke bed. In the real blast furnace, char remaining from coal injection is considered to contribute to iron oxide reduction as a reaction partner for the Boudouard reaction, where carbon dioxide originates from the iron oxides. Liquid phases are not yet included in the model, therefore also the reaction set to describe this transformation of chars is to be implemented in future work. However, modeling results are considered reliable in the raceway cavity as no liquid phases are present in this zone.

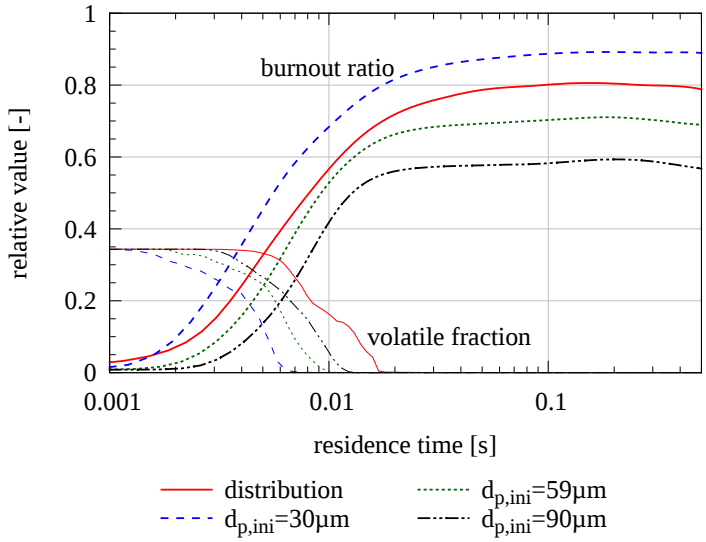

Figure 5.64: Evolution of mass-weighted coal particle volatile fraction and burnout ratio vs. residence time. Particle initialization: Size distribution as given by Rosin Rammler parameters (table 5.19), monodisperse (30, 59 and 90 µm).

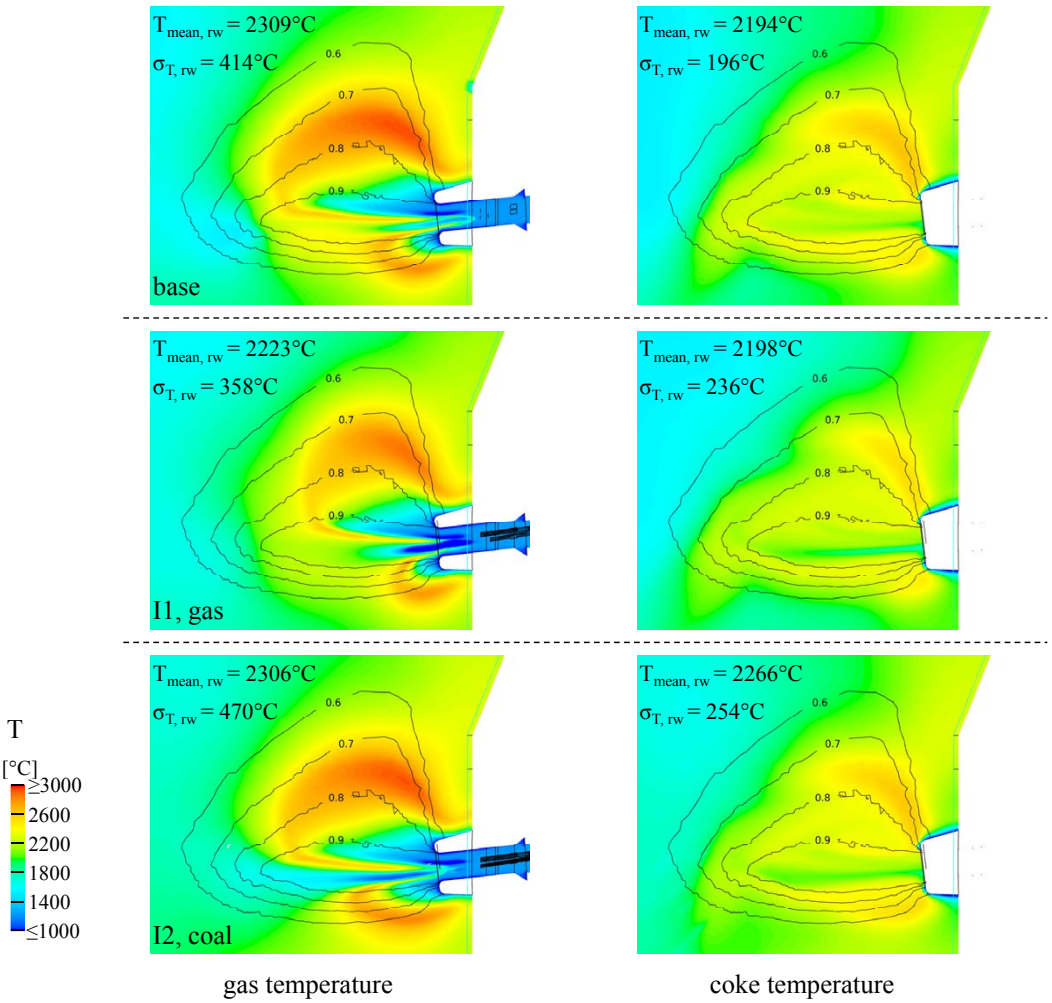

Figure 5.65: Contours of temperature field, vertical cut through tuyère. Left: Gas phase, right: Coke temperature.

The calculated temperature fields for gas and coke are shown in figure 5.65. In this sketch, also results of statistic evaluation in the raceway cavity (zone defined as void fraction > 0.5) are noted. Lowest temperatures are predicted for the case involving natural gas. This is expected as the hydrogen input is highest for this operation setup. However, the standard deviation of gas phase temperature is lowest for this case: Methane follows the path of injected hot blast through the raceway boundary, while the inertia of injected oil droplets and pulverized coal cause a narrower plume. In the core of these zones volatiles are released, the heat of pyrolysis and evaporation are partly withdrawn from the sensible heat of the surrounding gas phase, consequently lowering the gas temperature and increasing the temperature inhomogeneity. Comparing the base case and I2, the release of fuel oil is completed earlier and therefore temperatures rise earlier by the onset of oxidation reactions, as compared to coal utilization. Highest coke temperatures are predicted for the coal case. Here again the lower steam feed results in lower rates of steam gasification and less heat demand for endothermic reactions.

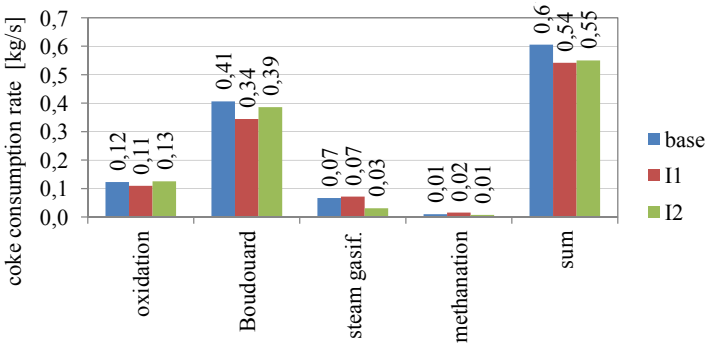

Figure 5.66: Integral coke consumption in the raceway cavity (void fraction > 0.5).

Table 5.20: Variation group I: Average conditions in the raceway zone.

case ID	T_{gas} [°C]	T_{coke} [°C]	O_2 [%v/v]	CO_2 [%v/v]	CO [%v/v]	H_2O [%v/v]	H_2 [%v/v]
base (oil)	2309	2194	3.59	10.20	16.1	3.01	9.00
I1 (gas)	2223	2198	3.02	9.65	14.1	3.33	14.80
I2 (coal)	2306	2266	3.70	9.52	19.5	1.33	6.46

The modeling results indicate that the integral coke consumption in the raceway zone is lowest for the case with natural gas injection. This case combines reduced partial pressures of carbon dioxide (dilution with hydrogen) as well as O_2 with lower raceway temperatures (table 5.20). However, as already stated at the beginning of this chapter, the applied boundary conditions introduce the highest amount of alternative reducing agents in the natural gas case in terms of additional hydrogen supply. The kinetics of the heterogeneous methanation reaction is slower as compared to the other coke reactions, also contributing to lower coke consumption rates.

In the model, CO_2 is also a gasification agent for the char from coal in the PCI case, a part of the released carbon dioxide is already consumed in the raceway cavity from char reactions, lowering the gasification rate of metallurgical coke in the raceway boundary. Consequently, the Boudouard reaction is partially shifted into the raceway cavity as pulverized coal injection is applied. As in this case the steam supply is also low, the overall coke consumption rate is comparingly low.

6 Conclusions

A steady-state CFD model describing the injection of auxiliary reducing agents injection into the raceway of ironmaking blast furnaces was developed. The focus was laid on studying the utilization of feed materials by homogeneous and heterogeneous reactions in the vicinity of the tuyère opening, also investigating the coke conversion. A new approach was implemented where the movement and utilization of metallurgical coke is computed on an additional computational grid. By solving conservation equations for gas and coke phase, driving forces for heterogeneous transfer processes such as heterogeneous reactions and heat transfer can be evaluated explicitly.

Model validation The model setup was implemented and validated stepwise, starting with heat transfer problems involving inert solid phases and gas flow. In the developed model the effective coke bed conductivity is estimated accounting for heat transport effects from solid radiation in the void volume between solid coke particles.

Increasing the model capabilities and complexity, also homogeneous gas-phase and heterogeneous coke reactions were implemented. The final test for the setup of heterogeneous coke reactions in the dual-grid model was the gasification of metallurgical coke, applied to a standardized testing routine that is used in the iron producing industry to evaluate the reactivity of metallurgical coke. In this work, apart from the standard routine, additional experimental data for varying temperature, coke particle sizes and gasification agent partial pressure were available. Good agreement was found for the range of parameter variation, indicating that the model setup is able to capture and reproduce the main physical processes involved in CO_2-gasification of coke, such as boundary layer diffusion, pore diffusion and the influence of intrinsic reaction kinetics.

The model for conversion of pulverized coal for injection was validated by implementing an experimental setup simulating the combustion of pulverized coal at raceway conditions. The coal type and its characteristic properties, e.g. the content of volatile matter and particle size distribution, have considerable influence on the overall burnout behavior of pulverized coal particles in the raceway cavity. Good model performance was found for the coals tested.

Blast furnace simulation The full model setup was applied to blast furnace A, operated by **voest**alpine Stahl GmbH. A baseline operating case involving the injection of heavy fuel oil and processed waste plastics was defined. The implemented simulation geometry features a detailed description of the tuyère geometry, including the lances for injection of auxiliary reducing agents. In the current model setup the shape of the raceway cavity that forms in the vicinity of the tuyère opening due to hot blast injection is not calculated explicitly but introduced as a boundary condition by defining a spatially variable coke bed porosity.

Due to the early release of reactive components from the fine oil droplets, fuel oil represents an effective reducing agent that is readily vaporized within the raceway cavity after several milliseconds. As compared to the fuel oil spray, plastic particles are introduced in much larger particle size classes and therefore have much longer residence times in the range of seconds. Consequently, plastic particles tend to have a deeper penetration into the coke bed. In these regions lower oxygen partial pressures are available for combustion

reactions, and the formation of char from plastics is to be expected.

Released volatiles are subjected to homogeneous gas-phase reactions. Oxygen injected with the hot blast is readily consumed within the raceway cavity, partially by oxidation of alternative reducing agents and also by combustion reactions of metallurgical coke. According to the modeling results, coke particles falling into the raceway cavity are accelerated by the hot blast jet towards the furnace center. During the short time of flight, these are not fully consumed, consequently a circulating movement is predicted. This flow characteristics contributes to transfer of heat from the hot zones where oxidation occurs towards regions where endothermic gasification reactions dominate.

According to the modeling results for the case with combined injection of liquid hydrocarbons and waste plastics, approx. 67 % of the coke consumed in the raceway cavity is depicted to the heterogeneous Boudouard reaction. Oxidation and steam gasification reaction are responsible for 20 % and 11 % of coke utilization in this zone, respectively. Due to its kinetic limitation, only approx. 2 % of overall coke consumption in the raceway arise from the reaction with hydrogen.

Blast furnace parameter variation In a parametric study operating conditions were varied in terms of hot blast supply, type and rates of auxiliary reducing agents injection as well as geometric issues concerning the tuyère diameter and length of injection lances.

In the range of parameter variation, changes regarding the tuyère and lance geometry showed little direct impact on the pyrolysis behavior of plastic particles in the raceway. This results from the fact that the residence time in the vicinity of the lance tip and tuyère zone is short as compared to the overall residence time to full gasification. Contrary to that, fierce conditions in fuel oil atomization provide for small droplets and therefore the oil spray is readily evaporated in the vicinity of the tuyère opening. Changes e.g. in the lance length considerably influence the location of oil vapor release.

The simulation results confirmed the cooling effect of hydrogen introduced into the raceway. The average raceway temperature decreases due to the more intense steam gasification reaction that is of endothermic nature. In the operating conditions studied, the cooling effect was highest in the case representing natural gas injection. In contrast, the lowest hydrogen input was modeled for the case with coal injection, resulting in highest raceway-average gas and coke temperatures.

The increase of hot blast oxygen enrichment rates tends to raise raceway temperatures due to higher rates of oxidation reactions. As a consequence, in the simulation cases considered, times for evaporation of liquid hydrocarbons and plastics release decrease in the order of 10 %. In the simulation runs a similar effect was achieved by increasing the hot blast temperature from 1100 to 1300 °C.

In general, the size distribution of injected alternative reducing agents has a strong influence on the grade of utilization prior to reaching the raceway boundary. In the case of pulverized coal injection, the estimated average conversion grade within the raceway cavity is approx. 80 %. Furthermore, due to the onset of heterogeneous reactions of char particles remaining after volatiles release, CO_2 is also consumed in the coal plume. Consequently, the Boudouard reaction is partly shifted from the coke bed into the raceway cavity.

In terms of numerical behavior, the model proved to be stable during the iterative solution. This was confirmed by monitoring the convergence behavior, and moreover consistent trends were found in the simulation results.

7 Outlook

Future work shall aim at the introduction of new features concerning the description of the multiphase nature of flow in the blast furnace, including:

Solid phase flow In the CFD model developed in this work, the shape of the raceway is implemented as a boundary condition from published work where raceway formation dynamics were studied. In future code development, the transition to a hybrid CFD-DEM model shall introduce the explicit computation of the raceway shape depending on the actual operating conditions. This idea might be realized by definition of an interface, where information from simulation of the gas-phase flow including the description of alternative reducing agents injection, e.g. temperature field, velocity and density profiles, will be provided from the presented CFD model to a discrete element model setup, where the movement of coke particles shall be calculated. The resulting raceway shape is in turn to be imported as a boundary to the CFD-solver to compute for new gas-flow properties. These outer iteration loops shall be continued until converged results for raceway shape, species and temperature distributions in the coke bed are obtained. As a consequence, e.g. the influence of volatiles release from alternative reducing agents on the raceway shape can be studied in detail.

Liquid phases At the current stage of model development, liquid phases such as molten iron oxides, slag and hot metal are not considered. This limits the accuracy of the CFD model in regions outside the raceway cavity where liquid phases are present. Consequently, by introducing liquids the applicability of the simulation model can be considerably widened. This also offers the opportunity to incorporate these phases in the reaction scheme: In the blast furnace shaft iron oxides provide oxygen that contributes to the utilization of coke via the Boudouard reaction. Consequently this new setup can also be applied to study the overall coke consumption in a large domain of the blast furnace.
In this context, a proper calculation of the liquid surface structure is crucial to reliably estimate the surface of the interface that is exposed to species transfer between liquid and gas phase, but also amongst liquid and solid coke (e.g. direct reduction reaction of liquid iron oxides).
Furthermore, also a detailed description of the fate of char that remains from coal and plastics devolatilization becomes possible. The introduction of interaction with liquid phases shall include the reactions of char with hot metal (e.g. carburization), but also the influence of fines on local coke bed porosity, i.e. potential blockage, can be considered.

Melting processes Another interesting feature that can be implemented after introducing liquid phases is the melting of burden in the upper region of the furnace shaft. This will allow for estimating the location of the cohesive zone, where softening of flux and iron oxides takes place.

The resulting model compilation shall avoid the restriction to the hearth zone and therefore allow for detailed investigation of full-scale blast furnace operation. Even the investigation of the impact from burden charging operation on conditions in the furnace shaft and hearth shall be rendered possible.

8 Appendix

In the following tables average properties integrated for the raceway cavity, defined as the volume zone where the coke bed void fraction exceeds 0.5, are summarized. The labeling of the simulation cases is given as listed in table 5.5.

Table 8.1: Conditions in raceway. Variation group A: Tuyère diameter.

		base	*A*1	*A*2
$T_{gas,mean}$	[°C]	2309	2332	2272
$\sigma_{T_{gas}}$	[°C]	414	465	493
$T_{coke,mean}$	[°C]	2194	2192	2109
$\sigma_{T_{coke}}$	[°C]	196	233	232
$v_{gas,mean}$	[m/s]	7.1	7.6	8
gas composition				
O_2	[%v/v]	3.59	4.67	4.92
H_2	[%v/v]	9	7.71	9.09
CO	[%v/v]	16.13	13.21	11.49
CO_2	[%v/v]	10.19	10.94	10.71
H_2O	[%v/v]	3.01	3.47	4.59
coke consumption				
oxidation	[kg/s]	0.123	0.13	0.121
CO_2 gasification	[kg/s]	0.406	0.364	0.301
H_2O gasification	[kg/s]	0.067	0.061	0.066
methanation	[kg/s]	0.01	0.007	0.006
sum	[kg/s]	0.606	0.561	0.494
raceway volume	[m^3]	1.18	0.94	0.81

Table 8.2: Conditions in raceway. Variation group B: Injection rates.

		base	*B*1	*B*2
$T_{gas,mean}$	[°C]	2309	2301	2301
$\sigma_{T_{gas}}$	[°C]	414	370	391
$T_{coke,mean}$	[°C]	2194	2233	2238
$\sigma_{T_{coke}}$	[°C]	196	245	242
$v_{gas,mean}$	[m/s]	7.1	7.2	7.2
gas composition				
O_2	[%v/v]	3.59	3.18	3.45
H_2	[%v/v]	9	11.02	10.12
CO	[%v/v]	16.13	15.22	15.42
CO_2	[%v/v]	10.19	10.2	10.18
H_2O	[%v/v]	3.01	3.69	3.39
coke consumption				
oxidation	[kg/s]	0.123	0.112	0.12
CO_2 gasification	[kg/s]	0.406	0.385	0.395
H_2O gasification	[kg/s]	0.067	0.079	0.074
methanation	[kg/s]	0.01	0.012	0.011
sum	[kg/s]	0.606	0.588	0.6

Table 8.3: Conditions in raceway. Variation group C: Lance length.

		base	*C*1	*C*2	*C*3
$T_{gas,mean}$	[°C]	2309	2287	2284	2282
$\sigma_{T_{gas}}$	[°C]	414	405	411	411
$T_{coke,mean}$	[°C]	2194	2164	2154	2147
$v_{gas,mean}$	[m/s]	7.1	7.1	7	7
gas composition					
O_2	[%v/v]	3.59	3.59	3.74	3.81
H_2	[%v/v]	9	9.73	9.78	10.16
CO	[%v/v]	16.13	15.36	14.96	14.63
CO_2	[%v/v]	10.19	10.4	10.38	10.38
H_2O	[%v/v]	3.01	3.29	3.47	3.59
coke consumption					
oxidation	[kg/s]	0.123	0.123	0.125	0.124
CO_2 gasification	[kg/s]	0.406	0.393	0.39	0.387
H_2O gasification	[kg/s]	0.067	0.071	0.076	0.081
methanation	[kg/s]	0.01	0.011	0.011	0.012
sum	[kg/s]	0.606	0.597	0.602	0.603

Table 8.4: Conditions in raceway. Variation group D: Hot blast moisture.

		base	*D*1	*D*2	*D*3
$T_{gas,mean}$	[°C]	2309	2293	2278	2265
$\sigma_{T_{gas}}$	[°C]	414	407	402	402
$T_{coke,mean}$	[°C]	2194	2174	2156	2141
$v_{gas,mean}$	[m/s]	7.1	7.2	7.2	7.2
gas composition					
O_2	[%$_{v/v}$]	3.59	3.49	3.4	3.4
H_2	[%$_{v/v}$]	9	9.45	9.9	10.1
CO	[%$_{v/v}$]	16.13	15.77	15.4	15.07
CO_2	[%$_{v/v}$]	10.19	10.41	10.66	10.85
H_2O	[%$_{v/v}$]	3.01	3.31	3.73	4.18
coke consumption					
oxidation	[kg/s]	0.123	0.12	0.117	0.116
CO_2 gasification	[kg/s]	0.406	0.4	0.397	0.394
H_2O gasification	[kg/s]	0.067	0.074	0.084	0.095
methanation	[kg/s]	0.01	0.01	0.011	0.011
sum	[kg/s]	0.606	0.604	0.608	0.616

Table 8.5: Conditions in raceway. Variation group E: Hot blast oxygen enrichment.

		*E*1	*E*2	*base*	*E*3	*E*4
$T_{gas,mean}$	[°C]	2279	2295	2309	2320	2331
$\sigma_{T_{gas}}$	[°C]	404	411	414	416	416
$T_{coke,mean}$	[°C]	2163	2179	2194	2204	2215
$v_{gas,mean}$	[m/s]	7.1	7.1	7.1	7.3	7.3
gas composition						
O_2	[%$_{v/v}$]	3.44	3.5	3.59	3.57	3.56
H_2	[%$_{v/v}$]	9.16	9.58	9	10.15	10.23
CO	[%$_{v/v}$]	15.39	15.67	16.13	16.14	16.47
CO_2	[%$_{v/v}$]	10.15	10.05	10.19	10.13	10.23
H_2O	[%$_{v/v}$]	3.09	3.17	3.01	3.18	3.14
coke consumption						
oxidation	[kg/s]	0.119	0.12	0.123	0.122	0.122
CO_2 gasification	[kg/s]	0.386	0.393	0.406	0.411	0.42
H_2O gasification	[kg/s]	0.066	0.07	0.067	0.072	0.072
methanation	[kg/s]	0.01	0.011	0.01	0.012	0.012
sum	[kg/s]	0.581	0.594	0.606	0.617	0.626

Table 8.6: Conditions in raceway. Variation group F: Hot blast temperature.

		$F1$	$F2$	$F3$	$F4$	$F5$
$T_{gas,mean}$	[°C]	2268	2284	2295	2309	2328
$\sigma_{T_{gas}}$	[°C]	419	416	414	405	399
$T_{coke,mean}$	[°C]	2217	2233	2245	2265	2285
$v_{gas,mean}$	[m/s]	7	7.1	7.1	7.2	7.3
gas composition						
O_2	[%v/v]	3.57	3.57	3.59	3.48	3.43
H_2	[%v/v]	9.11	9.14	9.11	9.39	9.23
CO	[%v/v]	15.54	15.73	15.88	16.09	16.4
CO_2	[%v/v]	10.49	10.38	10.27	10.22	10.11
H_2O	[%v/v]	3.18	3.13	3.11	3.08	3.02
coke consumption						
oxidation	[kg/s]	0.124	0.123	0.124	0.119	0.118
CO_2 gasification	[kg/s]	0.393	0.397	0.401	0.404	0.411
H_2O gasification	[kg/s]	0.067	0.067	0.068	0.069	0.069
methanation	[kg/s]	0.009	0.01	0.01	0.011	0.011
sum	[kg/s]	0.593	0.597	0.602	0.602	0.608

Table 8.7: Conditions in raceway. Variation group G: Oil lance cooling gas type.

		base	$G1$	$G2$
$T_{gas,mean}$	[°C]	2309	2318	2309
$\sigma_{T_{gas}}$	[°C]	414	412	409
$T_{coke,mean}$	[°C]	2194	2204	2193
$v_{gas,mean}$	[m/s]	7.1	7.2	7.2
gas composition				
O_2	[%v/v]	3.59	3.56	3.51
H_2	[%v/v]	9	8.75	9.17
CO	[%v/v]	16.13	16.32	16.07
CO_2	[%v/v]	10.19	10.06	10.08
H_2O	[%v/v]	3.01	2.84	2.89
coke consumption				
oxidation	[kg/s]	0.123	0.122	0.12
CO_2 gasification	[kg/s]	0.406	0.408	0.402
H_2O gasification	[kg/s]	0.067	0.064	0.065
methanation	[kg/s]	0.01	0.01	0.01
sum	[kg/s]	0.606	0.603	0.598

Table 8.8: Conditions in raceway. Variation group H: Heavy fuel oil water content.

		$H1$	*base*	$H2$
$T_{gas,mean}$	[°C]	2313	2309	2304
$\sigma_{T_{gas}}$	[°C]	413	414	424
$T_{coke,mean}$	[°C]	2197	2194	2189
$v_{gas,mean}$	[m/s]	7.1	7.1	7.2
gas composition				
O_2	[%v/v]	3.58	3.59	3.65
H_2	[%v/v]	9.03	9	10.13
CO	[%v/v]	16.26	16.13	15.73
CO_2	[%v/v]	10.12	10.19	10.13
H_2O	[%v/v]	2.91	3.01	3.19
coke consumption				
oxidation	[kg/s]	0.122	0.123	0.125
CO_2 gasification	[kg/s]	0.406	0.406	0.404
H_2O gasification	[kg/s]	0.065	0.067	0.07
methanation	[kg/s]	0.01	0.01	0.011
sum	[kg/s]	0.604	0.606	0.61

Table 8.9: Conditions in raceway. Variation group I: Comparison of oil, gas and coal injection.

		base	$I1$	$I2$
$T_{gas,mean}$	[°C]	2309	2223	2306
$\sigma_{T_{gas}}$	[°C]	414	358	470
$\sigma_{T_{gas}}$	[%]	17.9	16.1	20.4
$T_{coke,mean}$	[°C]	2194	2198	2266
$\sigma_{T_{coke}}$	[°C]	196	236	254
$\sigma_{T_{coke}}$	[%]	8.9	10.7	11.2
$v_{gas,mean}$	[m/s]	7.1	7.5	6.9
gas composition				
O_2	[%v/v]	3.59	3.02	3.7
H_2	[%v/v]	9	14.83	6.46
CO	[%v/v]	16.13	14.07	19.45
CO_2	[%v/v]	10.19	9.65	9.52
H_2O	[%v/v]	3.01	3.33	1.33
coke consumption				
oxidation	[kg/s]	0.123	0.109	0.126
CO_2 gasification	[kg/s]	0.406	0.345	0.387
H_2O gasification	[kg/s]	0.067	0.072	0.032
methanation	[kg/s]	0.01	0.016	0.008
sum	[kg/s]	0.606	0.542	0.552

Nomenclature

Roman symbols

$\dot{N}_i$	interfacial transfer rate of species i	$^{mol}/_{s}$
A	pre-exponential factor	units vary
a	absorption coefficient	–
a	speed of sound	$^{m}/_{s}$
A	particle surface	m^2
A_{coke}	specific coke surface	$^{m^2}/_{m^3}$
BO	coal particle burnout ratio	–
C	Constant	–
c_D	drag coefficient	–
c_i	molar concentration of species i in bulk gas flow	$^{mol}/_{m^3}$
c_p	specific heat capacity	$^{J}/_{kg \cdot K}$
$c_{i,S}$	molar concentration of species i at particle surface	$^{mol}/_{m^3}$
D	diffusion coefficient	$^{m^2}/_{s}$
d_m	equivalent diameter of average hollow space in porous material	m
d_p	particle diameter	m
$D_{i,j}$	diffusion coefficient of species i in species j	$^{m^2}/_{s}$
$D_{i,m}$	diffusion coefficient of species i in gas mixture m	$^{m^2}/_{s}$
$D_{K,i}$	Knudsen diffusion coefficient of component i in particle pores	$^{m^2}/_{s}$
E_a	activation energy	$^{J}/_{mol}$
f	specific volume force	$^{m}/_{s^2}$
$\mathbf{F}_p$	external force per unit particle mass	$^{m}/_{s^2}$
f_a	shape factor	–
g	gravitation	$^{m}/_{s^2}$
h	heat transfer coefficient	$^{W}/_{m^2 \cdot K}$
h	specific enthalpy	$^{J}/_{kg}$
I	radiation intensity	$^{W}/_{m^2 s \cdot r}$
$\mathbf{J}$	molecular flux vector	units vary
k	reaction rate	units vary
k	turbulent kinetic energy	$^{m^2}/_{s^2}$
$k_{G,i}$	surface specific mass transfer coefficient	$^{m}/_{s}$
k_c	mass transfer coefficient	$^{m}/_{s}$
l	length	m
M	molecular weight	$^{kg}/_{kmol}$
m	mass	kg
N	number of components	–
n	spread parameter, Rosin Rammler distribution	–
p	pressure	Pa
$\dot{Q}_{rad}$	heat transfer rate	W
$\dot{Q}_{rad}$	incident radiation	W
R	universal gas constant	$^{J}/_{mol\,K}$

r	reaction index	–
$\mathbf{r}$	position vector	m
R_m	universal gas constant, $R_m = 8.314\,\mathrm{J/mol \cdot K}$	$\mathrm{J/mol\,K}$
S	source term	$[\Phi]/\mathrm{m^3 \cdot s}$
$\mathbf{s}$	direction vector	m
S_L	laminar flame speed	$\mathrm{m/s}$
T	temperature	K
t	time	s
v	cartesian velocity component	$\mathrm{m/s}$
$\mathbf{v}$	velocity vector	$\mathrm{m/s}$
V_{CV}	control volume	$\mathrm{m^3}$
w_a	coal particle ash content	$\mathrm{kg/kg}$
$w_{a,0}$	ash content in virgin coal particle	$\mathrm{kg/kg}$
x_i	mole fraction of species i in bulk gas flow	$\mathrm{mol/mol}$
$x_{i,B}$	logarithmic mean mole fraction of species i in particle boundary layer	$\mathrm{mol/mol}$
$x_{i,S}$	mole fraction of species i at particle surface	$\mathrm{mol/mol}$
Y	mass fraction	$\mathrm{kg/kg}$
y_{BM}	logarithmic mean mole fraction in boundary layer	$\mathrm{mol/mol}$

Greek symbols

α	heat transfer coefficient	$\mathrm{W/m^2 \cdot K}$
β	parameter to determine share of CO or CO_2 release	–
Δt	interval for time averaging	s
Δ	length scale for filter (LES turbulence model)	m
δ_c	film thickness	m
δ_{ij}	Kronecker-symbol: $\delta_{ij} = 1$, if $i = j$, else $\delta_{ij} = 0$	–
ϵ	turbulent kinetic energy dissipation rate	$\mathrm{m^2/s^3}$
ε	void fraction	–
η	Kolmogorov length scale	m
Γ	molecular transport coefficient	units vary
γ	effectiveness factor of heterogeneous reactions in porous particles	–
λ	thermal conductivity	$\mathrm{W/m \cdot K}$
$\mathcal{L}$	mean free path length of fluid element motion	m
μ	dynamic viscosity	$\mathrm{kg/m \cdot s}$
μ_t	turbulent viscosity	$\mathrm{m^2/s^2}$
∇	Nabla operator, $\nabla = \left(\frac{\partial}{\partial x}, \frac{\partial}{\partial y}, \frac{\partial}{\partial z}\right)$	$1/\mathrm{m}$
ν	heterogeneous reactions: reaction order	–
ν	kinematic viscosity	$\mathrm{m^2/s}$
ϕ'	temporal fluctuation of a general transport quantity ϕ	units vary
Φ	extensive quantity	units vary
ϕ	intensive quantity	units vary
ϕ	particle non-sphericity	–
$\overline{\phi}$	time average of a general transport quantity ϕ	units vary
Ψ	shape factor	–
ψ	heterogeneous reactions in porous particles: Thiele-modulus	–
ρ	density	$\mathrm{kg/m^3}$
σ	Stefan-Boltzmann-constant, $\sigma = 5.672 \cdot 10^{-8} W/m^2K^4$	$\mathrm{W/m^2K^4}$
σ_s	refractive coefficient	–

τ	particle tortuosity	–
$\tau_{ij,turb}$	Reynolds shear stress tensor	Pa
τ_{ij}	shear stress tensor	Pa

Indices

d	droplet
E	Energy
ed	educt species index
eff	effective
F	Force
f	fluid
hm	hot metal
i	species index
i, j	coordinate axis
l	laminar
M	mass
m	gas mixture
n	mixture component index
p	particle
R	radiation
t	turbulent
x, y, z	cartesian coordinate

Dimensionless numbers

$Bi = \frac{\alpha\, d_p}{2\,\lambda_p}$	Biot number
$Kn = \frac{\mathcal{L}}{l_f}$	Knudsen number
$Le = \frac{\lambda}{\rho\, c_p\, D}$	Lewis number
$Ma = \frac{\nu}{a}$	Mach number
$Nu = \frac{\alpha \cdot l}{\lambda}$	Nusselt number
$Pe = \frac{S_L d_m c_p \rho}{\lambda_f}$	Péclet number
$Pr = \frac{\eta \cdot c_p}{\lambda}$	Prandtl number
$Re = \frac{u \cdot d}{\nu}$	Reynolds number
$Sc = \frac{\nu}{D}$	Schmidt number
$Sh = \frac{k_G\, d}{D}$	Sherwood number

Abbreviations

BF	Blast Furnace
CFD	Computational Fluid Dynamics
CPU	Central Processing Unit
DEM	Discrete Elements Method
DNS	Direct Numeric Simulation
DPM	Discrete Particle Model
DR	Direct Reduction
EDC	Eddy Dissipation Concept
LES	Large Eddy Simulation

NSC	Nippon Steel Company
PCI	Pulverized Coal Injection
PDA	Phase Doppler Anemometry
PIV	Particle Image Velocimetry
PVC	Poly Vinyl Chloride
RANS	Reynolds Averaged Navier-Stokes
SR	Smelting Reduction
VOF	Volume Of Fluid

Bibliography

[1] Remus, R., Aguado-Monsonet, M., Roudier, S. and Sancho, L. D. *Best Available Techniques (BAT) Reference Document for Iron and Steel Production: Industrial Emissions Directive 2010/75/EU.* E-41092 Seville, Spain, 2013. ISBN 978-92-79-26475-7.

[2] Lüngen, H. B. and Yagi, J.-I. *Iron, 2. Blast Furnace Processes.* In B. Elvers, ed., *Ullmann's encyclopedia of industrial chemistry*, pp. 657–710. Wiley-Blackwell, Weinheim, 2003-. ISBN 978-35-27-30673-2.

[3] Oeters, F., Ottow, M., Senk, D., Beyzavi, A., Güntner, J., Lüngen, H. B., Koltermann, M. and Buhr, A. *Iron, 1. Fundamentals and Principles of Reduction Processes.* In B. Elvers, ed., *Ullmann's encyclopedia of industrial chemistry*, pp. 577–656. Wiley-Blackwell, Weinheim, 2003-. ISBN 978-35-27-30673-2.

[4] Bureau of International Recycling, Ferrous Division. *World Steel Recycling in Figures 2007-2011.* available at: www.bir.org, accessed 15.10.2012.

[5] Grimes, S., Donaldson, J. and Gomez, C. *Report on the Environmental Benefits of Recycling.* available at: www.cari-acir.org, accessed 8.10.2014.

[6] World Steel Association. *Annual iron production archive.* available at www.worldsteel.org, accessed 7.11.2014.

[7] Gara, S. and Schrimpf, S. *Behandlung von Reststoffen und Abfällen in der Eisen- und Stahlindustrie.* M-092. Umweltbundesamt Österreich, 1998. ISBN 3-85457-394-4.

[8] Feilmayr, C. *Effect of an improved material distribution in the blast furnace process.* In *K1Met Metallurgical Competence Center - Scientific Exchange Day.* Vienna, Austria, March 19, 2012.

[9] Chatterjee, A. *Beyond the blast furnace.* CRC Press, Boca Raton, 1994. ISBN 0-8493-6676-3.

[10] Chu, M., Nogami, H. and Yagi, J.-I. *Numerical Analysis on Injection of Hydrogen Bearing Materials into Blast Furnace.* ISIJ International, 44(5):801–808, 2004.

[11] Carpenter, A. *Injection of coal and waste plastics in blast furnaces.* 2010. ISBN 978-92-9029-486-3.

[12] Slaby, S. *Modeling of Reducing Agent Injection into the Blast Furnace and its Behavior in the Raceway and the Bosh Belly Area.* Ph.D. thesis, Vienna University of Technology, Institute of Chemical Engineering, 2006.

[13] Collin, G. and Wetzel, W. *Zur Geschichte der Eisengewinnung mit Holzkohle und Steinkohlenkoks.* NTM Journal of the History of Science, Technology and Medicine, 12(2):65–79, 2004.

[14] Schauwinhold, D. and Toncourt, M. *Steel, 1. Introduction and History.* In B. Elvers, ed., *Ullmann's encyclopedia of industrial chemistry*, pp. 143–156. Wiley-Blackwell, Weinheim, 2003-. ISBN 978-35-27-30673-2.

[15] Steffen, R., Janke, D., Schäfer, K., Jacobi, H., Hammer, R. and Hentrich, R. *Steel, 2. Crude Steel Production.* In B. Elvers, ed., *Ullmann's encyclopedia of industrial chemistry*, pp. 157–214. Wiley-Blackwell, Weinheim, 2003. ISBN 978-352730673-2.

[16] Chen, W.-H., Lin, M.-R., Yu, A. B., Du, S.-W. and Leu, T.-S. *Hydrogen production from steam reforming of coke oven gas and its utility for indirect reduction of iron oxides in blast furnace.* International Journal of Hydrogen Energy, 37(16):11748–11758, 2012.

[17] Andahazy, D. *Simulation der Vorgänge in Windform und Raceway bei der Gas- und Öleindüsung in den Hochofen.* Ph.D. thesis, Technische Universität Wien, Institut für Verfahrenstechnik, Umwelttechnik und technische Biowissenschaften, Wien, 2005.

[18] Omori, Y. *Blast Furnace Phenomena and Modelling.* Elsevier Applied Science Publishers, 1987. ISBN 1-85166-057-7.

[19] Gupta, G. S. and Rudolph, V. *Comparison of Blast Furnace Raceway Size with Theory.* ISIJ International, 46(2):195–201, 2006.

[20] Hilton, J. E. and Cleary, P. W. *Raceway formation in laterally gas-driven particle beds.* Chemical Engineering Science, 80:306–316, 2012.

[21] Chung, J. K., Han, J. W. and Lee, J. H. *Coke properties at tuyere level in blast furnace with pulverized coal injection.* Metals and Materials, 2(1):1–7, 1996.

[22] Hooey, L., Sköld, B.-E., Ökvist, L. S., Seppänen, M., Oyj, R. and Zuo, G. *LKAB's Experimental Blast Furnace - The Learning Curve.* In European Coke and Ironmaking Congress, ed., *The 5th European Coke and Ironmaking Congress*, pp. Tu1:3–1 – Tu1:3–14. Jernkontoret, 2005. ISBN 9197413186.

[23] Matsui, Y., Yamaguchi, Y., Sawayama, M., Kitano, S., Nagai, N. and Imai, T. *Analyses on Blast Furnace Raceway Formation by Micro Wave Reflection Gunned through Tuyere.* ISIJ International, 45(10):1432–1438, 2005.

[24] Malmberg, D., Hahlin, P. and Nilsson, E. *Microwave Technology in Steel and Metal Industry, an Overview.* ISIJ International, 47(4):533–538, 2007.

[25] Kase, M., Sugata, M., Yamaguchi, K. and Nakagome, M. *Analysis of Coke Behaviour in Raceway Using Endoscope and High-speed Camera.* Transactions of the Iron and Steel Institute of Japan, 22(10):811–819, 1982.

[26] Inatani, T., Okabe, K., Nishiyama, T., Serizawa, Y., Takahashi, H. and Saino, M. *Heavy oil combustion in blowpipe and tuyere of blast furnace.* Tetsu-to-Hagane, 62(5):514–524, 1976.

[27] Greuel, M., Hillnhütter, F. W., Kister, H. and Krüger, B. *Untersuchung der Bewegungsvorgänge vor den Blasformen eines Hochofens mit einem Endoskop.* Stahl und Eisen, 12:533–539, 1974.

[28] Mondal, S. S., Som, S. K. and Dash, S. K. *Numerical predictions on the influences of the air blast velocity, initial bed porosity and bed height on the shape and size of raceway zone in a blast furnace.* Journal of Physics D: Applied Physics, 38:1301–1307, 2005.

[29] Dong, X., Yu, A., Yagi, J.-I. and Zulli, P. *Modelling of Multiphase Flow in a Blast Furnace: Recent Developments and Future Work.* ISIJ International, 47(11):1553–1570, 2007.

[30] Peacey, J. G and Davenport, W. G. *The Iron Blast Furnace. Theory and Practice.* Pergamon Press, 1979. ISBN 0-08-0232183.

[31] Sastry, G. S. S. R. K., Gupta, G. S. and Lahiri, A. K. *Cold model study of raceway under mixed particle conditions.* Ironmaking and Steelmaking, 30(1):61–65, 2003.

[32] Biswas, A. K. *Principles of blast furnace ironmaking: Theory and practice.* Cootha, Brisbane, Australia, 1981. ISBN 0949917001.

[33] Matsuhashi, S., Kurosawa, H., Natsui, S., Kon, T., Ueda, S., Inoue, R. and Ariyama, T. *Evaluation of Coke Mixed Charging Based on Packed Bed Structure and Gas Permeability Changes in Blast Furnace by DEM-CFD Model.* ISIJ International, 52(11):1990–1999, 2012.

[34] Ameling, D. *Steel - Innovative solutions for energy and resource challenges.* In 8^{th} *International Arab Iron and Steel Conference.* Doha, Qatar, 2008.

[35] Worrell, E., Blinde, P., Neelis, M., Blomen, E. and Masanet, E. *Energy efficiency improvement and cost saving opportunities for the U.S. iron and steel industry.* Ernest Orlando Lawrence Berkeley National Laboratory, University of California, Berkelay, CA 94720, US, October, Rep. No. LBNL-4779E, 2010.

[36] Jones, D. L. *Available and emerging technologies for reducing greenhouse gas emissions from the iron and steel industry.* United States Environmental Protection Agency, Research Triangle Park, North Carolina 27711, US, 2012.

[37] Ishii, K. *Advanced pulverized coal injection technology and blast furnace operation.* Pergamon, Oxford, UK, 2000. ISBN 008043651X.

[38] Plastics Europe. *Production of plastics worldwide from 1950 to 2011.* available at: http://www.statista.com/statistics/282732/global-production-of-plastics-since-1950/, accessed 24.1.2012.

[39] Al-Salem, S. M., Lettieri, P. and Baeyens, J. *Recycling and recovery routes of plastic solid waste (PSW): A review.* Waste Management, 29(10):2625–2643, 2009.

[40] Bürgler, T., Brunnbauer, G., Pillmair, G. and Ferstl, A. *Waste plastics as reducing agent in the blast furnace process - synergies between industrial production and waste management processes.* In Stahlinstitut VDEh, ed., *METEC InSteelCon 2007,* 3^{rd} *international steel conference on new developments in metallurgical process technologies.* Düsseldorf, Germany, June 11-15, 2007.

[41] Fink, J. K. *Pyrolysis and combustion of polymer wastes in combination with metallurgical processes and the cement industry.* Journal of Analytical and Applied Pyrolysis, 51:239–252, 1999.

[42] Ziebik, A. and Stanek, W. *Forecasting of the energy effects of injecting plastic wastes into the blast furnace in comparison with other auxiliary fuels.* Energy, 26(12):1159–1173, 2001.

[43] Gupta, S., Sahajwalla, V. and Wood, J. *Simultaneous Combustion of Waste Plastics with Coal for Pulverized Coal Injection Application.* Energy & Fuels, 20(6):2557–2563, 2006.

[44] Vermeulen, I., Caneghem, J. V., Block, C., Baeyens, J. and Vandecasteele, C. *Automotive shredder residue (ASR): Reviewing its production from end-of-life vehicles (ELVs) and its recycling, energy of chemicals valorisation.* Journal of Hazardous Materials, 190(1-3):8–27, 2011.

[45] Nourreddine, M. *Recycling of auto shredder residue.* Journal of Hazardous Materials, 139(3):481–490, 2007.

[46] Martens, H. *Recyclingtechnik: Fachbuch für Lehre und Praxis.* Heidelberg: Spektrum Akademischer Verlag, Heidelberg, 2011. ISBN 978-3-8274-2640-6.

[47] Asanuma, M., Ariyama, T., Sato, M., Murai, R., Nonaka, T., Okochi, I., Tsukiji, H. and Nemoto, K. *Development of Waste Plastics Injection Process in Blast Furnace.* ISIJ International, 40(3):244–251, 2000.

[48] Asanuma, M., Kajioka, M., Kuwabara, M., Fukumoto, Y. and Terada, K. *Establishment of advanced recycling technology for waste plastics in blast furnace.* JFE Steel Corporation, Rep. No. 13, May 2009.

[49] Gibson, J. and Pistorius, P. C. *Natural Gas in Ironmaking: On the Use of DRI and LRI in the Blast Furnace Process.* In *AISTech, The Iron and Steel Technology Conference and Exposition.* Cleveland, Ohio, USA, 2015. ISBN 978-1-935117-46-9.

[50] Geerdes, M. *Coal-Gas Co-Injection in Blast Furnaces: Are There Hidden Benefits?* In *AISTech, The Iron and Steel Technology Conference and Exposition*, pp. 908–916. Cleveland, Ohio, USA, 2015. ISBN 978-1-935117-46-9.

[51] Ghanbari, H., Pettersson, F. and Saxén, H. *Sustainable development of primary steelmaking under novel blast furnace operation and injection of different reducing agents.* Chemical Engineering Science, 129:208–222, 2015.

[52] Porzio, G. F., Fornai, B., Amato, A., Matarese, N., Vannucci, M., Chiappelli, L. and Colla, V. *Reducing the energy consumption and CO_2 emissions of energy intensive industries through decision support systems – An example of application to the steel industry.* Applied Energy, 112:818–833, 2013.

[53] Bennett, P. A. and Fukushima, T. *Impact of PCI Coal Quality on Blast Furnace Operations.* In *12^{th} International Conference on Coal Science.* Cairns, Australia, Nov 2-7, 2003.

[54] Ogaki, Y., Tomioka, K., Watanabe, A., Arita, K., Kuriyama, I. and Sugayoshi, T. *Recycling of waste plastic packaging in a blast furnace system.* 2001.

[55] Sekine, Y., Fukuda, K., Kato, K., Adachi, Y. and Matsuno, Y. *CO_2 reduction potentials by utilizing waste plastics in steel works.* The International Journal of Life Cycle Assessment, 14(2):122–136, 2009.

[56] Gerlinger, P. *Numerische Verbrennungssimulation.* Springer Berlin Heidelberg New York, 2005. ISBN 3-540-23337-7.

[57] Paschedag, A. R. *CFD in der Verfahrenstechnik.* Wiley-VCH, Weinheim, 2004. ISBN 3-527-30994-2.

[58] Ferziger, J. H. and Peric, M. *Numerische Strömungsmechanik.* Springer, 2008. ISBN 978-3-540-67586-0.

[59] Kuhlmann, H. *Strömungsmechanik.* Pearson Studium, München, Deutschland, 2007. ISBN 978-3-8273-7230-7.

[60] Maier, C., Jordan, C. and Harasek, M. *Numerical Simulation of the post combustion zone of biomass firing systems.* In *Proceedings of the European Combustion Meeting.* Vienna, Austria, April 14-17, 2009.

[61] Courant, R., Friedrichs, K. and Lewy, H. *On the Partial Difference Equations of Mathematical Physics.* IBM Journal, 11:215–234, 1967.

[62] Catalano, P. and Amato, M. *An evaluation of RANS turbulence modelling for aerodynamic applications.* Aerospace Science and Technology, 7(7):493–509, 2003.

[63] Wee Siang, L. *Upstream Influence of a Porous Screen on the Flow Field of a Free Jet.* University of New South Wales, Australian Defence Force Academy, 2008.

[64] Norton, T., Sun, D.-W., Grant, J., Fallon, R. and Dodd, V. *Applications of computational fluid dynamics (CFD) in the modelling and design of ventilation systems in the agricultural industry: A review.* Bioresource Technology, 98(12):2386–2414, 2007.

[65] FLUENT. *FLUENT User's Guide, Version 6.3.26.* ANSYS CFX Inc., Canterra Resource Park 10, Cavendish Court Lebanon, 2006.

[66] Launder, B. E. and Spalding, D. B. *Lectures in mathematical models of turbulence.* New York: Academic Press and Academic Press, London and New York, 1972. ISBN 9780124380509.

[67] Smith, E., Mi, J., Nathan, G. and Dally, B. *The Round Jet Inflow-Condition Anomaly for the k-ε Turbulence Model.* In M. Behnia, W. Lin and G. D. McBain, eds., *Proceedings of the 15th Australasian Fluid Mechanics Conference.* Sydney, December 13-17, 2004. ISBN 1-864-87695-6.

[68] Dally, B. B., Riesmeier, E. and Peters, N. *Effect of fuel mixture on moderate and intense low oxygen dilution combustion.* Combustion and Flame, 137(4):418–431, 2004.

[69] Shih, T.-H., Liou, W. W., Shabbir, A., Yang, Z. and Zhu, J. *A new k-ε Eddy-Viscosity Model for High Reynolds Number Tubulent Flows - Model Development and Validation.* Computers Fluids, 24(3):227–238, 1995.

[70] Görner, K. *Technische Verbrennungssysteme.* Springer-Verlag, 1991. ISBN 3-540-53947-6.

[71] Arnaut, L., Formosinho, S. and Burrows, H. *Chemical Kinetics.* Elsevier, 2007. ISBN 978-0-444-52186-6.

[72] Blokh, A. G. *Heat Transfer in Steam Boiler Furnaces.* Springer, 1988. ISBN 3-540-18045-1.

[73] Hua, Y., Flamant, G., Lu, J. and Gauthier, D. *3D modelling of radiative heat transfer in circulating fluidized bed combustors: Influence of the particulate composition.* International Journal of Heat and Mass Transfer, 48(6):1145–1154, 2005.

[74] ANSYS Fluent. *http://www.ansys.com.* 2015.

[75] Maier, C., Jordan, C., Harasek, M., Feilmayr, C. and Thaler, C. *Implementation and Validation of a Three-Dimensional Multiphase-CFD-Model for Blast Furnace Processes.* Chemical Engineering Transactions, 29:925–930, 2012.

[76] Maier, C., Jordan, C., Harasek, M., Feilmayr, C. and Thaler, C. *Development and Validation of a CFD-Model for Heterogeneous Transfer Phenomena in Blast Furnace Processes.* In *5th International Conference from Scientific Computing to Computational Engineering IC-SCCE*, pp. 162–169. Athens, Greece, 2012. ISBN 978-960-98941-9-7.

[77] Maier, C., Jordan, C., Feilmayr, C., Thaler, C. and Harasek, M. *CFD-Simulation of the Blast Furnace Process: Injection of Heavy Oil and Plastic Particles into the Raceway.* In *AISTech, The Iron and Steel Technology Conference and Exposition*, pp. 595–607. Pittsburgh, PA, USA, 2013. ISBN 978-1-935117-32-2.

[78] Maier, C., Jordan, C., Harasek, M., Feilmayr, C. and Thaler, C. *Investigation of Alternative Reducing Agent Injection into the Raceway of Blast Furnaces using CFD.* Chemical Engineering Transactions, 35:1345–1350, 2013.

[79] Maier, C., Jordan, C., Feilmayr, C., Thaler, C. and Harasek, M. *CFD-Modeling Study of the Blast Furnace Raceway with Direct Injection of Auxiliary Reducing Agents.* In *AISTech, The Iron and Steel Technology Conference and Exposition*, pp. 583–592. Indianapolis, Ind., USA, 2014. ISBN 978-1-935117-41-4.

[80] Maier, C., Jordan, C., Feilmayr, C., Thaler, C. and Harasek, M. *Multi-Scale Modeling of Hydrocarbon Injection into the Blast Furnace Raceway.* In SINTEF, ed., *10th International Conference on CFD in Oil & Gas, Metallurgical and Process Industries*, pp. 2C1–091. Trondheim, NORWAY, 2014. ISBN 978-82-14-05741-6.

[81] Maier, C., Jordan, C., Feilmayr, C., Thaler, C. and Harasek, M. *Numerical Analysis of Injection of Liquid Hydrocarbons, Processed Waste Plastics and Pulverized Coal into Blast Furnace Raceways.* In *AISTech, The Iron and Steel Technology Conference and Exposition*, pp. 1569–1580. Cleveland, Ohio, USA, 2015. ISBN 978-1-935117-46-9.

[82] VDI. *VDI Heat Atlas.* Springer, VDI-Platz 1, 40468 Düsseldorf, Deutschland, 2 edn., 2010. ISBN 978-3-540-77876-9.

[83] Bauer, R. and Schlünder, E.-U. *Effective radial thermal conductivity of packings in gas flow, Part II: Thermal conductivity of the packing fraction without gas flow.* Int. Chem. Eng., 18:189–204, 1978.

[84] Zehner, P. and Schlünder, E.-U. *Wärmeleitfähigkeit von Schüttungen bei mäßigen Temperaturen.* Chemie Ingenieur Technik, 42:933–941, 1970.

[85] Zehner, P. and Schlünder, E.-U. *Einfluss der Wärmestrahlung und des Druckes auf den Wärmetransport in nicht durchströmten Schüttungen.* Chemie Ingenieur Technik, 44:1303–1308, 1972.

[86] Antwerpen, W. V., Toit, C. G. d. and Rousseau, P. G. *A review of correlations to model the packing structure and effective thermal conductivity in packed beds of mono-sized spherical particles.* Nuclear Engineering and Design, 240:1803–1818, 2010.

[87] Tsotsas, E. and Martin, H. *Thermal conductivity of packed beds: A review.* Chemical Engineering and Processing, 22(1):19–37, 1987.

[88] Jordan, C., Miltner, M., Potetz, A. and Harasek, M. *Modellierung turbulenter Freistrahlen mit numerischer Strömungssimulation.* Chemie Ingenieur Technik, 77(8), 2005.

[89] Gnielinski, V. *Gleichungen zur Berechnung des Wärme- und Stoffaustausches in durchströmten ruhenden Kugelschüttungen bei mittleren und großen Peclètzahlen.* Verfahrenstechnik, 12(6):363–366, 1978.

[90] Gnielinski, V. *Berechnung des Wärme- und Stoffaustauschs in durchströmten ruhenden Schüttungen.* Verfahrenstechnik, 16(1):36–39, 1982.

[91] Magnussen, B. F. *On the structure of turbulence and a generalized eddy dissipation concept for chemical reaction in turbulent flow.* In *19th American Institute of Aeronautics and Astronautics Aerospace Science Meeting.* January 12-15, 1981.

[92] Chejne, F. and Hernandez, J. P. *Modelling and simulation of coal gasification process in fluidised bed.* Fuel, 81(13):1687–1702, 2002.

[93] Kok, M. V. and Gundogar, A. S. *DSC study on combustion and pyrolysis behaviors of Turkish crude oils.* Fuel Processing Technology, 116:110–115, 2013.

[94] Abbas, H. F. F. and Daud, W. A. M. *Thermocatalytic decomposition of methane using palm shell based activated carbon: Kinetic and deactivation studies.* Fuel Processing Technology, 90(9):1167–1174, 2009.

[95] Tepper, H. *Zur Vergasung von Rest- und Abfallholz in Wirbelschichtreaktoren für dezentrale Energieversorgungsanlagen.* Ph.D. thesis, Otto-von-Guericke-Universität Magdeburg, 2005.

[96] Rumpel, S. *Die autotherme Wirbelschichtpyrolyse zur Erzeugung heizwertreicher Stützbrennstoffe.* Ph.D. thesis, Institut für Technische Chemie, Universität Karlsruhe, 2000.

[97] Liu, G.-S. and Niksa, S. *Coal conversion submodels for design applications at elevated pressures. Part II. Char gasification.* Progress in Energy and Combustion Science, 30(6):679–717, 2004.

[98] Gemmen, R. S. and Trembly, J. *On the mechanisms and behavior of coal syngas transport and reaction within the anode of a solid oxide fuel cell.* Journal of Power Sources, 161:1084–1095, 2006.

[99] Perry, R. H., Perry, R. H., Green, D. W. and Maloney, J. O. *Perry's chemical engineers' handbook.* McGraw-Hill, New York, 7 edn., 1997. ISBN 0-07-049841-5.

[100] Wilke, C. R. *Diffusional properties of multicomponent gases.* Chem. Eng. Prog., 46(2):95–104, 1950.

[101] Fuller, E. N., Ensley, K. and Giddings, C. J. *Diffusion of halogenated hydrocarbons in helium. The effect of structure on collision cross sections.* The Journal of Physical Chemistry, 73(11):3679–3685, 1969.

[102] Petrovic, L. C. and Thodos, G. *Mass transfer in the flow of gases through packed beds.* Ind. Eng. Chem. Fundam., 7(2):274–280, 1968.

[103] Corella, J., Herguido, J., Toledo, J. M. and Gomez-Civicos, J. I. *Modeling Fluidized Bed Biomass Gasifiers. Part II: Gasification with Steam in a Bubbling Fluidized Bed.* In S. Kyritsis, ed., *1st World Conference on Biomass for Energy and Industry.* James & James, London, 2001. ISBN 9781902916156.

[104] Taba, L. E., Irfan, M. F., Daud, W. A. M. W. and Chakrabarti, M. H. *The effect of temperature on various parameters in coal, biomass and CO-gasification: A review.* Renewable and Sustainable Energy Reviews, 16(8):5584–5596, 2012.

[105] Irfan, M. F., Usman, M. R. and Kusakabe, K. *Coal gasification in CO_2 atmosphere and its kinetics since 1948: A brief review.* Energy, 36(1):12–40, 2011.

[106] Trommer, D., Noembrini, F., Fasciana, M., Rodriguez, D., Morales, A., Romero, M. and Steinfeld, A. *Hydrogen production by steam-gasification of petroleum coke using concentrated solar power. Thermodynamic and kinetic analyses.* International Journal of Hydrogen Energy, 30(6):605–618, 2005.

[107] Blasi, C. *Modeling wood gasification in a countercurrent fixed-bed reactor.* AIChE Journal, 50(9):2306–2319, 2004.

[108] Wall, T. F., Liu, G.-S., Wu, H.-W., Roberts, D. G., Benfell, K. E., Gupta, S., Lucas, J. A. and Harris, D. J. *The effects of pressure on coal reactions during pulverised coal combustion and gasification.* Progress in Energy and Combustion Science, 28(5):405–433, 2002.

[109] Hobbs, M. L., Radulovic, P. T. and Smoot, L. D. *Modeling Fixed-Bed Coal Gasifiers.* AIChE Journal, 38:681–702, 1992.

[110] Lemmon, E. W., McLinden, M. O. and Friend, D. G. *Thermophysical Properties of Fluid Systems in NIST Chemistry WebBook.* National Institute of Standards and Technology, 2014.

[111] Zaïmi, S. A., Akiyama, T., Guillot, J.-B. and Yagi, J.-I. *Validation of a Blast Furnace Solid Flow Model Using Reliable 3-D Experimental Results.* ISIJ International, 40(4):332–341, 2000.

[112] Wen, L. and Bi, X. T. *Simulation of cavity formation hysteresis in the presence of granular compaction.* Chemical Engineering Science, 66:674–681, 2011.

[113] Zhou, C. Q. *CFD Modeling for High Rate Pulverized Coal Injection (PCI) into the Blast Furnace.* Purdue University - Calumet, Dept. of Mechanical Engineering, Hammond, Indiana 46321, USA, Rep. No. DE-FC36-97ID13554, 2008.

[114] Fu, D., Zheng, D., Zhou, C. Q., D'Alessio, J., Ferron, K. J. and Zhao, Y. *Parametric studies on PCI performances.* In *Proceedings of the ASME/JSME 2011 8th Thermal Engineering Joint Conference.* Honolulu, Hawaii, USA, May 13-17, 2011.

[115] Nogami, H., Yamaoka, H. and Takatani, K. *Raceway Design for the Innovative Blast Furnace.* ISIJ International, 44(12):2150–2158, 2004.

[116] Hager, A. *CFD-DEM on Multiple Scales - An Extensive Investigation of Particle-Fluid Interactions.* Ph.D. thesis, Johannes Kepler Universität Linz, Linz, Österreich, 2014.

[117] Wright, B., Zulli, P., Zhou, Z. Y. and Yu, A. B. *Gas-solid flow in an ironmaking blast furnace - I: Physical modelling.* Powder Technology, 208(1):86–97, 2011.

[118] Zhang, J.-L., Chen, Y.-X., Fan, Z.-Y., Hu, Z.-W., Yang, T.-J. and Ariyama, T. *Influence of Profile of Blast Furnace on Motion and Stress of Burden by 3D-DEM.* Journal of Iron and Steel Research, International, 18(11):1–11, 2011.

[119] Zhou, Z. Y., Zhu, H. P., Yu, A. B., Wright, B. and Zulli, P. *Discrete particle simulation of gas-solid flow in a blast furnace.* Computers & Chemical Engineering, 32(8):1760–1772, 2008.

[120] Zhou, Z. Y., Zhu, H. P., Wright, B., Yu, A. B. and Zulli, P. *Gas-solid flow in an ironmaking blast furnace-II: Discrete particle simulation.* Powder Technology, 208(1):72–85, 2011.

[121] Nogami, H. and Yagi, J.-I. *An Application of Bingham Model to Viscous Fluid Modeling of Solid Flow in Moving Bed.* ISIJ International, 44(11):1826–1834, 2004.

[122] Zhang, S. J., Yu, A. B., Zulli, P., Wright, B. and Tüzün, U. *Modelling of the Solids Flow in a Blast Furnace.* ISIJ International, 38:1311–1319, 1998.

[123] Schatz, A. *Lump Ore, Pellets and Dead Men.* Ph.D. thesis, Johannes Kepler Universität Linz, Linz, Österreich, 2000.

[124] Chen, J., Akiyama, T., Nogami, H., Yagi, J.-I. and Takahashi, H. *Modeling of Solid Flow in Moving Beds.* ISIJ International, 33(6):664–671, 1993.

[125] Rajneesh, S. and Gupta, G. S. *Importance of frictional forces on the formation of cavity in a packed bed under cross flow of gas.* Powder Technology, 134(1-2):72–85, 2003.

[126] Haider, A. and Levenspiel, O. *Drag Coefficient and Terminal Velocity of Spherical and Nonspherical Particles.* Powder Technology, 58:63–70, 1989.

[127] Jordan, C., Maier, C., Polster, R., Harasek, F. and Winter, F. *Die Bildung von H_2 und CO durch Eindüsung von gasförmigen, flüssigen und festen Einsatzstoffen in den Hochofen.* Technische Universität Wien, Rep. No. TU-ThVT-1662-2008011, September 2008.

[128] Kirchbacher, F. *Experimentelle Untersuchung von industriellen Sprühdüsen.* BSc Thesis. Technische Universität Wien, Institut für Verfahrenstechnik, Umwelttechnik und technische Biowissenschaften, Wien, Österreich, 2011.

[129] Zauner, F. *Experimentelle Analyse von industriellen Sprühdüsen.* MSc Thesis. Technische Universität Wien, Institut für Verfahrenstechnik, Umwelttechnik und technische Biowissenschaften, Wien, Österreich, 2010.

[130] Nagy, J. *Untersuchung von mehrphasigen, kompressiblen Strömungen durch Simulation und Experiment.* Ph.D. thesis, Technische Universität Wien, Institut für Verfahrenstechnik, Umwelttechnik und technische Biowissenschaften, Wien, Österreich, 2012.

[131] Harasek, M., Jordan, C., Maier, C., Feilmayr, C. and Schuster, S. *Advances in the CFD Modeling of Raceway Injections.* In *AISTech 2012 The Iron & Steel Technology Conference and Exposition.* Atlanta, GA, 2012.

[132] Maier, C., Jordan, C., Bolhar-Nordenkampf, M. and Harasek, M. *Investigation of Reagent Injection in SNCR-Systems of Biomass Fired Combustion Facilities using Computational Fluid Dynamics.* In W. Leuckel, A. Reis and J. Ward, eds., *Proceedings of the 9th European Conference on Industrial Furnaces and Boilers.* Palacio Estoril Hotel, Estoril, Portugal, April 2011. ISBN 978-972-99309-6-6.

[133] Paloposki, T. and Hakala, J. *Injection of Residual Fuel Oil into a Blast Furnace.* In *Finnish-Swedish Flame Days.* Naantali, Finland, September 3-4, 1996.

[134] Lackner, M., Schwarzott, M., Liedl, G., Feilmayr, C., Schuster, S. and Winter, F. *Heat transfer to a single plastic resin particle - Experimental investigations by flames and laser pulses.* In *Proceedings of the 3rd European Combustion Meeting.* Crete, Greece, April 11-13, 2007.

[135] Shang, Q. and Zhang, J. *Simulation of gas-particle turbulent combustion in a pulverized coal-fired swirl combustor.* Fuel, 88(1):31–39, 2009.

[136] Belosevic, S. *Modeling Approaches to Predict Biomass Co-firing with Pulverized Coal.* The Open Thermodynamics Journal, 4(1):50–70, 2010.

[137] Wu, L., Paterson, N., Dugwell, D. R. and Kandiyoti, R. *Simulation of Blast-Furnace Tuyere and Raceway Conditions in a Wire Mesh Reactor: Extents of Combustion and Gasification.* Energy & Fuels, 21:2325–2334, 2007.

[138] Löffler, G., Andahazy, D., Wartha, C., Winter, F. and Hofbauer, H. *NO_x and N_2O Formation Mechanisms-A Detailed Chemical Kinetic Modeling Study on a Single Fuel Particle in a Laboratory-Scale Fluidized Bed.* Journal of Energy Resources Technology, 123(3):228, 2001.

[139] Puttiner, S. and König, B. *Hochgeschwindigkeitsaufnahme der Injektion alternativer Reduktionsmittel in die Raceway von Hochöfen.* 2013.

[140] Ranade, V. V. and Gupta, D. F. *Computational modeling of pulverized coal fired boilers.* CRC Press, 2014. ISBN 978-1-4822-1535-1.

[141] Ranz, W. E. and Marshall, W. R. *Evaporation from Drops, Part I.* Chem. Eng. Prog., 48(3):141–146, 1952.

[142] Ranz, W. E. and Marshall, W. R. *Evaporation from Drops, Part II.* Chem. Eng. Prog., 48(4):173–180, 1952.

[143] Maloney, D. J., Sampath, R. and Zondlo, J. W. *Heat capacity and thermal conductivity considerations for coal particles during the early stages of rapid heating.* Combustion and Flame, 116(1-2):94–104, 1999.

[144] Shen, Y. S., Guo, B. Y., Yu, A. B., Austin, P. R. and Zulli, P. *Three-dimensional modelling of in-furnace coal/coke combustion in a blast furnace.* Fuel, 90(2):728–738, 2011.

[145] Ubhayakar, S. K., Stickler, D. B., Rosenberg, C. W. and Ganon, R. E. *Rapid devolatilization of pulverized coal in hot combustion gases.* In *16th Symposium (International) on Combustion*, pp. 427–436. Pittsburgh, PA, USA, 1976.

[146] Shen, Y., Guo, B., Yu, A., Maldonado, D., Austin, P. and Zulli, P. *Three-dimensional Modelling of Coal Combustion in Blast Furnace.* ISIJ International, 48(6):777–786, 2008.

[147] Gale, T. K., Bartholomew, C. H. and Fletcher, T. H. *Decreases in the swelling and porosity of bituminous coals during devolatilization at high heating rates.* Combustion and Flame, 100(1-2):94–100, 1995.

[148] Lockwood, F. C., Rizvi, S. M. A. and Shah, N. G. *Comparative Predictive Experience of Coal Firing.* Proceedings of the Institution of Mechanical Engineers, Part C: Journal of Mechanical Engineering Science, 200(2):79–87, 1986.

[149] Gibb, J. *Combustion of residual char remaining after devolatilization.* In *Lecture at Course of Pulverised Coal Combustion.* Imperial College, London, 1985.

[150] Shen, Y., Yu, A., Austin, P. and Zulli, P. *Modelling in-furnace phenomena of pulverized coal injection in ironmaking blast furnace: Effect of coke bed porosities.* Minerals Engineering, 33:54–65, 2012.

[151] Marshall, E. M. and Bakker, A. *Computational Fluid Mixing.* John Wiley, 2003. ISBN 0-9719532-0-1.

[152] IAEA. *Heat Transport and Afterheat Removal for Gas Cooled Reactors Under Accident Conditions.* International Atomic Energy Agency, Nuclear Power Technology Development Section, Wagramerstrasse 5, A-1400 Vienna, Austria, Rep. No. IAEA-TECDOC-1163, 2000.

[153] Durst, F. and Trimis, D. *Compact low emission combustion reactors with integrated heat exchangers using porous medium combustion.* In *Proceedings of the First European Conference on Small Burner Technology and Heating Equipment.* Zürich, Switzerland, Septemer 25-26, 1996.

[154] Steene, L., Tagutchou, J. P., Mermoud, F., Martin, E. and Salvador, S. *A new experimental Continuous Fixed Bed Reactor to characterise wood char gasification.* Fuel, 89(11):3320–3329, 2010.

[155] Maier, C., Jordan, C., Harasek, M., Feilmayr, C. and Thaler, C. *Investigation of Alternative Reducing Agent Injection into the Raceway of Blast Furnaces using CFD.* In *16th Conference on Process Integration, Modelling and Optimisation for Energy Saving and Pollution Reduction.* Rhodes, Greece, September 29 - October 2, 2013. ISBN 978-88-95608-26-6.

[156] Shen, Y. S., Maldonado, D., Guo, B. Y., Yu, A. B., Austin, P. and Zulli, P. *Computational Fluid Dynamics Study of Pulverized Coal Combustion in Blast Furnace Raceway.* Industrial & Engineering Chemistry Research, 48(23):10314–10323, 2009.

[157] Maldonado, D., Austin, P., Zulli. P. and Guo, B. *Modelling Coal Combustion Behaviour in an Ironmaking Blast Furnace Raceway - Model Development and Applications.* In *AISTech 2008*, pp. 331–344. Association for Iron & Steel Technology, Warrendale, Pa., 2008. ISBN 978-193511701-8.

[158] Giese, M. *Strömung in porösen Medien unter Berücksichtigung effektiver Viskositäten.* Ph.D. thesis, TU München, 1998.

[159] Dixon, A. G. *Wall and particle-shape effects on heat transfer in packed beds.* Chemical Engineering Communications, 71:217–237, 1988.

[160] Babkin, V. S., Korzhavin, A. A. and Bunev, V. A. *Propagation of premixed gaseous explosion flames in porous media.* Combustion and Flame, 87(2):182–190, 1991.

[161] Mujeebu, M. Abdul, Abdullah, M. Z., Bakar, M. A., Mohamad, A. A. and Abdullah, M. K. *Applications of porous media combustion technology - A review.* Applied Energy, 86(9):1365–1375, 2009.

[162] Trimis, D. and Durst, F. *Combustion in a Porous Medium - Advances and Applications.* Combustion Science and Technology, 121(1):153–168, 1996.

[163] Mujeebu, M. Abdul, Abdullah, M. Zulkifly, Mohamad, A. A. and Bakar, M. A. *Trends in modeling of porous media combustion.* Progress in Energy and Combustion Science, 36(6):627–650, 2010.

[164] Durst, F. and Trimis, D. *Combustion by Free Flames Versus Combustion Reactors.* In *Proceedings of the 4^{th} International Conference on Technologies and Combustion for a Clean Environment*, vol. 11, p. IL 7. 1997.

[165] Magnussen, B. F. and Hjertager, B. H. *On mathematical modeling of turbulent combustion with special emphasis on soot formation and combustion.* Symposium (International) on Combustion, 16(1):719–729, 1977.

[166] Farzaneh, M., Ebrahimi, R., Shams, M. and Shafiey, M. *Numerical simulation of thermal performance of a porous burner.* Chemical Engineering and Processing, 48(2):623–632, 2009.

[167] Hsu, C. T., Cheng, P. and Wong, K. W. *Modified Zehner-Schlünder models for stagnant thermal conductivity of porous media.* Int. J. Heat Mass Transfer, 37(17):2751–2759, 1994.

[168] Maier, C., Jordan, C. and Harasek, M. *Investigation of the Gas-Phase Combustion in the Post Combustion Zone of Fluidized Bed Firing Systems.* In C. Jordan, ed., *Minisymposium Verfahrenstechnik*, vol. 5. June 25, 2009. ISBN 978-3950273106.

[169] Diez, M. A., Alvarez, R. and Barriocanal, C. *Coal for metallurgical coke production: predictions of coke quality and future requirements for cokemaking.* Coal Geology, 50:389–412, 2002.

[170] ASTM International. *Test Method for Measuring Coke Reactivity Index (CRI) and Coke Strength After Reaction (CSR).* West Conshohocken, PA, No. D5341, 2010.

[171] Lundgren, M., Okvist, L. S. and Björkman, B. *Coke Reactivity under Blast Furnace Conditions and in the CSR/CRI Test.* Steel Research, 80(6):396–401, 2009.

[172] Sakurovs, R. and Burke, L. *Influence of gas composition on the reactivity of cokes.* Fuel Processing Technology, 92(6):1220–1224, 2011.

[173] voestalpine Stahl GmbH. *www.voestalpine.com.* accessed 06.03.2015.